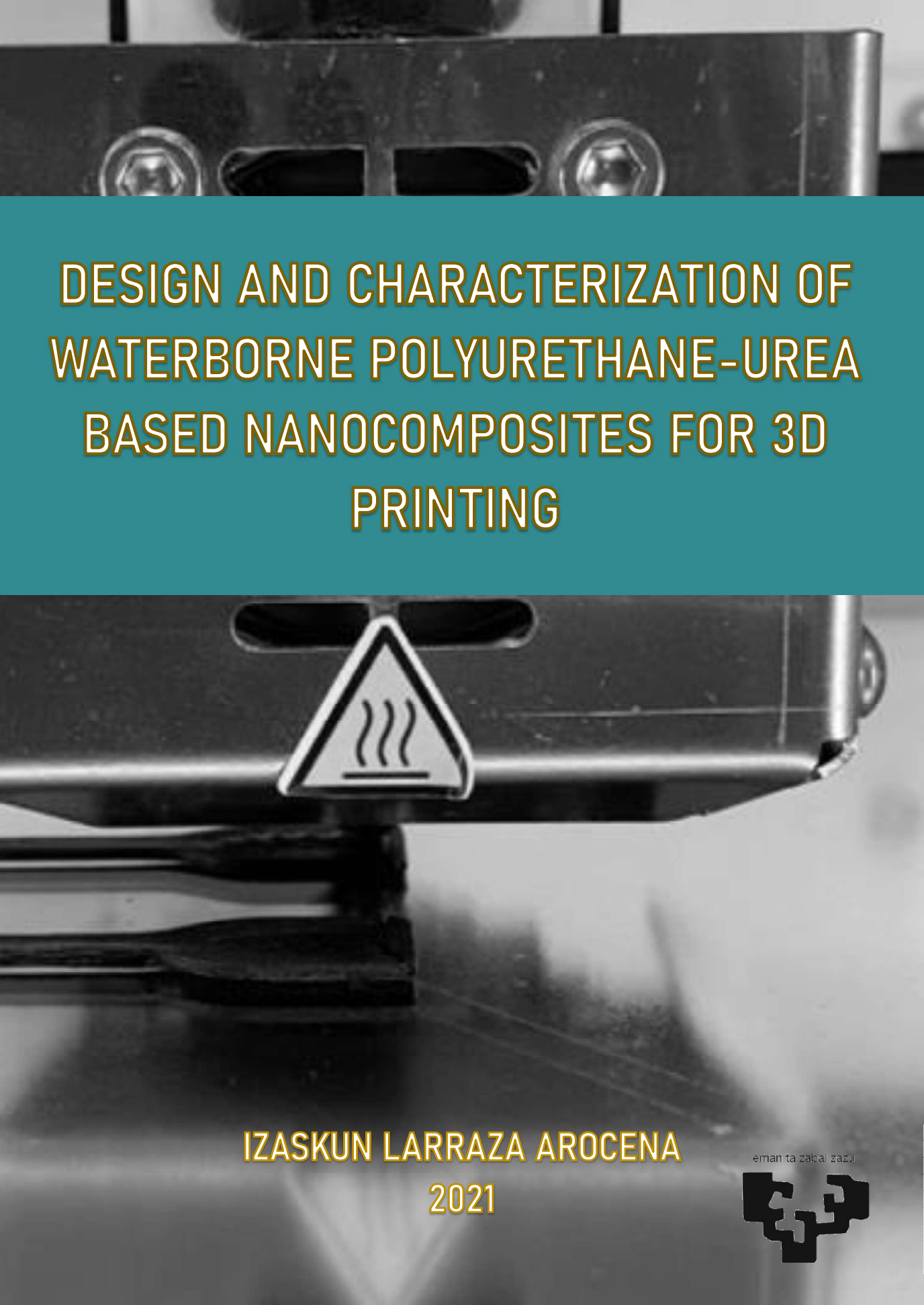

DESIGN AND CHARACTERIZATION OF WATERBORNE POLYURETHANE-UREA BASED NANOCOMPOSITES FOR 3D PRINTING

IZASKUN LARRAZA AROCENA

2021

eman ta zabal zazu

Izaskun Larraza Arocena
Faculty of Engineering, Gipuzkoa
Donostia/San Sebastian, December 2021

Design and Characterization of Waterborne Polyurethane-Urea based Nanocomposites for 3D Printing

PhD dissertation presented by

IZASKUN LARRAZA AROCENA

Supervised by

Dr. AITOR ARBELAIZ GARMENDIA and Dr. ARANTXA ECEIZA MENDIGUREN

Donostia/San Sebastian, December 2021

ACKNOWLEDGEMENTS

First of all, I would express my sincere gratitude to my supervisors, Dr. Arantxa Eceiza and Dr. Aitor Arbelaiz. Thank you for trusting me in the development of this work and thank you for your patience, disposition and support during these years.

I would also like to thank the Basque Government (PRE_2017_1_0085) and the University of the Basque Country (UPV/EHU) for the financial support in this professional opportunity.

I would like to thank the Advanced Research Facilities (SGIker) of the UPV/EHU for the technical and personal support, as well as for the chance to use the infrastructure and equipment necessary for the development of this work. I would specially like to thank the Macrobehavior-Mesostructure-Nanotechnology service and Dr. Loli Martin, for her unmeasurable help and advices.

I would also like to express my honest gratitude to Dr. Filomena Barreiro, from the Mountain Research Centre (CIMO) at the Polytechnic Institute of Bragança (IPB), for allowing me to collaborate with them during my three-month exchange in their laboratories.

In the same regard, I would also like to thank Dr. Ana Alonso Varona (Department of Cell Biology and Histology, Faculty of Medicine, UPV/EHU) for her help in the biocompatibility tests.

I would also like to show my earnest gratitude to all my colleagues from the 'Materials + Technologies' group (GMT), from the Department of Chemical and Environmental Engineering (UPV/EHU), from their unconditional help through these years.

Last, I want to thank my family and friends for their constant understanding and support.

SUMMARY

This research study focuses on the development of polyurethane-urea based materials suitable for 3D printing. For this, first, a waterborne polyurethane-urea was synthesized using a renewable sourced polyol and the stability of the dispersion, as well as the properties of the final polymer, were characterized.

Different types of reinforcements were prepared, optimized and characterized and were later used for nanocomposites films preparation. In this regards, cellulose nanofibers, carboxylated cellulose nanofibers, graphene and graphene oxide were employed. Films with different reinforcement type and content were characterized, regarding their morphology and physico-chemical, thermal and mechanical behavior, and composites showing best potential were selected for further processing in 3D printing.

Two types of 3D printing methods were analyzed in this study, fused deposition modeling and direct ink writing. For fused deposition modeling, selected nanocomposite compositions were used to prepare filaments. The effect of the incorporation route, ex-situ and in-situ addition of the nanoreinforcements, was also studied. Thermal and mechanical properties of the filaments were analyzed and were directly related to their printability.

On the other hand, the use of cellulose nanofibers and graphene containing nanocomposites on direct ink writing 3D printing was also studied. In order to prepare inks suitable for this type of 3D printing, the modulation of the rheology of the polyurethane-urea dispersion was necessary. To do so, in the case of cellulose nanofibers containing composites, the use of high quantities of reinforcement was necessary, whereas for graphene containing inks, the addition of a new component was employed. The composition of the inks strongly affected the rheological behavior of the materials, which directly related to the printability and shape fidelity exhibited by the inks. The properties of the 3D printed parts were also characterized.

Last, in order to supply new functionalities to the materials, as is bioactive behavior, different plant extracts were added to a waterborne polyurethane-urea matrix, via ex-situ and in-situ addition. In this case, for rheological optimization, high solid contents waterborne polyurethane-ureas were synthesized. The rheological behavior of the inks was analyzed, as well as the bioactive behavior of the freeze-dried samples. Inks showing best rheological properties were tested in direct ink writing 3D printing and morphology and mechanical properties of the printed parts were studied.

TABLE OF CONTENTS

Chapter 1

INTRODUCTION

1. INTRODUCTION

1.1. Motivation

The increasing environmental awareness has resulted in a growing demand for more environmentally friendly materials in order to substitute more polluting conventional alternatives [1,2], as well as in the development of new more efficient and lower-residue producing processing techniques [3]. The plastic industry is one of the most affected sectors and, due to the stricter legislations implemented in the last decade [4], there is a strong need for more eco-friendly materials.

Among different polymers, polyurethanes (PU) and polyurethane-ureas (PUU) have come up as a potential alternative to conventional materials, thanks to their great versatility and wide field of applications [5]. Though traditional PU and PUU are not environmentally friendly, in the last years the possibility to completely alter this is being studied. The will to reduce toxicity during PU and PUU synthesis resulted in the preparation of waterborne polyurethanes (WBPU) and waterborne polyurethane-ureas (WBPUU). WBPU and WBPUU are obtained in the form of aqueous dispersions and their synthesis is characterized by being organic solvent-free [6]. Moreover, the use of green precursors as a substitute for petrol-borne conventional ones has gain great interest. Polyols and isocyanates obtained from different eco-friendly sources can be used to produce polyurethanes and polyurethane-ureas, and have shown ability to form materials with great properties [7-10].

The aqueous dispersion state of these materials facilitates the preparation of nanocomposites. Hydrophilic reinforcements show great miscibility with WBPU and WBPUU and are, thus, a great option for composites preparation. Cellulose is the most abundant organic compound on Earth [11,12], and its nanoentities have shown great reinforcement capacity, thanks to their great specific mechanical and chemical properties, low density, biodegradability,

biocompatibility and natural availability [13,14]. Furthermore, cellulose nanoentities often show great affinity with polymer matrices, however, in order to further improve this affinity, the functionalization of the cellulose structure can be carried out [14-16]. By this functionalization, carboxylic groups can be inserted in the cellulose structure to optimize the miscibility of cellulose with different compounds.

The use of carbonaceous nanostructures as nanoreinforcements in a polymeric matrix can also be of great interest. The large natural availability of carbon and the great specific properties of carbon composed materials have popularized the use of these materials as reinforcements [17]. Graphene and graphene oxide present extraordinary properties, such as extremely high aspect ratio, stiffness and barrier properties [18-20]. Graphene shows, also, good electrical conductivity [21,22]. Moreover, the oxygenated groups in graphene oxide grant it strong hydrophilicity, which would be extremely beneficial for nanocomposites preparation with a WBPU or WBPUU matrix.

Regarding processing techniques, additive manufacturing (AM), also known as three-dimensional (3D) printing, has emerged as a new method for material processing. The simplicity to fabricate tailor-made parts has facilitated the creation of printed parts for personal use, and more importantly, has had a huge impact in the creation of custom made personalized parts for the very demanding biomedical field [23-25]. Though important advances in the development of this technology have taken place, a need for new materials valid for this processing method has emerged. In this field, the use of WBPUU/cellulose nanoentities and WBPUU/carbonaceous materials nanocomposites could be of great interest, due to their tailor-made properties and new functionalities that could be added.

The implementation of bioactive and bactericide behavior to the materials could be very beneficial for some fields of applications. The addition of natural extracts has shown great potential regarding these characteristics [26-28].

Moreover, their natural existence and very diverse structures make them a very appealing option for composite preparation.

Therefore, in this work, a waterborne polyurethane-urea matrix was synthesized, parting from a polyol from a renewable source, and it was later reinforced with different types of reinforcements to supply it with different properties. Cellulose nanofibers and carboxylated cellulosed nanofibers were used as reinforcements, as well as carbonaceous nanostructures. Natural plant extracts were employed with the intention to add bioactive properties. Furthermore, the use of these materials for different types of 3D printing was assessed, and the characteristics of the produced materials were analyzed.

1.2. Polyurethanes and polyurethane-ureas

Polyurethanes and polyurethane-ureas are polymers with a wide range of properties, which allows them to be used in a wide field of applications, such as the automotive, textile, construction, biomedical and aerospace sectors [6,29-33].

Polyurethanes are formed by the reaction between an alcohol and an isocyanate, from which the urethane groups is formed (Figure 1.1a). In the case of polyurethane-ureas, besides the urethane groups, urea groups are also present, which are formed by the reaction of isocyanate and amine groups (Figure 1.1b).

a)

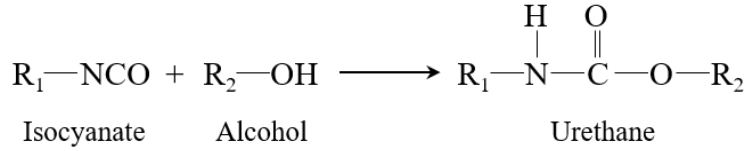

b)

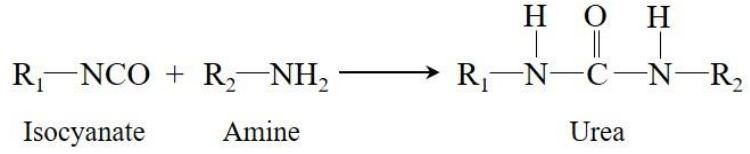

Figure 1.1. Addition reaction for a) urethane and b) urea groups formation

Polyurethanes and polyurethane-ureas are block-copolymers usually formed by two incompatible segments, usually denoted as the soft segment (SS) and the hard segment (HS). The soft segment is composed by a high molecular weight macrodiol, whereas the hard segment consists on the isocyanate and the chain extender [34]. A schematic representation of segments separation in polyurethane structures can be seen in Figure 1.2. Each segment of the polymer grants it different properties, thus, varying segment ratios, properties of the final material can be easily tailored [35]. Moreover, depending on the chemical structures of the precursors chosen, the properties of the final material will also be altered. Moreover, the different segments can be amorphous or semicrystalline, thus showing different characteristic thermal transitions that determine not only the mechanical properties at room temperature, but also the thermomechanical stability. The synthesis process for the polyurethane and polyurethane-urea preparation will further affect their properties.

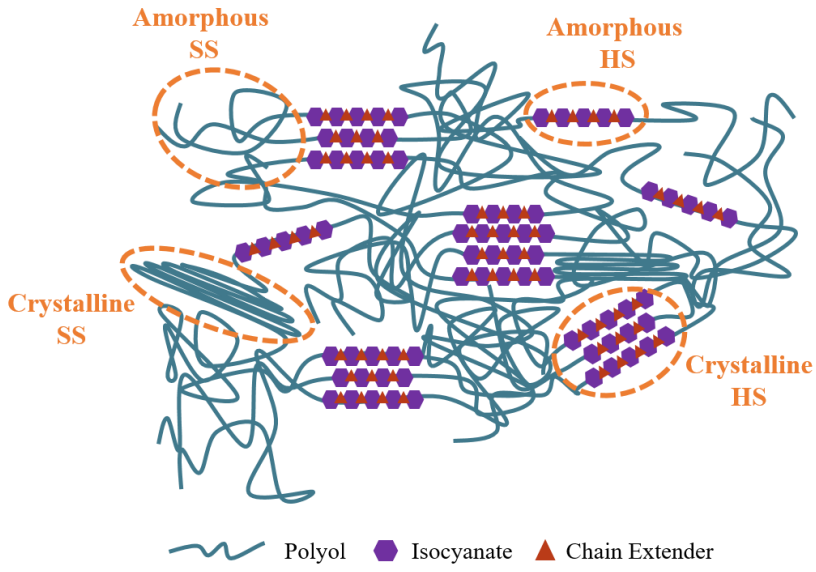

Figure 1.2. Schematic representation of the hard and soft segments separation in polyurethanes and polyurethane-ureas

1.2.1. Waterborne polyurethanes and polyurethane-ureas

Waterborne polyurethanes and polyurethane-ureas are a type of polyurethane obtained in a mainly solvent-free synthesis process. The evolution of legislation towards the reduction of volatile organic compounds (VOC) and the search for environmentally friendly products, resulted in a boom in the development of these materials [6].

PU and PUU are highly hydrophobic, thus for the obtention of an aqueous polyurethane and polyurethane-urea dispersions, a modification on their structure is necessary. For the synthesis of these waterborne polymers, the use of an internal emulsifier is necessary. Emulsifiers are usually hydrophilic monomers with ionic functionalities [6], which provide stability to the particle during the phase inversion step of the synthesis.

The eco-friendlier behavior of waterborne polyurethanes and waterborne polyurethane-ureas is not the only reason for their popularity, their main interest lays on the high quality shown by these materials. WBPU and WBPUU show high molecular weights, good processability and great properties regarding their thermal, mechanical and thermo-mechanical behavior [6,36,37]. Waterborne polyurethanes and polyurethane-ureas are used in many industrial applications, such as coatings, adhesives, synthetic leathers, biomaterials, packaging, textiles and many more [6].

1.2.2. Reactants

The characteristics of the reactants used in the synthesis of WBPU and WBPUU will have a huge impact in the properties of the resulting materials. The main reactants used in their synthesis are polyols, isocyanates and chain extenders. Other reactants such as the internal emulsifier and the catalyst are, also, to be considered when selecting components.

Polyols

Polyols are macromolecules containing hydroxyl functional groups on their chains. They show medium to high molecular weights, 200-8000 $g \cdot mol^{-1}$ and functionalities between 2 and 8. The most common types of polyols used in polyurethanes synthesis are polyester and polyether polyols.

Polyols constitute the soft segment of the polyurethane and polyurethane-urea chains and usually supply flexibility to the systems. However, there are many different types of polyols and the differences in their molecular weight, structure and crystallinity will have a strong effect in the final properties of the synthesized material. The functionality of the polyol also has a massive impact on the production of polyurethanes. For thermoplastic polyurethanes, polyols with a functionality of 2 are used, whereas higher functionalities are often used to produce thermoset systems [38,39].

Moreover, due to environmental concerns, in recent years there has been a growing interest in the use of polyols from renewable sources. The substitution of conventional polyols with polyols obtained from vegetable oils is a cheap and environmentally-friendly option [41-43]. Precursors obtained from renewable sources are already being used in the synthesis of polyurethane dispersions, such as polyols from castor oil [7] and soybean oil [8], and have shown great performance. Green sourced polyols provide many benefits to the materials, such as high resistance and stiffness, low toxicity and usually inherent biodegradability [42,43]

Isocyanates

There are many different types of isocyanates in the market, each with particular properties. Different isocyanates can be used depending on the intended application. In the case of waterborne polyurethanes and polyurethane-ureas, diisocyanates tend to be used. Moreover, the structure of

the compound will have a big influence in the properties of the resulting material.

Aromatic isocyanates are very popular, mainly due to the good mechanical properties they supply to the polymer, being toluene diisocyanate (TDI) and 4,4'-diphenylmethane diisocyanate (MDI) the most commonly used ones [44]. However, aliphatic diisocyanates also show some benefits, such as higher biocompatibility and higher thermal and hydrolytic stability [45,46]. Aliphatic diisocyanates also present lower reactivity, which is necessary in the case of waterborne polyurethanes and polyurethane-ureas. This lower reactivity allows a better control of the reaction process and reduces the risk of the reaction with water taking place [47]. Isophorone diisocyante (IPDI) is one of the most commonly used isocyanate in the synthesis of aqueous polyurethanes. IPDI is characterized by its non-linear and asymmetric structure, which leads to structures with lower crystallinity [48].

Chain extenders

Chain extenders are usually low molecular weight difunctional molecules [49]. However, in order to achieve crosslinked structures, chain extenders with higher functionalities can be used [50]. Chain extenders, though usually added in very low quantities, have a strong impact in the final properties of the polymers [51].

Low molecular weight diols and diamines are used as chain extenders for polyurethane and polyurethane-ureas, respectively [52]. The OH groups in the diol will react with the NCO groups in the isocyanate to form urethane groups. In contrast, the NH_2 groups in the diamine will react with the NCO groups to form urea groups, as seen in Figure 1.1. The most commonly used chain extenders in waterborne polyurethane-urea synthesis are hydrazine and ethylendiamine (EDA).

Internal emulsifiers

Different types of internal emulsifiers can be used in the synthesis of waterborne polyurethane and polyurethane-ureas. For different types of WBPU and WBPUU, emulsifiers with different natures will be used, being them classified into non-ionic and ionic, and among ionic into cationic and anionic [53]. In general, ionic dispersions are more common, and among them, anionic dispersions prevail, though cationic polyurethanes and polyurethane-ureas are gaining interest, since both types show good final properties. Regarding anionic emulsifiers, one of the most commonly used emulsifiers is 2,2-bis(hydroxymethyl) propionic acid (DMPA).

Neutralizing agent

The neutralizing agent consist in bases which are used to neutralize some or all of the carboxyl or sulfonic groups of the emulsifier. Often, tertiary amines, alkali metal hydroxides or mixtures of the two are used [54]. Tertiary amines are usually preferred, and among them triethylamine is the most commonly used one. The degree of neutralization is also important. Usually a neutralization between 70-100 equivalent % is used. The neutralizing agent, together with the internal emulsifier, form the electric double layer that grants stabilization to the polyurethane and polyurethane-urea particles.

Catalyst

The use of catalyst in polyurethane and polyurethane-ureas synthesis reactions are often necessary to accelerate the reaction between the polyol and the isocyanate, even more so for waterborne polyurethanes and polyurethane-ureas when lower reactivity precursors are employed. Often, tertiary amines such as 1,4-diazabicyclo octane (DABCO) and tryethylamine (TEA) are used, or organo tin compounds, such as dibutyltin dilaurate (DBTDL) and stannous octoate (SnOc) [32].

1.2.3. Synthesis process

The synthesis of waterborne polyurethanes and waterborne polyurethane-ureas can be carried out through different methods [6], however the two-step polymerization process is the most common one. In the first step, the prepolymer, formed by the polyol and the isocyanate, is obtained; and in the second step the chain extension is carried out.

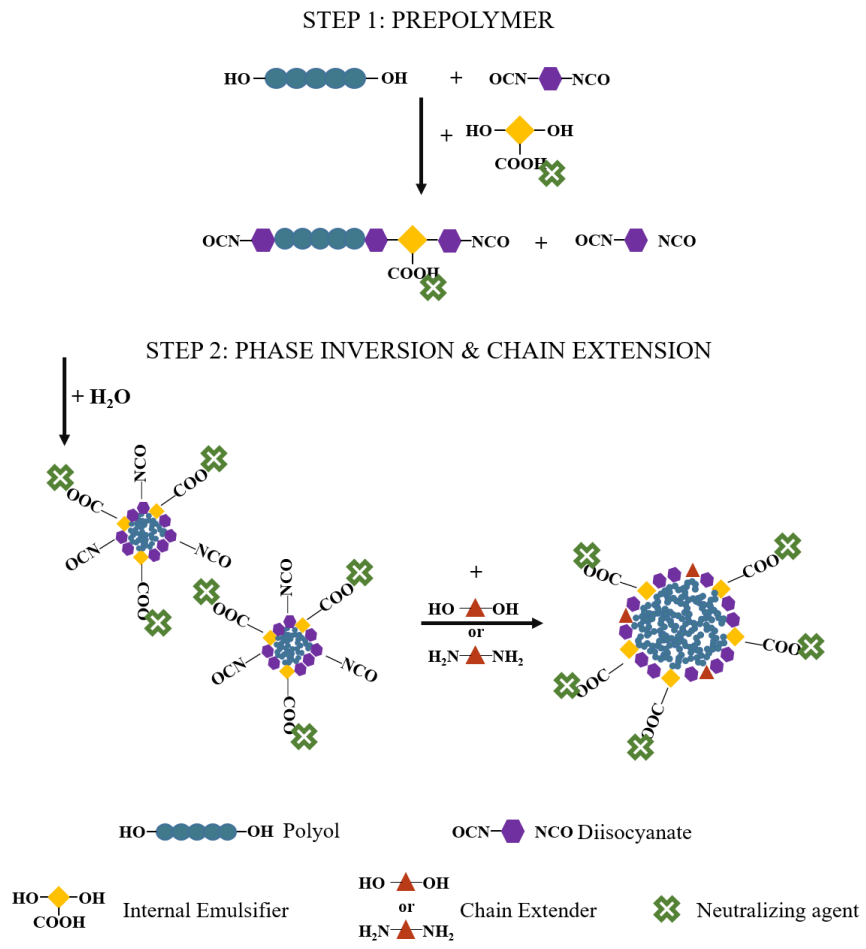

Figure 1.3. Schematic representation of the synthesis of a waterborne polyurethane or polyurethane-urea

After the polyol and the isocyanate are left to react, a NCO-terminated polyurethane prepolymer is obtained. This prepolymer is highly hydrophobic, thus, prior to the phase inversion step, the addition of an internal emulsifier is necessary. The internal emulsifier will add pendant acid groups to the prepolymer, which will be neutralized by the simultaneous addition of a counter-ion. When water is added to the reaction, polyurethane particles will form, surrounded by the ionic groups of the emulsifier and the counter-ions, forming and electrical double layer which will allow a good dispersion and grant good stability to the system [55,56]. A schematic representation of the synthesis and dispersion process is shown in Figure 1.3.

The chain extension step for polyurethane-ureas is often carried out in heterogeneous medium after the phase inversion. It is during this step where the molecular weight of the polymer is significantly increased, which will consequentially noticeably alter material properties [57].

1.3. Polyurethane and polyurethane-urea nanocomposites

Composites referred to the homogeneous dispersion of one or more entities in a continuous phase, called the matrix. When at least one of the dimensions of the employed entities is in the nanometric scale, this are considered nanoentities and prepared composites are called nanocomposites. The use of nanoscale entities in the reinforcements of a matrix has many advantages. The high interfacial area available between nanoentities and the matrix could promote the creation of strong interactions between them. In this way, the properties of the matrix are enhanced just by using a small quantity of nanoentities, unlike with standard composites, where a larger amount of reinforcement is necessary.

There is abundant literature referred to the addition of different reinforcements to waterborne polyurethane dispersions, such as clay, silica, silver, cellulose nanoentities, graphite derivatives and natural extracts among others [59-62]. The very wide variety of nanoentities allows the implementation of new

properties to the matrix, as well as the enhancement of some of its properties. This way, for example, nanoentities can improve the mechanical, thermal and optical properties of the matrix or form nanocomposites with newly added electrical, magnetic, shape memory or bactericide properties.

A good dispersion of the nanoentities in the matrix is necessary in order to obtain good properties on the final material, thus the incorporation method of the nanoreinforcements is crucial.

For waterborne polymers, its aqueous state strongly facilitates the addition of hydrophilic nanoentities, due to a great miscibility [62]. Reinforcements in aqueous solutions can be easily dispersed in the water based polymeric dispersion by mechanical stirring or sonication, and a homogeneous distribution is usually obtained.

1.3.1. Cellulose nanofibers

Cellulose is the most abundant renewable biopolymer on Earth and it is present in the cell wall of plants, animals, bacteria, fungi and algae [63]. Cellulose is a linear homopolymer composed by D-glucose units bonded together by β-1,4-glycosidic bonds, where each unit is rotated 180º to the next one (Figure 1.4).

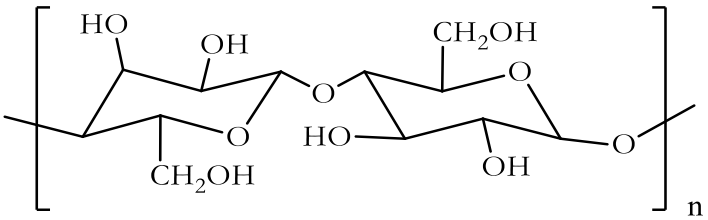

Figure 1.4. Chemical structure of cellulose

Cellulose nanoentities, such as cellulose nanocrystals (CNC) and cellulose nanofibers (CNF), are commonly used for nanocomposite preparation, thanks to their excellent reinforcement effect and great specific properties [13,14]. Cellulose nanofibers consist on alternating crystalline and amorphous domains,

they show a diameter of around 3-60 nm and lengths of a few micrometers. Cellulose nanocrystals can be isolated using different methods and show significantly lower lengths, 100-500 nm, and consist only on the crystalline regions of CNF [64–66]. A schematic representation of both nanoentities can be seen in Figure 1.5.

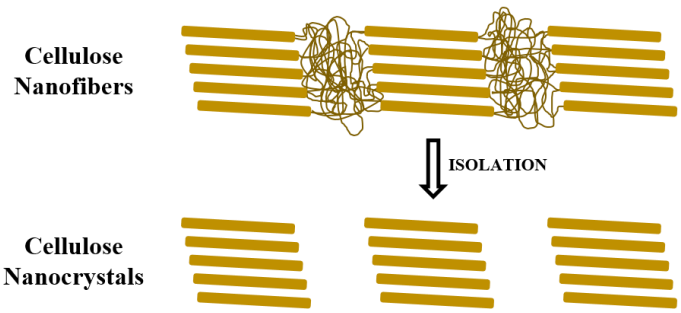

Figure 1.5. Schematic representation of cellulose nanofibers and cellulose nanocrystals structures

Cellulose nanoentities can be easily dispersed in water, which makes them a perfect candidate for nanocomposite preparations with waterborne polyurethane and polyurethane-ureas. It can be observed from literature, that cellulose nanoentities when added to WBPU and WBPUU are able to supply a remarkable reinforcement effect [6,66-70]. In some nanocomposites, the direct incorporation of nanocellulose into polymer matrix leads to a strong matrix/cellulose adhesion, resulting in overall improved properties. Nonetheless, depending on the nature of the polymeric matrix, often some sort of modification is necessary.

1.3.1.1. Functionalization of CNF

Cellulose nanoentities can be successfully added directly to polar matrices, such as polyvinyl alcohol [71,72], however, in the case of hydrophobic matrices, the derivatization of nanocellulose is necessary [14-16], in order to avoid the agglomeration of nanocellulose particles in the polymer matrix.

The modification of the nanocellulose surface by addition of new chemical groups has been extensively studied [15,73,74]. The most common chemical routes are based on chemical reactions or interactions through the numerous and highly reactive hydroxyl groups available on nanocellulose surface, in order to introduce carboxyl groups. TEMPO-mediated oxidation method [75] is the most extensively studied method for the oxidation of the primary OH groups. However, it is also possible to achieve carboxylation through the secondary OH groups by sequential periodate-chlorite oxidation (Figure 1.6) [64].

Moreover, the oxidation of OH groups into carboxylic moieties has been performed as a successful strategy to decrease the energy consumption in mechanical processes when isolating cellulose nanofibers (CNFs) from cellulose fibers.

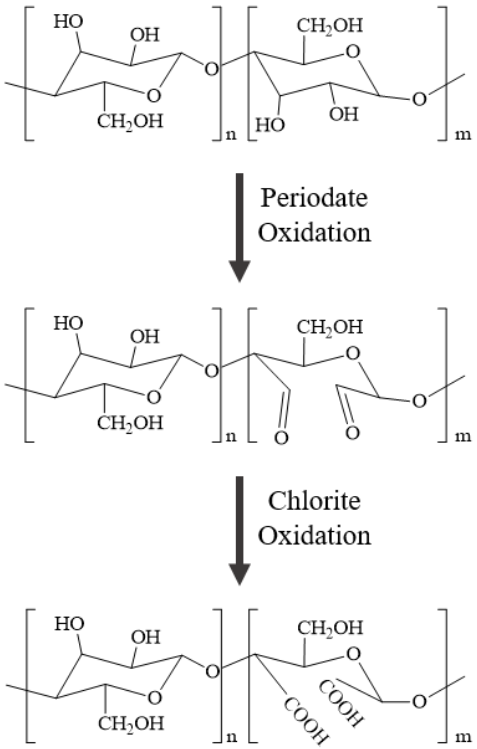

Figure 1.6. Schematic representation of carboxylation of the cellulose structure

1.3.2. Carbonaceous nanoreinforcements

Carbonaceous materials have gained great popularity, thanks to the large natural availability of carbon and the great specific properties of carbon composed materials, as is the case of carbon nanotubes, fullerenes and graphite derived nanostructures, such as graphene (G) and graphene oxide (GO) [17].

The reinforcement effect of carbonaceous nanostructures in polymer matrix has proven to be very successful, as shown by literature [76-79], as well as in polyurethane matrixes [18,19,80].

1.3.2.1. Graphene

Graphene is a two dimensional hexagonal network of sp^2 carbons (Figure 1.7). Graphene shows great mechanical, electrical and thermal properties, among others, making it an excellent reinforcement for polymeric composites [18,19].

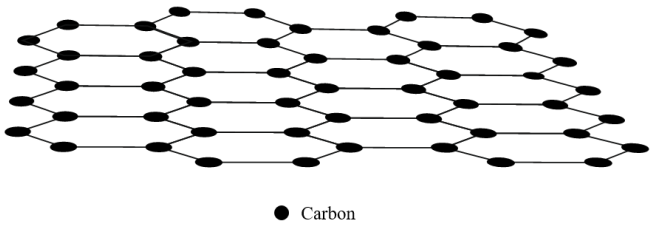

Figure 1.7. Structure of graphene

The obtaining process of graphene can result tricky. There are many different methods for graphene obtention from exfoliation of graphite (Gr), being liquid phase exfoliation through sonication the most commonly used method [81]. However, these methods can result time consuming and expensive. Moreover, the high hydrophobicity of graphene can be an obstacle when used with waterborne dispersions.

As a response to some of these drawbacks, an interest for graphene oxide has sprung.

1.3.2.2. Graphene oxide

Graphene oxide consists on a graphene layer with many functional groups on its surface (Figure 1.8). As graphene, it shows great specific properties, as well as interesting chemical and optical properties [20]. The oxygen containing groups on the structure of graphene oxide, grant it a strong hydrophilicity and, thus, good water dispersability and good miscibility with waterborne polymers. Graphene oxide acts a great reinforcement in waterborne polyurethane matrix, proving an enhancement of the properties taken place with its addition [82,83].

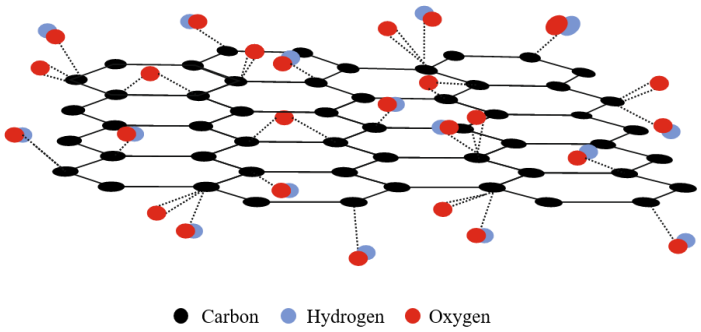

Figure 1.8. Structure of graphene oxide

Furthermore, the production of graphene oxide is much shorter and avoids long sonication times. By simply removing oxygen containing groups from the surface, graphene, as reduced graphene oxide (rGO), can be obtained. This can be done through different methods, such as thermal reduction, plasma or light exposure or chemical reduction [84,85].

1.4. Bioactive natural extracts

One of the main advantages of water-based polymers is the good affinity with not only water-dispersible nanoreinforcements, but also with water-soluble additives. Water-soluble additives can be easily incorporated into waterborne polyurethanes and polyurethane-ureas, for instance, and provide them with enhanced properties.

In this regard, the interest on using natural extracts as additive is growing, due to their large availability and interesting properties they can supply to the matrix. Plant extracts can be obtained from many different plants and different parts of said plants, granting plant extract with a very wide range of structures and properties. Plants are a rich source of bioactive compounds, mainly alkaloids, flavonoids, tannins and other phenolic compounds [86]. This bioactive behavior shown by many plant extracts grants them great potential to be used in the biomedical field. The bioactive properties shown by these extracts can usually be attributed to phytoalexins, secondary metabolites synthesized by plants in order to avoid insect, fungal and microbial infections [87-89]. Natural extracts often show multidirectional biological properties such as antioxidant, anti-inflammatory, anti-allergenic, antitumor, anticancer and antimicrobial activities [89,90]. In fact, natural extracts have been used for thousands of years in traditional folk medicine as treatment for infectious diseases [91].

In the fight against bacterial infections, the use of traditional treatments with antibiotics have started to lose effectiveness, due to the growing resistance of many strains to these treatments [89]. As a response to this problem, the use of plant extracts in common medicine as an approach to fight bacterial infections is being studied. Plant extracts have shown low risk to rising resistance from microorganisms. Moreover, plant extracts have also shown to have a synergetic effect with traditional pharmacological agents, further enhancing their effectiveness [89].

Many natural extracts and compounds from plants are currently used as natural food colorants. These colorants show many interesting bioactive properties, mainly antibacterial activity [92-94], which turns them in a great option for bioactive composite preparation. Among many of these colorants that have shown potential for antimicrobial use are *Haematoxylon campechianum L.*, *Castanea sativa L.* and *Rhamnus frangula L. Haematoxylon campechianum L.*,

commonly known as logwood, is a tree typical of Central and South America. Wood from this tree is commonly used to produce sweeteners and food colorants [95,96], due to its strong reddish color. The use of its wood to produced bioactive natural extract could be of great interest. *Castanea sativa* tree is the tree from which chestnut fruit is obtained and it is very abundant specially in central and southern Europe and in the Mediterranean basin [97]. Besides the clear interest for their fruit, other parts of these trees are also utilized, such as chestnut flowers being used as honey sources. However, in the processes of obtaining these products many byproducts are created, such as chestnut leaves, shells, burs and wood, which could be utilized for natural extracts production [98]. Last, *Rhamnus frangula L*. is a shrub native to Balkan peninsula and wester Asia, it pertains to the *Rhamnaceae* family [99,100]. This plant is traditionally used as a mild laxative, however it presents many other bioactive benefits, such as antifungal, antibacterial, antioxidant and anticancer activity [88,99].

The use of these additives in polymeric materials can be very beneficial, in order to supply them with bioactive properties and widen their fields of applications.

1.5. 3D printing

3D printing refers to the layer-by-layer fabrications of parts, guided by the information imported from a computer-aided design (CAD) file [101,102]. A CAD file of a specifically designed part is imported to the 3D printing software, where it is deconstructed in a stack of two dimensional layers, which will later be printed layer by layer, until the final 3D product is obtained, as schematized in Figure 1.9.

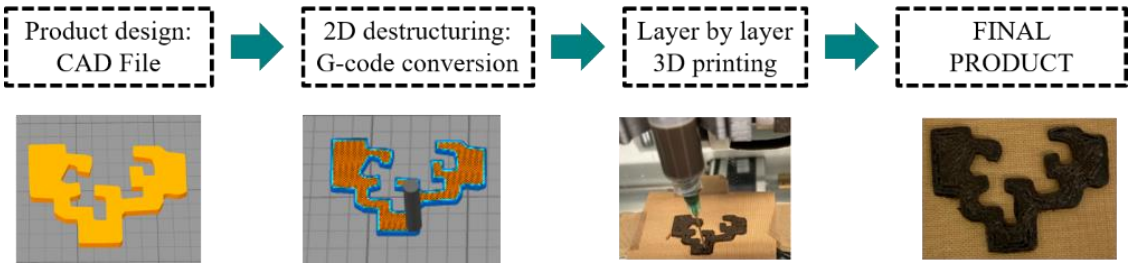

Figure 1.9. 3D printing process

Additive manufacturing was first introduced in the 1980s, however due to lack of efficient printing machines and good quality printable materials, it is not until recent years that its popularity and use have seen an important growth. Just in the last few years, the increase of the market value has been more than triple and it is expected this trend will continue. Figure 1.10 shows the world market value of the last few years and the predicted increase for the years to come, based on market analysis reports [103].

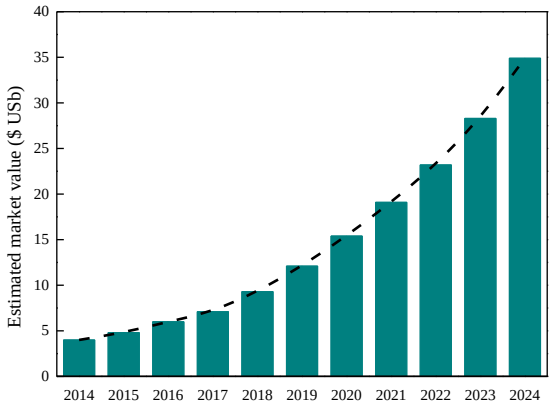

Figure 1.10. 3D printing market behaviors and estimated forecast (adapted from [103])

The main advantage of 3D printing is the possibility of designing one of a kind personalized items. Though, its one-at-a-time production method is a drawback, due to the small scale production capacity, when oriented to individually personalized items this is no longer a problem. Moreover, the designing of the parts by CAD allows the preparation of complex forms which could not be prepared by other polymer processing methods. The creation of this complex designs without the need of added expensive tools, facilitates the manufacturing

of said designs without further costs, in contrary to conventional production methods where complexity and cost are directly linked, as can be seen in Figure 1.11 [104].

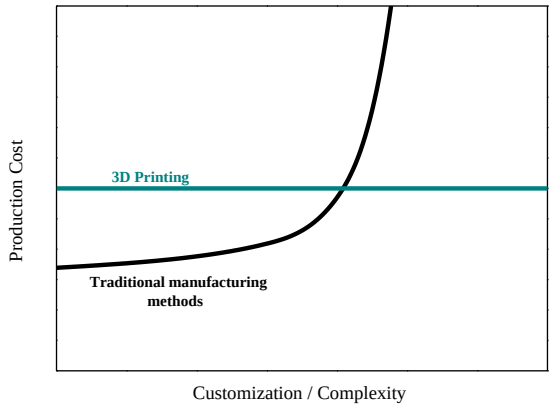

Figure 1.11. Effect of customization and complexity on the production cost for traditional manufacturing methods and 3D printing (adapted from [104])

Moreover, the direct printing of the imported design allows the direct obtention of the final shape, without the need to eliminate excess material. In conventional processing methods there is some part of the produced part that needs to be subtracted and discarded, as is the case of computer numerical control milling or moldings [104,105]. The use of just the needed material means a reduction in waste material, which is beneficial both economically, since material is saved, and environmentally speaking, since less residual materials are produced.

Regarding environmental impact, the production of less residue is not the only advantage of 3D printing. The simple reproduction of pieces by digital transference of the model file allows the production of the same part around the world. This way, production and distribution of products could become local based, reducing carbon footprint of transportation. Moreover, this method of manufacturing often has a positive effect on the energy consumption [104,106].

Since the initial states of 3D printing, this technology has been in constant growth and, thus, it has seen many advances on its field. Many different printing techniques have been developed and each has its own benefits, drawback and material limitations.

Some of the most popular printing techniques are stereolithography, fused deposition modeling (FDM), selective laser sintering, selective laser melting, electron beam melting and direct ink writing (DIW) [107,108].

The important advances in both printing equipment and materials has catapulted the use of 3D printing in many a field of applications, such as energy storage, tissue engineering, automotive, drug delivery or sensors among others [109-113].

The great advantage 3D printing offers regarding on-demand customization can be best exploited when used for the biomedical field. One-on-one personalization for each patient is of extreme importance for some biomedical applications, as is the case of prosthetic devices or tissue engineering scaffolds [106]. 3D printing shows potential for the preparation of many specific parts, such as stents, splints, contact lenses, bone implants, cartilage or tendon implants, intrauterine contraceptive devices, as well as artificial skin, parts of the ear and heart valves [114–122].

1.5.1. Fused deposition modeling

FDM is the most popular type of 3D printing. In FDM, a thermoplastic, usually in filament form, is fed to a heated nozzle, where it is melted and extruded. The melted material is collected in a plate, layer by layer, following the computer design. A schematic model of a FDM printing machine is shown in Figure 1.12.

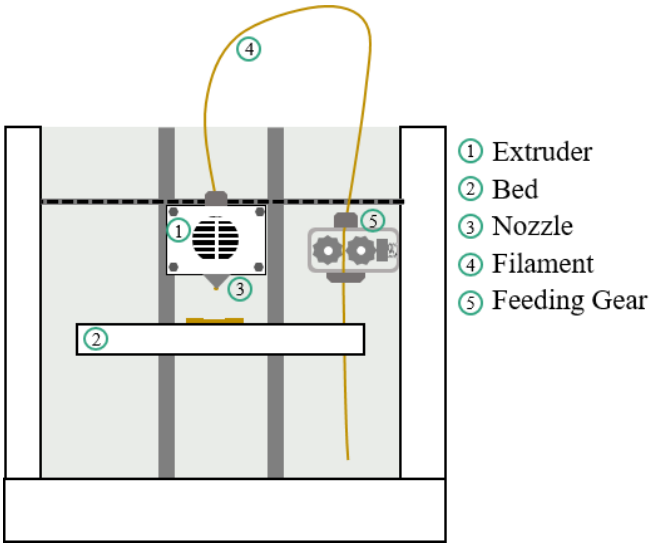

Figure 1.12. A schematic figure of a FDM 3D printer

FDM presents many advantages, such as its simplicity, high printing speed and cost-effectiveness [105,107,123]. Moreover, parts prepared by FDM need no further processing and are ready to be used, they show good shape fidelity and high resolution, 30-200 mm [124]. FDM's simple use and the availability of cheap printers, has made it a very popular technique in both industrial and personal use. However, FDM also present some drawbacks, mainly the high extrusion temperatures and complex process limiting the materials that can be used for this technique [105,124].

One of the most important parts of additive manufacturing is to ensure good adhesion between layers, to avoid mechanical problems due to layer separation. For this, after a layer is printed it is important that the subsequent layer is fused before the solidification of the fist layer takes place [105]. The optimization of the printing process will have a great impact on this. The many parameters in FDM printing will significantly influence the printing process, as well as the shape-fidelity and good properties of the final part. Some of the most important parameters in FDM 3D printing are layer height, speed of printing, extrusion temperature, nozzle diameter, build orientation, density of infill, infill pattern,

etc [105]. Each will have an impact on the printing process and final part properties. For example, nozzle diameter and layer height will influence the precision of the printed shape; on the other hand, extrusion temperature and printing speed will significantly affect the layer adhesion and the continuous feeding. Extrusion temperature will also have a massive effect in the viscosity of the material, which is a key parameter for 3D printing.

The biggest challenge of FDM 3D printing lays in the obtention of printable materials, that at the same time offer good properties. Rigidity, strength, roughness, thermal behavior and many other parameters of material will have a strong effect on its printing capacity and quality [106].

The mechanical behavior of filaments is crucial for the feeding process. Feeding in FDM is often carried out by Bowden extruders, which are constituted by a small drive gear which pushes the filament through a polytetrafluoroethylene tube to the extruder head. Materials with high flexibility often show problems due to the friction between the feeding tube and the filaments, as well as due to the formation of entanglement in the feeding gear (Figure 1.13a) [125,126].

The rheological behavior of the filament material at high temperatures is also a key parameter. Filaments with enhanced viscoelastic behavior show better printing capacity. It is important for filaments to show a viscosity, at the extrusion temperature, that will allow a good flowing capacity so they will be easily extruded, but will also be able to quickly begin to solidify in order to maintain the given shape and support the weight of the next layers (Figure 1.13b).

Moreover, often by a combination of too high viscosity and high flexibility the printing process is not possible in FDM 3D printer model like the one shown in Figure 1.12, due to obstructions form on the nozzle caused by low pressure on the nozzle (Figure 1.13c).

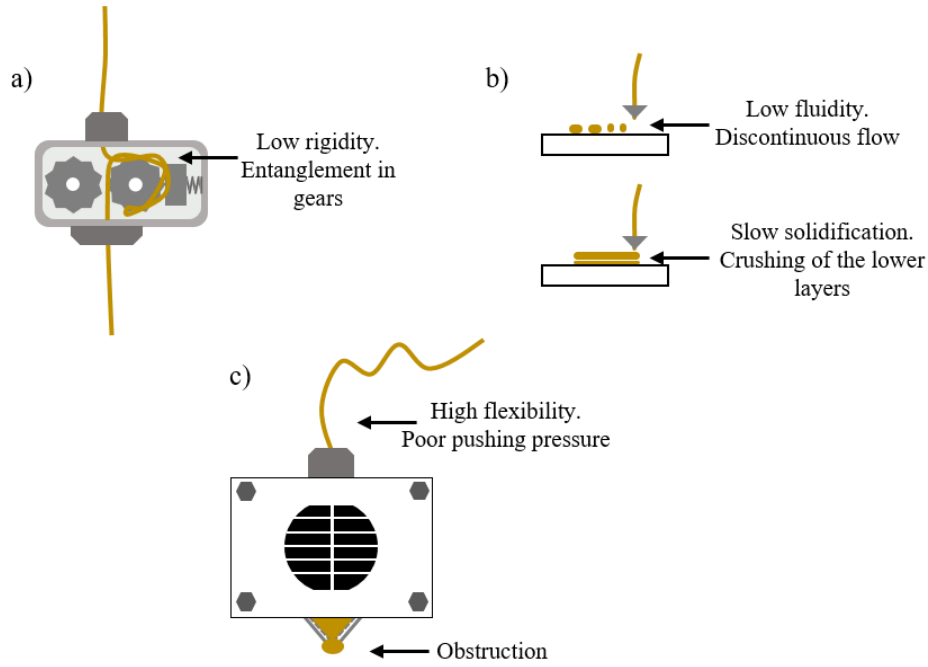

Figure 1.13. Common material difficulties in FDM printing

The use of nanocomposite filaments is a helpful option to overcome these drawbacks. When reinforcement with higher thermal stability are used, the printing process of the polymer matrix is significantly improved. This non-melting nanoentities allow a more consistent flow and improve parts reproducibility [124].

Filaments of PLA and ABS are the most popular commercially available filaments [106]. However, because of the continuous development of this technique, there is an increasing need for new materials which can offer new properties, such as higher flexibility or biocompatibility. In this regards, the use of polyurethane-urea nanocomposites could be of great interest [127], as has been seen in different studies for carbon nanotube/polyurethane nanocomposites, where flexible filaments have been successfully used in FDM 3D printing [123,128,129].

1.5.2. Direct ink writing

Another 3D printing technology that has been gaining more interest is direct ink writing. DIW consists on the low temperature extrusion through a needle of materials in a gel-like or liquid-viscous state. The extrusion process can be carried out by pneumatic pressure or by the action of a piston or a rotating screw. As for FDM, the printer follows a design imported from CAD and the printed layers are collected layer by layer. A schematic model of a piston based DIW printing machine is shown in Figure 1.14.

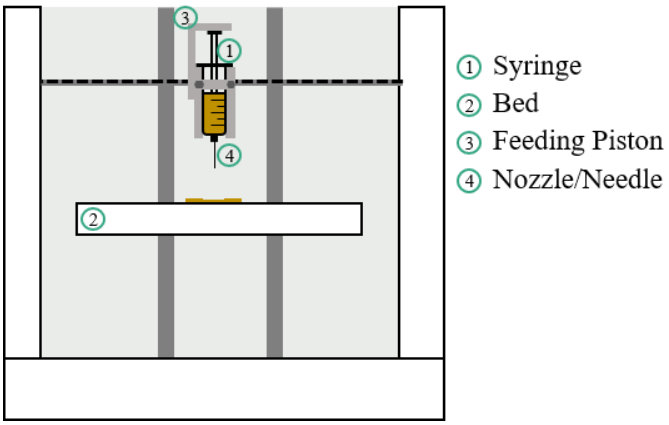

Figure 1.14. A schematic figure of a DIW 3D printer

One of the main advantages of DIW is the low processing temperatures, which opens the possibility of printing biomaterials without damaging them, as could be the case for cell containing inks [130]. However, there are also some drawbacks to this type of printing, as are its low printing speed and the complexity of adequate printing inks.

As happens for FDM, the printing parameters are key for a satisfactory printing process, in this case printing speed, layer height, nozzle diameter, infill density and pattern are also important. However, more important for DIW is the treatment that might be needed for the used inks. Regarding this, different types of DIW can be chosen.

DIW can be separated in three categories regarding the processing of the inks: hot melt extrusion, cold extrusion and gel printing [131,132].

Holt melt extrusion follows a similar concept of FDM, where the materials needs to be heated in order to activate its flow and cooled to solidify. However, working temperatures in this case are noticeably lower than in FDM, just above the gel point of the ink. In cold extrusion, inks are directly printed without any previous treatment. The printing capability and shape fidelity depends only on the rheological properties of the ink. Last, gel printing is based on the chemical or physical crosslinking of the inks. In order to activate ink gelation, often the use of UV light or the addition of anionic compounds is necessary, either prior or after printing process.

The use of cold extrusion inks is gaining interest due to the advantage they present against other inks regarding the lack of need of further processing of the inks during or after the printing process, as the need of temperature or UV light. However, this advantage brings with it the drawback of the ink needing to fulfill very specific rheological properties in order to be satisfactorily printed.

Certain rheological behaviors must be met by the inks for both a good printing process and a good final product. In this regard, two major factors need to be studied; the processability (or printability) of the inks and the shape fidelity of the obtained 3D printed part. The printability of the ink refers to the capacity of the ink to properly and continuously flow when extruded. The shape fidelity, on the other hands, is related to the ability of the ink to retain the shape produced in the printing process while supporting the weight of later layers.

In order to assess the printability of a material, first the viscosity analysis must be carried out. During a 3D printing process an ink will be subjected to pressure applied by the feeding mechanism, thus its behavior when shear is applied is of great interest. The ideal DIW ink will present a non-Newtonian behavior, more specifically a shear thinning behavior, allowing the material to easily flow at

high shear rates (extrusion process) and to maintain a given shape due to its higher viscosity at low shear rates (Figure 1.15). The viscosity of the materials also has a great influence in the shape fidelity of the printed parts. Inks with higher viscosities tend to show better shape fidelity, since they show more resistance to flow and can more easily maintain the given shape.

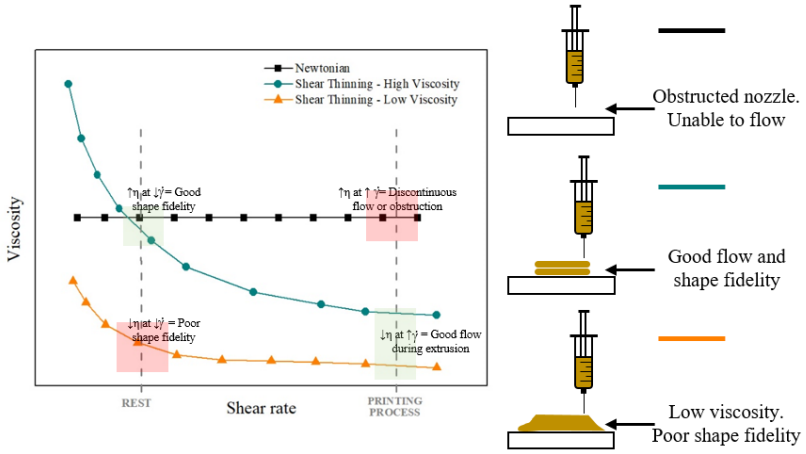

Figure 1.15. Representation of the viscosity behavior of Newtonian and non-Newtonian liquids for a shear rate sweep

Moreover, viscosity vs shear rate curves can be adjusted to the Power Law model (equation 1.1), to further describe the rheological behavior of fluids. The n index is indicative of the nature of fluid, regarding its viscosity under shear stress behavior.

$$\eta(\dot{\gamma}) = K\dot{\gamma}^{n-1} \qquad (equation\ 1.1)$$

where η is the viscosity (Pa ·s), $\dot{\gamma}$ is the shear rate (s^{-1}), K is the consistency index (Pa s^n) and n is the flow index (dimensionless).

For Newtonian fluids n = 1, since for these materials viscosity is independent of shear stress. A nonlinear variation of the viscosity as a function of the shear rate can be described for non-Newtonian fluids. In these cases, for shear thickening materials n > 1, viscosity increases with shear stress, and for shear thinning materials n < 1, viscosity is reduced at higher shear rates [133].

Furthermore, the lower the n value, the stronger the shear thinning behavior, which will facilitate the extruding process during the 3D printing process [134].

The yield point is also an important parameter for the printing of the materials. The yield point studies the stress at which a material's structure begins to break down and the material starts flowing. It is calculated by the study of the storage and loss moduli regarding the applied shear stress. The yield point is usually determined at the shear stress value at which the deviation of the storage modulus from the constant plateau takes place. The printability of a material is directly related to the yield point (Figure 1.16). High yield points will result in materials with poor printability, showing a non-continuous flow or no flow at all. The shape fidelity is also influenced by the yield point, since it is important for the material to show a defined yield point, so at lower stress they will show higher storage than loss moduli, elastic behavior, in order for the material to maintain its shape after deposition and after later layers are deposit on top. Moreover, materials with higher storage modulus present more structured networks, showing a higher shape maintaining capacity.

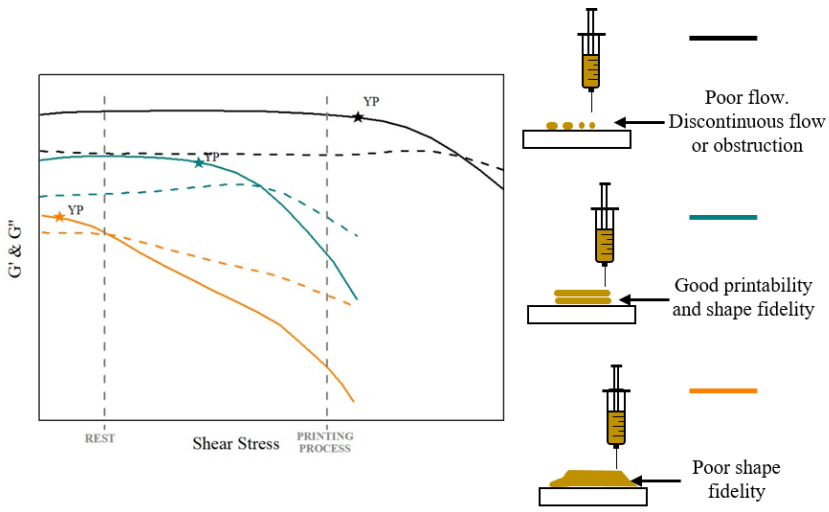

Figure 1.16. Representation for different types of materials of their storage and loss moduli behavior and (★) yield point (determined as the point of deviation of stress form linearity) in a shear stress sweep and their printability

In a DIW process the material is summited to a shear force which may affect the properties of the ink after deposition, thus the study of the capacity of the material to recover its initial state is common. After the ink is subjected to high shear rates, it often shows lower viscosity, due to the breaking of the network and the entanglements of the polymer chains. The capacity of the material to quickly recover initial state is related to the shape fidelity of the printed part (Figure 1.17).

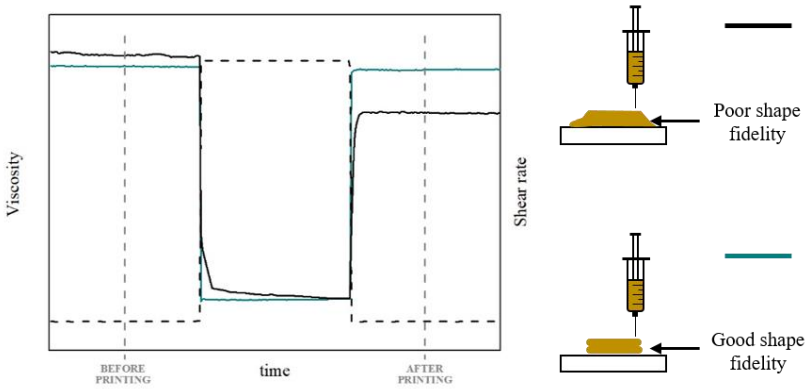

Figure 1.17. Representation of recovery test for different types of materials and their shape fidelity

The wide field of properties offered by polyurethane-ureas makes them of interest for this technology as well. In order to adapt waterborne polyurethane-ureas for DIW, their rheology will need to be modulated, either by solid content variations in water, control of molecular weights, variation of their chemical structure or addition of other components. Moreover, cold extrusion inks often show poor mechanical properties, as a result to this problem the addition of nanoentities is being used. In this regard, cellulose nanoentities (nanofibers, nanocrystals, carboxymethyl cellulose and methylcellulose) have been extensively studied and have shown good potential. Carbonaceous materials have also been used in inks productions, resulting in materials with enhance mechanical properties and supplied with electrical conductivity (graphene oxide or carbon nanotubes) [135–140].

One of the methods used to modulate the rheology of a low viscosity dispersion is the addition of high molecular weight hydrophilic components, such as polyvinyl alcohol [141] or polyethylene oxide [142,143]. Moreover, the use of natural polymers obtained from natural sources and with promising properties could be of interests for DIW applications. In this regard, due to the great properties it offers, carrageenan (CAR) could be a great option for 3D printing of WBPUU dispersions.

1.5.2.1. The use of carrageenan for gel preparation

Carrageenan is a very high molecular weight natural polymer (with an average molecular weight of over 100 kDa [144,145]), extracted from red algae. It is a linear sulphated polysaccharide, its structure consists on a repeating disaccharide of alternating units of D-galactose and 3,6-anhydro-galactose joined by α-1,4 and ß-1,3-glycosidic linkages [146,147]. Depending on the content of 3,6-anhydro-D-galactose and the number and position of sulphate groups, it can be classified in different types, λ, κ, ι, υ, μ and θ carrageenan [144]. κ-carrageenan (Figure 1.18) is one of the most commonly used types, thanks to its good gelling properties. Furthermore, carrageenan is often used as thickener, stabilizer and gelling agent in the food, pharmaceutical and cosmetic industry, due to its biocompability, non-toxicity and low cost [144,148,149].

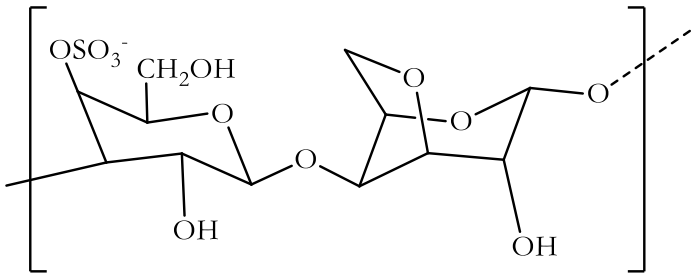

Figure 1.18. Structure of κ-carrageenan

In aqueous solutions, κ-carrageenan chains can form helix structures, which tend to aggregate, forming a gel [144,150–152]. The content of carrageenan on

the dispersion strongly affects its rheological behavior [152]. Hence, varying this content could help modulate the rheology of the prepared inks for a satisfactory printing process. Moreover, its thixotropic behavior makes a perfect option for this application [151].

1.6. General objectives

The main objective of this work was the preparation of polyurethane based materials suitable for 3D printing. For that purpose, a greener sourced waterborne polyurethane-urea was synthesized and nanocomposites were prepared using different nanoreinforcements. Materials were adapted for fused deposition modeling and direct ink writing 3D printing, variating nanoreinforcements type and content, addition method and solid content.

After a brief introduction to the topic in Chapter 1 and specifications of the reactants and characterization methods in Chapter 2, this work is divided as follows:

- In Chapter 3, a stable waterborne polyurethane-urea is synthesized and characterized. The obtention process of cellulose nanofibers with different carboxylation degrees, graphene and graphene oxide is described and the properties of the nanoreinforcements are studied.
- In Chapter 4, WBPU/CNF nanocomposite films with different reinforcement contents were prepared and characterized, using CNF with different carboxylation degrees. Moreover, WBPU/CNF composites filaments were prepared using different incorporation methods, and the use of these filaments for FDM 3D printing was assessed.
- In Chapter 5, WBPU/CNF composites inks were prepared, varying CNF content, type and incorporation route. Prepared inks were characterized rheologically and used in DIW 3D printing. Obtained 3D printed parts were characterized.

- In Chapter 6, WBPU/GO and WBPU/G nanocomposite films are prepared and characterized. WBPU/rGO filaments are prepared by different incorporation routes and these filaments are used in FDM printing. The properties of the 3D printed parts are studied.
- In Chapter 7, WBPU/rGO inks are prepared and their use in DIW is assessed. Inks' rheology is studied, as well as the properties of the 3D printed parts.
- In Chapter 8, plant extracts are used to supply the material with bioactive properties. Inks are prepared for DIW. The rheology of the inks and the properties of the printed parts are studied. Antimicrobial behavior supplied by the natural extracts is assessed.

1.7. References

[1] Sun SX. Chapter 1. Overview of plant polymers: resources demands, and sustainability. Bio-based Polym. Compos., Elsevier Academic Press; 2015.

[2] Mülhaupt R. Green polymer chemistry and bio-based plastics: Dreams and reality. Macromol Chem Phys 2013;214:159–74. doi:10.1002/macp.201200439.

[3] Liu Z, Jiang Q, Zhang Y, Li T, Zhang HC. Sustainability of 3D printing: A critical review and recommendations. ASME 2016 11th Int Manuf Sci Eng Conf MSEC 2016 2016;2:1–8. doi:10.1115/MSEC2016-8618.

[4] UNFCCC. Conference of the Parties (COP). Adoption of the Paris agreement. Proposal by the president. Paris Clim Chang Conf - Novemb 2015, COP 21 2015;21932:32.

[5] Akindoyo JO, Beg MDH, Ghazali S, Islam MR, Jeyaratnam N, Yuvaraj AR. Polyurethane types, synthesis and applications-a review. RSC Adv 2016;6:114453–82. doi:10.1039/c6ra14525f.

[6] Honarkar H. Waterborne polyurethanes: A review. J Dispers Sci

Technol 2018;39:507–16. doi:10.1080/01932691.2017.1327818.

[7] Madbouly SA, Xia Y, Kessler MR. Rheological behavior of environmentally friendly castor oil-based waterborne polyurethane dispersions. Macromolecules 2013;46:4606–16. doi:10.1021/ma400200y.

[8] Lu Y, Larock RC. Soybean-oil-based waterborne polyurethane dispersions: Effects of polyol functionality and hard segment content on properties. Biomacromolecules 2008;9:3332–40. doi:10.1021/bm801030g.

[9] Çaylı G, Küsefoğlu S. Biobased polyisocyanates from plant oil triglycerides: Synthesis, polymerization, and characterization. J Appl Polym Sci 2008;109:2948–55. doi:10.1002/app.28401.

[10] Hojabri L, Kong X, Narine SS. Fatty acid-derived diisocyanate and biobased polyurethane produced from vegetable oil: Synthesis, polymerization, and characterization. Biomacromolecules 2009;10:884–91. doi:10.1021/bm801411w.

[11] Široký J, Blackburn RS, Bechtold T, Taylor J, White P. Attenuated total reflectance Fourier-transform Infrared spectroscopy analysis of crystallinity changes in lyocell following continuous treatment with sodium hydroxide. Cellulose 2010;17:103–15. doi:10.1007/s10570-009-9378-x.

[12] Tejado A, Alam MN, Antal M, Yang H, van de Ven TGM. Energy requirements for the disintegration of cellulose fibers into cellulose nanofibers. Cellulose 2012;19:831–42. doi:10.1007/s10570-012-9694-4.

[13] Santamaria-Echart A, Ugarte L, García-Astrain C, Arbelaiz A, Corcuera MA, Eceiza A. Cellulose nanocrystals reinforced environmentally-friendly waterborne polyurethane nanocomposites. Carbohydr Polym

2016;151:1203–9. doi:10.1016/j.carbpol.2016.06.069.

[14] Wang L, Ando M, Kubota M, Ishihara S, Hikima Y, Ohshima M, et al. Effects of hydrophobic-modified cellulose nanofibers (CNFs) on cell morphology and mechanical properties of high void fraction polypropylene nanocomposite foams. Compos Part A Appl Sci Manuf 2017;98:166–73. doi:10.1016/j.compositesa.2017.03.028.

[15] Moon RJ, Schueneman GT, Simonsen J. Overview of cellulose nanomaterials, their capabilities and applications. JOM 2016;68:2383–94. doi:10.1007/s11837-016-2018-7.

[16] Žepič V, Poljanšek I, Oven P, Čop M. COST-FP1105: Properties of PLA films reinforced with unmodified and acetylated freeze dried nanofibrillated cellulose. Holzforschung 2016;70:1125–34. doi:10.1515/hf-2016-0096.

[17] Hoheisel TN, Schrettl S, Szilluweit R, Frauenrath H. Nanostructured carbonaceous materials from molecular precursors. Angew Chemie - Int Ed 2010;49:6496–515. doi:10.1002/anie.200907180.

[18] Li C, Hui B, Ye L. Construction of polyurethane-imide/graphene oxide nanocomposite foam with gradient structure and its thermal mechanical stability. Ind Eng Chem Res 2018;57:13742–52. doi:10.1021/acs.iecr.8b02911.

[19] Kausar A. Emerging research trends in polyurethane/graphene nanocomposite: a review. Polym Plast Technol Eng 2017;56:1468–86. doi:10.1080/03602559.2016.1277240.

[20] Guerrero-Contreras J, Caballero-Briones F. Graphene oxide powders with different oxidation degree, prepared by synthesis variations of the Hummers method. Mater Chem Phys 2015;153:209–20. doi:10.1016/j.matchemphys.2015.01.005.

[21] Potts JR, Dreyer DR, Bielawski CW, Ruoff RS. Graphene-based polymer nanocomposites. Polymer 2011;52:5–25. doi:10.1016/j.polymer.2010.11.042.

[22] Eswaraiah V, Jyothirmayee Aravind SS, Ramaprabhu S. Top down method for synthesis of highly conducting graphene by exfoliation of graphite oxide using focused solar radiation. J Mater Chem 2011;21:6800. doi:10.1039/c1jm10808e.

[23] Haryńska A, Gubanska I, Kucinska-Lipka J, Janik H. Fabrication and characterization of flexible medical-grade TPU filament for Fused Deposition Modeling 3DP technology. Polymers 2018;10. doi:10.3390/polym10121304.

[24] Bandyopadhyay A, Bose S, Das S. 3D printing of biomaterials. MRS Bull 2015;40:108–14. doi:10.1557/mrs.2015.3.

[25] Haryńska A, Kucinska-Lipka J, Sulowska A, Gubanska I, Kostrzewa M, Janik H. Medical-grade PCL based polyurethane system for FDM 3D printing - characterization and fabrication. Materials 2019;12:887. doi:10.3390/ma12060887.

[26] Ahn J, Grün IU, Mustapha A. Antimicrobial and antioxidant activities of natural extracts in vitro and in ground beef. J Food Prot 2004;67:148–55. doi:10.4315/0362-028X-67.1.148.

[27] Gonelimali FD, Lin J, Miao W, Xuan J, Charles F, Chen M, et al. Antimicrobial properties and mechanism of action of some plant extracts against food pathogens and spoilage microorganisms. Front Microbiol 2018;9:1–9. doi:10.3389/fmicb.2018.01639.

[28] Santamaria-Echart A, Fernandes I, Barreiro F, Retegi A, Arbelaiz A, Corcuera MA, et al. Development of waterborne polyurethane-ureas added with plant extracts: Study of different incorporation routes and their influence on particle size, thermal, mechanical and antibacterial

properties. Prog Org Coatings 2018;117:76–90. doi:10.1016/j.porgcoat.2018.01.006.

[29] Marzec M, Kucińska-Lipka J, Kalaszczyńska I, Janik H. Development of polyurethanes for bone repair. Mater Sci Eng C 2017;80:736–47. doi:10.1016/j.msec.2017.07.047.

[30] Kapatel PM, Patel RH. Green approach for the development of novel flame retardant waterborne polyurethanes: synthesis and its characterizations. Mater Today Proc 2020;23:389–99. doi:10.1016/j.matpr.2020.02.058.

[31] Shirke A, Dholakiya B, Kuperkar K. Novel applications of castor oil based polyurethanes: a short review. Polym Sci - Ser B 2015;57:292–7. doi:10.1134/S1560090415040132.

[32] Chattopadhyay DK, Raju KVSN. Structural engineering of polyurethane coatings for high performance applications. Prog Polym Sci 2007;32:352–418. doi:10.1016/j.progpolymsci.2006.05.003.

[33] Hao H, Shao J, Deng Y, He S, Luo F, Wu Y, et al. Synthesis and characterization of biodegradable lysine-based waterborne polyurethane for soft tissue engineering applications. Biomater Sci 2016;4:1682–90. doi:10.1039/c6bm00588h.

[34] Calvo-Correas T, Martin MD, Retegi A, Gabilondo N, Corcuera MA, Eceiza A. Synthesis and characterization of polyurethanes with high renewable carbon content and tailored properties. ACS Sustain Chem Eng 2016;4:5684–92. doi:10.1021/acssuschemeng.6b01578.

[35] Tharcis M, Badel T, Jéol S, Fleury E, Méchin F. High elongation thermoplastic polyester-urethanes based on widely available diacid intermediates. J Appl Polym Sci 2016;133:n/a-n/a. doi:10.1002/app.43410.

[36] Liu N, Zhao Y, Kang M, Wang J, Wang X, Feng Y, et al. The effects of the molecular weight and structure of polycarbonatediols on the properties of waterborne polyurethanes. Prog Org Coatings 2015;82:46–56. doi:10.1016/j.porgcoat.2015.01.015.

[37] Liu X, Hong W, Chen X. Continuous production of water-borne polyurethanes: A review. Polymers 2020;12:2875. doi:10.3390/polym12122875.

[38] Zlatani? A, Lava C, Zhang W, Petrovi? ZS. Effect of structure on properties of polyols and polyurethanes based on different vegetable oils. J Polym Sci Part B Polym Phys 2004;42:809–19. doi:10.1002/polb.10737.

[39] Gorna K, Polowinski S, Gogolewski S. Synthesis and characterization of biodegradable poly(ε-caprolactone urethane)s. I. Effect of the polyol molecular weight, catalyst, and chain extender on the molecular and physical characteristics. J Polym Sci Part A Polym Chem 2002;40:156–70. doi:10.1002/pola.10096.

[40] Sharma V, Kundu PP. Condensation polymers from natural oils. Prog Polym Sci 2008;33:1199–215. doi:10.1016/j.progpolymsci.2008.07.004.

[41] Galià M, de Espinosa LM, Ronda JC, Lligadas G, Cádiz V. Vegetable oil-based thermosetting polymers. Eur J Lipid Sci Technol 2010;112:87–96. doi:10.1002/ejlt.200900096.

[42] Maisonneuve L, Chollet G, Grau E, Cramail H. Vegetable oils: a source of polyols for polyurethane materials. OCL 2016;23:D508. doi:10.1051/ocl/2016031.

[43] Seniha Güner F, Yağci Y, Tuncer Erciyes A. Polymers from triglyceride oils. Prog Polym Sci 2006;31:633–70. doi:10.1016/j.progpolymsci.2006.07.001.

[44] Ashida K. Polyurethane and related foams: Chemistry and Technology. Boca Raton: CRC Press; 2007.

[45] Lee DK, Tsai HB. Properties of segmented polyurethanes derived from different diisocyanates. J Appl Polym Sci 2000;75:167–74. doi:10.1002/(SICI)1097-4628(20000103)75:1<167::AID-APP19>3.0.CO;2-N.

[46] Fernández-D'Arlas B, Alonso-Varona A, Palomares T, Corcuera MA, Eceiza A. Studies on the morphology, properties and biocompatibility of aliphatic diisocyanate-polycarbonate polyurethanes. Polym Degrad Stab 2015;122:153–60. doi:10.1016/j.polymdegradstab.2015.10.023.

[47] Wang K, Peng Y, Tong R, Wang Y, Wu Z. The effects of isocyanate index on the properties of aliphatic waterborne polyurethaneureas. J Appl Polym Sci 2010;116:n/a-n/a. doi:10.1002/app.32454.

[48] Cakic SM, Stamenkovic J V., Djordjevic DM, Ristic IS. Synthesis and degradation profile of cast films of PPG-DMPA-IPDI aqueous polyurethane dispersions based on selective catalysts. Polym Degrad Stab 2009;94:2015–22. doi:10.1016/j.polymdegradstab.2009.07.015.

[49] Lei L, Zhong L, Lin X, Li Y, Xia Z. Synthesis and characterization of waterborne polyurethane dispersions with different chain extenders for potential application in waterborne ink. Chem Eng J 2014;253:518–25. doi:10.1016/j.cej.2014.05.044.

[50] Woods G. The ICI polyurethanes book. John Wiley & Sons; 1990.

[51] Gisselfält K, Helgee B. Effect of soft segment length and chain extender structure on phase separation and morphology in poly(urethane urea)s. Macromol Mater Eng 2003;288:265–71. doi:10.1002/mame.200390023.

[52] Spaans CJ, De Groot JH, Dekens FG, Pennings AJ. High molecular

weight polyurethanes and a polyurethane urea based on 1,4-butanediisocyanate. Polym Bull 1998;41:131–8. doi:10.1007/s002890050343.

[53] Li B, Peng D, Zhao N, Mu Q, Li J. The physical properties of nonionic waterborne polyurethane with a polyether as side chain. J Appl Polym Sci 2013;127:1848–52. doi:10.1002/app.37915.

[54] Toman A. Method of providing an aqueous dispersion suitable for use as a chemically produced toner. WO 2008/109000 A1, n.d.

[55] Pandya H, Mahanwar P. Fundamental insight into anionic aqueous polyurethane dispersions. Adv Ind Eng Polym Res 2020;3:102–10. doi:10.1016/j.aiepr.2020.07.003.

[56] Kim BK. Aqueous polyurethana dispersions. Colloid Polym Sci 1996;274:599–611. doi:10.1007/BF00653056.

[57] Yoon Jang J, Kuk Jhon Y, Woo Cheong I, Hyun Kim J. Effect of process variables on molecular weight and mechanical properties of water-based polyurethane dispersion. Colloids Surfaces A Physicochem Eng Asp 2002;196:135–43. doi:10.1016/S0927-7757(01)00857-3.

[58] Kwon JY, Kim H Do. Preparation and properties of acid-treated multiwalled carbon nanotube/waterborne polyurethane nanocomposites. J Appl Polym Sci 2005;96:595–604. doi:10.1002/app.21436.

[59] Kim BK, Seo JW, Jeong HM. Morphology and properties of waterborne polyurethane/clay nanocomposites. Eur Polym J 2003;39:85–91. doi:10.1016/S0014-3057(02)00173-8.

[60] Santamaria-Echart A, Ugarte L, Arbelaiz A, Gabilondo N, Corcuera MA, Eceiza A. Two different incorporation routes of cellulose nanocrystals in waterborne polyurethane nanocomposites. Eur Polym J

2016;76:99–109. doi:10.1016/j.eurpolymj.2016.01.035.

[61] Khatoon H, Ahmad S. A review on conducting polymer reinforced polyurethane composites. J Ind Eng Chem 2017;53:1–22. doi:10.1016/j.jiec.2017.03.036.

[62] Santamaria-Echart A, Ugarte L, Arbelaiz A, Barreiro F, Corcuera MA, Eceiza A. Modulating the microstructure of waterborne polyurethanes for preparation of environmentally friendly nanocomposites by incorporating cellulose nanocrystals. Cellulose 2017;24:823–34. doi:10.1007/s10570-016-1158-9.

[63] Klemm D, Heublein B, Fink HP, Bohn A. Cellulose: Fascinating biopolymer and sustainable raw material. Angew Chemie - Int Ed 2005;44:3358–93. doi:10.1002/anie.200460587.

[64] Yang H, Tejado A, Alam N, Antal M, van de Ven TGM. Films prepared from electrosterically stabilized nanocrystalline cellulose. Langmuir 2012;28:7834–42. doi:10.1021/la2049663.

[65] Sulaiman S, Mokhtar MN, Naim MN, Baharuddin AS, Sulaiman A. A Review: Potential Usage of Cellulose Nanofibers (CNF) for Enzyme Immobilization via Covalent Interactions. Appl Biochem Biotechnol 2015;175:1817–42. doi:10.1007/s12010-014-1417-x.

[66] Moohan J, Stewart SA, Espinosa E, Rosal A, Rodríguez A, Larrañeta E, et al. Cellulose nanofibers and other biopolymers for biomedical applications. A review. Appl Sci 2020;10. doi:10.3390/app10010065.

[67] Kong L, Xu D, He Z, Wang F, Gui S, Fan J, et al. Nanocellulose-reinforced polyurethane for waterborne wood coating. Molecules 2019;24:1–13. doi:10.3390/molecules24173151.

[68] Lin Y, Zeng J, Ma J, Gong J. Preparation and property of waterborne polyurethane/cellulose nanofiber nanocomposite films. Mater Sci

Forum 2020;993 MSF:631–7. doi:10.4028/www.scientific.net/MSF.993.631.

[69] Santamaria-echart A, Fernandes I, Ugarte L, Barreiro F, Arbelaiz A, Angeles M, et al. Waterborne polyurethane-urea dispersion with chain extension step in homogeneous medium reinforced with cellulose nanocrystals. Compos Part B 2018;137:31–8. doi:10.1016/j.compositesb.2017.11.004.

[70] Wu GM, Chen J, Huo SP, Liu GF, Kong ZW. Thermoset nanocomposites from two-component waterborne polyurethanes and cellulose whiskers. Carbohydr Polym 2014;105:207–13. doi:10.1016/j.carbpol.2014.01.095.

[71] Barick AK, Tripathy DK. Effect of nanofiber on material properties of vapor-grown carbon nanofiber reinforced thermoplastic polyurethane (TPU/CNF) nanocomposites prepared by melt compounding. Compos Part A Appl Sci Manuf 2010;41:1471–82. doi:10.1016/j.compositesa.2010.06.009.

[72] Castro C, Vesterinen A, Zuluaga R, Caro G, Filpponen I, Rojas OJ, et al. In situ production of nanocomposites of poly(vinyl alcohol) and cellulose nanofibrils from Gluconacetobacter bacteria: effect of chemical crosslinking. Cellulose 2014;21:1745–56. doi:10.1007/s10570-014-0170-1.

[73] Habibi Y. Key advances in the chemical modification of nanocelluloses. Chem Soc Rev 2014;43:1519–42. doi:10.1039/C3CS60204D.

[74] Eyley S, Thielemans W. Surface modification of cellulose nanocrystals. Nanoscale 2014;6:7764–79. doi:10.1039/C4NR01756K.

[75] Isogai A, Saito T, Fukuzumi H. TEMPO-oxidized cellulose nanofibers. Nanoscale 2011;3:71–85. doi:10.1039/C0NR00583E.

[76] Ammar A, Al-Enizi AM, AlMaadeed MAA, Karim A. Influence of graphene oxide on mechanical, morphological, barrier, and electrical properties of polymer membranes. Arab J Chem 2016;9:274–86. doi:10.1016/j.arabjc.2015.07.006.

[77] Liang K, Spiesz EM, Schmieden DT, Xu AW, Meyer AS, Aubin-Tam ME. Bioproduced polymers self-assemble with graphene oxide into nanocomposite films with enhanced mechanical performance. ACS Nano 2020;14:14731–9. doi:10.1021/acsnano.0c00913.

[78] Spitalsky Z, Tasis D, Papagelis K, Galiotis C. Carbon nanotube–polymer composites: Chemistry, processing, mechanical and electrical properties. Prog Polym Sci 2010;35:357–401. doi:10.1016/j.progpolymsci.2009.09.003.

[79] Kuilla T, Bhadra S, Yao D, Kim NH, Bose S, Lee JH. Recent advances in graphene based polymer composites. Prog Polym Sci 2010;35:1350–75. doi:10.1016/j.progpolymsci.2010.07.005.

[80] Bansala T, Joshi M, Mukhopadhyay S. Electromagnetic interference shielding behavior of chemically and thermally reduced graphene based multifunctional polyurethane nanocomposites: A comparative study. J Appl Polym Sci 2019;136:1–12. doi:10.1002/app.47666.

[81] Hadi A, Zahirifar J, Karimi-Sabet J, Dastbaz A. Graphene nanosheets preparation using magnetic nanoparticle assisted liquid phase exfoliation of graphite: The coupled effect of ultrasound and wedging nanoparticles. Ultrason Sonochem 2018;44:204–14. doi:10.1016/j.ultsonch.2018.02.028.

[82] Lei L, Xia Z, Zhang L, Zhang Y, Zhong L. Preparation and properties of amino-functional reduced graphene oxide/waterborne polyurethane hybrid emulsions. Prog Org Coatings 2016;97:19–27. doi:10.1016/j.porgcoat.2016.03.011.

[83] Kim YJ, Kim BK. Synthesis and properties of silanized waterborne polyurethane/graphene nanocomposites. Colloid Polym Sci 2014;292:51–8. doi:10.1007/s00396-013-3054-2.

[84] Pei S, Cheng H. The reduction of graphene oxide. Carbon 2011;50:3210–28. doi:10.1016/j.carbon.2011.11.010.

[85] Gómez-Navarro C, Weitz RT, Bittner AM, Scolari M, Mews A, Burghard M, et al. Electronic transport properties of individual chemically reduced graphene oxide sheets. Nano Lett 2009;9:2206–2206. doi:10.1021/nl901209z.

[86] Santamaria-Echart A, Fernandes I, Barreiro F, Retegi A, Arbelaiz A, Corcuera MA, et al. Development of waterborne polyurethane-ureas added with plant extracts: Study of different incorporation routes and their influence on particle size, thermal, mechanical and antibacterial properties. Prog Org Coatings 2018;117:76–90. doi:10.1016/j.porgcoat.2018.01.006.

[87] Santamaria-Echart A. Synthesis and characterization of waterborne polyurethane and polyurethane-urea towards eco-friendly materials by cellulose nanocrystals and plant extracts incorporation. University of the Basque Country, 2017.

[88] Đukanović S, Cvetković S, Lončarević B, Lješević M, Nikolić B, Simin N, et al. Antistaphylococcal and biofilm inhibitory activities of Frangula alnus bark ethyl-acetate extract. Ind Crops Prod 2020;158. doi:10.1016/j.indcrop.2020.113013.

[89] Sadowska B, Paszkiewicz M, Podsędek A, Redzynia M, Rózalska B. Vaccinium myrtillus leaves and Frangula alnus bark derived extracts as potential antistaphylococcal agents. Acta Biochim Pol 2014;61:163–9. doi:10.18388/abp.2014_1939.

[90] Nejabatdoust A, Daemi HB, Salehzadeh A, Azimi SC. Comparing of

effects of hydro-alcoholic , ethanolic , and methanolic extracts of the frangula alnus : Chemical composition , antimicrobial , and synergism 2020;6:20–33. doi:10.22080/jgr.2020.2538.

[91] Yasunaka K, Abe F, Nagayama A, Okabe H, Lozada-Pérez L, López-Villafranco E, et al. Antibacterial activity of crude extracts from Mexican medicinal plants and purified coumarins and xanthones. J Ethnopharmacol 2005;97:293–9. doi:10.1016/j.jep.2004.11.014.

[92] Helmy HM KM. Antibacterial activity of cationised cotton dyed with some natural dyes. J Text Sci Eng 2015;05. doi:10.4172/2165-8064.1000180.

[93] Gupta D, Khare SK, Laha A. Antimicrobial properties of natural dyes against Gram-negative bacteria. Color Technol 2004;120:167–71. doi:10.1111/j.1478-4408.2004.tb00224.x.

[94] Singh R, Jain A, Panwar S, Gupta D, Khare SK. Antimicrobial activity of some natural dyes. Dye Pigment 2005;66:99–102. doi:10.1016/j.dyepig.2004.09.005.

[95] Masuda H, Ohtani K, Mizutani K, Ogawa S, Kasai R, Tanaka O. Chemical study on Haematoxylon campechianum: a sweet principle and new dibenz(b,d)oxocin derivatives. Chem Pharm Bull 1991;39:1382–4. doi:10.1248/cpb.39.1382.

[96] Escobar-Ramos A, Lobato-García CE, Zamilpa A, Gómez-Rivera A, Tortoriello J, González-Cortazar M. Homoisoflavonoids and chalcones isolated from haematoxylum campechianum L., with spasmolytic activity. Molecules 2017;22:2–11. doi:10.3390/molecules22091405.

[97] Kolayli S, Can Z, Yildiz O, Sahin H, Karaoglu SA. A comparative study of the antihyaluronidase, antiurease, antioxidant, antimicrobial and physicochemical properties of different unifloral degrees of chestnut (Castanea sativa Mill.) honeys. J Enzyme Inhib Med Chem 2016;31:96–

104. doi:10.1080/14756366.2016.1209494.

[98] Silva V, Falco V, Dias MI, Barros L, Silva A, Capita R, et al. Evaluation of the phenolic profile of Castanea sativa mill. By-products and their antioxidant and antimicrobial activity against multiresistant bacteria. Antioxidants 2020;9:87. doi:10.3390/antiox9010087.

[99] Bacha A Ben, Jemel I, Moubayed NMS, Abdelmalek I Ben. Purification and characterization of a newly serine protease inhibitor from Rhamnus frangula with potential for use as therapeutic drug. Biotech 2017;7:1–13. doi:10.1007/s13205-017-0764-z.

[100] Kremer D, Kosalec I, Locatelli M, Epifano F, Genovese S, Carlucci G, et al. Anthraquinone profiles, antioxidant and antimicrobial properties of Frangula rupestris (Scop.) Schur and Frangula alnus Mill. bark. Food Chem 2012;131:1174–80. doi:10.1016/j.foodchem.2011.09.094.

[101] Camargo JC, Machado ÁR, Almeida EC, Silva EFMS. Mechanical properties of PLA-graphene filament for FDM 3D printing. Int J Adv Manuf Technol 2019;103:2423–43. doi:10.1007/s00170-019-03532-5.

[102] Ngo TD, Kashani A, Imbalzano G, Nguyen KTQ, Hui D. Additive manufacturing (3D printing): A review of materials, methods, applications and challenges. Compos Part B Eng 2018;143:172–96. doi:10.1016/j.compositesb.2018.02.012.

[103] 3DHubs. 3D printing trends 2020. Industry highlights and market trends 2020. https://downloads.hubs.com/3D_printing_trends_report_2020.pdf (accessed September 10, 2021).

[104] Wimmer R, Steyrer B, Woess J, Koddenberg T, Mundigler N. 3D printing and wood. Pro Ligno 2015;11:144–9. doi:1841-4737.

[105] Solomon IJ, Sevvel P, Gunasekaran J. A review on the various

processing parameters in FDM. Mater Today Proc 2020:10–5. doi:10.1016/j.matpr.2020.05.484.

[106] Mazzanti V, Malagutti L, Mollica F. FDM 3D printing of polymers containing natural fillers: A review of their mechanical properties. Polymers 2019;11. doi:10.3390/polym11071094.

[107] Chen Q, Mangadlao JD, Wallat J, De Leon A, Pokorski JK, Advincula RC. 3D printing biocompatible polyurethane/poly(lactic acid)/graphene oxide nanocomposites: Anisotropic properties. ACS Appl Mater Interfaces 2017;9:4015–23. doi:10.1021/acsami.6b11793.

[108] Guo H, Lv R, Bai S. Recent advances on 3D printing graphene-based composites. Nano Mater Sci 2019;1:101–15. doi:10.1016/j.nanoms.2019.03.003.

[109] Bose S, Vahabzadeh S, Bandyopadhyay A. Bone tissue engineering using 3D printing. Mater Today 2013;16:496–504. doi:10.1016/j.mattod.2013.11.017.

[110] Lim CWJ, Le KQ, Lu Q, Wong CH. An overview of 3-D printing in manufacturing, aerospace, and automotive industries. IEEE Potentials 2016;35:18–22. doi:10.1109/MPOT.2016.2540098.

[111] Ambrosi A, Webster RD. 3D printing for aqueous and non-aqueous redox flow batteries. Curr Opin Electrochem 2020;20:28–35. doi:10.1016/j.coelec.2020.02.005.

[112] Ni Y, Ji R, Long K, Bu T, Chen K, Zhuang S. A review of 3D-printed sensors. Appl Spectrosc Rev 2017;52:623–52. doi:10.1080/05704928.2017.1287082.

[113] Prasad LK, Smyth H. 3D Printing technologies for drug delivery: a review. Drug Dev Ind Pharm 2016;42:1019–31. doi:10.3109/03639045.2015.1120743.

[114] Pourchet LJ, Thepot A, Albouy M, Courtial EJ, Boher A, Blum LJ, et al. Human skin 3D bioprinting using scaffold-free approach. Adv Healthc Mater 2017;6:1601101. doi:10.1002/adhm.201601101.

[115] Zhao F, Wang J, Wang L, Chen L. An approach for simulating the fitting of rigid gas-permeable contact lenses using 3D printing technology. Contact Lens Anterior Eye 2019;42:165–9. doi:10.1016/j.clae.2018.10.003.

[116] Lee JS, Hong JM, Jung JW, Shim JH, Oh JH, Cho DW. 3D printing of composite tissue with complex shape applied to ear regeneration. Biofabrication 2014;6. doi:10.1088/1758-5082/6/2/024103.

[117] Gill DK, Walia K, Rawat A, Bajaj D, Gupta VK, Gupta A, et al. 3D modelling and printing of craniofacial implant template. Rapid Prototyp J 2019;25:397–403. doi:10.1108/RPJ-12-2017-0257.

[118] Kim T, Lee YG. Shape transformable bifurcated stents. Sci Rep 2018;8:1–9. doi:10.1038/s41598-018-32129-3.

[119] Nam HS, Seo CH, Joo SY, Kim DH, Park DS. The application of three-dimensional printed finger splints for post hand burn patients: A case series investigation. Ann Rehabil Med 2018;42:634–8. doi:10.5535/arm.2018.42.4.634.

[120] Yi H-G, Choi Y-J, Jung JW, Jang J, Song T-H, Chae S, et al. Three-dimensional printing of a patient-specific engineered nasal cartilage for augmentative rhinoplasty. J Tissue Eng 2019;10:204173141882479. doi:10.1177/2041731418824797.

[121] Tappa K, Jammalamadaka U, Ballard DH, Bruno T, Israel MR, Vemula H, et al. Medication eluting devices for the field of OBGYN (MEDOBGYN): 3D printed biodegradable hormone eluting constructs, a proof of concept study. PLoS One 2017;12:e0182929. doi:10.1371/journal.pone.0182929.

[122] Lind JU, Busbee TA, Valentine AD, Pasqualini FS, Yuan H, Yadid M, et al. Instrumented cardiac microphysiological devices via multimaterial three-dimensional printing. Nat Mater 2017;16:303–8. doi:10.1038/nmat4782.

[123] Kim K, Park J, Suh J hoon, Kim M, Jeong Y, Park I. 3D printing of multiaxial force sensors using carbon nanotube (CNT)/thermoplastic polyurethane (TPU) filaments. Sensors Actuators, A Phys 2017;263:493–500. doi:10.1016/j.sna.2017.07.020.

[124] Sadia M, Sośnicka A, Arafat B, Isreb A, Ahmed W, Kelarakis A, et al. Adaptation of pharmaceutical excipients to FDM 3D printing for the fabrication of patient-tailored immediate release tablets. Int J Pharm 2016;513:659–68. doi:10.1016/j.ijpharm.2016.09.050.

[125] Hullette T. Direct Drive vs Bowden Extruder: The Differences n.d. https://all3dp.com/2/direct-vs-bowden-extruder-technology-shootout/ (accessed February 2, 2021).

[126] Simplify3D n.d. https://www.simplify3d.com/support/materials-guide/flexible/ (accessed February 2, 2021).

[127] Przybytek A, Gubańska I, Kucińska-Lipka J, Janik H. Polyurethanes as a potential medical-grade filament for use in fused deposition modeling 3D printers – a brief review. Fibres Text East Eur 2018;26:120–5. doi:10.5604/01.3001.0012.5168.

[128] Tzounis L, Petousis M, Grammatikos S, Vidakis N. 3D Printed thermoelectric polyurethane/multiwalled carbon nanotube nanocomposites: A novel approach towards the fabrication of flexible and stretchable organic thermoelectrics. Materials 2020;13:2879. doi:10.3390/ma13122879.

[129] Xiang D, Zhang X, Li Y, Harkin-Jones E, Zheng Y, Wang L, et al. Enhanced performance of 3D printed highly elastic strain sensors of

carbon nanotube/thermoplastic polyurethane nanocomposites via non-covalent interactions. Compos Part B Eng 2019;176:107250. doi:10.1016/j.compositesb.2019.107250.

[130] Kirchmajer DM, Gorkin III R, in het Panhuis M. An overview of the suitability of hydrogel-forming polymers for extrusion-based 3D-printing. J Mater Chem B 2015;3:4105–17. doi:10.1039/C5TB00393H.

[131] Karyappa R, Hashimoto M. Chocolate-based ink three-dimensional printing (Ci3DP). Sci Rep 2019;9:14178. doi:10.1038/s41598-019-50583-5.

[132] Gholamipour-Shirazi A, Norton IT, Mills T. Designing hydrocolloid based food-ink formulations for extrusion 3D printing. Food Hydrocoll 2019;95:161–7. doi:10.1016/j.foodhyd.2019.04.011.

[133] Irgens F. Rheology and non-newtonian fluids. Cham: Springer International Publishing; 2014. doi:10.1007/978-3-319-01053-3.

[134] Faes M, Valkenaers H, Vogeler F, Vleugels J, Ferraris E. Extrusion-based 3D Printing of Ceramic Components. Procedia CIRP 2015;28:76–81. doi:10.1016/j.procir.2015.04.028.

[135] Valentin TM, Landauer AK, Morales LC, DuBois EM, Shukla S, Liu M, et al. Alginate-graphene oxide hydrogels with enhanced ionic tunability and chemomechanical stability for light-directed 3D printing. Carbon 2019;143:447–56. doi:10.1016/j.carbon.2018.11.006.

[136] Wu Y, Lin ZY, Wenger AC, Tam KC, Tang X. 3D bioprinting of liver-mimetic construct with alginate/cellulose nanocrystal hybrid bioink. Bioprinting 2018;9:1–6. doi:10.1016/j.bprint.2017.12.001.

[137] Li H, Tan YJ, Leong KF, Li L. 3D bioprinting of highly thixotropic alginate/methylcellulose hydrogel with strong interface bonding. ACS Appl Mater Interfaces 2017;9:20086–97. doi:10.1021/acsami.7b04216.

[138] Markstedt K, Mantas A, Tournier I, Martínez Ávila H, Hägg D, Gatenholm P. 3D bioprinting human chondrocytes with nanocellulose-alginate bioink for cartilage tissue engineering applications. Biomacromolecules 2015;16:1489–96. doi:10.1021/acs.biomac.5b00188.

[139] Habib A, Sathish V, Mallik S, Khoda B. 3D printability of alginate-carboxymethyl cellulose hydrogel. Materials 2018;11. doi:10.3390/ma11030454.

[140] Li L, Qin S, Peng J, Chen A, Nie Y, Liu T, et al. Engineering gelatin-based alginate/carbon nanotubes blend bioink for direct 3D printing of vessel constructs. Int J Biol Macromol 2020;145:262–71. doi:10.1016/j.ijbiomac.2019.12.174.

[141] Yang JH, Yoon NS, Park JH, Kim IK, Cheong IW, Deng Y, et al. Electrospinning fabrication and characterization of poly(vinyl alcohol)/waterborne polyurethane nanofiber membranes in aqueous solution. J Appl Polym Sci 2011;120:2337–45. doi:10.1002/app.33435.

[142] Chen SH, Chou PY, Chen ZY, Lin FH. Electrospun water-borne polyurethane nanofibrous membrane as a barrier for preventing postoperative peritendinous adhesion. Int J Mol Sci 2019;20. doi:10.3390/ijms20071625.

[143] Santamaria-Echart A, Ugarte L, Gonzalez K, Martin L, Irusta L, Gonzalez A, et al. The role of cellulose nanocrystals incorporation route in waterborne polyurethane for preparation of electrospun nanocomposites mats. Carbohydr Polym 2017;166:146–55. doi:10.1016/j.carbpol.2017.02.073.

[144] Bui TNTV. Structure, rheological properties and connectivity of gels formed by carrageenan extracted from different red algae species. Le Mas Université, 2019.

[145] Necas J, Bartosikova L. Carrageenan: A review. Vet Med (Praha) 2013;58:187–205. doi:10.17221/6758-VETMED.

[146] Liu S, Chan WL, Li L. Rheological properties and scaling laws of κ-carrageenan in aqueous solution. Macromolecules 2015;48:7649–57. doi:10.1021/acs.macromol.5b01922.

[147] Chen Y, Liao M-L, Dunstan DE. The rheology of K+-κ-carrageenan as a weak gel. Carbohydr Polym 2002;50:109–16. doi:10.1016/S0144-8617(02)00009-7.

[148] Sedayu BB, Cran MJ, Bigger SW. A review of property enhancement techniques for carrageenan-based films and coatings. Carbohydr Polym 2019;216:287–302. doi:10.1016/j.carbpol.2019.04.021.

[149] Savadekar NR, Karande VS, Vigneshwaran N, Bharimalla AK, Mhaske ST. Preparation of nano cellulose fibers and its application in kappa-carrageenan based film. Int J Biol Macromol 2012;51:1008–13. doi:10.1016/j.ijbiomac.2012.08.014.

[150] Ikeda S, Nishinari K. "Weak gel"-type rheological properties of aqueous dispersions of nonaggregated κ-carrageenan helices. J Agric Food Chem 2001;49:4436–41. doi:10.1021/jf0103065.

[151] Goonoo N, Khanbabaee B, Steuber M, Bhaw-Luximon A, Jonas U, Pietsch U, et al. κ-Carrageenan enhances the biomineralization and osteogenic differentiation of electrospun polyhydroxybutyrate and polyhydroxybutyrate valerate fibers. Biomacromolecules 2017;18:1563–73. doi:10.1021/acs.biomac.7b00150.

[152] Liu S, Huang S, Li L. Thermoreversible gelation and viscoelasticity of κ-carrageenan hydrogels. J Rheol 2016;60:203–14. doi:10.1122/1.4938525.

Chapter 2

MATERIALS AND METHODS

2. MATERIALS AND METHODS

2.1. Aim of the chapter

In this chapter, materials employed in the synthesis of the WBPUU are described, as well as those used for the obtaining of CNF, carboxylated CNF, graphene, graphene oxide and reduced graphene oxide. Furthermore, the characterization techniques and the conditions used for the analysis of the prepared materials are also indicated, regarding the study of the dispersion properties and material's rheology, physico-chemical properties, morphology, thermal, mechanical, electrical behavior and their biocompatible and antimicrobial behavior.

2.2. Materials

For the synthesis of the waterborne polyurethane-urea, a difunctional polyol coming from a renewable source, Priplast 3192® (M_w= 2000 g mol^{-1}), purchased from Croda, has been used as soft segment. Isophorone diisocyanate (IPDI), kindly supplied from Covestro, 2,2-bis (hydroxymethyl) propionic acid (DMPA), used as internal emulsifier, provided from Aldrich and ethylene diamine (EDA), as chain extender, provided from Fluka, were used as hard segment. Triethylamine (TEA), provided by Fluka, was employed to neutralize the carboxylic groups of DMPA, and dibutyltin dilaurate (DBTDL), provided from Aldrich, was used as catalyst. Both the polyol and the DMPA were dried under vacuum at 60 °C for 4 h prior to their use.

The structure of the reactants used during the synthesis process are shown in Figure 2.1.

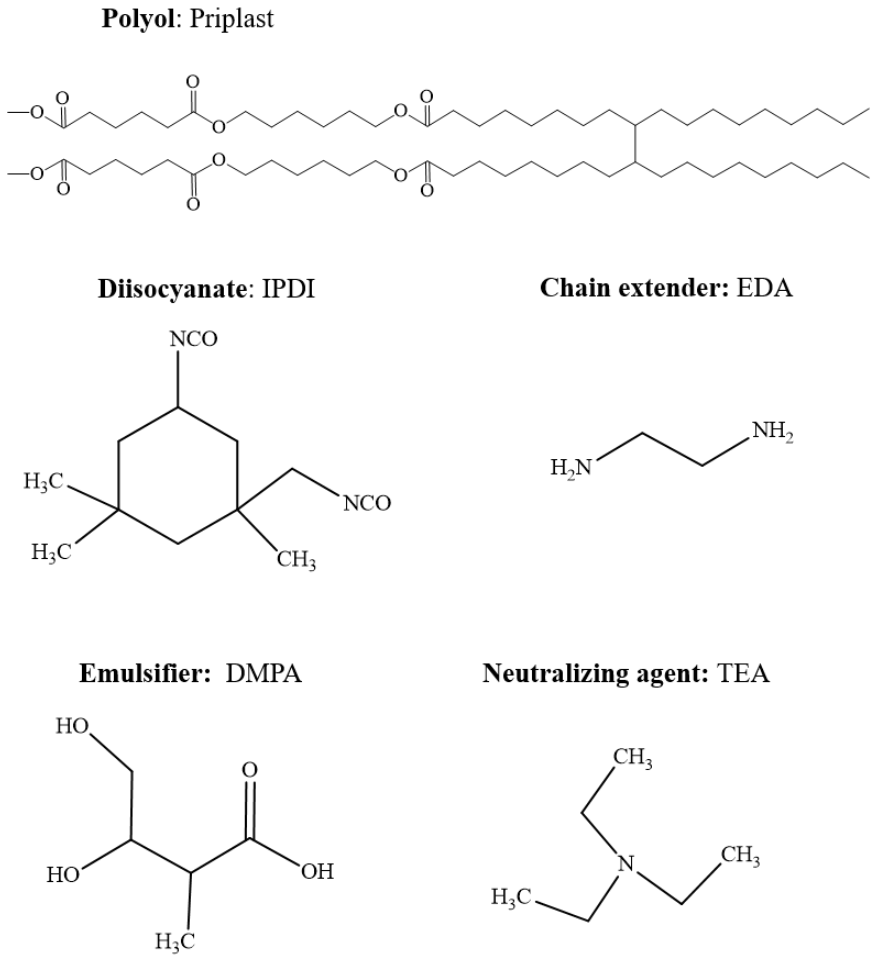

Figure 2.1. Structure of reagents used in WBPUU synthesis

For cellulose nanofibers preparation, standard bleached hardwood kraft pulp (bHKP) from *Eucalyptus globulus*, obtained from a local paper mill, was used as raw material. Sodium metaperiodate ($NaIO_4$), sodium chloride (NaCl), hydrogen peroxide (H_2O_2), sodium hydroxide (NaOH) and sodium chlorite ($NaClO_2$), used for the carboxylation treatment of the cellulose, were purchased from Scharlab and used as received. Moreover, a commercial cellulose was employed as reference and for CNF content optimization. For this freeze-dried cellulose nanofibers provided by the University of Maine (Lot. 9004-34-6) were used.

Graphene and graphene oxide were prepared parting from graphite flakes (Aldrich). N-methyl pyrrolidone (NMP), used when exfoliating graphene, was purchased from Sigma-Aldrich. Sulfuric acid (H_2SO_4,), sodium nitrate ($NaNO_3$), potassium permanganate ($KMnO_4$), hydrogen peroxide (H_2O_2) and hydrochloric acid (HCl) used to obtain GO were supplied by Panreac. Cyclohexane was purchased from Scharlab. *Salvia officinalis L.* dry material was purchased at a local herbalist. κ-carrageenan (Lot. #BCBX5072) was purchase from Sigma-Aldrich.

Natural plant-based colorants, namely C11 - Logwood extract, C15 – Chestnut extract and C25 - Alder Buckthorn extract were purchased from Couleurs de plantes.

2.3. WBPUU dispersion characterization

2.3.1. pH

The pH of the WBPUU dispersion was measured using a pH meter GLP22 of Crison, which was calibrated with pH 4.00 and 7.00 buffer solution standards.

2.3.2. Dynamic Light Scattering

The particle size of the WBPUU dispersion and its distribution was measured by dynamic light scattering, using a BI-200SM goniometer from Brookhaven. The intensity of dispersed light was measured using a luminous source of He-Ne laser (Mini L-30, wavelength 637 nm, 400 mW) and a detector (BI–APD) placed on a rotary arm which allows measuring the intensity at 90º. Samples were prepared mixing a small amount of aqueous dispersion with ultrapure water and measurements were carried out at 25 ºC by triplicate.

2.3.3. Zeta potential

The stability of the polyurethane-urea dispersions was analyzed by zeta potential tests. For this a Zetasizer Ultra from Malvern Panalytical was

employed. This technique measures the zeta potential of the dispersion by applying an electric field across the dispersion. Particles within the dispersion with a zeta potential will migrate toward the electrode of opposite charge with a velocity proportional to the magnitude of the zeta potential, allowing to determine the stability of the dispersion.

2.4. Rheological properties

Rheological characterization of WBPUU dispersion and gels was performed using a Haake Viscotester iQ (Thermo Scientific). Tests were performed at 25 °C using a coaxial cylinder or a plate-plate geometry, depending on the viscosity of the tested material. In the case of coaxial cylinders, CC25 DIN/Ti adapter was used, with piston radius of 12.54 mm and a ring gap (difference between radii) of 1.06 mm. For plate-plate geometry, a P35/Al adapter was used, where plates with a diameter of 35 mm were employed and a working gap of 1 mm was set.

For flow tests, shear rate sweeps from 0.2 to 1000 s^{-1} were performed. For yield point determination tests, dynamic oscillatory tests were performed in a shear stress range of 10 up to 10000 Pa, depending on the tested sample. Last, structure recovery tests were performed in a three stage experiment. In this test, viscosity values were measured at a shear rate of 0.2 s^{-1} during 100 s, followed by a shear rate of 100 s^{-1} for 100 seconds in the second step and ending with the same initial condition for the third step.

The determination of yield point can be done by many different methods [1-5]. In this work, yield point was determined as the point of deviation of G' from linearity. Flow point, on the other hand, is measured as the crossover point for G' and G".

For the determination of the structural recovery capacity of the inks, a relation of the ink's viscosity after the high shear rate process and before it was calculated, as expressed in equation 2.1.

$$Structural\ Recovery = \frac{\eta_{AS}}{\eta_{BS}} \cdot 100 \qquad (equation\ 2.1)$$

where η_{BS} is the viscosity of the material before the high shear rate process and η_{AS} is the viscosity after the high shear rate process; in both cases the viscosity was measured after 60 seconds of the beginning of that part of the test.

2.5. Physico-chemical characterization

2.5.1. Gel Permeation Chromatography

Average molecular weight (M_W) and polydispersity index (PI) of the synthesized polyurethane-urea was determined by Gel Permeation Chromatography (GPC), using a Thermo Scientific chromatograph, equipped with an isocratic Dionex UltiMate 3000 pump and a RefractoMax 521 refractive index detector. The separation was carried out at 30 °C within four Phenogel GPC columns from Phenomenex, with 5 µm particle size and 10^5, 10^3, 100 and 50 Å porosities, respectively, located in an UltiMate 3000 Thermostated Colum Compartment. THF was used as mobile phase at a flow rate of 1 $mL \cdot min^{-1}$. For the preparation of the sample, the polyurethane-urea was dissolved in THF at 1 wt% and filtered by using nylon filters with 2 µm pore size. M_W and PI were reported as weight average polystyrene standards.

2.5.2. Fourier Transform Infrared spectroscopy

Infrared spectra of samples were obtained by Fourier Transform Infrared spectroscopy (FTIR) by using a Nicolet Nexus spectrometer. In this technique, the sample is irradiated by an infrared light source of different frequencies and the absorbed quantity for each beam is measured.

WBPUU, nanocomposites, CNF and natural extracts samples were analyzed using a MKII Golden Gate accessory (Specac) with a diamond crystal at a nominal incidence angle of 45º and ZnSe lens. Spectra were recorded in

attenuated reflection (ATR) mode between 4000 and 650 cm^{-1} averaging 32 scans with a resolution of 4 cm^{-1}.

For carbonaceous nanostructure and *Salvia* extract characterization, KBr pellets (0.0025 mg sample·g^{-1} KBr) were employed for the analysis. Single-beam spectra of the samples were obtained after averaging 32 scans in the range of 4000 to 400 cm^{-1}, with a resolution of 4 cm^{-1}.

2.5.3. Ultraviolet-Visible spectroscopy

The absorbance of graphite and graphene oxide was measured by Ultraviolet-Visible spectrophotometry (UV-Vis), using open-top quartz cells. For sample preparation, low concentration dispersions were prepared (0.5 g sample·mL^{-1} solvent) by using ethanol and deionized water for graphite and graphene oxide, respectively. The spectra were obtained in a UV-3600 UV-VIS-NIR spectrophotometer (Shidmazu, Kioto, Japan) in the wavelength range of 200 to 600 nm.

2.5.4. Elemental Analysis

Elemental Analysis (EA) was performed in order to determine the changes in composition of the carbonaceous samples. For this, a Euro EA3000 Elemental Analyzer of Eurovector was used. In this way, the sample is combusted and the resultant products are analyzed in a chromatographic column, where a thermal conductivity detector provides a signal of each element and then determines its percentage.

2.5.5. X-Ray Diffraction

X-Ray Diffraction (XRD) patterns were collected by using a Philips X'pert PRO automatic diffractometer (Malvern Panalytical, Malvern, UK) operating at 40 kV and 40 mA, in theta-theta configuration, a secondary monochromator with Cu-Kα radiation (λ = 1.5418 Å) and a PIXcel solid state detector (active

length in 2θ 3.347º). Data were collected from 5 to 75º 2θ for cellulose nanofibers and from 2 to 40º 2θ for carbonaceous structures (step size 0.026 and time per step 80 s) at room temperature. A fixed divergence and antiscattering slit giving a constant volume of sample illumination were used.

For cellulose nanofibers, the Crystallinity Index (C.I.) of the systems was calculated following the equation proposed by Hermans et al. (equation 2.2) [6].

$$C.I.(\%) = \left(\frac{A_c}{A_c + A_a}\right) x\ 100 \qquad (equation\ 2.2.)$$

where A_c and A_a are the areas related to the crystalline and amorphous peaks, respectively.

For carbonaceous materials, in order to determine the distance between planes, Bragg's law was used [7] (equation 2.3).

$$n\lambda = 2d \sin\theta \qquad (equation\ 2.3)$$

In which, n is a whole number, λ is the wavelength of the incident radiation, d is the shortest distance between two successive identical planes in the crystal and θ is the angle of incidence of the primary rays.

2.5.6. Raman spectroscopy

For the characterization of the carbonaceous structures, Raman spectroscopy was used. Raman spectroscopy consists on the irradiation of a sample by monochromatic light and the analysis of scattered phonons. Dispersed phonons will suffer frequency changes characteristic of the molecules of the sample. Raman spectra were obtained with a Renishaw InVia spectrometer (Renishaw, Wotton-under-Edge, UK), coupled to a Leica microscope (50X) with a laser of 514 nm wavelength (Modu Laser) at 5% potency. Data were collected in the

range of 150-3500 cm^{-1}. Exposure time and accumulations were set at 20 seconds and 5, respectively.

2.6. Morphological characterization

2.6.1. Atomic Force Microscopy

The morphology of WBPUU was determined by Atomic Force Microscopy (AFM). Phase images were obtained at room temperature in tapping mode, using a Nanoscope IIIa scanning probe microscope (Multimode TM Digital instruments) with an integrated force generated by cantilever/silicon probes, applying a resonance frequency of about 180 kHz. The cantilever had a tip radius of 5-10 nm and was 125 μm long.

For sample preparation a drop of the WBPUU dispersion was placed in a glass support and were spin-coated using a Spincoater P6700, operating at 1200 rpm for 130 s.

The morphology of graphene oxide flakes was also analyzed by AFM. Height images were obtained in a Dimension Icon (Bruker) scanning probe microscope equipped with a Nanoscope V controller (Bruker). Tapping mode was employed in air, using an integrated tip/cantilever (125 μm length with ca. 300 kHz resonant frequency).

For sample preparation, GO fractions were dispersed in water (0.1 $mg \cdot mL^{-1}$) using an ultrasonic tip for 1 h. A droplet of graphene oxide dispersion was put on a prewashed silicon wafer substrate and water was eliminated by spin coating at 1200 rpm for 120 s.

2.6.2. Scanning Electron Microscopy

The morphology of the cellulose nanofibers was analyzed via Scanning Electron Microscopy (SEM) using a JSM-6400 scanning microscope working at a 7 mm distance to the mat and 20 kV. Samples were coated (Quorum

Q150TES) with a 20 nm gold coat in order to make them conductors. Nanofiber dimensions were measured from these images via ImageJ software.

Morphology of WBPUU/CNF composites and G and rGO coated films was also studied through SEM. Images were obtained with a FEI ESEM Quanta 200, operating at 5-20 kV. In order to prepare samples, they were first frozen in liquid nitrogen and a cryofracture of the cross-section was done. Samples were held with a clamp and the analyses took place under vacuum.

The morphology of the printed and freeze-dried scaffolds was also observed by SEM, using Field Emission Gun Scanning Electron Microscopy (FEG-SEM) Hitachi S-4800N, at a voltage of 5 kV. Prior to the test, and in order to analyze the cross section of prepared scaffolds, the samples were cryofractured in liquid nitrogen and sputter coated with a thin layer of gold (~ 10 nm) in a Emitech K550X ion sputter.

2.6.3. Transmission Electron Microscopy

In order to further analyse the morphologies of the carbonaceous reinforcements, Transmission Electron Microscopy (TEM) analysis was performed. Measurements were carried out on a FEI Titan Cubed G2 60-300 microscope (Thermofisher Scientific), equipped with a Schottky X-FEG field emission electron gun, monochromator and CEOS GmbH spherical aberration (Cs) corrector on the image side. The microscope was operated at 80 kV. The third-order spherical aberration (Cs) was tuned to -10 μm. Images were obtained for an underfocus of -8 nm and were recorded on a CCD camera (2kx2k, Gatan UltraScan 1000, Gatan), using exposition times of 1s per image.

For sample preparation, 0.1 mg of the carbonaceous sample was dispersed in 20 mL of distilled water. For the dispersion of graphene in water, *Salvia* extract, acting as a surfactant, was employed.

2.7. Thermal characterization

2.7.1. Differential Scanning Calorimetry

The thermal properties of the different prepared systems were determined by Differential Scanning Calorimetry (DSC) using a Mettler Toledo DSC 3+ equipment provided with a robotic arm and an electric intracooler as refrigerator unit. Between 5 and 10 mg of sample were encapsulated in aluminum pans and heated from -65 to 200 ºC at a scanning rate of 10 ºC min^{-1} in nitrogen atmosphere. From the heating thermograms, order-disorder transition temperature (T_{HS}), related to the short range ordering of the hard segment segment, and enthalpy, as the maximum of the peak and the area below the peak, respectively, as well as glass transition temperature (T_g), as the inflection point of the curve, were determined.

The relative crystallinity or short range ordering degree of the composites was calculated following equation 2.4, proposed by *Wunderlich* [8].

$$X_{HS} = \frac{\Delta H_{HSc}}{w \cdot \Delta H_{HS}} \cdot 100 \qquad (equation\ 2.4)$$

Where ΔH_{HSc} represents the measured enthalpy of the composite transition, whereas ΔH_{HS} is related to the measured enthalpy of the neat polyurethane short range ordering transition and w is the weight fraction of the WBPUU in the composite.

2.7.2. Thermogravimetric Analysis

The thermal stability of WBPUU, the different reinforcements and the nanocomposites was determined by Thermogravimetric Analysis (TGA) performed in a Mettler Toledo TGA/DSC 3+ equipment. The samples were heated from 30 to 700 ºC in a nitrogen atmosphere at a scanning rate of 10 ºC min^{-1}. From the weight loss and its first derivative curves, the onset degradation temperature (T_0) (calculated as temperature at which a weight loss of 5 wt%

takes place), and the maximum degradation temperature (T_d) (calculated as the minimum of the degradation peak in the derivative curve) were determined. Samples between 5 and 10 mg were employed in the tests.

2.7.3. Dynamic Mechanical Analysis

The viscoelastic behavior of the prepared films, filaments and printed 3D parts were determined by Dynamic Mechanical Analysis (DMA) using an Eplexor 100 N analyzer Gabo (Selb, Germany) equipment.

For films, filaments and 3D printed dog-bone specimens, measurements were carried out in tensile mode from -100 to 180 ºC at a scanning rate of 2 ºC min^{-1}. The initial strain was established as 0.05% and the operating frequency was fixed at 1 Hz.

For coated 3D printed parts, measurements were performed in compression mode. The temperature scan was maintained -100 to 180 ºC at a scanning rate of 2 ºC·min^{-1}. The frequency was kept in 1 Hz and a contact force of 0.50 N was applied.

2.8. Mechanical characterization

2.8.1. Tensile tests

Tensile analysis was performed in an Instron 5967 testing machine provided with a 500 N load cell and pneumatic grips to hold the samples. Tensile modulus (E), stress at yield (σ_y), stress at break (σ_b) and elongation at break (ε_b) were determined from stress-strain curves. Five tests were carried out for each series and average values were calculated. For neat polymer and composite films, samples were cut in 2.8 mm in width and 0.4 mm in thickness pieces and specimens with a length of 10 mm were tested. Filaments with a 1.75 mm diameter were also tested with a distance between clamps of 10 mm. For FDM 3D printed parts, dog bone specimens were used, with a gauge length, width

and thickness of 50, 3.25 and 1.3 mm, respectively. Specimens were tested at a crosshead speed of 20 mm min^{-1} at room temperature.

2.8.2. Compression tests

For 3D printed and freeze-dried cylindrical samples (Ø = 10 mm and height = 5 mm), compression tests were carried out. Tests were carried out at room temperature using a Instron 5967 universal testing machine provided with a 500 N load cell. Compression force was applied in the normal direction from the layer by layer printing. Samples were compressed to a fixed length of 2 mm at a crosshead speed of 10 mm·min^{-1}.

The average value of compression modulus was calculated as the slope of the stress-strain curve at low deformations, the stress was measured at the maximum applied strain (60%) and densification strain as the strain at the intersection point between the stress plateau and a line extrapolated from the densification line. Moreover, specific Young modulus values were measured as the ratio between each sample's Young modulus and its density. The density of the 3D printed and freeze-dried samples was calculated as the ratio between their measures weight and volume. Compression values were averaged for five specimens.

2.9. Electrical characterization

2.9.1. Electrical conductivity

Electrical properties of carbonaceous reinforcements, polyurethane/graphene nanocomposites and coated systems were analyzed by a Keithley 4200-SCS (Keithley Instruments) equipment for semiconductor analysis. Two point measurements were carried out, performing 0-5 V linear scans, with 0.01 V step and a compliance of 0.1 A. Electrical resistance (R) values were calculated from intensity vs. voltage curves. Resistivity (ρ) and conductivity (σ) values were calculated using equations 2.5 and 2.6.

$$\rho = R\frac{A}{L} \qquad (equation\ 2.5)$$

$$\sigma = \frac{1}{\rho} \qquad (equation\ 2.6)$$

where R is the resistance and A and L are the area and the length of the analyzed sample respectively.

2.9.2. Electrostatic Force Microscopy

Electrical conductivity properties for composites that show a semiconductive behavior were further analyzed by Electrostatic Force Microscopy (EFM). In EFM analysis, an electrostatic field is created between the tip and the substrate. Analyzing the phase shifts occurring due to electrostatic interactions, conductive and insulating parts of the sample can be distinguished. Measurements were performed with Pt/Ir coated tips (75 kHz resonant frequency) in a Dimension ICON (Bruker) equipment, working at lift mode (100 nm) and at room temperature. For each system, a sample size of 2 x 2 mm^2 was cut and stuck to an AFM stainless steel specimen disk. To analyze the distribution of the electrostatic field on the sample surface, bias voltages from 0 to 12V were applied to the cantilever/tip system.

2.10. Biocompatibility test

In order to analyze biocompatibility of the WBPUU and its potential for biomedical applications, in vitro biocompatibility test were carried out, by performing cytotoxicity and cell adhesion analysis.

2.10.1. Short-term cytotoxicity test

Cytotoxicity was evaluated following ISO 10993-5:2009 standard protocol and by PrestoBlue® (Invitrogen), a resazurin-based solution that functions as a colorimetric cell viability indicator. Briefly, murine fibroblasts (L929 cells) were seeded into 96-well plates at a density of 4 x 10^3 cells/well in 100 µL of

complete culture medium (Dulbecco's modified Eagle's medium (DMEM) supplemented with sodium pyruvate 1 mM, 1% of non-essential amino acids, 1% penicillin-streptomycin and fetal bovine serum 10%). After 24 h, the medium was replaced with 100 µL of negative control (fresh complete culture medium), positive control (DMSO, 10% in complete culture medium) or biomaterial's extractive media and a 10% of PrestoBlue® was added. The optical density (OD) was measured at 570 and 600 nm in a spectrophotometer (Synergy HT spectrophotometer, Biotek) at different time points (0, 24, 48 and 72 h). The viability of the cells was calculated from equation 2.7. All assays were conducted in triplicate and average values and their standard deviations were calculated. For the in vitro biocompatibility assay, two-way analysis of variance (ANOVA) followed by Bonferroni post-test was performed using GraphPad Prism software (San Diego, CA, U.S.). The results were expressed as mean ± SD and values of $p<0.05$ were considered statistically significant with respect to the positive control. All assays were conducted in triplicate.

$$Viability\ (\%) = \frac{Abs_{sample}}{Abs_{negative\ control}}\ x\ 100 \quad (equation\ 2.7)$$

where Abs_{sample} is the absorbance of the sample cells cultured in biomaterial's extractive media and $Abs_{negative}$ control is the absorbance of the negative control.

2.10.2. Live/Dead assay

The adhesion of the L929 cells on the surface of the materials was studied by performing Live/Dead assay. 0.5 cm^2 samples were prepared and sterilized under ultra-violet light for 30 minutes prior to analysis. The material was placed in 24-well ultra-low attachment plate and incubated at 37 °C for 24 hours in 500 µL of a complete culture medium. After that, the medium was removed from the wells and L929 were seeded on the surface of the material at a density of 5 x 10^4 cells in 20 µL of complete culture medium and were incubated for 2 h at 37 °C to enhance cell adhesion onto the materials surface. To maintain a

hydrated environment, 500 µL of PBS were added in the adjacent wells plates. After the period of adhesion, 500 µL of complete culture medium were added to each sample. Fluorescent images were obtained in a confocal microscope (Olympus LV500, Japan) after 3 and 7 days. The medium was removed and the samples were rinsed twice with PBS and later dyed with Calcein AM 4 µM and propidium iodide 5 µM in 1 mL of PBS. Finally, samples were incubated for 20 minutes at 37 °C in the dark. Live cells were observed thanks to the green fluorescence of the Calcein AM (λex/λem: 495/515) and dead cells due to the red fluorescence of the propidium iodide (λex/λem: 535/617 nm).

2.11. Antibacterial characterization

The antibacterial behaviour of the composites prepared with additives that often show antimicrobial capacity (carbonaceous structures and natural extracts) was studied. For this, antibacterial assays were performed using Gram positive bacteria Staphylococcus aureus CECT 239, and one Gram negative, Escherichia Coli CECT 405 in the case of graphene and *Salvia* extract containing materials and Staphylococcus aureus ATCC 19213 and Escherichia coli ATCC 10536 in Logwood, Chestnut and Alder Buckthorn extracts containing materials.

The method was based on the Kirby-Bauer modified test. Briefly, the bacteria inoculums were prepared by aseptically transferring 4 isolated colonies of each microorganisms to separate test tubes containing nutrient broth and were then incubated for 24 h at 37 °C. The inoculums were diluted to 0.5 McFarland turbidity standard (corresponding to a concentration of 1.5–3.0 x 10^8 CFU/mL) using sterilized Ringer solution. The concentrations of the bacteria dilutions were also controlled by UV-visible spectrophotometry by measuring the absorbance at 625 nm. Then, the bacteria solutions were inoculated in Mueller Hinton Agar plates, using a sterilized swab. Afterwards, the sample was placed in the center of the plate and the plates were incubated at 37 ºC. The plates were analyzed after 24 and 96 hours and the existence and diameter of an inhibition

zone were studied, as well as the possible growth of the bacteria on the surface of the materials.

For graphene and graphene oxide containing composites and G and rGO coated composite films, 5 x 5 cm^2 samples were cut and used as is. For sample preparation, WBPUU/natural extracts composites samples with a diameter of 6 mm were used after freeze-dried. In order to study the behavior of just the active ingredient, natural extracts were studied by themselves. For this, solutions containing the same mass of extract as their composite counterpart were prepared and placed on a paper filter disc with a diameter of 6 mm, which were later left to dry. As reference, antibiotic discs with a 6 mm diameter were used.

2.12. References

[1] Cyriac F, Lugt PM, Bosman R. On a new method to determine the yield stress in lubricating grease. Tribol Trans 2015;58:1021–30. doi:10.1080/10402004.2015.1035414.

[2] Shih WY, Shih WH, Aksay IA. Elastic and yield behavior of strongly flocculated colloids. J Am Ceram Soc 1999;82:616–24. doi:10.1111/j.1151-2916.1999.tb01809.x.

[3] Sharma M, Kristo E, Corredig M, Duizer L. Effect of hydrocolloid type on texture of pureed carrots: Rheological and sensory measures. Food Hydrocoll 2017;63:478–87. doi:10.1016/j.foodhyd.2016.09.040.

[4] De Graef V, Depypere F, Minnaert M, Dewettinck K. Chocolate yield stress as measured by oscillatory rheology. Food Res Int 2011;44:2660–5. doi:10.1016/j.foodres.2011.05.009.

[5] Lille M, Nurmela A, Nordlund E, Metsä-Kortelainen S, Sozer N. Applicability of protein and fiber-rich food materials in extrusion-based 3D printing. J Food Eng 2018;220:20–7. doi:10.1016/j.jfoodeng.2017.04.034.

[6] Hermans PH, Weidinger A. Quantitative X-Ray investigations on the crystallinity of cellulose fibers. A background analysis. J Appl Phys 1948;19:491–506. doi:10.1063/1.1698162.

[7] Bragg WL. The diffraction of short electromagnetic waves by a crystal. Proc Camb Philol Soc 1913;17:43–57.

[8] Wunderlich B. Thermal analysis of polymeric materials. Knoxville: Springer Berlin Heidelberg; 2005.

Chapter 3

WBPUU SYNTHESIS AND NANOENTITIES PREPARATION

3. WBPUU SYNTHESIS AND NANOENTITIES PREPARATION

3.1. Aim of the chapter

This chapter focuses on the synthesis and characterization of a waterborne polyurethane-urea, as well as in the preparation of different types of nanostructures which show potential in the field of nanoreinforcements. The synthesis process of the polyurethane-urea is described and its properties are studied. The obtaining process of cellulose nanofibers and its oxidation process for the production of cellulose nanofibers with different degrees of carboxylation are described. The obtaining of different types of carbonaceous structures are also explained, more specifically the production of nanostructuctures coming from graphite. The exfoliation process of graphene, the different parameters affecting the production of graphene oxide and the reduction of graphene oxide into graphene are studied.

A waterborne polyurethane-urea was synthesized and the obtained dispersion was characterized regarding its solid content, stability, particle size and presence of remaining isocyanate groups. A WBPUU film was prepared and characterized as well. Its morphology, physicochemical, thermal and mechanical properties and biocompatibility were analyzed by means of different characterization techniques.

The characteristics of the prepared nanostructures were also studied. The effect of the carboxylation degree on the morphology, crystalline structure, physicochemical and thermal properties of the cellulose nanofibers was studied. Regarding the carbonaceous structures, the effect that different parameter during the oxidation and exfoliation process have on the production of graphite oxide and graphene oxide were studied, analyzing their physicochemical properties and morphology. Considering the obtained results, parameters were selected for optimized graphene oxide obtaining. Carbonaceous structures were further characterized by Transmission Electron

Microscopy, Elemental Analysis, X-Ray Diffraction, Raman spectroscopy, Fourier Transform Infrared spectroscopy, Thermogravimetric Analysis and electrical conductivity measurements.

3.2. Synthesis of WBPUU

WBPUU was synthesized in a two-step polymerization process. The synthesis was carried out in a 250 mL four-necked jacketed flask, equipped with a mechanical stirrer, a thermometer and a nitrogen inlet. In the first step of the process, the prepolymer, formed by a polyol and a diisocyante, was prepared. The polyol chosen for this synthesis was a Priplast 3192 and the employed diisocyanate was IPDI. Both components were added to the flask with 0.037 wt.% of a catalyst, DBTL, and the mixture was left to react for 5 h at 100 ºC. The reaction was then cooled down to 50 ºC, where the internal emulsifier, in this case DMPA, neutralized with TEA was added, dissolved in a small amount of acetone. The reaction was kept under stirring for 1 more hour. Then the second step of the reaction was carried out, the phase inversion. Before this could take place, the reaction was first cooled until room temperature, in order to avoid isocyanate reaction with water. Under vigorous stirring, deionized water was added dropwise, using a peristaltic pump. Lastly, the reaction was heated to 35 ºC and the chain extender, EDA, was added and left to react for 2 more hours, after which a WBPUU dispersion was obtained.

At low temperatures, isocyanate reactivity with amines is higher than with OH groups, and more so than with water [1–3]. For this reason, it is necessary to work at low temperatures during the phase inversion and chain extension steps.

A molar ratio of 1/1.1/3.5/0.6 of polyol/DMPA/IPDI/EDA was chosen for the WBPUU, following a previously optimized protocol [27]. The reaction times and temperatures were optimized monitoring the reaction progress with the dibutylamine back titration method according to ASTM D 2572-97. The polyol employed for this work was a partially crystalline bifunctional polyester polyol

from the Priplast line of Croda polyols, synthesized from Croda Pripol™ C36 dimer fatty acids, a renewable, natural resource. The chosen polyol has a molecular weight of 2000 g/mol.

3.2.1. Characterization of WBPUU dispersion

The obtained WBPUU aqueous dispersion was characterized regarding its solid content, particle size, stability, pH and physico-chemical structure.

Solid content of the waterborne polyurethane-urea dispersion was determined by weight difference. The measurements were done by duplicate, to minimize possible errors. An average solid content of 33.0 ± 0.1% was measured.

The particle size and distribution of the synthetized WBPUU dispersion were analyzed by dynamic light scattering. The particle size is an important parameter when studying the stability of the WBPUU dispersion. Dispersions with larger particle sizes tend to be less stable, due to the precipitation of these particles. On the other hand, dispersions with small particle sizes have better stability, thanks to the formation of thicker electrochemical double layer [4,5]. Results showed an average particle size of 100.9 ± 0.5 nm with a polydispersity of 0.08. Moreover, the particle size was also measured after 6 months, and did not change significantly, 104.7 ± 0.6 nm, denoting that the synthesized dispersion is stable for prolonged periods of time.

In order to further study dispersion stability, zeta potential tests were carried out. The zeta potential value obtained for the WBPUU dispersion was -63.12 mV. As far as the stability of the dispersion is concerned, WBPUU dispersion presented a zeta potential below -30 mV, thus proving the stability of the synthesized material, since stable dispersions show a zeta potential above +30 mV and below -30 mV [6].

pH measured for WBPUU dispersion was 7.3 ± 0.2. This value was similar to those reported in the literature for waterborne polyurethanes [4-6]. pH measurements help corroborate a successful reaction of components.

To further study the complete consumption of isocyanate groups, FTIR analysis was carried out. FTIR spectrum for WBPUU dispersion is shown in Figure 3.1. Besides the bands of water being very pronounced on the spectrum, bands typical of polyurethanes can also be observed, from which the presence of unreacted isocyanate can be determined. When free isocyanate groups are present, a band appears at 2270 cm^{-1} [10], as this band was not observed in the spectrum, this fact indicated a complete reaction of isocyanate groups.

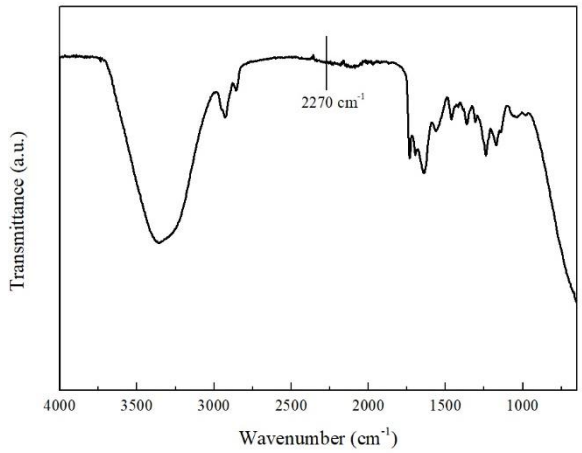

Figure 3.1. FTIR spectrum for WBPUU dispersion

3.2.2. Characterization of WBPUU film

A film with an approximate thickness of 0.4 mm was prepared in an 8 x 8 cm^2 Teflon mold. 9.7 mL of WBPUU dispersion was poured on the mold and left to dry at room temperature for 7 days, followed by 3 days under vacuum (400 mbar) to completely eliminate any entrapped residual water. A photograph of the prepared WBPUU film can be seen in Figure 3.2.

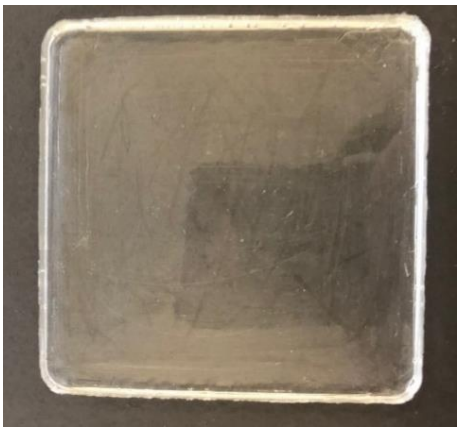

Figure 3.2. Photograph of WBPUU film

WBPUU film morphology was analyzed through AFM and obtained images are shown in Figure 3.3. Images show a homogeneous morphology formed by bright and dark regions related with to crystalline and amorphous domains, respectively.

As can be observed, WBPUU presented a microphase segregated structure. The SS, corresponding to the polyol, is shown in dark contrast and shows a spherical microstructure. Surrounding the SS, and in a shell-like structure, the HS can be observed in a lighter color.

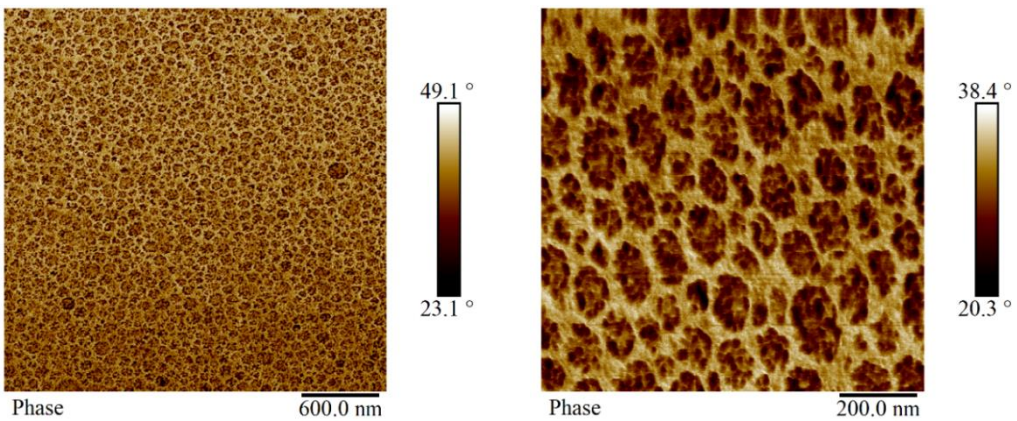

Figure 3.3. AFM phase images of WBPUU at different magnifications

Molecular weight and polydispersity of WBPUU film was measured by GPC. The synthesis procedure followed in this work led to a WBPUU with a high molecular weight of 54600 g·mol^{-1} and a polydispersity of 2.8. This value is similar and even higher to others reported in literature for similar systems [8-10]. The addition of EDA clearly resulted in a proper extension of the chains and long polymer chains with high molecular weight were obtained.

WBPUU structure and functional groups were analyzed through FTIR technique. WBPUU film spectrum is shown in Figure 3.4. First, an absorption band at 3369 cm^{-1} can be seen, which is related to the hydrogen-bonded N-H groups of the urethane and urea functional groups [14,15]. Following this, bands related to the symmetric and asymmetric stretching vibration of the C–H bonds appear at 2927 and 2858 cm^{-1}, respectively [16,17]. A band at 1731 cm^{-1} can be observed, assigned to the carbonyl vibration of the polyol [18] and urethane groups [10], followed by a shoulder at 1645 cm^{-1} from the carbonyl group stretching vibration of urea group [15]. The band at 1545 cm^{-1}, in amide II region, is related to the C-N stretching vibration and N-H bending of urethane and urea groups [4,19]. The bands observed between 1250 and 1000 cm^{-1} are related to C-O-C stretching vibrations [9].

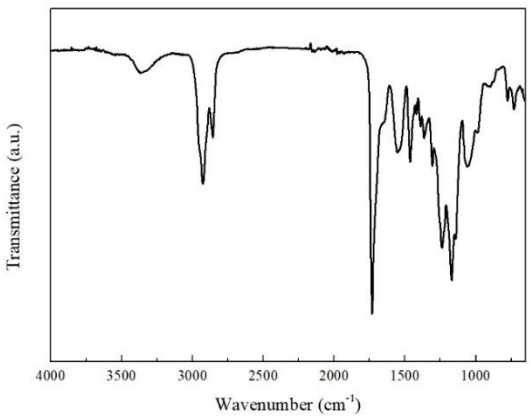

Figure 3.4. FTIR spectrum of WBPUU film

Moreover, and in agreement with results previously observed in the FTIR spectrum of the WBPUU dispersion, the absence of the band at 2270 cm^{-1} indicated that there are no free isocyanate groups in the polymer structure.

In order to analyze the thermal transitions of the WBPUU, DSC tests were performed. The obtained thermogram of the heating scan is represented in Figure 3.5. Thermogram shows the glass transition of the soft segment (T_{gSS}) at -52.0 °C, followed by a melting related to the hard segment transition, at a temperature (T_{HS}) of 81.4 °C and with an enthalpy (ΔH_{HS}) of 10.5 $J \cdot g^{-1}$. This peak is not too sharp and extends over a wide temperature range. This endothermic peak can be due to a disordering of the short range ordered hard segment domains [20], due to the use of non-symetrical isocyanate which results in shorter range ordering in the system. It is worth noting that, despite the materials being vacuum dried, residual water could remain on the sample and, whose removal temperature would match the observed T_{HS}. However, the melting of the polymer taking place at that temperature was corroborated since the melting process was visible.

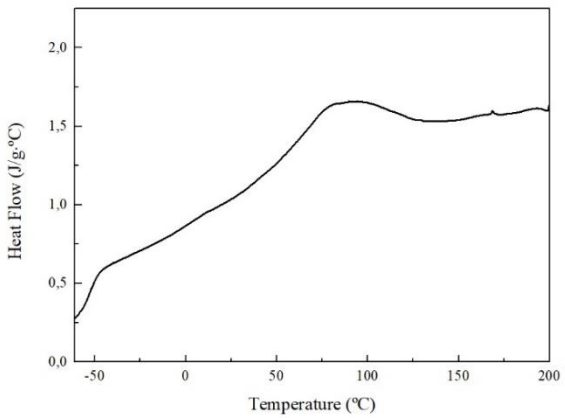

Figure 3.5. DSC curve of WBPPUU film

The degradation process of the WBPUU was analyzed through TGA. Thermogram curve, as well as fist derivative curve, are shown in Figure 3.6.

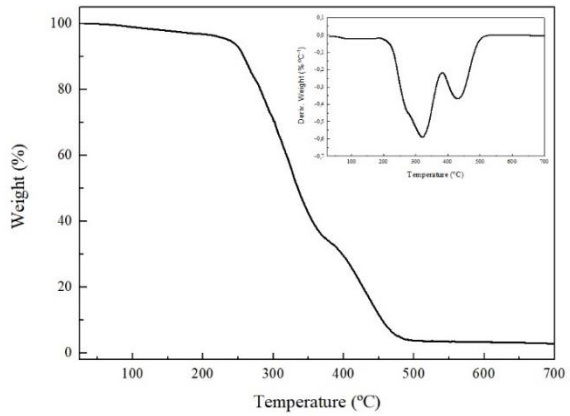

Figure 3.6. TGA and DTG (inset) curve for WBPUU film

The thermal degradation of the polyurethane took places in two steps. In the first step, the thermal degradation of the hard domain occured, whereas in the second step degradation of soft segment took place. Derivative curve shows a peak around 330 ºC with a shoulder around 265 ºC related to the degradation of urethane and urea groups in the hard segment, respectively. The second step is centered around 400 ºC and it is related to the degradation of the soft domain, mainly formed by the polyol [21].

Cytotoxicity analyses, using L929 murine fibroblast cells, were carried out in order to analyze the biocompatible behavior of the synth+esized WBPUU. Figure 3.7a shows short term cell viability with respect to the negative control, after 24, 48 and 72 hours. WBPUU showed higher viability values than the acceptable minimum establishes by the ISO 10993-5 (70% of the negative control value), proving a non-toxic behavior of the material.

On the other hand, cell adhesion and proliferation assays were also performed (Figure 3.7b). It could be observed that after three days the cells were viable (cells in green) and they showed a homogenous distribution throughout the surface of the WBPUU film. The amount of dead cells, marked in red, was very low. The cellular density was shown to be very high, leaving very few uncolonized zones. After a week, this behavior continued, with an even higher

density of the viable cells. At this point, the cell density was so high, that cells had begun to grow on top of each other.

The viability study of the L929 cells showed a good adhesion and proliferation taken place on the material, thus, the material proved to be a perfect environment for the adhesion and growth of the cells.

a)

b)

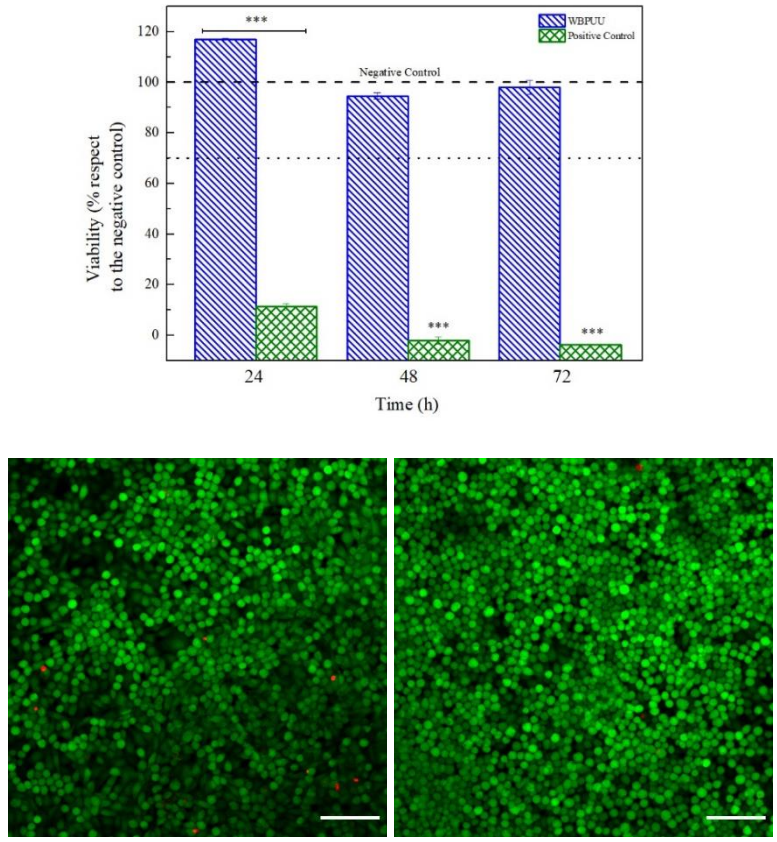

*Figure 3.7. a) Viability of L929 murine fibroblast cells on WBPUU as function of incubation time. *Dashed line represents the maximum value of viability given by the negative control and dotted line represents the minimum acceptable viability value. b) Adhesion and viability of L929 cells on WBPUU after 3 and 7 days. Images obtained by confocal microscopy (20x) and scale bar represents 100 µm*

3.3. Isolation and functionalization of CNF

Cellulose nanofiber were prepared parting from bleached hardwood kraft pulp (bHKP) and were later treated to obtain carboxylated fibers.

Initially, bHKP sheets, cut in 2-4 cm^2 pieces, were soaked in tap water for 24 h, in order to allow a complete swelling. The mixture was then dispersed mechanically until no agglomeration of fibers could be observed, and the final consistency was then adjusted to 1 wt.%. An unmodified CNF sample (CNF0) was obtained directly from this pulp suspension by passing it through a Masuko Supermass Colloider (MKZA10-15J) until no microstructure were seen under an optical microscope, which happened after 10 passes.

On the other hand, in order to add carboxylic groups to the CNF structure, the pulp suspension was subjected to a sequential periodate-chlorite oxidation (Figure 1.6) [22,23]. First, 5 g of cellulose fibers were dispersed in 500 g deionized water. 3.33 g of sodium metaperiodate (50% molar ratio of cellulose anhydroglucopyranose units, 0.03 M overall concentration) and 14.5 g of NaCl (0.75 M) were added and the mixture was allowed to react under total darkness and agitation for alternatively 2 and 24 h, in order to prepare CNFs with different carboxylation degrees. Afterwards, both mixtures were washed four times with deionized water and used as starting material for the second oxidation reaction. In this second reaction, a new 500 g deionized water suspension was prepared with 5 g of dialdehyde cellulose fibers resulting from the previous step, and it was mixed with 3.5 g of $NaClO_2$ (0.04 M concentration), 14.5 g of NaCl (0.75 M) and 3.3 g of H_2O_2. The mixtures were left to react for 2 h at room temperature, while maintaining their pH between 4.2 and 4.5 by dropwise addition of NaOH 0.5 N. The slight excess of chlorite is expected to fully convert aldehyde groups introduced by periodate into carboxylic groups with the aid of the co-oxidant hydrogen peroxide. In both oxidation reactions, the presence of sodium chloride increases the ionic strength of the medium boosting up the efficiency of the reactions due to the

decrease of the electrical double layer [24]. Finally, the reaction mixtures were filtered and the dicarboxylated cellulose fibers washed repeatedly with deionized water.

The carboxylated cellulose preparations were fully disintegrated in the Masuko Supermass Colloider until no presence of the fiber wall could be found under the optical microscope, what happened only after 8 and 3 passes for CNF1 and CNF2, respectively, due to the strong effect of carboxylated groups on fibrillation, via repulsive forces. Table 3.1. summarizes the name and characteristics of the three CNF preparations. The cellulose nanofibers with three different carboxylation degrees were named as CNF0, CNF1 and CNF2.

Table 3.1. Characteristics of the CNF preparations used in this study

Name / Treatment	CNF0	CNF1	CNF2
IO_4 oxidation time (h)	-	2	24
ClO_2 oxidation time (h)	-	2	2
#Passes Masuko	10	8	3

The carboxyl group concentration of the different types of nanocellulose systems was measured via conductometric titration [22,23]. The measured values were 0.14 mmol·g^{-1} for CNF0, and it went up to 0.59 and 0.88 mmol·g^{-1} for CNF1 and CNF2, respectively. As it can be observed, systems showed a higher carboxylation degree after having undergone chemical treatments, increasing as the periodate-oxidation time increases, proving a good oxidation process.

3.3.1. Characterization of CNF

Scanning Electron Microscopy was used to study the morphology of the nanofibers. SEM images of the nanofibers are shown in Figure 3.8. In all CNF systems, the applied chemical and mechanical treatments resulted in a network of nanofibers of 15-30 nm in diameter and several micrometers in length. No

significant differences were observed regarding fiber size regardless the carboxylation degree.

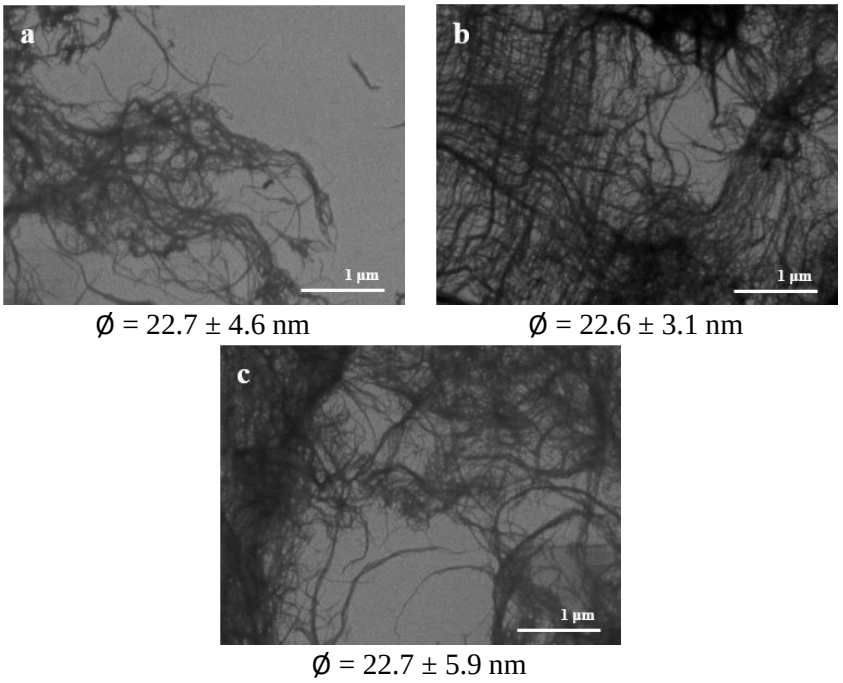

Figure 3.8. SEM images of cellulose nanofibers with different carboxylation degrees: a) CNF0, b) CNF1 and c) CNF2

Crystallinity degree changes of cellulose nanofibers were studied by means of XRD technique and obtained diffractograms are shown in Figure 3.9a.

All nanofiber's diffractograms showed the characteristic diffraction peaks of cellulose I at 15, 16.5, 23 and 34º, related to (101), ($10\bar{1}$), (002) and (040) crystallographic planes [25].

In order to further analyze these results, diffraction curves were deconvoluted by the Lorentz function (Figure 3.9b), in the aforementioned diffraction peaks and an amorphous peak at 21.5º [26]. The Crystallinity Index (C.I.) of cellulose nanofibers was calculated following the equation proposed by Hermans et al. (equation 2.2) [27].

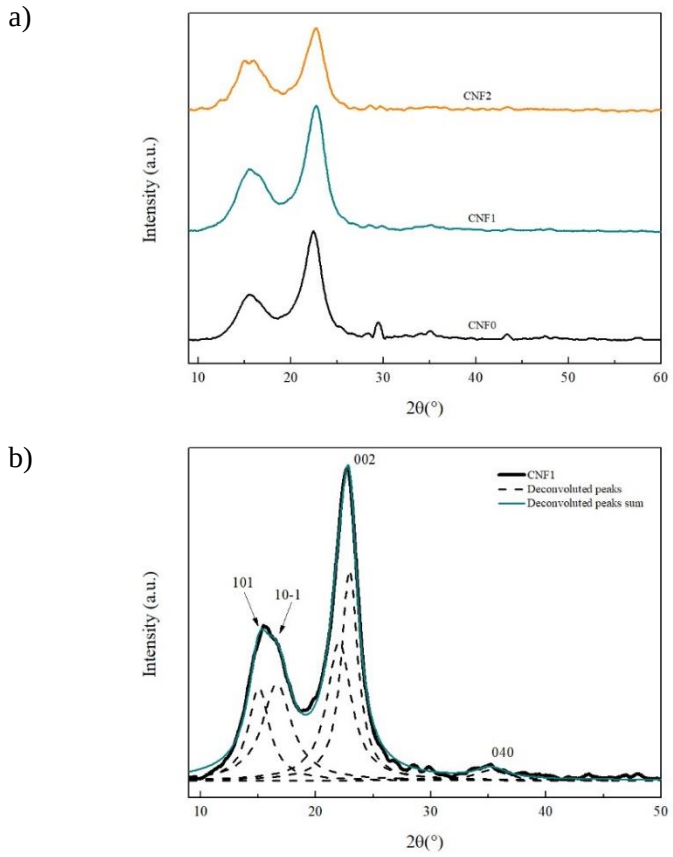

Figure 3.9. a) XRD diffractograms of cellulose nanofibers with different carboxylation degrees and b) deconvolution of peaks for CNF1 sample

The calculated crystallinity index for CNF0, CNF1 and CNF2 are shown in Table 3.2. Cellulose nanofibers with higher carboxylation degree showed lower crystallinity index. The undergone chemical treatment allowed the insertion of carboxyl groups, but during this process, and due to the opening of the glucopyranose rings, the crystalline structure was damaged and, thus, less crystalline cellulose nanofibers nets were obtained [28,29].

Table 3.2. Crystallinity index of nanofibers with different carboxylation degrees

Sample	C.I. (%)
CNF0	79
CNF1	68
CNF2	61

Fourier Transform Infrared spectra of cellulose nanofibers are represented in Figure 3.10. All systems showed a very pronounced band in the 3000-3700 cm^{-1} range, corresponding to the stretching vibration of the O-H groups. At 2900-2800 cm^{-1}, a band assigned to the C-H stretching vibration is present [30], followed by a band at 1635 cm^{-1} of the absorbed water [31]. At 1429 cm^{-1} the band of the symmetric bending of CH_2 can be observed [32]. The bands situated at 1160 and 897 cm^{-1} are attributed to C-O-C asymmetric stretching in β-glycosidic linkages, and the band at 1031 cm^{-1} to C-O stretching at C6 [24,26-28].

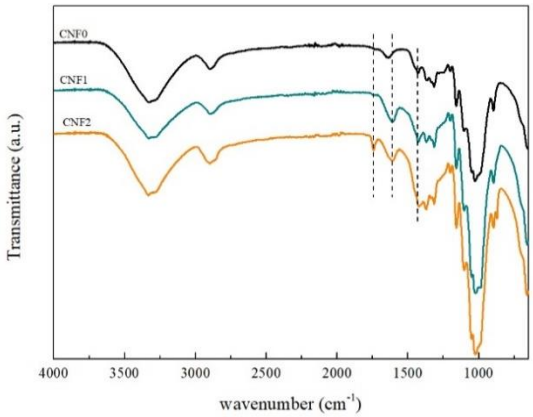

Figure 3.10. FTIR spectra of cellulose nanofibers with different degrees of carboxylation

Differences of the three prepared CNF systems can be seen when further analyzing the carbonyl stretching vibration region (dotted lines in Figure 3.10). The wavenumber value at which this band appears can be affected by the humidity, temperature and pH of the sample, as well as by the protonation state of the carbonyl groups [35]. When protonated, this band appears at 1735 cm^{-1}, whereas when in salt form it shifts to lower wavenumbers, around 1610 cm^{-1}. For CNF0, only a small shoulder at 1735 cm^{-1} can be seen, just before the absorbed water band. On the other hand, for CNF1 and CNF2, the bands corresponding to protonated and unprotonated carboxyl groups can both be seen. CNF1 shows the same shoulder at 1735 cm^{-1} observed for CNF0.

However, a new band can be observed at 1610 cm^{-1}, related to the COONa groups. In the case of CNF2, both bands can be clearly distinguished by two noticeable bands, at 1610 and 1742 cm^{-1}. The more pronounced band in the CNF2 spectrum suggests a higher presence of COOH groups. Moreover, the formation of COONa is also seen in the increase of intensity of the band located at 1430 cm^{-1} in CNF1 and CNF2 spectra [36].

The thermogram curves of cellulose, obtained from thermogravimetric analysis, are shown in Figure 3.11 and the characteristic temperatures are reported in Table 3.3. A small weight loss at low temperatures took place, due to the elimination of absorbed water from the fibers. As can be seen in CNF0 derivative curve, this nanofiber system presented a one-step degradation process, centered at 346 ºC and starting around 220 ºC, related to the degradation of cellulose crystalline domains.

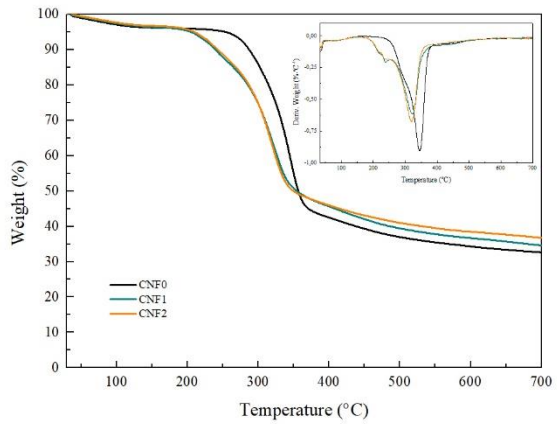

Figure 3.11. TGA and DTG (inset) curves of cellulose nanofibers with different degrees of carboxylation

A change in the degradation process can be observed for carboxylated fibers. As can be seen in DTG curves, the degradation of the carboxylated systems took place at lower degradation temperatures than CNF0 ones, being the maximum degradation temperature located at 322 and 320 ºC, for CNF1 and

CNF2, respectively, while for CNF0 it took place at 346 ºC. The onset degradation temperature, calculated as the temperature at which a weight loss of 5 wt% takes place, also shifted to lower temperature values for carboxylated systems. This fact is attributed to the damaging of the crystalline structure taken place during the carboxylation process, as observed by the reduction of crystallinity index values [28]. Moreover, CNF1 and CNF2 DTG curves show also an intense shoulder at 230 ºC, that has been attributed in the literature to their nanometric size and the larger amount of free ends present [30].

Table 3.3. Thermal degradation behavior of cellulose nanofibers with different degrees of carboxylation

Sample	T_{onset} (ºC)	T_{max} (ºC)	Char Residue (%)
CNF0	282	346	34.3
CNF1	232	320	36.7
CNF2	233	322	38.5

Table 3.3 summarizes the onset and maximum degradation temperatures shown by the nanofiber systems, as well as the remaining char after 600 ºC. Systems with higher carboxylation degree showed high char remaining. The carboxyl groups in the surface difficulted their decomposition into smaller units [37].

3.4. Obtaining of graphene oxide and graphene

3.4.1. Isolation of graphene

Graphene was obtained by exfoliation of graphite with sonication (Figure 3.12), following the process described by Ugarte et al. [38]. Briefly, 20 g of graphite flakes were sonicated in 1500 mL NMP for 100 hours in an ultrasonic bath. The obtained dispersion was afterwards centrifuged at 4000 rpm, in order to separate and keep the smallest fractions, and filtered. Obtained graphene was left to dry at 50 °C for 24 h.

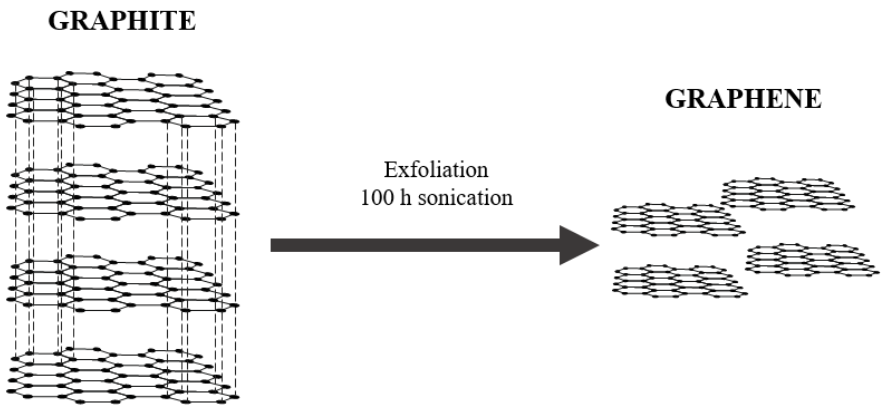

Figure 3.12. Scheme of the graphene obtaining process

3.4.2. Obtaining of graphene oxide

Graphene oxide (GO) was obtained from graphite using the modified Hummers' method [39]. Graphite flakes (1 g) were mixed with 0.5 g of $NaNO_3$ and 23 mL H_2SO_4 and left to react for half an hour in an iced water bath under magnetic agitation. After that, 3 g of $KMnO_4$ was added and was left to react for 2 more hours, until a purple color could be seen. Thereafter, it was heated to 35 ºC for 30 min and 46 mL of deionized water was added drop by drop. The mixture was moved to an oil bath heated to 98 ºC and maintained during two different oxidation times, 15 min and 30 min. Finally, 10 mL of H_2O_2 was added slowly. The mixture was kept under agitation until the formation of bubbles stopped and it reach room temperature and, then, 150 mL water was added.

A yellow-like mixture was obtained. The mixture was washed through centrifugation, 5 times with 5% HCl to get rid of Mn ions, and afterwards with deionized water until a neutral pH was measured. Finally, the mixture was filtered through polyamide filters (Sartorious, 0.2 µm pore size) and was dried at 50 °C for 24 h. Graphite oxide films, GrO15 (oxidation time = 15 min) and GrO30 (oxidation time = 30 min), were obtained.

The obtained graphite oxide was exfoliated in water (5 $mg \cdot mL^{-1}$), by ultrasonication using a sonication probe. Samples prepared with the longest oxidation time (GrO30) were ultrasonicated for 3 h and 4 h, and were designated as GO30S and GO30L, respectively. The resulting graphene oxide flakes were then size selected by centrifugation. First, they were centrifuged at 4000 rpm for 45 min and the supernatant fraction was collected. This was done for GO30L and GO30S and collected fractions were named GO30L-4000 and GO30S-4000, respectively. The remaining sediment of GO30L-4000 fraction was redispersed in water using an ultrasonic bath for 15 minutes. Centrifugation and dispersion steps were repeated for 2000 and 1000 rpm centrifugation rates to obtain size-selected graphene oxide flakes [40], and were named GO30L-2000 and GO30L-1000, respectively.

The supernatant fractions were filtered through polyamide filters and dried for 48 h at room temperature. A summary of the oxidation time, exfoliation time and size-selection of each system can be seen in Table 3.4.

Table 3.4. Designation and treatment of GO fractions

Sample	Oxidation time (min)	Ultrasonication time (h)	Centrifugation rate (rpm)
GrO15	15	-	-
GrO30	30	-	-
GO30L	30	4	-
GO30S	30	3	-
GO30L-4000	30	4	4000
GO30L-2000	30	4	2000
GO30L-1000	30	4	1000
GO30S-4000	30	3	4000

3.4.3. Reduction of graphene oxide

There are different methods to reduce GO and achieve a graphene-like structure, depending in the method and conditions used different structures will be obtained. In this study, reduction of GO was carried out by two different

methods, a thermal treatment and a chemical treatment. The obtained materials were analyzed in order to select the most interesting one.

For thermally reduced graphene oxide (rGO_T), GO was kept at 500 ºC for 30 min, during that time the oxygen containing groups were reduced and thus rGO_T was obtained. For the chemical reduction, ascorbic acid was employed. The GO was submerged in ascorbic acid and was kept at 95 ºC for 2 hours. Afterwards, it was clean with water and was left to dry and chemically reduced graphene oxide (rGO_C) was obtained.

The scheme of the obtaining process of graphene oxide and reduced graphene oxide is shown in Figure 3.13.

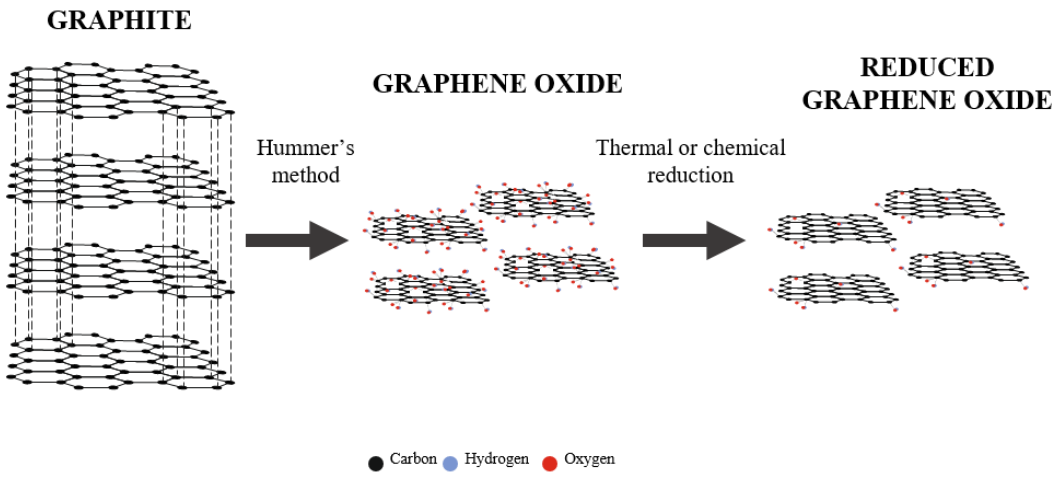

Figure 3.13. Schematic representation of obtaining of graphene oxide and reduced graphene oxide

3.4.4. Characterization of different GO systems

Effect of the oxidation time

FTIR analyses were carried out, in order to analyse the formation of funtional groups in the graphite structure during the oxidation process and the effect of the oxidation time. FTIR spectra of graphite, GrO15 and GrO30 are shown in

Figure 3.14. Graphite (Gr) spectra shows no significant bands throughout it, but only at 1590 cm^{-1} a band corresponding to the C=C bonds is present [41]. However, other additional very low intensity bands can be seen at 3419, 2924, 2854, 1118, 1041 cm^{-1}, which reflect small defects in the graphite structure.

After oxidation process, new bands corresponding to the new funtional groups appeared, proving a successful oxidation. Both oxidized systems showed a pronounced band around 3400 cm^{-1}, which was attributed to the vibration of the O-H groups from the new hydroxide and carboxylic acid groups [42]. A band realed to the O-H bending is also present around 1640 cm^{-1}. The C=O bonds of the new carboxylic groups resulted also in a band at 1735 cm^{-1} [43]. A band at 1050 cm^{-1} can also be observed, corresponging to the stretching vibration of C-O-C [44].

The spectra obtained for GrO samples confirmed the success introduction of oxygen-containing funtional groups on the graphite structure. Regarding the effect of oxidation time, no significant diffrerences were observed in the spectra of GrO15 and GrO30.

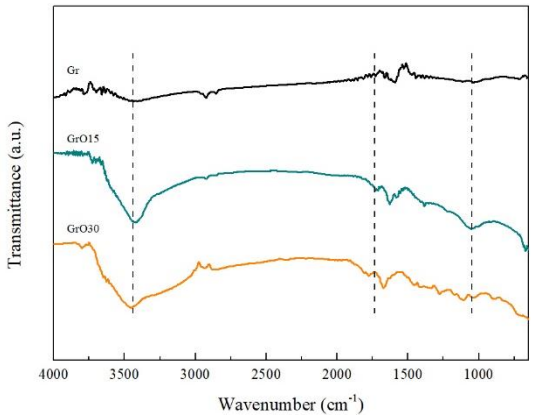

Figure 3.14. FTIR spectra of graphite, GrO15, and GrO30 samples

The effect of the oxidation time on the graphite structure can also be assessed by UV-Vis spectroscopy. Gr spectrum (Figure 3.15) showed no significant

peaks throughout the wavelength scan. However, after oxidation, samples showed two absorption maximums, at 230 nm and at 300 nm. The peak around 230 nm can be attributed to the π-π* transitions of aromatic C-C bonds, while the peak at 300 nm corresponds to the n-π* transitions of carbonyl (C=O) groups [44,45] and both can be bathochromically shifted by conjugation [46]. The UV-Vis spectra, in agreement with FTIR spectra, corroborated a successful oxidation process of graphite.

Small differences in the π-π* peak position can be observed for the systems prepared with different oxidation times. For GrO15, the maximum of the peak appeared at 233 nm, whereas for GrO30 it shifted to 231 nm. This change in wavelength suggests a higher disruption of the sp^2 domain, thereby reducing the concentration of π electrons, and thus, more energy is needed for the π-π* transitions [44,47]. This small shift could suggest a higher oxidation degree for GrO30.

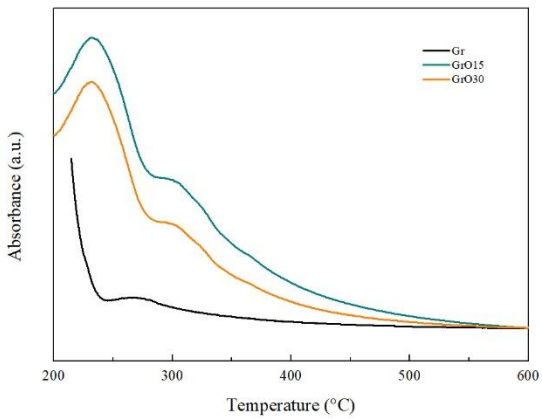

Figure 3.15. UV-Vis spectra of graphite, GrO15, and GrO30 samples

In order to analyze changes taken place on the graphite structure, Raman spectroscopy analyses were carried out. Raman spectra for graphite, GrO15 and GrO30 were normalized to the G band and spectra are shown in Figure 3.16. All spectra show the typical G, D and 2D bands of carbon based materials. The G band, around 1570 cm^{-1}, is attributed to sp^2 atoms, the D band,

near 1354 cm^{-1}, to the presence of defects, and the 2D band, at 2700 cm^{-1}, to the second order of zone boundary phonons [28]. These three bands can be observed in the graphite spectrum, however, intensity of the D band is very reduced, signaling a low degree of disorder.

The oxidation process resulted in materials with very altered structures. In the oxidized systems the G band shifted to higher Raman shifts, being it 1596 and 1600 cm^{-1} for GrO15 and GrO30, respectively. This shift to higher values was attributed to the formation of new sp^3 carbon atoms in the graphite lattice [51]. Moreover, a very significant change in the intensity of the D peak can be observed. This increase was attributed to the formation of more defects in the structure, which were formed when new functional groups were introduced, thus disturbing the order in the graphite structure. Both spectra of the two kinds of graphite oxide, GrO15 and GrO30, showed also a band at 2950 cm^{-1}, related to the combination of the D and D' phonons [48,49]. Furthermore, a decrease in the intensity of the 2D band can also be seen for GrO30, signaling the breaking of the staking order of graphene sheets [50], due to the oxidation taken place and signaling to a higher degree of oxidation for GrO30, agreeing with UV-Vis results.

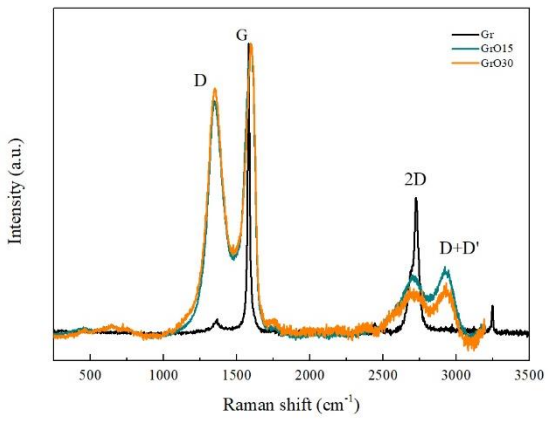

Figure 3.16. Raman spectra of graphite, GrO15, and GrO30 samples

In order to further study the degree of disorder, the intensity ratio of D and G bands (I_D/I_G) is often used [38]. This ratio can also be used to calculate crystallite size, using the equation proposed by Cancodo et al. [51] (equation 3.1). The I_D/I_G ratios and crystal size values obtained for graphite, GrO15, and GrO30 samples are shown in Table .3.5.

$$L_a = \frac{(2.4 \cdot 10^{-10})(\lambda_1)^4}{I_D/I_G} \qquad (equation\ 3.1)$$

where L_a is the average size of the sp^2 domain crystals and λ_1 is the input laser energy.

It can be observed that higher degrees of oxidation result in a higher I_D/I_G ratio value, signaling a higher degree of disorder. The introduction of new oxygen containing groups to the graphite structure disrupted the ordering of the graphene layering. Higher oxidation degrees resulted also in smaller crystallites.[42,52].

Table 3.5. I_D/I_G ratios and L_a values for graphite, GrO15, and GrO30 samples

Sample	I_D/I_G	L_a (nm)
Graphite	0.06	264.4
GrO15	0.81	20.7
GrO30	0.85	19.8

To study the crystalline structure of the systems, X-Ray analyses were performed. The resulting diffractograms for graphite, GrO15 and GrO30 are shown in Figure 3.17. Graphite diffractogram shows a very pronounced peak at 2θ=26.63°, corresponding to (002) plane [52,53] and taken as indicative of pure graphite [45]. For GrO15 and GrO30 this peak was still present, suggesting the systems were not completely oxidized, maintaining still some pure graphite structures.

However, for both oxidized systems a new peak appeared at lower angles, 2θ = 10.63° for GrO15 and at 2θ = 10.53° for GrO30. This new peak was

attributed to the intercalation of oxygen containing groups between GO layers [52]. The 2θ value at which this peak appears depends on the degree of oxidation and the newly formed groups. In the current study this peak appeared at slightly lower 2θ values for GrO30. The data obtained agrees with previous characterization techniques suggesting a higher oxidation degree for GrO30 system.

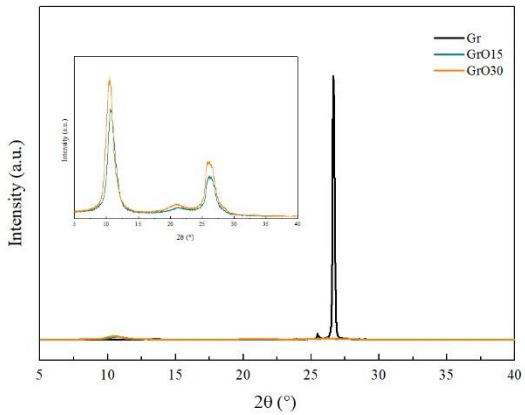

Figure 3.17. XRD patterns obtained for graphite, GrO15 and GrO30 samples

The interplanar distances for the three systems were calculated according to Bragg's law (equation 2.3), results are shown in Table 3.6. It can be seen that the oxidation process of the graphite structure increased the distance between planes of the systems. The presence of new functional groups impeded the closer position of graphene layers in the structure, enlarging the interplanar distance [41,45]. This larger distance was proportional to the degree of oxidation, being it slightly bigger for GrO30.

Table 3.6. Interplanar distance (d) values calculated for graphite, GrO15, and GrO30

Sample	2θ (°)	*d* (nm)
Graphite	26.63	0.34
GrO15	10.63	0.83
GrO30	10.53	0.84

Considering all different characterization techniques employed, it was observed that results show a successful oxidation of the samples through the method used and a higher degree of oxidation was determined for GrO30. In view of these results, the sample GrO30 was chosen and was subjected to an exfoliation and posterior centrifugation process to eliminate the residual graphite fraction and obtain small-thickness graphene oxide flakes, according to the previously described procedure. The GrO30 sample was selected due to the higher content of oxygen-containing hydrophilic groups that make graphite oxide easier to exfoliate in a polar medium.

Exfoliation and size selection of graphene oxide

Graphite oxide flakes were exfoliated into graphene oxide by ultrasonication and were later size selected by centrifugation, as previously described. In order to study the differences of the different separated fractions, GO30S-4000, GO30L-4000, GO30L-2000 and GO30L-1000 were characterized. Prepared samples were analyzed by XRD and AFM, in order to assess changes in crystalline structure and morphology.

X-Ray analysis was performed for samples ultrasonicated at different times and centrifuged at different rates, to study the effect these parameters have on the structure of the samples. Obtained diffractograms can be seen in Figure 3.18. The presence of graphite on the systems is seen by the intensity of the peak at $2\theta = 26^{o}$. It can be observed that the content of residual graphite decreased as the centrifugation rate increased, being it almost non-existent for GO30L-4000 and most pronounced for GO30L-1000. This decrease was attributed to a good exfoliation during the sonication process [45] and, thus, a successful elimination of the bigger graphitic structures through centrifugation. Regarding the effect of the ultrasonication time, it can be observed that for a longer sonication time a better exfoliation of the systems was obtained. The graphite peak in GO30S-4000 diffractogram was significantly more pronounced than in the case of GO30L-4000.

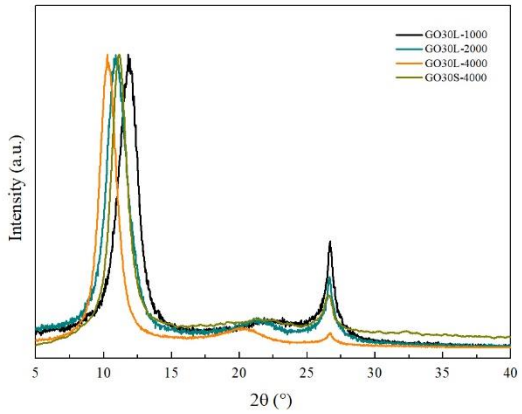

Figure 3.18. XRD analysis of GO30L series and GO30S-4000

Moreover, the degree of oxidation and the distance between planes, determined by Bragg's Law, were also analyzed. The peak related to graphite oxide and interplanar distance were influenced by the ultrasonication time, as well as by the centrifugation rates (Table 3.7). Higher ultrasonication time and centrifugation rates resulted in more exfoliated structures and a successful separation of these exfoliated fractions. Moreover, higher centrifugation rates allowed the obtaining of the more oxidized structures. Hence, the highest interplanar distance were measure for GO30L-4000 [42]. For lower centrifugation rates less exfoliated fractions remained and, thus, this distance was smaller. In the case of GO30S-4000, the shorter ultrasonication process did not allow for a further exfoliation and, in comparison with GO30L-4000, shorter distances were measure.

Table 3.7. Interplanar distance (d) values for GO30L-1000, GO30L-2000, GO30L-4000, and GO30S-4000 samples

Sample	2θ (°)	*d* (nm)
GO30L-1000	12.0	0.73
GO30L-2000	10.9	0.81
GO30L-4000	10.3	0.87
GO30S-4000	11.2	0.79

The morphology of the different GO flakes was observed by AFM, obtained images and the cross-sectional profiles of three arbitrarily selected flakes are shown in Figure 3.19. Regarding flake size, it was observed that the size distribution was more heterogeneous for GO samples centrifuged at lower rates. GO30L-1000 and GO30L-2000 showed flake sizes of 300-500 nm. In the GO30L-4000 sample, homogeneous flakes of size at around 250 nm were observed. Ugarte et al. reported a similar effect on centrifugation-based size selection of graphene [38]. When comparing samples with different sonication times, GO30S-4000 and GO30L-4000, it can be seen that shorter sonication times led to larger flakes. GO30S-4000 showed flakes with an average size of 450 nm. Thus, flake size proved to be dependent of both sonication time and centrifugation rate.

Regarding thickness of the flakes, it was analyzed by cross-sectional profiles (Figure 3.19). Once again, GO30L-1000 and GO30L-2000 showed a heterogeneous distribution, with values ranging from 4 to 10 nm. Samples obtained with higher centrifugation rates showed lower thickness, due to the elimination of thicker fractions in the centrifugation process. GO30L-4000 showed flakes with an average thickness of 2 nm, which may be related to few-layer graphene oxide flakes. This value was slightly higher for GO30S-4000, thickness of around 3 nm was measured on this system. Thickness of the flakes was no significantly altered by the ultrasonication time, however the centrifugation rate had a big impact in the thickness values.

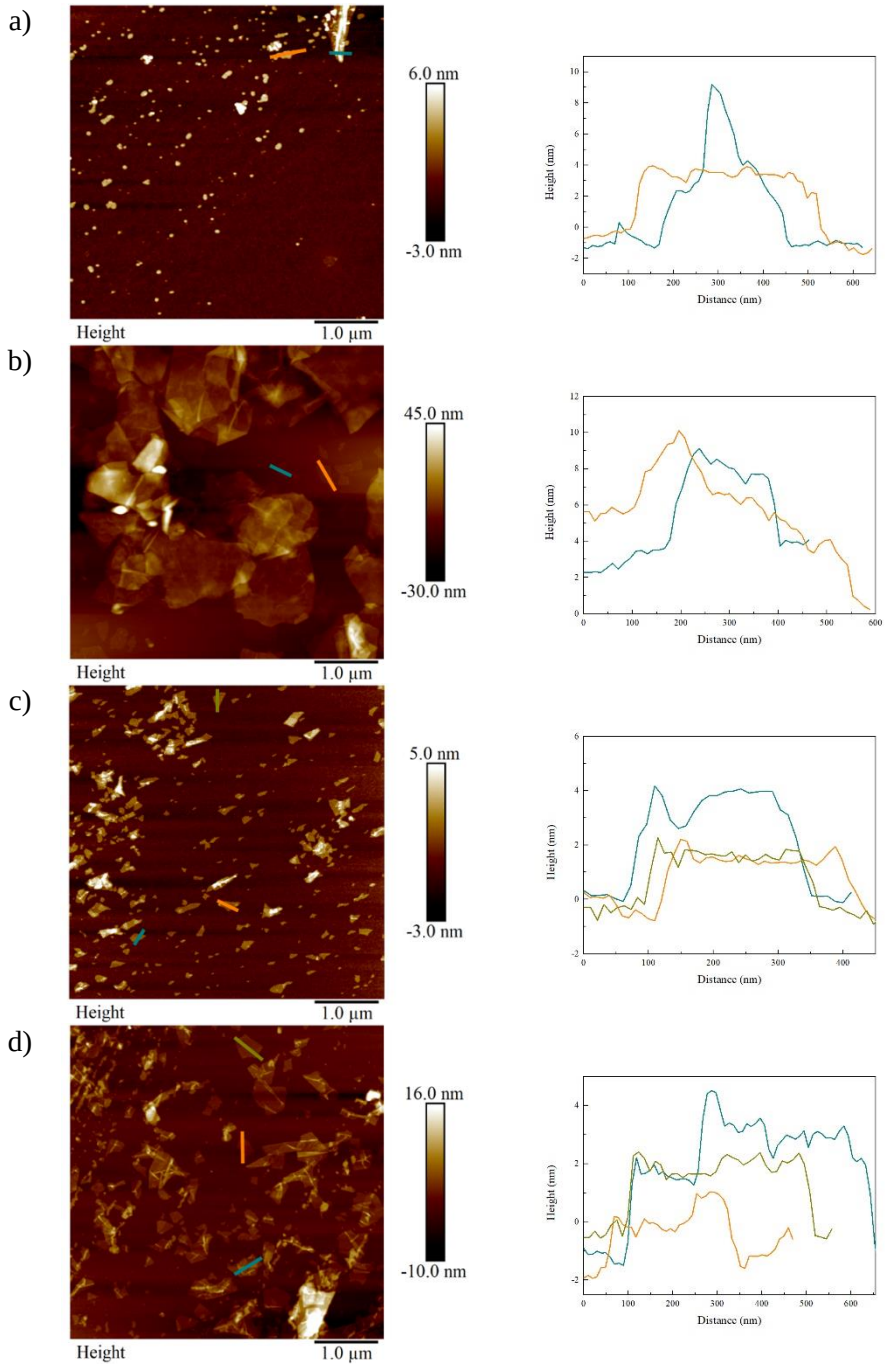

Figure 3.19. AFM height images(left) and cross-sectional profiles (right) of (a) GO30L-1000, (b) GO30L-2000, (c) GO30L-4000, and (d) GO30S-4000 GO fractions

Based on the obtained results it was decided to keep using the 30 min oxidation time during the oxidation process, in order to obtain a higher degree of oxidation. Regarding centrifugation rates, 4000 rpm was chosen, for a further removal of remaining graphitic structures and a more homogeneous sample. In regard of the sonication time, it was clearly observed that longer times resulted in more broken flakes, with significantly smaller flakes. Different sized flakes supply a different reinforcement effect in composites. The use of larger flakes with a similar thickness can significantly improve mechanical properties. For this reason, GO30S-4000 was chosen to use throughout the study and it is named as just GO from now on.

Effect of the reduction method

In order to determine the better reduction method, obtained reduced graphene oxide systems were characterized and compared. In order to do this, Raman spectroscopy, X-Ray Diffraction and electrical conductivity tests were carried out.

Raman spectra for thermally reduced and chemically reduced systems are shown in Figure 3.20, and for comparison purposes the spectra of the parting GO is also shown. It can be observed that the reduction method had a big impact in the structure of the produced graphene, since both systems show significantly different spectra.

The D band, related to defects, showed big differences depending on the reduction method used. For chemically reduced GO, the intensity of the D band increased, whereas the opposite happened for thermally reduced GO. For a better analysis the degree of disorder was calculated. (I_D/I_G) values of 0.20 and 1.25 were obtained for rGO_T and rGO_C, respectively, showing a significantly higher order in the structure produced by thermal reduction. Chemical reduction process, however, resulted in an increase of the disorder degree of the systems. This structural response to the reduction methods has been reported previously

[50-52]. The increase of disorder observed for chemical reduction is attributed to the creation of defects in the sp^2 domain during the reduction, due to elimination of oxygen containing groups [57,58]. On the other hand, the lower presence of defects shown by thermally reduced graphene oxide suggests the reparation of the defects by reforming of the aromatic structures [59].

The reduction of graphene oxide can be seen in the shift of the G band to lower wavelengths, due to the formation of sp^2 carbon atoms, characteristic of the graphene structure [55,56]. During the reduction process this band shifted from 1596 cm^{-1} in GO to 1589 cm^{-1} in rGO_C and 1582 cm^{-1} in rGO_T. The lower values obtained for thermally reduced graphene oxide proved a higher reduction obtained by this method.

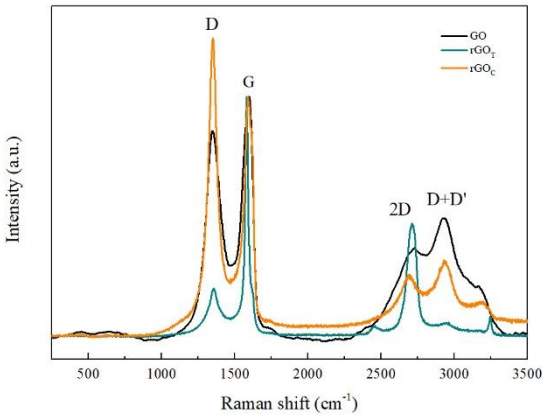

Figure 3.20. Raman spectra for thermally and chemically reduced graphene oxide, and GO as reference

To further study the effect of the reduction method on the structure of the obtained reduced graphene oxides, XRD analyses were performed, obtained diffractograms are shown in Figure 3.21.

For oxidized graphene the main peak appeared at around 11º, however, with the reduction process this peak shifts back to higher values, around 26º, corresponding to graphene like structures. Both reduced structures showed a

peak around 26.6º, suggesting a successful reduction process. However, wide peaks observed in both systems signaled to only a partial reduction being achieved, since partially oxidized graphene tends to show lower 2θ [60]. For rGO_T this peak was sharper and more defined than for rGO_C, pointing to a more successful reduction being achieved. On the contrary, the wider peak of rGO_C and the observed shoulder at lower 2θ values suggested that a more limited reduction was obtained by the chemical treatment.

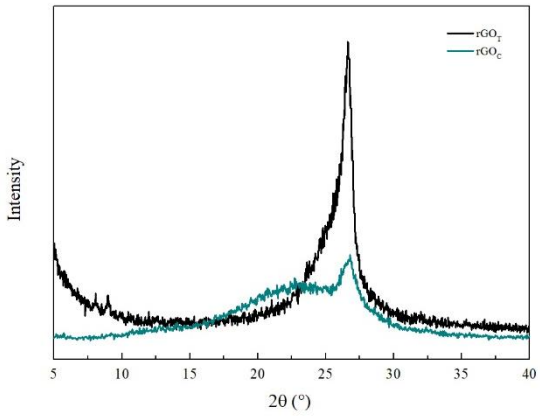

Figure 3.21. X-ray diffractograms for thermally and chemically reduced graphene oxide

Electrical conductivity of the reduced systems was also evaluated. The degree of reduction obtained, as well as the structure of the final material, will impact the electrical conductive capacity of the materials. Current/Voltage curves of both rGO systems are shown in Figure 3.22.

Though both systems showed similar values, it can be observed that thermally obtained rGO shows slightly higher conductive capacity. This could be attributed to higher degree of reduction achieved, as seen by XDR, and the lower presence of defects in the material, as shown by Raman spectroscopy.

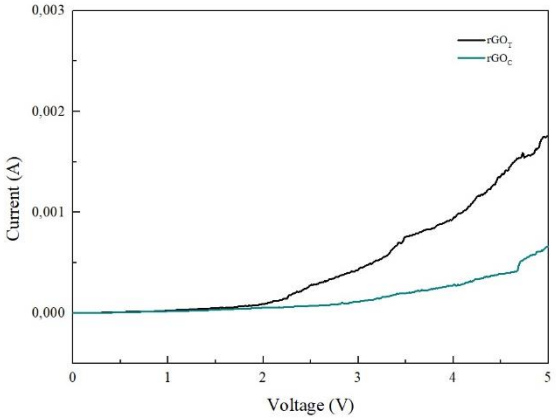

Figure 3.22. Current/Voltage curves for thermally and chemically reduced graphene oxide

The higher degree of reduction, better structure and, thus, better electrical conductivity show thermal reduction to be a better option. For these reasons, rGO_T was selected for further use and it is from now on referred to as rGO.

3.3.4. Characterization of carbonaceous structures: graphene, graphene oxide and reduced graphene oxide

The selected GO and rGO systems, as well as the prepared graphene and the parting graphite were further characterized.

Wishing to avoid the use of unnecessary VOC solvents and in order to, later, obtain a better miscibility with the polymer prepared in aqueous dispersion, the dispersability of the carbonaceous structures in water was assessed.

Water dispersability of graphene and graphene oxide by ultrasonication was studied. GO was sonicated in water (5 $mg \cdot mL^{-1}$) using a sonication probe for 1 hour and a good dispersion was obtained (Figure 3.23a). The functional groups in the surface of GO facilitated the water dispersion. Graphene was sonicated for 5 h and a poor dispersion remained (Figure 3.23b). In order to improve water dispersability of graphene, the use of a surfactant was necessary. Plant extracts

have shown the ability to act as natural surfactants [61] and have great affinity with graphene due to the π-π interactions [62]. In this case a plant extract, *Salvia officinalis (E)*, was used as proposed by Gonzalez et al.[62], with a weight ratio of G/E: 2/1. Salvia extracts were obtained by infusion method [63] and are mainly composed by terpenoids, phenolic acids, flavonoids and diterpenes [64,65].

For graphene aqueous dispersion, first the Salvia extract was dissolved in water (2.5 mg·mL-1) and then graphene was added (5 mg·mL^{-1}) and dispersed on it using a probe sonicator for 6 hours. Graphene was successfully dispersed in this water/plant extract blend (Figure 3.23c).

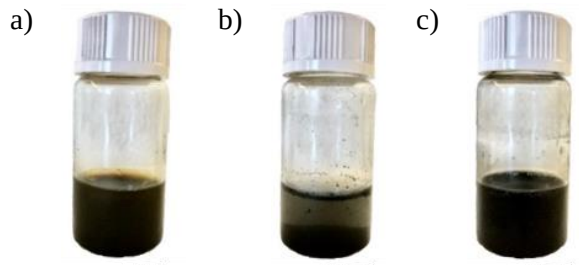

Figure 3.23. Dispersability in water for a) graphene oxide, b) graphene and c) graphene + plant extracts

The morphology of graphene and graphene oxide was analyzed by TEM. Obtained images can be seen in Figure 3.24. Figures 3.24a and 3.24d show well defined flakes with lengths of 650 ± 170 nm and 875 ± 260 nm for G and GO, respectively. High resolution TEM (HRTEM) images were also obtained (Figure 3.24b and 3.24e), in which highly ordered zones can be observed. Figure 3.24c and 3.24f show zoomed images, in which atomic distribution can be seen and distance between atoms can be measured. In these images a hexagonal shaped atomic distribution with an atom sitting on the center of the hexagon can be observed (red dotted hexagons). Distances between atoms of 0.26 and 0.25 nm were measured for GO and G, respectively. This distribution and distance are attributed to the presence of at least a bi-layer structure, as

seen in literature [66,67]. In these cases, the second layer does not lie directly under the layer above but is slightly displaced from it and, thus, these data are obtained [67].

For graphene images, it can be observed that G flakes are attached to the extracts (marked by arrow) and some holes appear on its structure (circled in yellow in Figure 3.24a), signaling to more damages flakes. This more damaged structure could be due to the effect of the long sonication process.

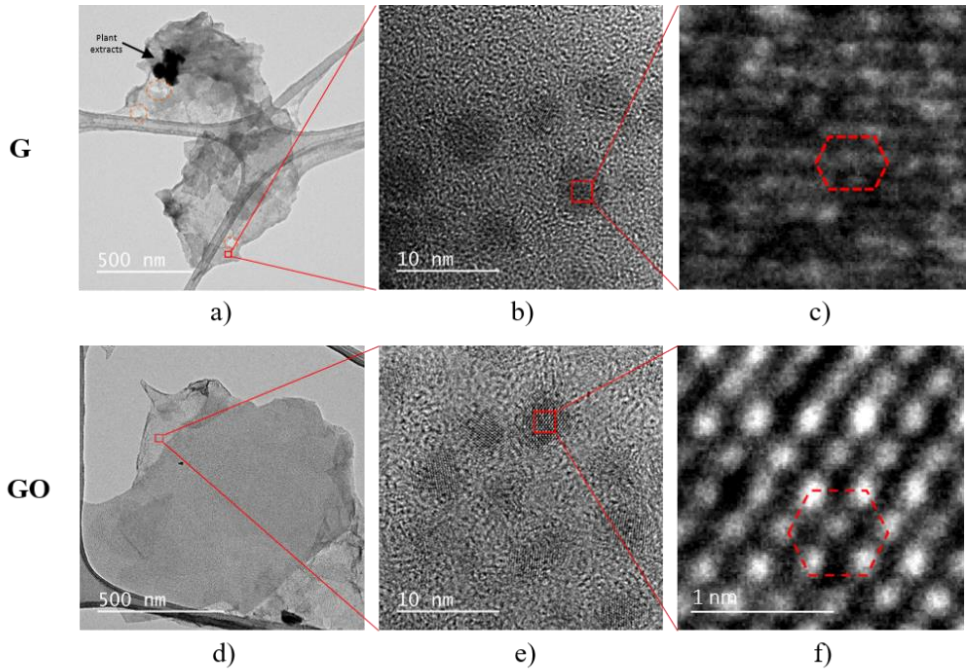

Figure 3.24. TEM images for graphene and graphene oxide

The chemical composition of the carbonaceous structures was analyzed by elemental analysis, aiming to observe the changes produced during the production of each material. For this purpose, elemental analysis tests were carried out, where C, H and O contents were measured. Results can be seen on Table 3.8.

Table 3.8. Elemental Analyses for content of C, H and O in graphite, graphene, graphene oxide and reduced graphene oxide

Sample	C (%)	H (%)	O (%)
Gr	95.85	1.55	-
G	94.99	1.91	2.23
GO	55.55	2.86	38.28
rGO	90.74	2.31	6.20

Elemental analysis results show that graphite and graphene samples were mainly composed of carbon, as was to be expected and as shown in the literature [68,69]. However, both entities showed also some traces of H and O, which suggested the presence of impurities in the systems. It can be observed that for GO, the composition was significantly altered. Though mainly it was still composed by carbon, oxygen also comprised a big part of its composition, thus, further proving a successful oxidation process. During the thermal reduction process, most of the oxygenated groups were eliminated and, therefore, the oxygen content in rGO significantly decreased to lower percentage values, while the composition of carbon increased. The hydrogen and oxygen content shown by rGO, suggested that there are still some remaining oxygen containing groups in the structure. These results suggest only a partial reduction of GO, which is in agreement with previously observed results. In the literature, for similar systems, a partial reduction of GO is reported [70].

FTIR analysis were performed for Gr, G, GO and rGO (Figure 3.25). As previously observed, graphite did not show many significant bands, mainly only low intensity bands associated to small imperfections on its structure. For graphene small changes were observed, its spectrum shows bands around 3435 and 1655 cm^{-1}, attributed to O-H stretching and bending vibrations, respectively, suggesting the presence of water or some hydroxyl groups in the structure [71], agreeing with elemental analysis results. For GO an overall higher intensity spectrum was obtained, where more bands are present. GO

spectrum shows a very intense O-H band at 3404 cm^{-1}, as well as a carbonyl band at 1735 cm^{-1}, and bands at 1400 and 1050 cm^{-1}, attributed to tertiary C-OH groups and C-O stretching, respectively [65-68]. Moreover, bands related with C-H stretching vibration can be seen at 2929 and 2854 cm^{-1}. The O-H bending band can also be seen in GO spectrum at 1630 cm^{-1}. rGO spectrum is similar to that of GO but with significantly decreased intensity of the bands. The presence of these bands once again suggested only a partial reduction.

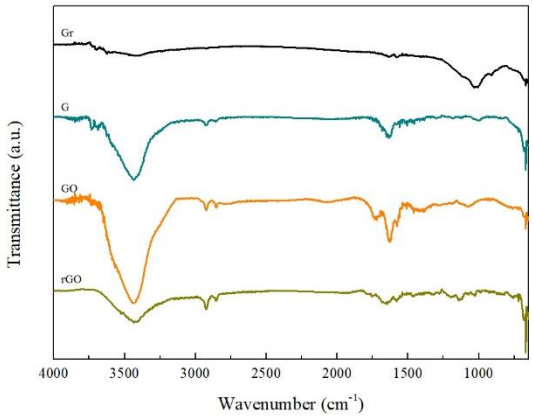

Figure 3.25. FTIR spectra of graphite, graphene, graphene oxide and reduced graphene oxide

The crystalline structures of the prepared carbonaceous reinforcements were studied by X-Ray analyses and resulting diffractograms are shown in Figure 3.26. The 002 plane peak, previously observed for graphite, is also observed in the graphene diffractogram, however, it was less sharp and with very reduced intensity. GO diffractogram showed a small peak at 26°, due to only a partial oxidation, but its main peak shifted to $2\theta=11.2°$. In the case of rGO the peak shifted back to $2\theta=26.63°$, but as previously explained the peak was wider due to only a partial reduction being achieved. This partial reduction is in agreement with elemental analysis and FTIR results. Significantly lower intensities shown by G, GO and rGO with respect to the parting graphite prove

a good exfoliation during the process of obtaining of the nanoreinforcements [76].

The interplanar distances for the carbonaceous structures were calculated using Bragg's Law. Interplanar distances for Gr, G, GO and rGO were calculated as 0.335 nm for Gr and G, and 0.790 nm for GO. Distance between planes became larger for GO due to the presence of oxygen containing groups, thus impeding a further proximity between layers. For rGO the interplanar distance calculated according to the 2θ value of the peak maximum went back to 0.335 nm, however the broader peak reflected a not so constant distance, but a range due only some oxygenated groups present throughout the structure.

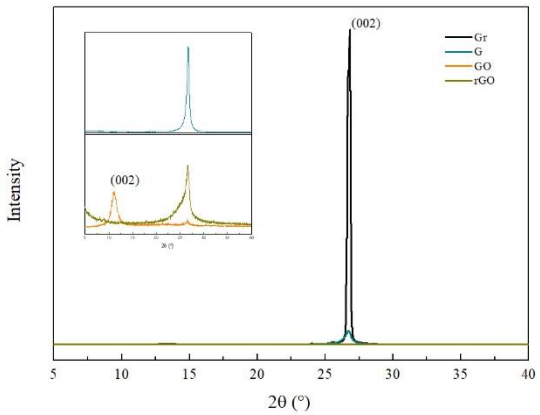

Figure 3.26. X-Ray diffractograms for graphite, graphene, graphene oxide and reduced graphene oxide

All systems were analyzed by Raman spectroscopy, in order to obtain information of structural changes in the systems (Figure 3.27). All spectra showed the typical G, D and 2D bands, but for G, GO and rGO a D+D' was also present. All spectra were normalized to the intensity of the G peak [52], therefore changes in wavelength and peaks intensity showed the efficiency of the process undergone to exfoliate graphite to graphene and oxidize graphite to graphene oxide.

The D peak for graphite showed very low intensity, due to its extremely high order, however, for exfoliated graphene, this peak significantly increased in intensity. The D and D' band, related to defects, was also observed in G diffractogram. For GO, bands related to disorder showed much higher intensity. The formation of new oxidized groups was directly reflected in the increase of the D and D+D' bands. It can also be observed that the G peak shifted to higher wavenumbers, 1599 cm^{-1}, due to the formation of new sp^3 carbon atoms in the graphite lattice [55]. Moreover, the 2D band intensity decreased due to the breaking of the stacking order. rGO spectrum showed very reduced defect bands, signaling the effective reduction of the oxygen containing groups and a quite good reorganization of the structure.

The degree of disorder was further analyzed with the (I_D/I_G) ratio. The I_D/I_G ratio was calculated for graphite, graphene, GO and rGO and values of 0.06, 0.56, 0.86 and 0.20 were obtained. These values showed the almost complete lack of defects in the graphite structure. The ratio values were higher for graphene, and even more so for graphene oxide, suggesting the formation of defects during their production processes. rGO showed a much lower I_D/I_G value and, thus, a much highly ordered structure. As previously seen, the thermal reduction of GO, resulted in less defected structures, ought to the proper reparation of the aromatic structures. Moreover, the intensity ratio between 2D and G peaks (I_{2D}/I_G) can also be used to determine the layering of the materials. Luo et al. found that a ratio >1.6 belongs to monolayer structures, whereas a ratio around 0.8 to bilayer structure and ratio values lower than this correspond to multilayer structures, respectively [77]. I_{2D}/I_G calculated values for G, GO and rGO were 0.54, 0.37 and 0.47, respectively, suggesting a very exfoliated structure for both graphene and reduced graphene oxide and slightly less so for graphene oxide.

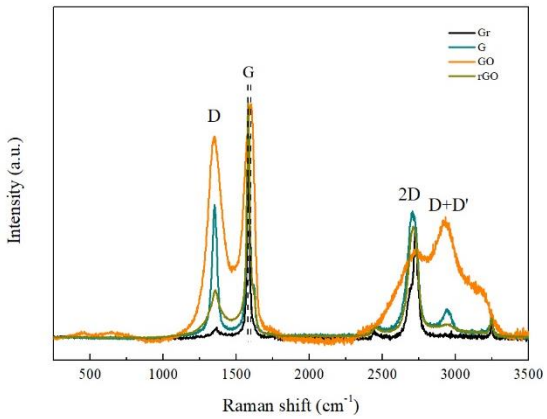

Figure 3.27. Raman spectra of graphite, graphene, graphene oxide and reduced graphene oxide

TGA analyses were performed for all four systems (Figure 3.28). Graphite thermogram showed a really high thermal stability characteristic of well-ordered fully carbonaceous structures [78]. Graphene showed also high thermal stability, however, a small weight loss starting above 100 ºC and taking place gradually in a wide temperature interval was observed, this small weight loss was attributed to the presence of defects [79].

A significantly higher weight loss can be observed throughout the GO curve. Two main degradation steps can be observed in the TGA and DTG curves. The first step took place at low temperatures and was attributed to the elimination of absorbed water. The second, and more pronounced, step was centered around 250 ºC. This mass loss was attributed to the decomposition of oxygen containing functional groups (i.e. C=O, C-O-C and O-H) in the GO structure [80]. After the reduction process, a higher thermal stability was restored, as shown by rGO curve. For rGO a small weight loss related to water was seen at low temperatures, this peak is clearly observed in the DTG curve. A slight weight loss around 660 ºC can also be observed, attributed to degradation of the remaining oxygen containing groups [80].

For later comparative purposes, the weight loss and DTG curves of *Salvia* were included in Figure 3.28. It can be observed that after the initial humidity loss, most of the weight loss occurred between 150 and 400 ºC, which was attributed to the decomposition of polysaccharides, and a 40% of residue remained after the degradation process, as also seen with other plant extracts [81,82].

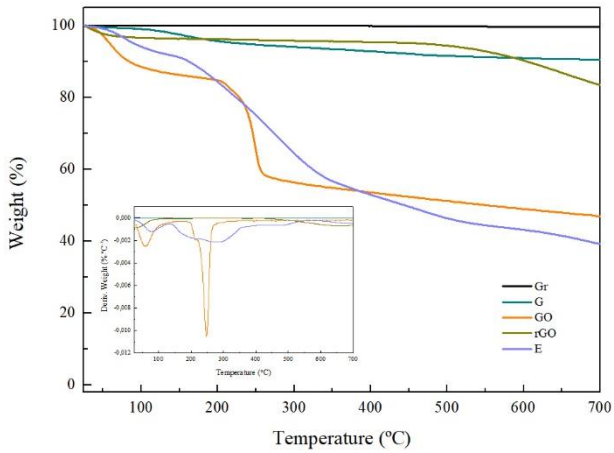

Figure 3.28. TGA and DTG of graphite, graphene, graphene oxide and reduced graphene oxide

Electrical conductive capacity of the carbonaceous structures was analyzed measuring transmitted current when a voltage ranging from 0 to 5 V was applied, resulting curves are shown in Figure 3.29. Resistivity and conductivity values were calculated using equations 2.5 and 2.6. Both G and rGO showed conductivity proper of semiconductors. Graphene showed higher conductivity than reduced graphene oxide [83], 3,1 ± 1,2 and (5,3 ± 1.5) x 10^{-3} S·cm^{-1}, respectively. Graphene oxide showed no electrical conductivity (5.6 ± 3.8) x 10^{-7} S·cm^{-1}, values corresponding to insulator materials [84]. The conductivity measured for graphene is similar to values reported in literature and lower than those found for graphite [83]. rGO showed lower conductivity than graphene due the only partial reduction obtained.

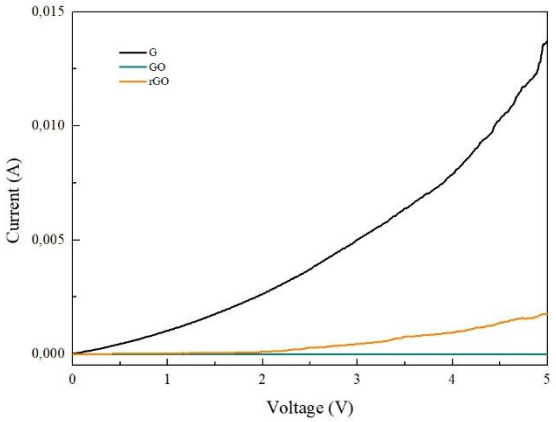

Figure 3.29. Current/Voltage curves for different carbonaceous nanostructures

3.5. Conclusions

In this chapter a waterborne polyurethane-urea was synthesized parting form a green polyol. The successful synthesis process was proven by the complete elimination of free isocyanate groups, as seen by FTIR analyses and titration results through the synthesis process. The obtained dispersion was characterized and showed good stability, with small particles. Moreover, the molecular weight of the WBPUU was studied and a high molecular weight was measured, proving a good chain extension process. The AFM analyses showed a micro-phase separated morphology, where the HS and the SS could be distinguished. In order to analyze the possible use of this material in biomedical application, biocompatibility tests were performed. WBPUU showed promising potential, with no cytotoxicity and excellent cell adhesion.

Three types of cellulose nanofibers were produced, with varying degrees of carboxylation, which was achieved by a periodate-clorite oxidation process. It was observed that the incorporation of carboxyl groups damaged the cellulose structure and, therefore, CNF systems with lower crystallinity degree were obtained. Thermal stability was also affected, the opening of the glucopyranose ring resulted in less stable structures that begin to degrade at lower temperatures.

As another type of reinforcements, carbonaceous structures were produced, graphene, graphene oxide and reduced graphene oxide. Graphene oxide was produced by Hummers method, and its process was optimized regarding oxidation degree and flake size. It was observed that oxidation time affected oxidation degree, high sonication times helped exfoliate graphite but also broke flakes in to smaller ones, and centrifugation speed could be used to size select the GO flakes. Therefore, longer oxidation times were used to produce highly oxidized GO, and sonication time and centrifugation speed were adjusted to obtain successfully exfoliated systems with size appropriate flakes. The reduction process to obtain reduced graphene oxide was also studied, namely chemical and thermal treatments. It was observed that thermal reduction resulted in a more effective reduction process, with less amount of defects on their structures and better electrical conductivity. Nonetheless, both systems showed only a partial reduction, since some oxidized groups were still present on their structure.

Graphene and the optimized GO and rGO were characterized and compared. They all show extremely exfoliated structures parting from graphite as seen by Raman, but XRD show that their production process caused defects on their structures. Thermal stability analyses showed the good thermal stability of the carbonaceous materials. Electrical conductive capacity of both graphene and reduced graphene oxide was studied and it was observed that both presented electrical conductivity in the range of semiconductive materials. rGO, however, showed higher resistivity values, attributed to the remaining oxygen containing groups not allowing a good electron transference.

3.6. References

[1] Cakic S, Nikolic G, Lacnjevac C, Gligoric M, Stamenkovic J, Rajkovic MB, et al. Thermal stability of aqueous polyurethanes depending on the applied catalysts. Sensors 2006;6:1697–707. doi:10.3390/s6111697.

[2] Bernardini J, Licursi D, Anguillesi I, Cinelli P, Coltelli MB, Antonetti

C, et al. Exploitation of arundo donax L. hydrolysis residue for the green synthesis of flexible polyurethane foams. BioResources 2017;12:3630–55. doi:10.15376/biores.12.2.3630-3655.

[3] Polymer properties database 2020. https://polymerdatabase.com/polymer chemistry/Urethanes.html (accessed October 14, 2021).

[4] Santamaria-Echart A, Arbelaiz A, Saralegi A, Fernández-d'Arlas B, Eceiza A, Corcuera MA. Relationship between reagents molar ratio and dispersion stability and film properties of waterborne polyurethanes. Colloids Surfaces A Physicochem Eng Asp 2015;482:554–61. doi:10.1016/j.colsurfa.2015.07.012.

[5] Gaddam SK, Palanisamy A. Anionic waterborne polyurethane dispersions from maleated cotton seed oil polyol carrying ionisable groups. Colloid Polym Sci 2016;294:347–55.

[6] Lee J, Kim M, Hong CK, Shim SE. Measurement of the dispersion stability of pristine and surface-modified multiwalled carbon nanotubes in various nonpolar and polar solvents. Meas Sci Technol 2007;18:3707–12. doi:10.1088/0957-0233/18/12/005.

[7] García-Pacios V, Iwata Y, Colera M, Martín-Martínez JM. Influence of the solids content on the properties of waterborne polyurethane dispersions obtained with polycarbonate of hexanediol. Int J Adhes Adhes 2011;31:787–94. doi:10.1016/j.ijadhadh.2011.05.010.

[8] Diani J, Gall K. Finite strain 3D thermoviscoelastic constitutive model. Society 2006:1–10. doi:10.1002/pen.

[9] Pérez-Limiñana MA, Arán-Aís F, Torró-Palau AM, Orgilés-Barceló AC, Martín-Martínez JM. Characterization of waterborne polyurethane adhesives containing different amounts of ionic groups. Int J Adhes Adhes 2005;25:507–17. doi:10.1016/j.ijadhadh.2005.02.002.

[10] Ugarte L, Fernández-d'Arlas B, Valea A, González ML, Corcuera MA, Eceiza A. Morphology-properties relationship in high-renewable content polyurethanes. Polym Eng Sci 2014;54:2282–91. doi:10.1002/pen.23777.

[11] Čulin J, Andreis M, Šmit I, Veksli Z, Anžlovar A, Žigon M. Motional heterogeneity and phase separation of functionalized polyester polyurethanes. Eur Polym J 2004;40:1857–66. doi:10.1016/j.eurpolymj.2004.02.029.

[12] Díez-García I, Santamaría-Echart A, Eceiza A, Tercjak A. Synthesis and characterization of environmentally-friendly waterborne poly(urethane-urea)s. Eur Polym J 2018;99:240–9. doi:10.1016/j.eurpolymj.2017.12.026.

[13] Vadillo J, Larraza I, Arbelaiz A, Corcuera MA, Save M, Derail C, et al. Influence of the addition of PEG into PCL-based waterborne polyurethane-urea dispersions and films properties. J Appl Polym Sci 2020;137:1–12. doi:10.1002/app.48847.

[14] Yilgör I, Yilgör E, Wilkes GL. Critical parameters in designing segmented polyurethanes and their effect on morphology and properties: A comprehensive review. Polymer 2015;58:A1–36. doi:10.1016/j.polymer.2014.12.014.

[15] Santamaria-Echart A, Fernandes I, Saralegi A, Costa MRPFN, Barreiro F, Corcuera MA, et al. Synthesis of waterborne polyurethane-urea dispersions with chain extension step in homogeneous and heterogeneous media. J Colloid Interface Sci 2016;476:184–92. doi:10.1016/j.jcis.2016.05.016.

[16] Mohammadi A, Barikani M, Barmar M. Synthesis and investigation of thermal and mechanical properties of in situ prepared biocompatible Fe3O4/polyurethane elastomer nanocomposites. Polym Bull

2015;72:219–34. doi:10.1007/s00289-014-1268-1.

[17] Xiao Y, Huang H, Peng X. Synthesis of self-healing waterborne polyurethanes containing sulphonate groups. RSC Adv 2017;7:20093–100. doi:10.1039/C6RA28416G.

[18] Etxaniz I, Llorente O, Aizpurua J, Martín L, González A, Irusta L. Dispersion characteristics and curing behaviour of waterborne UV crosslinkable polyurethanes based on renewable dimer fatty acid polyesters. J Polym Environ 2019;27:189–97. doi:10.1007/s10924-018-1334-0.

[19] Pei A, Malho JM, Ruokolainen J, Zhou Q, Berglund LA. Strong nanocomposite reinforcement effects in polyurethane elastomer with low volume fraction of cellulose nanocrystals. Macromolecules 2011;44:4422–7. doi:10.1021/ma200318k.

[20] Seymour RW, Cooper SL. Thermal analysis of polyurethane block polymers. Macromolecules 1973;6:48–53. doi:10.1021/ma60031a008.

[21] Ou CW, Su CH, Jeng US, Hsu SH. Characterization of biodegradable polyurethane nanoparticles and thermally induced self-assembly in water dispersion. ACS Appl Mater Interfaces 2014;6:5685–94. doi:10.1021/am500213t.

[22] Tejado A, Alam MN, Antal M, Yang H, van de Ven TGM. Energy requirements for the disintegration of cellulose fibers into cellulose nanofibers. Cellulose 2012;19:831–42. doi:10.1007/s10570-012-9694-4.

[23] Yang H, Tejado A, Alam N, Antal M, van de Ven TGM. Films prepared from electrosterically stabilized nanocrystalline cellulose. Langmuir 2012;28:7834–42. doi:10.1021/la2049663.

[24] Alam MN, Antal M, Tejado A, van de Ven TGM. Salt-induced

acceleration of chemical reactions in cellulose nanopores. Cellulose 2012;19:517–22. doi:10.1007/s10570-011-9649-1.

[25] He J, Cui S, Wang S. Preparation and crystalline analysis of high-grade bamboo dissolving pulp for cellulose acetate. J Appl Polym Sci 2008;107:1029–38. doi:10.1002/app.27061.

[26] Park S, Baker JO, Himmel ME, Parilla PA, Johnson DK. Cellulose crystallinity index: measurement techniques and their impact on interpreting cellulase performance. Biotechnol Biofuels 2010;3:10. doi:10.1186/1754-6834-3-10.

[27] Hermans PH, Weidinger A. Quantitative X-Ray investigations on the crystallinity of cellulose fibers. A background analysis. J Appl Phys 1948;19:491–506. doi:10.1063/1.1698162.

[28] Hou QX, Liu W, Liu ZH, Bai LL. Characteristics of wood cellulose fibers treated with periodate and bisulfite. Ind Eng Chem Res 2007;46:7830–7. doi:10.1021/ie0704750.

[29] Kim U-J, Kuga S, Wada M, Okano T, Kondo T. Periodate oxidation of crystalline cellulose. Biomacromolecules 2000;1:488–92. doi:10.1021/bm0000337.

[30] Široký J, Blackburn RS, Bechtold T, Taylor J, White P. Attenuated total reflectance Fourier-transform Infrared spectroscopy analysis of crystallinity changes in lyocell following continuous treatment with sodium hydroxide. Cellulose 2010;17:103–15. doi:10.1007/s10570-009-9378-x.

[31] Sain M, Panthapulakkal S. Bioprocess preparation of wheat straw fibers and their characterization. Ind Crops Prod 2006;23:1–8. doi:10.1016/j.indcrop.2005.01.006.

[32] Jonoobi M, Harun J, Shakeri A, Misra M, Oksmand K. Chemical

composition, crystallinity, and thermal degradation of bleached and unbleached kenaf bast (Hibiscus cannabinus) pulp and nanofibers. BioResources 2009;4:626–39. doi:10.15376/BIORES.4.2.626-639.

[33] Gwon JG, Lee SY, Doh GH, Kim JH. Characterization of chemically modified wood fibers using FTIR spectroscopy for biocomposites. J Appl Polym Sci 2010;21. doi:10.1002/app.31746.

[34] Mondragon G, Fernandes S, Retegi A, Peña C, Algar I, Eceiza A, et al. A common strategy to extracting cellulose nanoentities from different plants. Ind Crops Prod 2014;55:140–8. doi:10.1016/j.indcrop.2014.02.014.

[35] Zhbankov RG. Infrared spectra of cellulose and its derivatives. Boston, MA: Springer US; 1995.

[36] Bellamy LJ. The infra-red spectra of complex molecules. Dordrecht: Springer Netherlands; 1975.

[37] Soni B, Hassan EB, Mahmoud B. Chemical isolation and characterization of different cellulose nanofibers from cotton stalks. Carbohydr Polym 2015;134:581–9. doi:10.1016/j.carbpol.2015.08.031.

[38] Ugarte L, Gómez-Fernández S, Tercjak A, Martínez-Amesti A, Corcuera MA, Eceiza A. Strain sensitive conductive polyurethane foam/graphene nanocomposites prepared by impregnation method. Eur Polym J 2017;90:323–33. doi:10.1016/j.eurpolymj.2017.03.035.

[39] Hummers WS, Offeman RE. Preparation of graphitic oxide. J Am Chem Soc 1958;80:1339. doi:10.1021/ja01539a017.

[40] Khan U, O'Neill A, Porwal H, May P, Nawaz K, Coleman JN. Size selection of dispersed, exfoliated graphene flakes by controlled centrifugation. Carbon 2012;50:470–5.

doi:10.1016/j.carbon.2011.09.001.

[41] Dinari M, Salehi E, Abdolmaleki A. Thermal and morphological properties of nanocomposite materials based on graphene oxide and L-leucine containing poly(benzimidazole-amide) prepared by ultrasonic irradiation. Ultrason Sonochem 2018;41:59–66. doi:10.1016/j.ultsonch.2017.09.025.

[42] Krishnamoorthy K, Veerapandian M, Yun K, Kim S. The chemical and structural analysis of graphene oxide with different degrees of oxidation. Carbon 2012;53:38–49. doi:10.1016/j.carbon.2012.10.013.

[43] Sharifi-Bonab M, Arjomandi Rad F, Talat Mehrabad J. Preparation of laccase-graphene oxide nanosheet/alginate composite: Application for the removal of cetirizine from aqueous solution. J Environ Chem Eng 2016;4:3013–20. doi:10.1016/j.jece.2016.06.012.

[44] Chen Y, Yin Q, Zhang X, Jia H, Ji Q, Xu Z. Impact of various oxidation degrees of graphene oxide on the performance of styrene–butadiene rubber nanocomposites. Polym Eng Sci 2018;58:1409–18. doi:10.1002/pen.24729.

[45] Todorova N, Giannakopoulou T, Boukos N, Vermisoglou E, Lekakou C, Trapalis C. Self-propagating solar light reduction of graphite oxide in water. Appl Surf Sci 2017;391:601–8. doi:10.1016/j.apsusc.2016.04.088.

[46] Paredes JI, Villar-Rodil S, Martínez-Alonso A, Tascón JMD. Graphene oxide dispersions in organic solvents. Langmuir 2008;24:10560–4. doi:10.1021/la801744a.

[47] Ferrari AC. Raman spectroscopy of graphene and graphite : Disorder , electron – phonon coupling , doping and nonadiabatic effects 2007;143:47–57. doi:10.1016/j.ssc.2007.03.052.

[48] Gayathri S, Jayabal P, Kottaisamy M, Ramakrishnan V. Synthesis of few layer graphene by direct exfoliation of graphite and a Raman spectroscopic study. AIP Adv 2014;4. doi:10.1063/1.4866595.

[49] Eckmann A, Felten A, Mishchenko A, Britnell L, Krupke R, Novoselov KS, et al. Probing the nature of defects in graphene by Raman spectroscopy. Nano Lett 2012;12:3925–30. doi:10.1021/nl300901a.

[50] Lespade P, Al-Jishi R, Dresselhaus MS. Model for Raman scattering from incompletely graphitized carbons. Carbon 1982;20:427–31. doi:10.1016/0008-6223(82)90043-4.

[51] Cançado LG, Takai K, Enoki T, Endo M, Kim YA, Mizusaki H, et al. General equation for the determination of the crystallite size la of nanographite by Raman spectroscopy. Appl Phys Lett 2006;88:1–4. doi:10.1063/1.2196057.

[52] Guerrero-Contreras J, Caballero-Briones F. Graphene oxide powders with different oxidation degree, prepared by synthesis variations of the Hummers method. Mater Chem Phys 2015;153:209–20. doi:10.1016/j.matchemphys.2015.01.005.

[53] Mu S-J, Su Y-C, Xiao L-H, Liu S-D, Hu T, Tang H-B. X-Ray difraction pattern of graphite oxide. Chinese Phys Lett 2013;30:096101. doi:10.1088/0256-307X/30/9/096101.

[54] Chen D, Li L, Guo L. An environment-friendly preparation of reduced graphene oxide nanosheets via amino acid. Nanotechnology 2011;22. doi:10.1088/0957-4484/22/32/325601.

[55] Perumbilavil S, Sankar P, Priya Rose T, Philip R. White light Z-scan measurements of ultrafast optical nonlinearity in reduced graphene oxide nanosheets in the 400–700 nm region. Appl Phys Lett 2015;107:051104. doi:10.1063/1.4928124.

[56] Cuong TV, Pham VH, Tran QT, Hahn SH, Chung JS, Shin EW, et al. Photoluminescence and Raman studies of graphene thin films prepared by reduction of graphene oxide. Mater Lett 2010;64:399–401. doi:10.1016/j.matlet.2009.11.029.

[57] Vu THT, Tran TTT, Le HNT, Nguyen PHT, Bui NQ, Essayem N. A new green approach for the reduction of graphene oxide nanosheets using caffeine. Bull Mater Sci 2015;38:667–71. doi:10.1007/s12034-015-0896-x.

[58] Gómez-Navarro C, Weitz RT, Bittner AM, Scolari M, Mews A, Burghard M, et al. Electronic transport properties of individual chemically reduced graphene oxide sheets. Nano Lett 2007;7:3499–503. doi:10.1021/nl072090c.

[59] Johra FT, Lee J, Jung W. Facile and safe graphene preparation on solution based platform. J Ind Eng Chem 2014;20:2883–7. doi:10.1016/j.jiec.2013.11.022.

[60] Lee M, Balasingam SK, Jeong HY, Hong WG, Lee HBR, Kim BH, et al. One-step hydrothermal synthesis of Graphene decorated V2O5 nanobelts for enhanced electrochemical energy storage. Sci Rep 2015;5:1–8. doi:10.1038/srep08151.

[61] Santamaria-Echart A, Fernandes I, Barreiro F, Retegi A, Arbelaiz A, Corcuera MA, et al. Development of waterborne polyurethane-ureas added with plant extracts: Study of different incorporation routes and their influence on particle size, thermal, mechanical and antibacterial properties. Prog Org Coatings 2018;117:76–90. doi:10.1016/j.porgcoat.2018.01.006.

[62] González K, García-Astrain C, Santamaria-Echart A, Ugarte L, Avérous L, Eceiza A, et al. Starch/graphene hydrogels via click chemistry with relevant electrical and antibacterial properties.

Carbohydr Polym 2018;202:372–81. doi:10.1016/j.carbpol.2018.09.007.

[63] Martins N, Barros L, Santos-Buelga C, Henriques M, Silva S, Ferreira ICFR. Evaluation of bioactive properties and phenolic compounds in different extracts prepared from Salvia officinalis L. Food Chem 2014;170:378–85. doi:10.1016/j.foodchem.2014.08.096.

[64] Jassbi AR, Zare S, Firuzi O, Xiao J. Bioactive phytochemicals from shoots and roots of Salvia species. Phytochem Rev 2016;15:829–67. doi:10.1007/s11101-015-9427-z.

[65] Pavlić B, Teslić N, Vidaković A, Vidović S, Velićanski A, Versari A, et al. Sage processing from by-product to high quality powder: I. Bioactive potential. Ind Crops Prod 2017;107:81–9. doi:10.1016/j.indcrop.2017.05.031.

[66] Velasco-Vélez JJ, Jones TE, Streibel V, Hävecker M, Chuang CH, Frevel L, et al. Electrochemically active Ir NPs on graphene for OER in acidic aqueous electrolyte investigated by in situ and ex situ spectroscopies. Surf Sci 2019;681:1–8. doi:10.1016/j.susc.2018.10.021.

[67] HOPG detailed description n.d. http://nanoprobes.aist-nt.com/apps/HOPG info.htm (accessed April 26, 2019).

[68] Uysal Unalan I, Wan C, Trabattoni S, Piergiovanni L, Farris S. Polysaccharide-assisted rapid exfoliation of graphite platelets into high quality water-dispersible graphene sheets. RSC Adv 2015;5:26482–90. doi:10.1039/c4ra16947f.

[69] Raccichini R, Balduccu A, Varzi A, Passerini S. Method of producing graphene by exfoliation of graphite. WO 2015/131933 Al, 2015.

[70] Appel A-K, Thomann R, Mülhaupt R. Polyurethane nanocomposites

prepared from solvent-free stable dispersions of functionalized graphene nanosheets in polyols. Polymer 2012;53:4931–9. doi:10.1016/j.polymer.2012.09.016.

[71] Hadi A, Zahirifar J, Karimi-Sabet J, Dastbaz A. Graphene nanosheets preparation using magnetic nanoparticle assisted liquid phase exfoliation of graphite: The coupled effect of ultrasound and wedging nanoparticles. Ultrason Sonochem 2018;44:204–14. doi:10.1016/j.ultsonch.2018.02.028.

[72] Vermisoglou E, Todorova N, Pilatos G, Romanos G, Likodimos V, Boukos N, et al. Few layer graphenes decorated with silver nanoparticles. ECCM 2012 - Compos Venice, Proc 15th Eur Conf Compos Mater 2012:24–8.

[73] Ghobadi M, Gharabaghi M, Abdollahi H, Boroumand Z, Moradian M. MnFe2O4-graphene oxide magnetic nanoparticles as a high-performance adsorbent for rare earth elements: Synthesis, isotherms, kinetics, thermodynamics and desorption. J Hazard Mater 2018;351:308–16. doi:10.1016/j.jhazmat.2018.03.011.

[74] Nethravathi C, Rajamathi M. Chemically modified graphene sheets produced by the solvothermal reduction of colloidal dispersions of graphite oxide. Carbon 2008;46:1994–8. doi:10.1016/j.carbon.2008.08.013.

[75] Goncalves G, Marques PAAP, Granadeiro CM, Nogueira HIS, Singh MK, Grácio J. Surface modification of graphene nanosheets with gold nanoparticles: The role of oxygen moieties at graphene surface on gold nucleation and growth. Chem Mater 2009;21:4796–802. doi:10.1021/cm901052s.

[76] Saiful Badri MA, Salleh MM, Md Noor NF ain, Rahman MYA, Umar AA. Green synthesis of few-layered graphene from aqueous processed

graphite exfoliation for graphene thin film preparation. Mater Chem Phys 2017;193:212–9. doi:10.1016/j.matchemphys.2017.02.029.

[77] Luo H, Dong J, Yao F, Yang Z, Li W, Wang J, et al. Layer-by-layer assembled bacterial cellulose/graphene oxide hydrogels with extremely enhanced mechanical properties. Nano-Micro Lett 2018;10. doi:10.1007/s40820-018-0195-3.

[78] Ren PG, Yan DX, Ji X, Chen T, Li ZM. Temperature dependence of grapheme oxide reduced by hydrazine hydrate. Nanotechnology 2011;22. doi:10.1088/0957-4484/22/5/055705.

[79] Zhang X, Browne WR, Feringa BL. Preparation of dispersible graphene through organic functionalization of graphene using a zwitterion intermediate cycloaddition approach. RSC Adv 2012;2:12173–6. doi:10.1039/c2ra22440b.

[80] Dehghanzad B, Razavi Aghjeh MK, Rafeie O, Tavakoli A, Jameie Oskooie A. Synthesis and characterization of graphene and functionalized graphene via chemical and thermal treatment methods. RSC Adv 2016;6:3578–85. doi:10.1039/c5ra19954a.

[81] Khan M, Al-Marri AH, Khan M, Mohri N, Adil SF, Al-Warthan A, et al. Pulicaria glutinosa plant extract: A green and eco-friendly reducing agent for the preparation of highly reduced graphene oxide. RSC Adv 2014;4:24119–25. doi:10.1039/c4ra01296h.

[82] Amina M, Al-Youssef HM, Amna T, Hassan S, El-Shafae AM, Kim HY, et al. Poly(urethane)/G. Mollis Composite Nanofibers for Biomedical Applications. J Nanoeng Nanomanufacturing 2012;2:85–90. doi:10.1166/jnan.2012.1056.

[83] Marinho B, Ghislandi M, Tkalya E, Koning CE, de With G. Electrical conductivity of compacts of graphene, multi-wall carbon nanotubes, carbon black, and graphite powder. Powder Technol 2012;221:351–8.

doi:10.1016/j.powtec.2012.01.024.

[84] Britannica TE of E. Semiconductors. Encycl Br 2021. https://www.britannica.com/science/semiconductor (accessed May 6, 2021).

Chapter 4

WBPUU/CNF NANOCOMPOSITE FILMS AND FILAMENTS FOR FDM 3D PRINTING

4. WBPUU/CNF NANOCOMPOSITE FILMS AND FILAMENTS FOR FDM 3D PRINTING

4.1. Aim of the chapter

In this chapter, the use of cellulose nanofibers as reinforcements for a WBPUU matrix is studied. Three different nanocelluloses, with different carboxylation degree, are used for nanocomposite films preparation. Composites were loaded with 1.5, 3 and 5 wt.% of CNF. Films were characterized morphologically, physico-chemically, thermally and mechanically. The effects that the nanocellulose content and its characteristics have on the final composite properties were analyzed.

On the other hand, in order to study the possibility of using WBPUU/CNF composites in FDM 3D printing, filaments were prepared and characterized. For filament preparation, based on the results obtained in the characterization of the films, 3 wt.% content of nanoreinforcements was chosen and two CNF samples were selected, the unmodified CNF sample (CNF0) and one of the carboxylated systems (CNF1). Furthermore, the effect of nanocellulose incorporation route, in-situ and ex-situ, on the properties of the nanocomposite filaments was studied. The prepared composites were extruded into filaments, which were characterized by FTIR, DSC, TGA, DMA and mechanical test. Finally, the printability of the prepared filaments was tested using FDM 3D printing technique.

4.2. Preparation of WBPUU/CNF nanocomposite films

WBPUU/CNF nanocomposites were prepared using the WBPUU synthesized in Chapter 3 as matrix and cellulose nanofibers with different carboxylation degrees as reinforcements. The characteristics of different nanocellulose fibers are summarized in Chapter 3. Nanocomposite films were prepared by solvent casting. First, nanocellulose aqueous suspensions were sonicated in a bath for 1 hour, in order to ensure a good dispersion of the fibers. After that, the

WBPUU dispersion was added and mixtures were sonicated for 1 hour. Nanocomposites containing 1.5, 3 and 5 wt.% of nanocellulose were prepared. The total mass of all mixtures was adjusted with deionized water, employed contents of each component for prepared systems can be seen in Table 4.1.

Mixtures were then poured in Teflon molds and left to dry at room temperature for 7 days, followed by three days under vacuum (400 mbar). 8 x 8 cm^2 films were prepared with a thickness of approximately 0.5 mm. Nanocomposites were named as "xCNFy", where "x" denotes nanocellulose wt.% respect to the total mass of the nanocomposite and "y" refers to the type of nanocellulose used, namely CNF0, CNF1 or CNF2.

Table 4.1. WBPUU and CNF contents for composite preparation

Sample	WBPUU dispersion (g) (* solid content 33wt.%)	CNF suspension (g) (* solid content 0.6 wt.%)	Deionized water (g)	Total mass (g)
WBPUU	9.46	-	25.89	35.35
1.5CNF0	9.35	7.83	18.17	35.35
3CNF0	9.23	15.70	10.42	35.35
5CNF0	9.08	26.27	-	35.35
1.5CNF1	9.35	7.83	18.17	35.35
3CNF1	9.23	15.70	10.42	35.35
5CNF1	9.08	26.27	-	35.35
1.5CNF2	9.35	7.83	18.17	35.35
3CNF2	9.23	15.70	10.42	35.35
5CNF2	9.08	26.27	-	35.35

Neat WBPUU and nanocomposite films reinforced with 3 wt.% of cellulose nanofibers (3CNF0) and carboxylated cellulose nanofibers (3CNF1 and 3CNF2) can be observed in Figure 4.1. Transparent films, with no significant differences between them, were obtained for all systems.

Figure 4.1. Photographs of the prepared films of neat WBPUU and composites

4.2.1. Characterization of nanocomposites films

Nanocomposites reinforced with different nanocellulose fibers were characterized and the effect of the nanocellulose content and carboxylation degree was assessed.

A cryofractured cross-section of the systems was analyzed by Scanning Electron Microscopy to observe WBPUU morphology and CNF distribution within the matrix. SEM images were obtained for neat WBPUU and nanocomposites reinforced with 3 wt.% of CNF0, CNF1 and CNF2, as well as 5CNF1. SEM images of these systems are shown in Figure 4.2.

SEM images of composites containing 3 wt.% of CNF showed a good dispersion of the fibers within the matrix, with no visible agglomerations. Even at the highest nanocellulose content, 5 wt.%, (Figure 4.2e), a homogenous dispersion of the fibers can still be observed. SEM images suggest good dispersion of the fibers regardless the carboxylation degree of the CNF used, and its content.

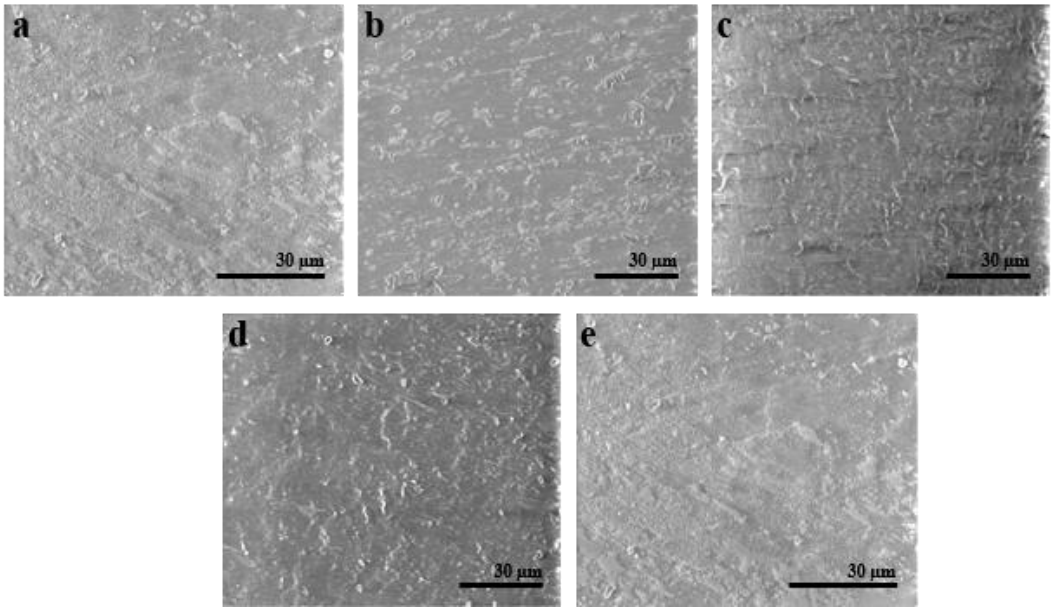

Figure 4.2. SEM images for cryofractured cross-sections of a) WBPUU, b) 3CNF0, c) 3CNF1, d) 3CNF2 and e) 5CNF1

FTIR spectroscopy was used to assess possible interactions taking place between the matrix and the nanoreinforcements employed. All spectra (Figure 4.3) showed the characteristic bands of polyurethanes discussed on Chapter 3. A band corresponding to N-H groups of urethane and urea functional groups can be seen for all systems, followed by a carbonyl vibration band of the polyol and urethane groups and a band related to the carbonyl group stretching vibration of urea groups [1-3], as well as a C-N stretching vibration and N-H bending band of the urethane and urea groups [4,5].

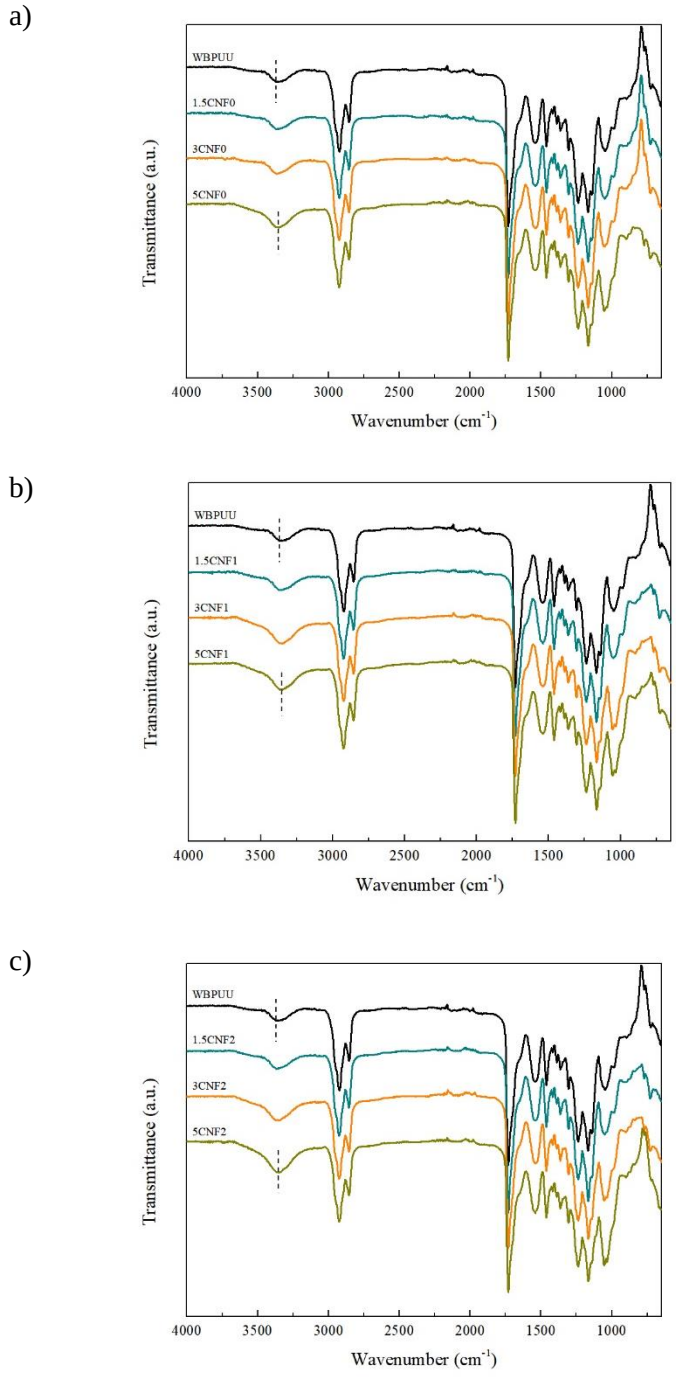

Figure 4.3. FTIR spectra of neat WBPUU and reinforced composites with different nanocellulose contents: a) CNF0, b) CNF1 and c) CNF2

Though all systems showed these characteristic bands, small changes were observed with the addition of cellulose nanofibers. Spectra of reinforced composites showed increased intensity of the band located between 3700-3100 cm^{-1}, the intensity is higher for systems with higher CNF contents. Moreover, for the nanocomposites with the highest CNF content, a slight shift of this band to lower wavenumber values can be observed (Figure 4.3a-c). Changes in this region suggested interactions between polyurethane N-H groups and cellulose O-H and COOH groups. When comparing composites prepared with different CNFs, a slight increase of the intensity of this band can be observed with the increase of the nanocellulose.

FTIR spectra second derivative curves are used to observe changes in the stretching bond strength and length due to variation of chemical environment of the atoms involved in bonds. In second derivative curves, interactions taking place and changes in wavenumber are seen by displacement of maximum peaks [6].

Figure 4.4 shows second derivative curves for neat WBPUU and composites reinforced with 5 wt.% of CNF, where interactions formed can be more clearly observed. Figure 4.4a shows the 1200-1500 cm^{-1} region, where there are no changes between the neat WBPUU and the reinforced composites spectra. However, in the interval of 3390-3320 cm^{-1}, differences between curves are distinguished (Figure 4.4b). In the case of nanocomposites, the band shifted to lower wavenumbers compared to neat WBPUU. This fact could be related to the formation of new hydrogen bonds between matrix N-H and cellulose O-H groups.

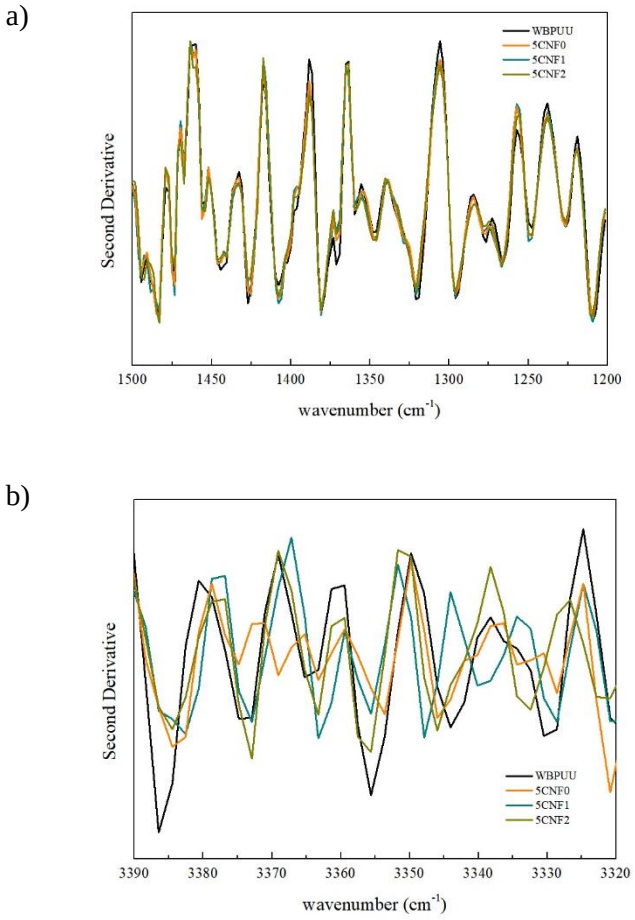

Figure 4.4. Second derivative curves for WBPUU and 5 CNF composite around a) 1500-1200 cm^{-1} and b) 3390-3320 cm^{-1}

In the figure 4.5 the possible interactions between the WBPUU and the carboxylated cellulose nanofibers are schematically represented. When carboxylated fibers were used, in addition to O-H groups, treated fibers counte also with carboxylic groups in their surface, able to form hydrogen bonds with urethane and urea groups of the polyurethane.

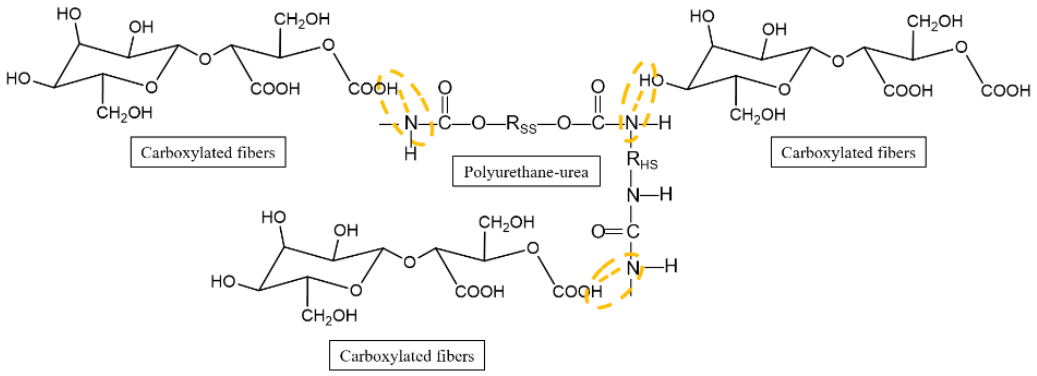

Figure 4.5. Schematic representation of the interactions between WBPUU and carboxylated CNF, where R_{SS} refers to soft segment chain and R_{HS} to hard segment chain

DSC test were performed to study the thermal transitions of prepared composites films. The obtained thermograms are shown in Figure 4.6 and Table 4.2 summarizes the values of endothermic transition attributed to short range ordering of the hard segment domains (T_{HS}), the soft segment glass transition (T_g) temperatures and the relative short range ordering degrees (X_{HS}). The relative short range ordering degree (X_{HS}) of the composites was calculated from equation 2.4 [7].

Table 4.2. Values of different thermal transitions observed from the DSC curves

Sample	T_g (ºC)	T_{HS} (ºC)	ΔH_{HS} ($J \cdot g^{-1}$)	X_{HS} (%)
WBPUU	-52.0	81.4	10.5	100
1.5CNF0	-52.9	83.2	12.4	117
3CNF0	-53.2	81.9	13.9	132
5CNF0	-52.6	85.7	15.0	142
1.5CNF1	-51.3	81.9	14.1	133
3CNF1	-53.9	86.1	15.0	142
5CNF1	-52.3	85.1	17.4	165
1.5CNF2	-53.2	82.4	14.4	137
3CNF2	-52.5	85.4	15.8	150
5CNF2	-51.9	86.1	16.8	159

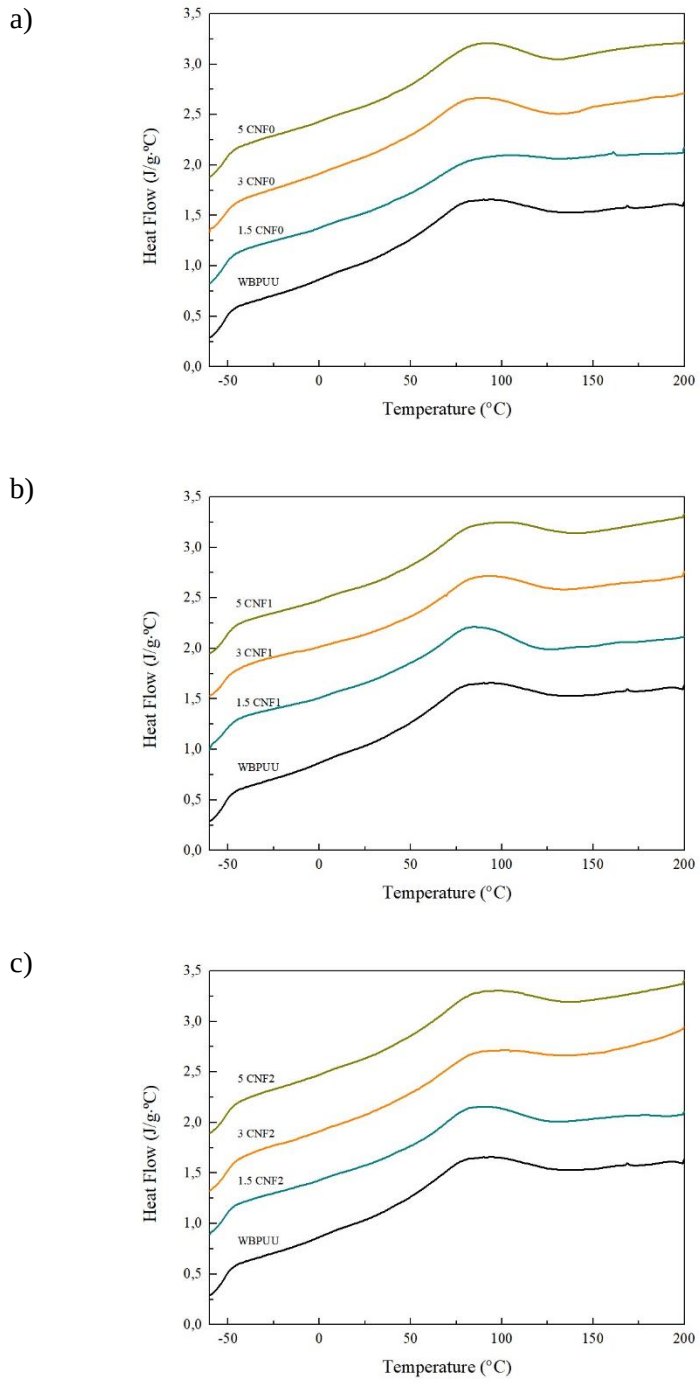

Figure 4.6. DSC curves of WBPUU and reinforced nanocomposites with different nanocellulose contents: a) CNF0, b) CNF1 and c) CNF2

It can be observed that the soft segment glass transition remained unaltered, however, regarding the short range ordering, some changes were observed in the transition of the composite materials. When CNF was added, the short range ordering transition temperature and enthalpy increased and, therefore, so did the relative short range ordering degree of the composites (Table 4.2). This increase to higher temperatures and enthalpy values suggested interactions between matrix and CNF, agreeing with FTIR results. The new assembling in the materials hindered the disruption of the short range ordered structures of the composite.

It can be seen that the addition of CNFs significantly increased the relative short range ordering of the nanocomposites and it is worth noting that this increase was more pronounced for carboxylated fibers, CNF1 and CNF2. Carboxylation seems to improve the interactions between the matrix and the fibers, resulting in composites with higher degree of short range ordering. Even for low reinforcement contents, there was a significant increase in the X_{HS}, going up 17% for 1.5CNF0 and up to 37% for 1.5CNF2.

The thermal stability of the materials was studied by Thermogravimetric Analysis (Figure 4.7). As happens with neat WBPUU films, the thermal degradation of the composites took places in two steps. As it was previously observed in Chapter 3, the first degradation step is related to the degradation of the hard domain and it is centered around 330 ºC for neat WBPUU. The second step is related to the degradation of the soft segment and the derivative peak is centered around 400 ºC for WBPUU.

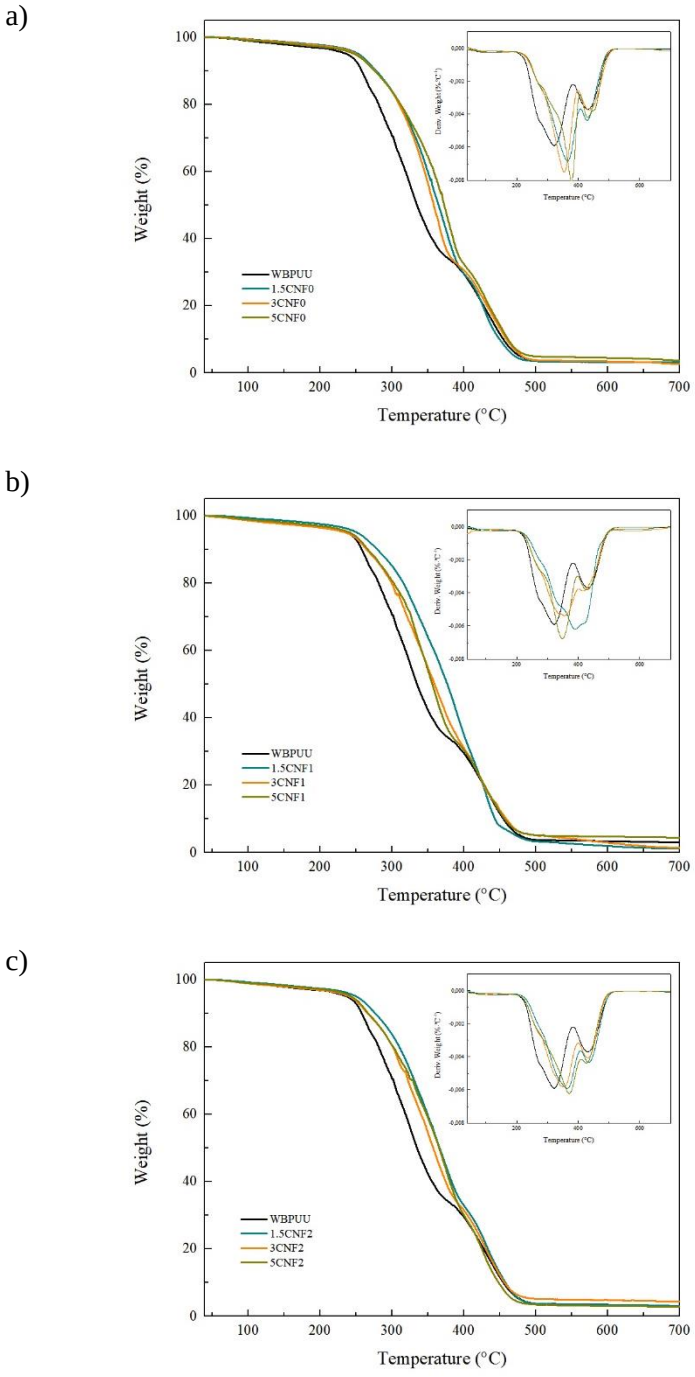

Figure 4.7. Thermogravimetric analysis curves of neat WBPUU and composites with different nanocellulose contents: a) CNF0, b) CNF1 and c) CNF2

For WBPUU/CNF composites, although the degradation trend was maintained, variations on degradation temperatures can be observed. When analyzing composites degradation and derivative curves it is clear that a change in the degradation of the hard segment took place. In composites, a delay in the degradation temperatures of the urea and urethanes groups can be observed. An improvement of the thermal stability of the materials with the addition of cellulose nanofibers can be clearly seen. This higher thermal stability can be attributed to the stabilization of the urethane groups and, thus, the resulting more confined structures, caused by the interactions formed between the CNFs and the WBPUU [8,9], which is in agreement with the data reported form DSC. However, the degradation of the SS related with the polyol remained quite constant.

Regarding the effect of the carboxylation of the cellulose nanofibers, there was a slight deterioration in thermal stability for composites reinforced with carboxylated fibers, CNF1 and CNF2, when compared to composites reinforced with unmodified fibers, CNF0. In Chapter 3, the faster degradation of carboxylated fibers was observed, due to their new rearranging and damages of their crystalline structure. Therefore, for composites reinforced with carboxylated fibers, interactions between matrix and reinforcement helped improve thermal stability of the matrix, but the damaged crystalline zones of the carboxylated CNFs resulted in composites with lower thermal stability than composites reinforced with CNF0.

The effect of the addition of CNF on the thermomechanical behavior of the material was studied by dynamic mechanical tests. The resulting storage modulus and loss factor vs. temperature curves are shown in Figure 4.8. DMA results showed a clear reinforcement effect of the CNFs in the thermomechanical properties of the materials. Prior to the glass transition, a very similar behavior can be seen for all systems. The modulus values were higher for reinforced nanocomposites than for neat polymer. Among

composites, composites reinforced with carboxylated fibers showed slightly higher values than composites reinforced with CNF0. Once the rubbery state was achieved, more significant changes were observed between neat polymer and nanocomposites performance. At approximately -45 ºC, glass transition temperature was reached, which can be seen as a drop in the storage modulus curve and a peak in the tan δ. From this point on, modulus curve of neat WBPUU film continued dropping, showing poor thermomechanical stability. This behavior was not shared by reinforced nanocomposites, for which a more gradual drop of the storage modulus was observed. This increase in stability and modulus values was proportional to the content of reinforcement present in the nanocomposite.

This behavioral change can also be seen in the tan δ curves. The damping peak decreased with the addition and content of cellulose nanofibers. This fact may be due to the new interactions created between the matrix and the fibers, which hampered the mobility of the WBPUU chains [10]. In the tan δ curves, nanocomposites showed a second transition peak around 50 ºC, which is attributed to the breaking of the short range ordering of the hard segment domains, as previously seen in DSC results. This transition cannot be seen for WBPUU films, since the material started to flow and was not capable to resist long enough to show this transition. However, for nanocomposites, CNFs supplied a higher integrity to the systems, impeding the flowing and, thus, presenting this new peak.

Regarding the effect of carboxylation degree, it can be seen that composites reinforced with carboxylated fibers showed a higher enhancement in stability and higher modulus values than composites reinforced with CNF0. As seen in DSC results, composites with carboxylated fibers resulted in materials with a higher amount of interactions and higher ordering degrees, which improved the thermomechanical behavior of the materials.

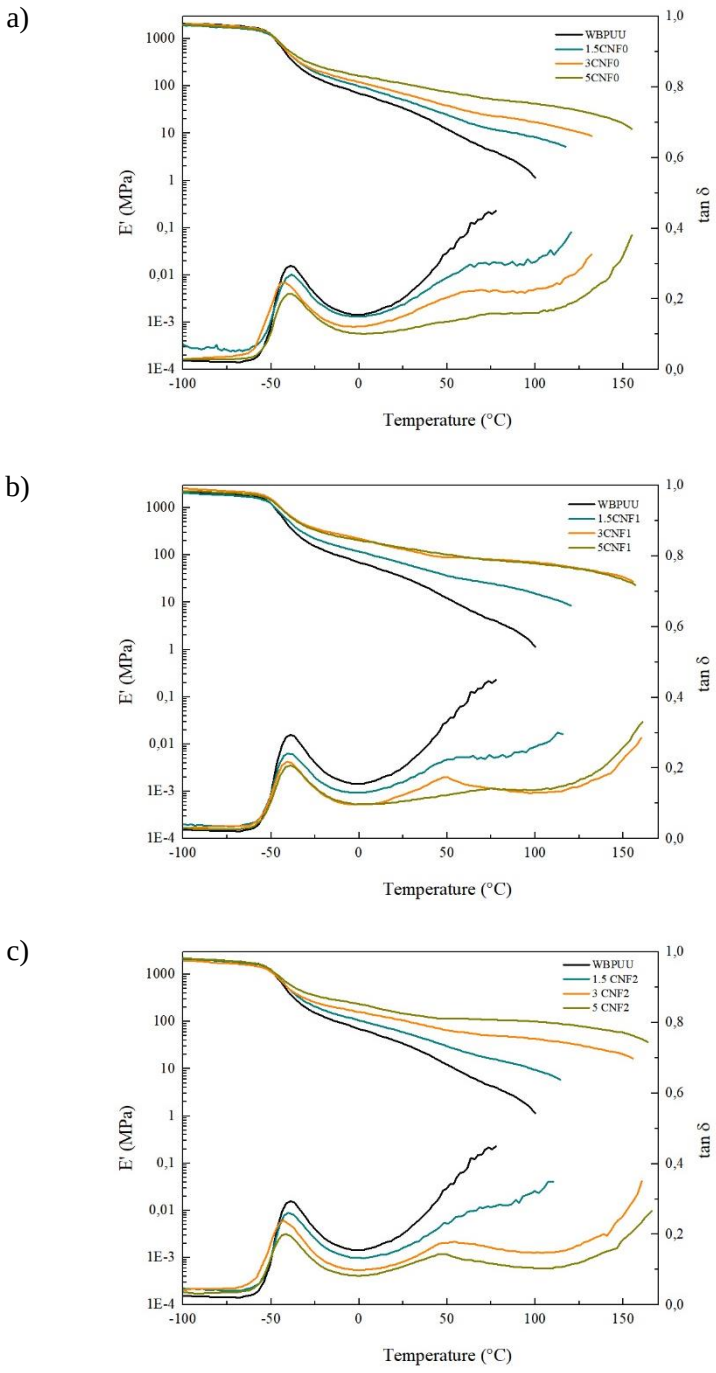

Figure 4.8. Dynamic-mechanical curves of neat WBPUU and composites with different nanocellulose contents: a) CNF0, b) CNF1 and c) CNF2

The effect of the addition of the reinforcement can also be seen when studying the mechanical properties of the systems. Mechanical behavior was influenced by the addition of nanoreinforcements, as can be observed in tensile stress/strain curves shown in Figure 4.9. Tensile properties are summarized in Table 4.3.

Table 4.3. Young modulus, stress at yield, stress at break and strain at break values for neat WBPUU and composites reinforced with CNF0, CNF1 and CNF2

Sample	Young modulus (MPa)	Stress at yield (MPa)	Stress at break (MPa)	Strain at break (%)
WBPUU	9.8 ± 1.9	2.0 ± 0.1	8.6 ± 0.8	469.6 ± 20.8
1.5CNF0	11.9 ± 1.8	3.1 ± 0.1	12.6 ± 0.6	587.7 ± 13.7
3CNF0	52.5 ± 8.5	6.6 ± 0.9	14.8 ± 2.2	527.9 ± 86.2
5CNF0	81.7 ± 8.4	8.0 ± 0.3	10.9 ± 0.2	272.3 ± 30.1
1.5CNF1	25.6 ± 4.8	3.7 ± 0.1	13.5 ± 1.4	519.6 ± 41.6
3CNF1	59.6 ± 6.2	4.8 ± 0.2	11.5 ± 1.7	441.0 ± 58.6
5CNF1	173.7 ± 19.1	9.4 ± 0.2	13.6 ± 0.4	393.3 ± 51.7
1.5CNF2	12.4 ± 2.9	3.2 ± 0.1	14.3 ± 1.3	604.5 ± 45.4
3CNF2	55.6 ± 8.7	5.0 ± 0.3	14.4 ± 2.4	506.9 ± 99.4
5CNF2	98.0 ± 11.0	6.6 ± 0.5	10.6 ± 0.6	382.9 ± 28.7

The addition of cellulose nanofibers to the waterborne polyurethane-urea matrix resulted in an evident improvement of the Young modulus values. This significant increase in value could be attributed to the increase in relative short range ordering degree of the composites, as well as to the reinforcement effect of CNFs. These results, as previously seen in literature [11], proved the good interaction between both components of the composites. Regarding the effect of the carboxylation degree of cellulose, only for nanocomposites with 5 wt.% content of nanofibers could significant differences be observed. Composite with 5 wt.% CNF1 showed the highest Young's modulus, which is in correlation with the properties observed for neat CNF1 fibers and with the short range ordering degree observed by DSC for the nanocomposite.

The reinforcement effect of the CNF can also be seen in the stress at yield and stress at break values of the composites. Small amounts of CNF were able to

significantly alter these properties, with just 1.5 wt.% of nanocellulose an increase of over 60% in the stress at yield values was obtained. In the case of stress at break, most systems showed differences from the neat polyurethane-urea but remained at similar values among them. Nanocomposites containing the highest nanocellulose content showed the lowest values, which suggests the presence of agglomerates in these composites, which is in agreement with literature results [12]. The increase observed for stress at yield and stress at break values suggested an effective stress transfer from the matrix to the reinforcement.

Finally, when assessing the strain at break, it can be observed that the content of reinforcement present had a big impact in this property. Nanocomposites with low CNF contents (1.5 and 3 wt.%) maintained high strain at beak values, similar and even higher than neat WBPUU. Contrarily, most studies found in the literature show a decrease in strain to failure from the matrix, due to an interfacial debonding which grows into a crack in the material [9,13,14]. However, there are also some works where strain to failure values are maintained [4,8,15], modulated by reinforcement aspect ratio and matrix-reinforcement interaction, resulting in overall mechanically improved composites. For nanocomposites prepared with 5 wt.% of CNF, the strain at break suffered a drop in values, this behavior agrees with the possible agglomeration of nanofibers suggested by stress at break values.

It can be concluded that both content and type of cellulose had a significant effect on the mechanical properties of the nanocomposites. Being the most significant changes observed for Young modulus and stress at yield values.

a)

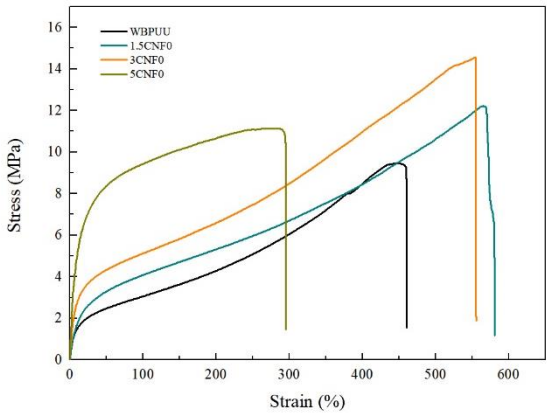

b)

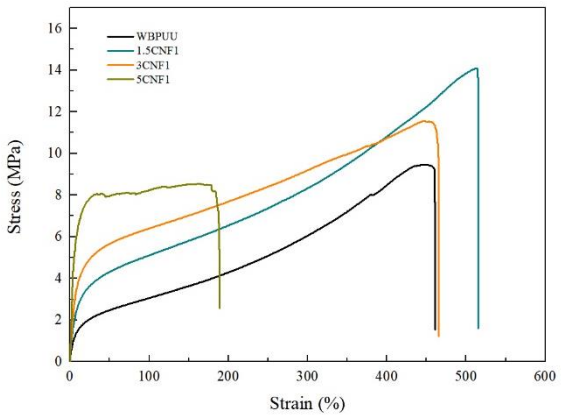

c)

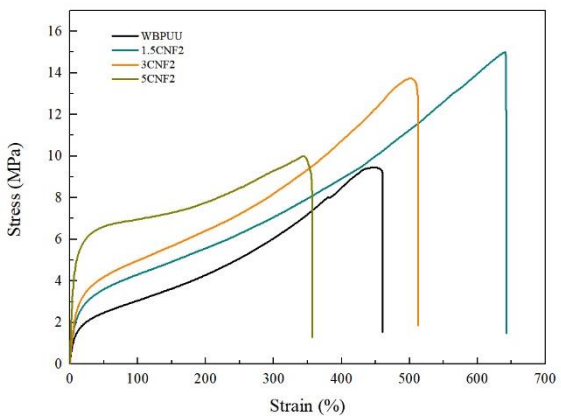

Figure 4.9. Stress/Strain curves for neat WBPUU and composites with different nanocellulose contents: a) CNF0, b) CNF1 and c) CNF2

4.3. Preparation of WBPUU/CNF filaments

In order to assess the use of WBPUU/CNF composites in FDM 3D printing, filaments were prepared. For filament preparation unmodified fibers (CNF0) and one of the carboxylated fibers, CNF1, were used. CNF1 was chosen over CNF2 due to its less damaged structure and good properties shown by prepared composites. It has been observed that the incorporation method of the reinforcement can also alter composite properties [8]. Thus, two incorporation routes, ex-situ and in-situ, were used when preparing filaments containing 3 wt.% of cellulose nanofibers. In ex-situ method, where fibers were incorporated by sonication of the WBPUU and the reinforcement, and in-situ, where fibers were added during the synthesis of the WBPUU.

For ex-situ method, composites were prepared following the same procedure as previously explained for WBPUU/CNF nanocomposite films. First, a good water dispersion of the reinforcements was ensured. CNF0 and CNF1, already in aqueous dispersion (6 $mg \cdot mL^{-1}$), were sonicated for 1 hour in a sonication bath for a better dispersion and then the WBPUU was added, and the new mixtures were further sonicated for 1 hour. For in-situ method, the CNF suspensions were also sonicated for a good dispersion and these aqueous dispersions were later added drop by drop to the synthesis during the phase inversion step. Each composite preparation, as well as the neat polyurethane-urea, was poured in Teflon molds and left to dry as previously explained. Thus, films were obtained for the neat polymer (WBPUU), the ex-situ prepared nanocomposites ($3CNF0_{EX}$, $3CNF1_{EX}$) and in-situ prepared nanocomposites ($3CNF0_{IN}$, $3CNF1_{IN}$).

For filament preparation, prepared films were pelletized and 0.3 g of pellets were fed every 25 s in a twin screw extruder, HAAKE MiniLab extruder, working at 50 rpm. Extrusion temperature was optimized for each system, WBPUU was extruded at 160 °C, whereas WBPUU/CNF composites needed a higher temperature, ex-situ and in-situ composites were extruded at 180 °C and

190 °C, respectively. The filaments were extruded directly from a 1.75 mm diameter nozzle onto a conveyer belt where they cooled down and completely solidified. Prepared filaments of neat WBPUU and nanocomposites were named FWBPUU, F3CNF0$_{EX}$, F3CNF0$_{IN}$, F3CNF1$_{EX}$, F3CNF1$_{IN}$.

4.3.1. Characterization of WBPUU/CNF filaments

Prepared filaments were characterized regarding physico-chemical, thermal and mechanical properties.

Filament pictures are shown in Figure 4.10. As it can be observed, FWBPUU had a translucent aspect, which changed with the addition of the nanoreinforcements. WBPUU/CNF0 filaments showed a slightly more yellow tonality, more noticeable for the composite prepared by in-situ method. This yellow tonality was also seen in CNF1-reinforced filaments, for these materials this yellow-brownish color was more intense. This change in the pigmentation during the extrusion process of the composites could indicate the cellulose beginning to degrade. Thermoxidative conditions used in addition to the shear stress suffered by the materials could have started to degrade the materials. The darker tonality shown by nanocomposites containing carboxylated cellulose nanofibers agrees with the faster degradation observed for CNF1 in TGA (Chapter 3).

It is also worth noting that the extrusion of composites containing cellulose was more difficult to control and needed a higher extrusion temperature than neat polyurethane-urea. The worse flux of nanocomposite materials and the obstruction of the nozzle resulted in a high variation of the obtained filaments' diameter.

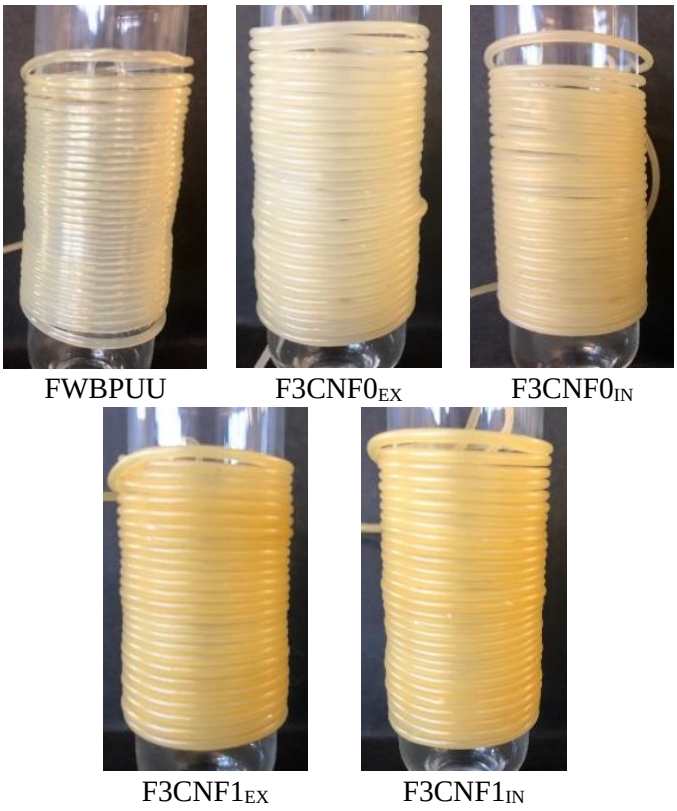

Figure 4.10. Photographs of neat WBPUU and WBPUU/CNF filaments

Fourier Transform Infrared spectroscopy analyses were carried out for filament systems, in order to assess possible interactions taken place between the WBPUU matrix and the nanoreinforcements. FTIR spectra of WBPUU filament and nanocomposite filaments are shown in Figure 4.11.

As happened for composites films, when reinforcements are added, spectra show only differences in the N-H band, where this band was displaced to lower wavenumbers for composites, indicating hydrogen bonds taking place. This change took place for all WBPUU/CNF composite filaments, however no differences were observed based on the type of cellulose employed or the incorporation route.

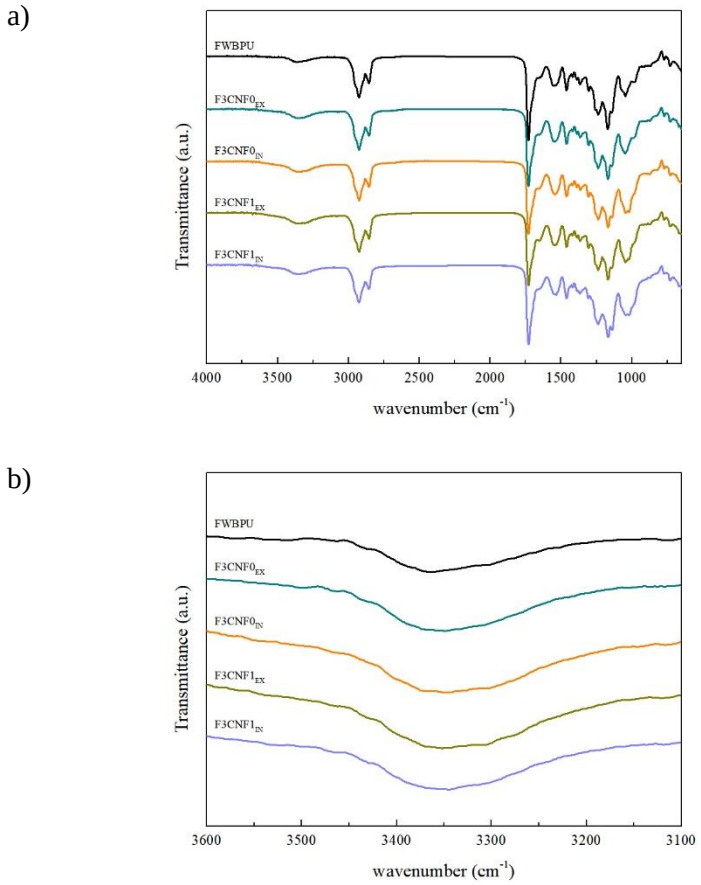

Figure 4.11. FTIR spectra of WBPUU and WBPUU/CNF nanocomposites filaments and b) zoomed FTIR spectra for the 3600-3100 cm^{-1} region

Thermal degradation curves of neat polymer and nanocomposites filaments are shown in Figure 4.12., where the same degradation trend observed for films was followed. For WBPUU/CNF composite filaments, slight changes can be observed, $F3CNF0_{EX}$ and $F3CNF0_{IN}$ showed higher stability during the initial part of the degradation process, attributed to the stabilization of urethane groups from the formation of hydrogen bonds [8,9].

However, this improvement in stability was not observed for WBPUU/CNF1 filaments. In this case, no significant changes in trend could be seen. The faster

degradation of the modified cellulose could be responsible for diminishing the reinforcement effect the interactions may have supposed.

It can be observed that filaments showed higher maximum temperature peaks than their films counterparts. The extrusion process of the filaments may have caused the alignment of the polyurethane chains and as results materials with higher order and, thus, higher stability were obtained.

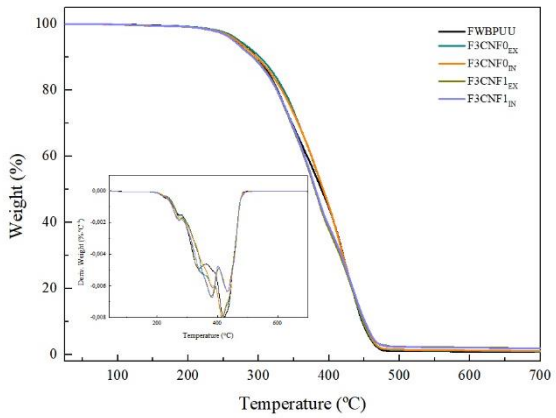

Figure 4.12. TGA and DTG curves for WBPUU and WBPUU/CNF nanocomposites filaments

The mechanical properties of the filaments were also studied to observe possible changes taken place after the extrusion process, as well as with the addition of CNF and the incorporation route. Tensile stress/strain curves are shown in Figure 4.13 and the filament properties are summarized in Table 4.4.

Comparing with the unreinforced filament, it can be observed that ex-situ preparation of composites resulted in a stronger improvement of mechanical properties than in-situ method. Young modulus for ex-situ composites increased up to a 383% in the case of F3CNF0$_{EX}$ and a 245% for F3CNF1$_{EX}$. F3CNF0$_{EX}$ showed also a significant enhancement in the stress at break value. This mechanical enhancement with the addition of cellulose nanofibers showed

the reinforcement effect supplied by CNF and is in agreement with reports in literature [11]. This trend, however, was not maintained for in-situ composites, showing F3CNF0$_{IN}$ similar values than neat polyurethane-urea filament, and F3CNF1$_{IN}$ even slightly deteriorated properties. The disposition of the CNF in ex-situ prepared composites may have allowed the alignment of the fibers during the extrusion process, resulting in highly reinforced materials in the tested direction. However, the more embedded state of the CNF in in-situ prepared materials, as well as the possibility of chemical interactions taken place, did not allow for a proper alignment of the fibers and, hence, a lower reinforcement effect than for ex-situ materials is observed.

Table 4.4. Young modulus, stress at yield, stress at break and strain at break values for WBPUU and WBPUU/CNF filaments

	Young modulus (MPa)	Stress at yield (MPa)	Stress at break (MPa)	Strain at break (%)
FWBPUU	6.9 ± 1.3	1.5 ± 0.1	5.4 ± 0.6	821.6 ± 35.4
F3CNF0$_{EX}$	33.3 ± 5.8	5.3 ± 0.3	9.1 ± 0.4	341.7 ± 53.4
F3CNF0$_{IN}$	13.7 ± 2.9	3.1 ± 0.6	4.6 ± 0.8	427.9 ± 131.0
F3CNF1$_{EX}$	23.8 ± 7.4	3.7 ± 0.3	4.6 ± 0.7	394.5 ± 62.9
F3CNF1$_{IN}$	8.6 ± 2.3	1.3 ±0.6	2.1 ± 1.2	248.5 ± 136.0

When comparing the effect of the type of cellulose used, it was clearly seen that unmodified cellulose nanofibers resulted in systems with better mechanical properties than carboxylated ones. The faster degradation observed for carboxylated fibers (Chapter 3) may have caused higher degradation of the composites during the extrusion process, as a result less enhanced properties were observed.

All composite filaments suffered a pronounced drop in the strain at break values, which could probably be ought to small degradation taken place during the extrusion process, as suggested by changes in material color, which would also explain the poor reinforcement effect supplied by the incorporation of CNF. When compared to films' tensile properties, it can be observed that a

lower reinforcement effect was supplied in filaments. Filaments showed lower Young modulus, stress at yield, stress at break and strain at break values than their film counterparts. This fact suggested the degradation of the material taking place during the extrusion process. Moreover, the fast solidification process in filament preparation may not have allowed for the slow crystallization process that took place in the preparation of the films.

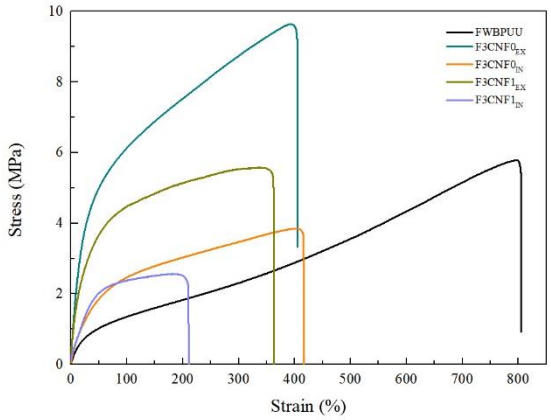

Figure 4.13. Stress/Strain curves for WBPUU and WBPUU/CNF filaments

The thermo-mechanical behavior of the filaments was analyzed by Dynamic Mechanical Analysis. The reinforcement effect of CNF can be clearly seen in DMA results, as well as the effect of the incorporation route (Figure 4.14).

Comparing modulus values, it can be clearly seen that, at a same temperature, nanocomposite filaments showed higher storage modulus values than neat polymer filament, due to the reinforcement effect provided by the cellulose nanofibers. It can also be observed that, as happened for tensile properties, composites prepared by ex-situ method showed also higher values than their in-situ composites counterparts.

The addition of nanoreinforcements resulted also in materials with highly enhanced thermomechanical stability, seen in the storage modulus curves,

where the drop of the curves is delayed about 50 °C. The reduced mobility of the chains, due to the hydrogen bonds observed by FTIR, and the reinforcement effect of the fibers increased material stiffness and thus storage modulus [16]. The incorporation method did not majorly affect the thermomechanical behavior of the materials. All composite filaments showed a higher thermomechanical stability than the neat FWBPUU, as happened in the case of nanocomposites films. Regarding the effect of the carboxylation degree, no changes were observed for WBPUU/CNF1 nanocomposite filaments compared to WBPUU/CNF0 filaments.

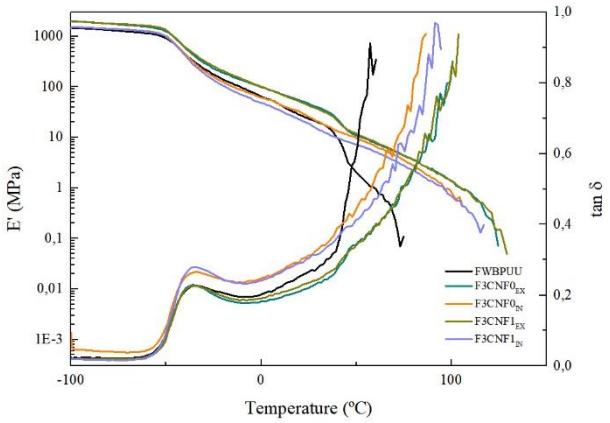

Figure 4.14. Dynamic mechanical curves of WBPUU and WBPUU/CNF filaments

Comparing with their films counterparts, it can be observed that the thermomechanical stability of the materials was deteriorated during the extrusion process, due to the degradation suffered by the material.

4.4. FDM 3D printing of prepared filaments

Neat WBPUU and WBPUU/CNF filaments were used for FDM 3D printing, using a Tumaker VOLADORA NX. Changing printing parameters, such as extrusion temperature and printing speed, as well as manually adjusting feeding gear position, printing process was optimized for each filament.

However, even after optimization process, it remained impossible to successfully 3D print most of the filaments. FWBPUU, $FCNF0_{EX}$, $FCNF0_{IN}$, $FCNF1_{EX}$ and $FCNF1_{IN}$ showed several problems during printing process. The filament presented too low stiffness for a good feeding of the material, which resulted in the filament bending around feeding gear and being unable to advance through the feeding tube (Figure 4.15), as often happens with high flexibility filaments in Bowden extruders. Moreover, after optimization and for filaments showing slightly higher stiffness, namely reinforced filaments, a better feeding process was achieved, however, the extruding flow was remained slow and discontinuous and often caused nozzle obstruction. This fact could be attributed to low pressure on the nozzle due to the extreme flexibility of the filaments and to the high viscosity of these filaments due to the matrix and reinforcement interactions observed by FTIR [17,18]

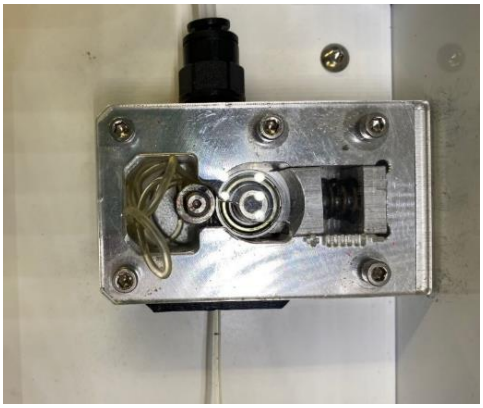

Figure 4.15. Photograph of filament entanglement on the feeding gear due to low rigidity of filament

4.5. Conclusions

In this chapter WBPUU based nanocomposite films were prepared using three types of cellulose nanofibers, CNF0, CNF1 and CNF2. Nanocomposites with different reinforcement contents were prepared and the effect of both the content and the type of CNF used were studied.

When CNF was added hydrogen bond interactions were formed between the matrix and the systems and materials with more ordered structures were obtained, which resulted in an increase in the enthalpy of the systems. This effect was more pronounced for carboxylated fibers, the new functional groups in the CNF structure promoted the formation of interactions. The stabilization of the urethane and urea groups by the addition of CNF delayed the degradation of the materials to higher temperatures, enhancing their thermal stability. The reinforcement effect supplied by CNF was also reflected on the mechanical properties of the films, which show significantly higher Young modulus and stress at break values. However, for 5 wt.% CNF containing composites strain at break values began to drop, suggesting the formation of fiber agglomerations.

Based on observed results, 3 wt.% reinforced composites were prepared with CNF0 and CNF1, via ex-situ and in-situ, which were used to prepared filaments. For filament preparation composites materials show higher difficulties to flow and needed higher temperatures during the extrusion process than neat polyurethane-urea. As a result, slightly degraded materials were obtained. CNF containing filaments show better mechanical and thermomechanical behavior than neat polymer filament. However, the degradation produced during the extrusion process reduced the reinforcement effect of nanocellulose.

The use of these filaments in FDM 3D printing was assessed. However, the material presented too high flexibility and poor flow, which did not allow for a successful feeding process and for good printability.

4.6. References

[1] Yilgör I, Yilgör E, Wilkes GL. Critical parameters in designing segmented polyurethanes and their effect on morphology and properties: A comprehensive review. Polymer 2015;58:A1–36. doi:10.1016/j.polymer.2014.12.014.

[2] Ugarte L, Fernández-d'Arlas B, Valea A, González ML, Corcuera MA, Eceiza A. Morphology-properties relationship in high-renewable content polyurethanes. Polym Eng Sci 2014;54:2282–91. doi:10.1002/pen.23777.

[3] Santamaria-Echart A, Fernandes I, Saralegi A, Costa MRPFN, Barreiro F, Corcuera MA, et al. Synthesis of waterborne polyurethane-urea dispersions with chain extension step in homogeneous and heterogeneous media. J Colloid Interface Sci 2016;476:184–92. doi:10.1016/j.jcis.2016.05.016.

[4] Pei A, Malho JM, Ruokolainen J, Zhou Q, Berglund LA. Strong nanocomposite reinforcement effects in polyurethane elastomer with low volume fraction of cellulose nanocrystals. Macromolecules 2011;44:4422–7. doi:10.1021/ma200318k.

[5] Santamaria-Echart A, Arbelaiz A, Saralegi A, Fernández-d'Arlas B, Eceiza A, Corcuera MA. Relationship between reagents molar ratio and dispersion stability and film properties of waterborne polyurethanes. Colloids Surfaces A Physicochem Eng Asp 2015;482:554–61. doi:10.1016/j.colsurfa.2015.07.012.

[6] Orue A, Santamaria-Echart A, Eceiza A, Peña-Rodriguez C, Arbelaiz A. Office waste paper as cellulose nanocrystal source. J Appl Polym Sci 2017;134:45257. doi:10.1002/app.45257.

[7] Wunderlich B. Thermal analysis of polymeric materials. Knoxville: Springer Berlin Heidelberg; 2005.

[8] Santamaria-Echart A, Ugarte L, Arbelaiz A, Gabilondo N, Corcuera MA, Eceiza A. Two different incorporation routes of cellulose nanocrystals in waterborne polyurethane nanocomposites. Eur Polym J 2016;76:99–109. doi:10.1016/j.eurpolymj.2016.01.035.

[9] Cao X, Habibi Y, Lucia LA. One-pot polymerization, surface grafting, and processing of waterborne polyurethane-cellulose nanocrystal nanocomposites. J Mater Chem 2009;19:7137–45. doi:10.1039/b910517d.

[10] Ly B, Thielemans W, Dufresne A, Chaussy D, Belgacem MN. Surface functionalization of cellulose fibres and their incorporation in renewable polymeric matrices. Compos Sci Technol 2008;68:3193–201. doi:10.1016/j.compscitech.2008.07.018.

[11] Auad ML, Contos VS, Nutt S, Aranguren MI, Marcovich NE. Characterization of nanocellulose- reinforced shape memory polyurethanes. Polym Int 2008;57:651–9. doi:10.1002/pi.2394.

[12] Jimenez GA, Jana SC. Composites of carbon nanofibers and thermoplastic polyurethanes with shape-memory properties prepared by

chaotic mixing. Polym Eng Sci 2009;49:2020–30. doi:10.1002/pen.21442.

[13] Cao X, Dong H, Li CM. New nanocomposite materials reinforced with flax cellulose nanocrystals in waterborne polyurethane. Biomacromolecules 2007;8:899–904. doi:10.1021/bm0610368.

[14] Mondragon G, Santamaria-Echart A, Hormaiztegui ME V., Arbelaiz A, Peña-Rodriguez C, Mucci V, et al. Nanocomposites of waterborne polyurethane reinforced with cellulose nanocrystals from sisal fibres. J Polym Environ 2018;26:1869–80. doi:10.1007/s10924-017-1089-z.

[15] Santamaria-Echart A, Fernandes I, Ugarte L, Barreiro F, Arbelaiz A, Corcuera MA, et al. Waterborne polyurethane-urea dispersion with chain extension step in homogeneous medium reinforced with cellulose nanocrystals. Compos Part B Eng 2018;137:31–8. doi:10.1016/j.compositesb.2017.11.004.

[16] Pokharel P, Lee DS. Thermal and mechanical properties of reduced graphene oxide/polyurethane nanocomposite. J Nanosci Nanotechnol 2014;14:5718–21. doi:10.1166/jnn.2014.8824.

[17] Sadia M, Sośnicka A, Arafat B, Isreb A, Ahmed W, Kelarakis A, et al. Adaptation of pharmaceutical excipients to FDM 3D printing for the fabrication of patient-tailored immediate release tablets. Int J Pharm 2016;513:659–68. doi:10.1016/j.ijpharm.2016.09.050.

[18] Cho SY, Park HH, Yun YS, Jin HJ. Influence of cellulose nanofibers on the morphology and physical properties of poly(lactic acid) foaming by supercritical carbon dioxide. Macromol Res 2013;21:529–33. doi:10.1007/s13233-013-1057-y.

Chapter 5

WBPUU/CNF NANOCOMPOSITE INKS FOR DIRECT INK WRITING 3D PRINTING

5. WBPUU/CNF NANOCOMPOSITE INKS FOR DIRECT INK WRITING 3D PRINTING

5.1. Aim of the chapter

In this chapter, WBPUU/CNF nanocomposites gels were developed and adapted for Direct Ink Writing (DIW). To analyze the effect of carboxylation degree of CNF on composite gels formation, two different nanofibers were selected for this, CNF0 and CNF1. Gels with 2 and 3 wt.% of CNF regarding the total weight of the gels were prepared and characterized. Two different nanocellulose incorporation routes, ex-situ and in-situ, were used. For nanocellulose content optimization in in-situ prepared inks and as reference, nanocomposites inks were also prepared using a commercial cellulose nanofiber sample.

The rheological behavior of the prepared inks was analyzed and they were later used in DIW to produced 3D printed parts. The obtained parts were characterized morphologically, physico-chemically, thermally and mechanically.

The addition of nanoentities can be used to modulate the rheological behavior of a material and enhance its printing capacity. In this chapter, different types and contents of cellulose nanofibers were added to a WBPUU matrix to modulate the rheological properties and to obtain inks with good printing behavior.

5.2. Preparation and characterization of WBPUU/CNF nanocomposite inks

WBPUU/CNF gels were prepared using the procedure described in Chapter 3. Nanocomposite gels were prepared by using two incorporation methods of nanocellulose, and the effect of the incorporation route on the final properties of the gels and printed parts was studied.

For ex-situ prepared compositions, nanocomposite gels were prepared by vigorous mechanical stirring, using an ultraturrax homogenizer (Polytron PT 2500E, KINEMATICA). First, CNF suspensions were freeze-dried, and dried CNF systems were stored in a desiccator until used, to avoid humidity. Dried CNF were added to the WBPUU dispersion and were stirred for 10 minutes at 12000 rpm. Stirring was carried out in an iced bath, in order to avoid high temperatures and degradation of the systems. Nanocomposites gels with 2 and 3 wt.% of CNF, regarding the total weight of the gels, were prepared with CNF0 ($2CNF0_{EX}$ and $3CNF0_{EX}$) and CNF1 ($2CNF1_{EX}$ and $3CNF1_{EX}$) (Table 5.1).

Table 5.1. WBPUU and CNF contents for ex-situ nanocomposite gels preparation

Sample	WBPUU dispersion (g) (* 33wt.%)	Dried CNF (g)	Deionized water (g)	Total mass (g)
$2CNF0_{EX}$	19.4	0.4	0.2	20
$3CNF0_{EX}$	19.6	0.6	-	20
$2CNF1_{EX}$	19.4	0.4	0.2	20
$3CNF1_{EX}$	19.6	0.6	-	20

For in-situ prepared composites, the addition of CNF was carried out in the phase inversion step of the polyurethane synthesis. First, CNF content was optimized using a commercial cellulose nanofiber system (University of Maine, Lot. 9004-34-6). Said reference commercial cellulose was named as CNFr. CNF were dispersed in water in the right concentration in order to obtain gels with 2 and 3 wt.%, regarding their total weight. In-situ prepared nanocomposites gels with 2 and 3 wt.% of CNFr were name $2CNFr_{IN}$ and $3CNFr_{IN}$, respectively. After quantity optimization process for proper rheological behavior, inks with 3 wt.% of CNF0 and CNF1 were prepared and named $3CNF0_{IN}$ and $3CNF1_{IN}$, respectively. Quantities used for in-situ prepared nanocomposite gels are shown in Table 5.2.

Table 5.2. WBPUU and CNF contents for in-situ nanocomposite gels preparation

Sample	Prepolymer mass (g)	Dried CNF (g)	Deionized water (g)
$2CNFr_{IN}$	30	1.82	59.09
$3CNFr_{IN}$	30	2.73	58.18
$3CNF0_{IN}$	30	2.73	58.18
$3CNF1_{IN}$	30	2.73	58.18

5.2.1. Characterization of WBPUU/CNF nanocomposite inks

The rheological behavior of the prepared WBPUU/CNF inks was characterized in order to preliminarily study the printability and shape fidelity that gels will show when used in direct ink writing 3D printing. In order to analyze this, flow (viscosity vs shear rate), dynamic oscillatory (storage and loss modulus vs shear stress) and a structural recovery tests were carried out. Depending on the viscosity of the gels, the adequate geometry was chosen when performing the tests. In this regard, the WBPUU dispersion and $2CNFr_{IN}$ inks were tested with coaxial cylinders, while the other inks were tested with a plate-plate geometry.

When studying the rheological behavior of a shear thinning ink for 3D printing, it is worth noting that its non-Newtonian behavior will cause the flow on a capillary to deviate from a parabolic velocity profile [1]. Thus, for the correct calculation of the shear stress the ink will be subjected to, the equation proposed by Li et al. [2] (equation 5.1.), containing the necessary adjustments, can be use.

$$\dot{\gamma}_n{}^n = \left[\frac{V \cdot R^2}{\left(\frac{n}{3n+1}\right)\left(R^{\frac{3n+1}{n}}\right)}\right]^n \cdot r \qquad (equation\ 5.1.)$$

where $\dot{\gamma}_n$ is the shear rate the ink is submitted to at the nozzle, n is the flow index calculated form Power Law, V is the printing speed, r is a distance located between the center of the nozzle and its radius and R is the radius of the nozzle.

In order to study the viscosity of the prepared nanocomposite inks, flow tests were carried out to analyze the effect of the shear rate in the viscosity of the materials. Obtained flow curves are shown in Figure 5.1 and 5.2 for ex-situ and in-situ prepared inks, respectively. Moreover, viscosity values at a shear rate of 0.2 and 100 s^{-1}, as well as at the shear rate on the wall of the nozzle (γ_{nz}), calculated with equation 5.1, are summarized in Table 5.3. In order to further analyze the rheological behavior of the inks, the flow index, n, value for each system was calculated by Power Law equation (equation 1.1), and are reported in Table 5.3.

As can be observed from flow curves, all systems showed shear-thinning behavior that is ideal for DIW [3,4]. All inks present n values corresponding to shear-pseudo-plastic fluids (n<1). However, differences in the viscosities of the systems depending on the nanocellulose content and addition route were evident.

Table 5.3. Viscosity and rheological parameters for ex-situ and in-situ prepared WBPUU and CNF containing inks

	Sample	η at 0.2 s^{-1} (Pa·s)	η at γ_{nw} (Pa·s)	η at 100 s^{-1} (Pa·s)	n
ex-situ	WBPUU	1.1	0.1	0.1	0.725
	$2CNF0_{EX}$	217.9	18.5	1.5	0.198
	$3CNF0_{EX}$	434.8	18.7	1.9	0.189
	$2CNF1_{EX}$	289.2	13.4	1.9	0.204
	$3CNF1_{EX}$	730.6	44.5	2.7	0.111
in-situ	$2CNFr_{IN}$	6.2	0.9	0.1	0.361
	$3CNFr_{IN}$	222.9	9.2	1.0	0.184
	$3CNF0_{IN}$	256.0	14.0	2.0	0.254
	$3CNF1_{IN}$	348.2	19.9	2.3	0.204

The addition of CNF to the polyurethane dispersion resulted in a very intense increase of the viscosity of the systems, the same trend on viscosity was observed in the literature [5–9]. Figure 5.1 shows that the viscosity values increased as CNF content increased. At a same shear rate higher viscosity values were observed for composites containing 3 wt.% of CNF compared to

their 2 wt.% homologues (Table 5.3), agreeing with literature reports [10–13]. Regarding the type of cellulose used, results show that carboxylated cellulose nanofibers resulted in inks with higher viscosity [8,10,14]. The higher viscosities shown by CNF1 containing inks may be due to more interactions taking place between the nanocellulose and the polyurethane, as seen in Chapter 4, thanks to the carboxylated groups of the modified cellulose.

The highest viscosity was observed when carboxylated nanocellulose and 3 wt.% of nanofiber content was incorporated. This system may result in 3D printed pieces with better shape fidelity [9], ought to a lower tendency to flow at low shear rates, i.e. at rest.

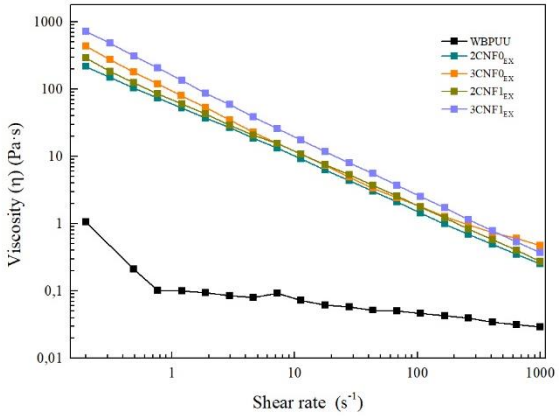

Figure 5.1. Viscosity as a function of shear rate of ex-situ prepared WBPUU and CNF containing inks

For in-situ prepared inks, significantly higher differences were observed depending on the content of cellulose used. The content of cellulose was adjusted with a reference cellulose, CNFr. 2CNFr$_{IN}$ showed very low viscosity values, which pointed to an excessive flow at rest of the material for a proper printing process, 3CNFr$_{IN}$, however, showed significantly higher viscosity. Considering the behavior shown by this 2 wt.% in-situ prepared ink, inks

containing 3 wt.% of reinforcement were prepared with different types of cellulose.

Differences on viscosity depending on the type of cellulose used can be observed in Figure 5.2. As happened in the case of ex-situ prepared inks, in-situ ink prepared with carboxylated cellulose showed higher viscosity than unmodified cellulose containing inks, once again suggesting more hydrogen bonds taking place.

Regarding the effect of the incorporation routes, it can be observed that, in general, in-situ prepared inks showed lower viscosity values. Though the carboxylation of CNF allowed the formation of more interactions with the matrix, it also could result into a repulsion effect between the particles, caused by the presence of COO^- groups in both entities. This repulsive force, in turns, could have impeded the physical approach of the WBPUU particles and the CNF, hindering the formation of interactions [15].

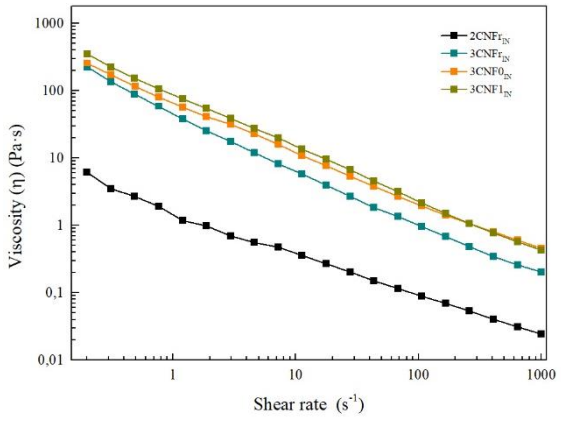

Figure 5.2. Viscosity as a function of shear rate of in-situ prepared WBPUU and CNF containing inks

For in-situ preparations, the strong agitation during the phase inversion step supplied enough energy to force both components together and allowed the hydrogen bonds taking place. Moreover, the in-situ addition of cellulose, containing high amounts of OH and COOH groups, may have allowed the

chemical bonding of the components during the synthesis process. On the other hand, in ex-situ method, the polyurethanes particles, already in a more stable state, were less likely to interact. The fewer interactions formed between the matrix and the reinforcement allowed for the interactions between the CNF and the water taking place, which in turns resulted into a better gel formation.

The dependence of the storage and loss moduli on the shear stress were analyzed in spectromechanical analysis. The obtained curves (Figure 5.3 for ex-situ and Figure 5.4 for in-situ prepared inks) were used to determine the yield point, as proposed by Cyriac et al. [16], as well as the flow point, as the crossover point for G' and G", of the materials (Table 5.4).

Table 5.4. Yield and flow point values for ex-situ and in-situ prepared WBPUU and CNF containing inks

	Sample	Yield point (Pa)	Flow point (Pa)
ex-situ	$2CNF0_{EX}$	16.5	89.4
	$3CNF0_{EX}$	23.6	140.0
	$2CNF1_{EX}$	15.3	59.2
	$3CNF1_{EX}$	26.6	225.6
in-situ	$2CNFr_{IN}$	-	-
	$3CNFr_{IN}$	14.5	40.1
	$3CNF0_{IN}$	14.7	61.6
	$3CNF1_{IN}$	16.5	105.1

As can be observed, nanocellulose containing inks showed a gel-like behavior at low shear stress values, with G' values being higher than G". Moreover, all systems showed relatively low yield points, signaling that all systems begin to flow at low shear stresses, which could be beneficial for the printability of the ink. Ex-situ prepared composites containing 3 wt.% of cellulose showed a slightly higher yield point, suggesting the higher amount of cellulose in the system resulted in a resistance to flow, agreeing with literature results [5,6,9].

Regarding the flow point, for ex-situ prepared inks it can be observed that it was directly related to the content and type of cellulose used. Being it higher

for inks with higher contents of CNF, as well as for systems with carboxylated CNF at the highest content. The higher amount of cellulose and of interactions in these systems were able to maintain a more stable network at higher shear stress.

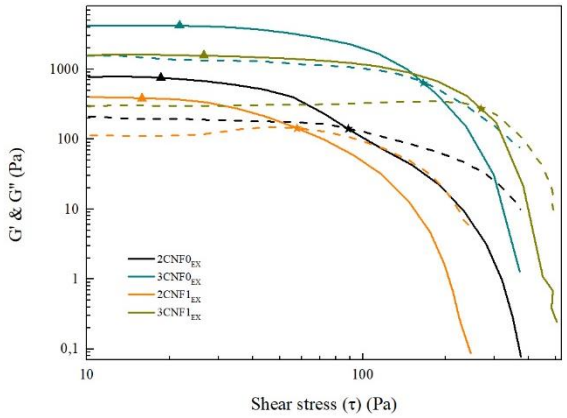

Figure 5.3. Storage (solid line) and loss (dotted line) moduli as a function of shear stress and (▲) yield and (★) flow points of ex-situ prepared CNF containing inks

For in-situ prepared inks, similar yield points were observed, regardless the type of CNF used. However, when analyzing the flow point, it can be observed that for CNFs with higher carboxylation degree higher flow point values were measured. The more possible interactions granted the systems with higher stability, resulting in systems able to maintain a gel-like structure at higher shear stress. $2CNFr_{IN}$ did not show a gel like behavior, as seen by its G'' values being higher than G' throughout the stress sweep. In this case, the amount of cellulose was not enough to form a gel-like structure by this method. Because of the non-gel-like behavior and low viscosity shown by $2CNFr_{IN}$, this system was discarded since it does not fulfill the requirements to be used in DIW 3D printing.

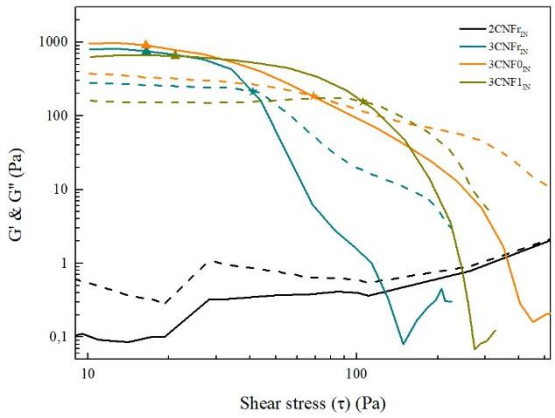

Figure 5.4. Storage (solid line) and loss moduli (dotted line) as a function of shear stress and (◢) yield and (★) flow points of in-situ prepared CNF containing inks

Regarding the effect of the CNF incorporation route, it can be observed that less gelled structures were formed when nanocellulose was added by in-situ method, since yield and flow points of in-situ prepared inks show lower values than their ex-situ homologues. This fact suggests that the higher amount of interactions taking place between CNF and water in ex-situ systems resulted in stronger gel structures, which is in agreement with viscosity test results.

The low yield points shown by all inks, i.e. their ability to flow at low stresses may be beneficial to a satisfactory extrusion process [17–19].

Last, in order to simulate how the inks will behave after printing process, structure recovery tests were performed in a three step test, where the viscosity of the systems at a shear rate of 0.2 s^{-1}, 100 s^{-1} and, again, 0.2 s^{-1} was studied. Obtained results are summarized in Table 5.5. and shown in Figure 5.5 and 5.6 for ex-situ and in-situ prepared inks. Ideally, inks for DIW should show low viscosity when subjected to a shear force, but will quickly recover high viscosity when this force is removed [2].

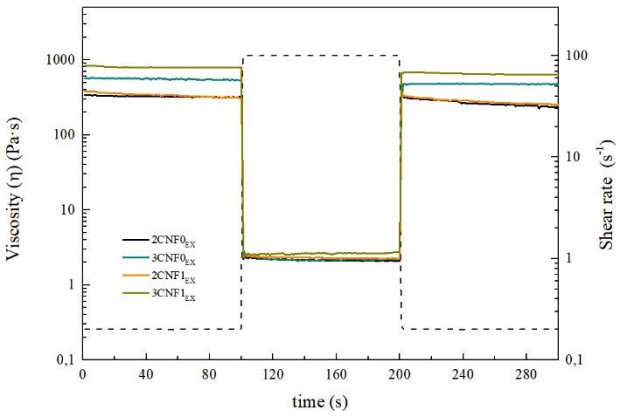

Figure 5.5. Structure recovery tests of ex-situ prepared CNF containing inks

For ex-situ composites, a good recovery capacity was observed for all systems, with values around 80%, which suggested a good shape fidelity after printing process [20]. No notable differences were observed for these system regarding the amount nor the type of cellulose used.

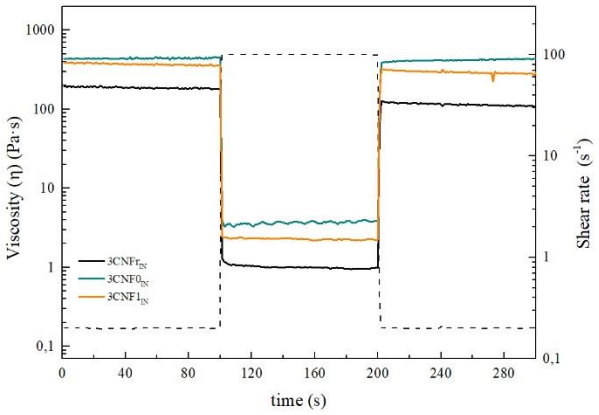

Figure 5.6. Structure recovery tests of in-situ prepared CNF containing inks

In the case of in-situ prepared composites, lower recovery values were observed. In this case, the interactions present suffered more damaged during the high shear rate studied step, and were not able to recover as quick as in the case of ex-situ prepared inks. The lower recovery capacity observed for these systems may later result in lower shape fidelity of the printed parts, due to a

higher likelihood to flow suggested by the lower viscosity they show after being under high shear rates.

Table 5.5. Structure recovery capacity of ex-situ and in-situ prepared WBPUU and CNF containing inks

	Sample	Structural recovery (%)
ex-situ	$2CNF0_{EX}$	78 ± 4
	$3CNF0_{EX}$	80 ± 9
	$2CNF1_{EX}$	75 ± 9
	$3CNF1_{EX}$	79 ± 3
in-situ	$3CNFr_{IN}$	62 ± 2
	$3CNF0_{IN}$	67 ± 7
	$3CNF1_{IN}$	72 ± 9

5.3. DIW 3D printing of WBPUU/CNF inks

The prepared CNF containing inks were used in DIW 3D printing, using an adapted Tumaker Voladora printer and working with a Simplify3D software. Printing process was carried out at room temperature, at a printing speed of 6 $mm \cdot s^{-1}$, using a needle with 0.8 mm internal diameter. The material was printed on a Teflon surface. Obtained printed parts were right away frozen in order to freeze-dry them. As printing design, a cylinder was chosen, with a diameter of 10 mm and a height of 5 mm (Figure 5.7). Printed parts were named as "3D-X", where "X" is the name of their corresponding inks.

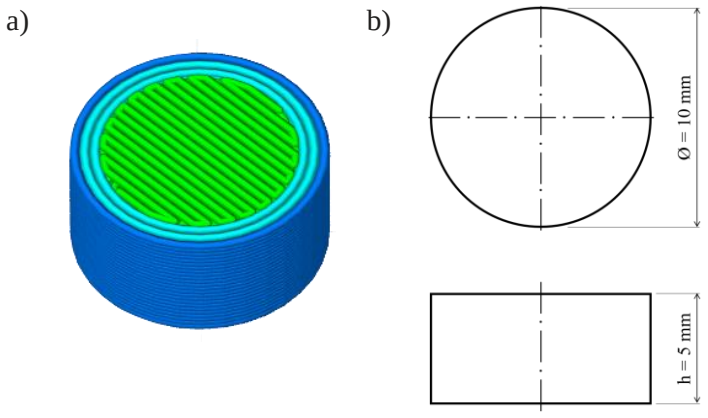

Figure 5.7. a) 3D model of imported cylinder design and b) dimensions (in mm)

Figure 5.8 and 5.9 show pictures of the printed cylinders from the different inks. As can be observed, the differences in rheology translated in different printing precision. For ex-situ prepared inks, inks containing higher amount of cellulose resulted in printed parts with better shape fidelity. The low viscosity of $2CNF0_{EX}$ ink did not allow the material to retain the shape it was printed on. The ink $3CNF1_{EX}$, due to the good rheological behavior it presented, showed the best shape fidelity and was able to support layers upon layers without flowing or being crushed. Overall, the shear-thinning behavior and low flow stress of the inks allowed for a continuous extrusion.

For ex-situ based 3D printed parts, occasionally the nozzle would get obstructed, indicating the presence of CNF agglomerations caused by less homogenous dispersion by ex-situ method.

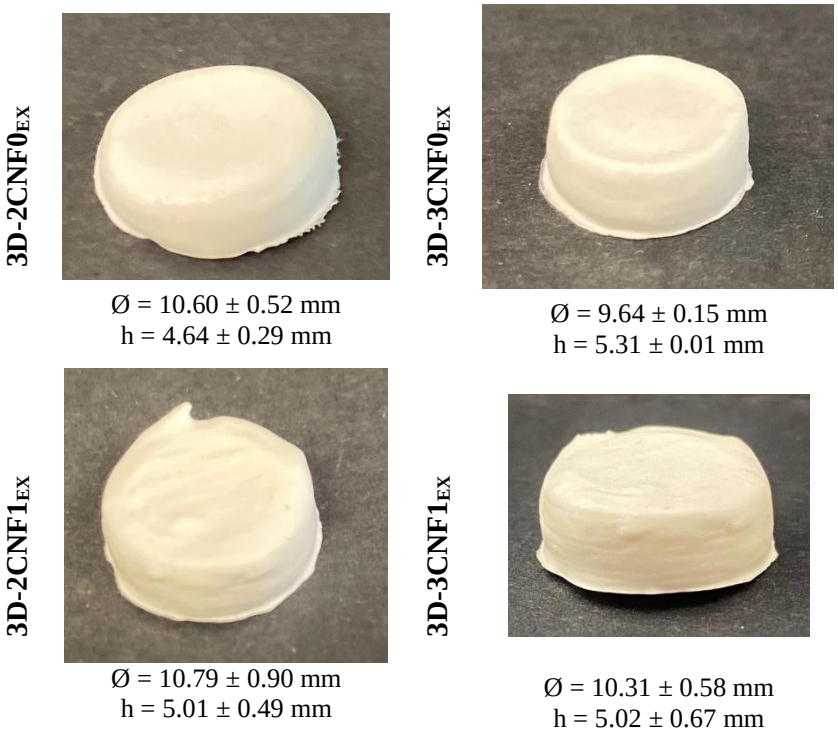

Figure 5.8. Photographs of 3D printed cylinders from ex-situ prepared CNF containing inks

For in-situ prepared inks, it was observed that their lower viscosity and, thus, higher tendency to flow resulted in a lower shape fidelity when compared with ex-situ inks. The effect of viscosity was clearly seen in the final printed parts, with the material with the lowest viscosity, $3CNFr_{IN}$, showing the worst shape fidelity and the ink with the higher viscosity values, $3CNF1_{IN}$, showing the better shape fidelity.

Moreover, it is worth noting that the low yield point shown by all inks allowed the good flow and, therefore, the printing of the materials.

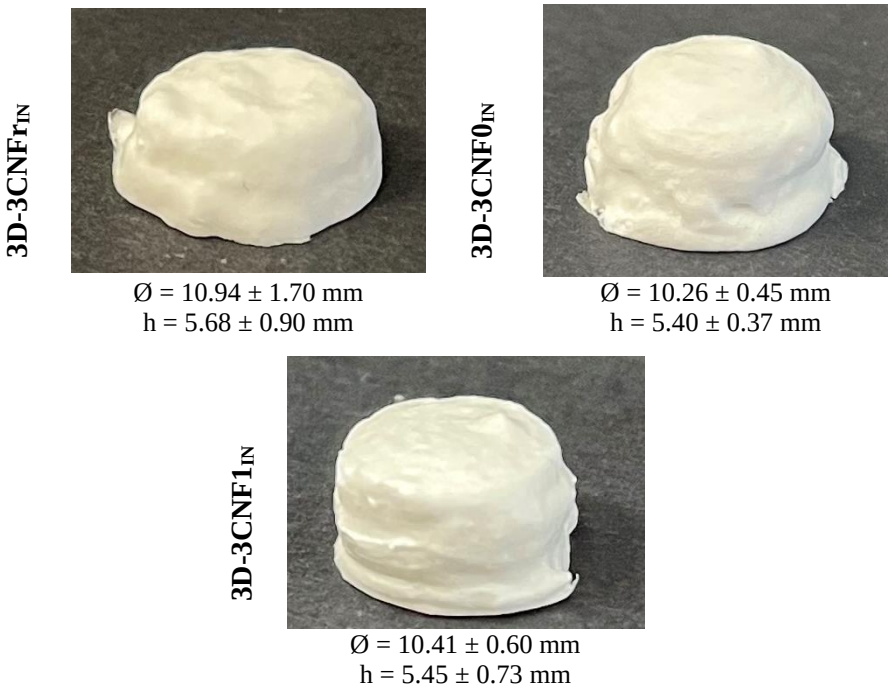

Figure 5.9. Photographs of 3D printed cylinders from in-situ prepared CNF containing inks

5.3.1. Characterization of 3D printed pieces

FTIR spectroscopy analyses were carried out in order to study possible interactions taken place between the polyurethane matrix and the added cellulose nanofibers. As reference, some of WBPUU was freeze-dried and

analyzed as well. Resulted spectra for 3D printed parts from ex-situ and in-situ inks and freeze-dried WBPUU are shown in Figure 5.10 and 5.11.

As it can be observed, all systems showed a similar spectrum, constituted by the characteristic bands of polyurethane seen in the previous chapters.

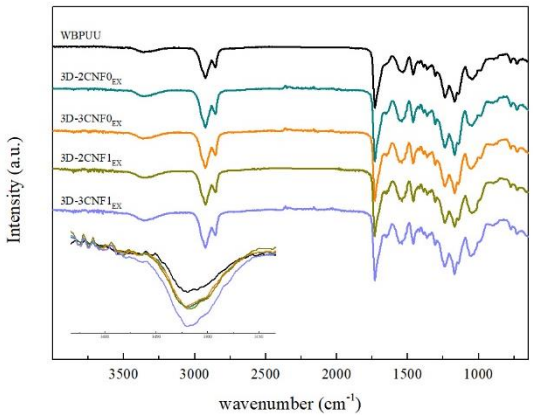

Figure 5.10. FTIR spectra of 3D printed parts from ex-situ prepared CNF containing inks

The main difference between spectra took place in the 3600-3100 cm^{-1} range (insets in Figure 5.10 and 5.11). In this range, bands corresponding to N-H and O-H are found. For ex-situ parts, an increase in the intensity of the N-H band was observed, which could be due to the overlapping of the N-H and O-H bands.

When studying in-situ parts, a similar behavior is observed, with the major difference being in the N-H band. In this case, printed part containing the reference cellulose did not show a significant increase in intensity. For CNF0 and CNF1 reinforced composites, once again the increase of intensity of this band was observed.

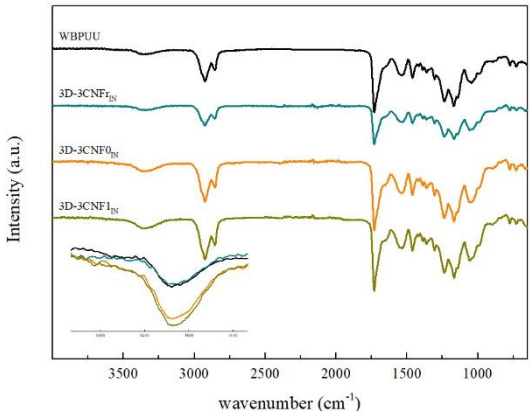

Figure 5.11. FTIR spectra of 3D printed parts from in-situ prepared CNF containing inks

The morphology of the printed parts was studied by SEM micrographies at different magnifications of a cryofractured cross section. The obtained images are shown in Figure 5.12 and 5.13 for parts obtained from ex-situ and in-situ inks, respectively.

Regarding 3D printed parts from ex-situ preparations, it can be observed that all systems showed a similar morphology, composed by spherical pores. Systems showed a homogeneous morphology, with evenly distributed pores. Pore diameters were measured and averaged out of 50 measurements. Pore diameters of 54.7 ± 10.7, 54.1 ± 9.1, 45.0 ± 9.8 and 47.9 ± 6.1 μm were measured for 3D-2CNF0$_{EX}$, 3D-3CNF0$_{EX}$, 3D-2CNF1$_{EX}$ and 3D-3CNF1$_{EX}$, respectively. Results suggest that the pore size was not influenced by the nanocellulose content of the ink. However, the printed pieces with carboxylated nanocellulose, CNF1, showed lower pore size than their CNF0 counterparts. This smaller pore size could be attributed to the higher amount of interactions, that increased the viscosity, as well as the interaction degree, that took place when carboxylated cellulose nanofibers were used instead of unmodified ones. This higher amount of interactions resulted in smaller porous, as also seem for chemical crosslinking [21].

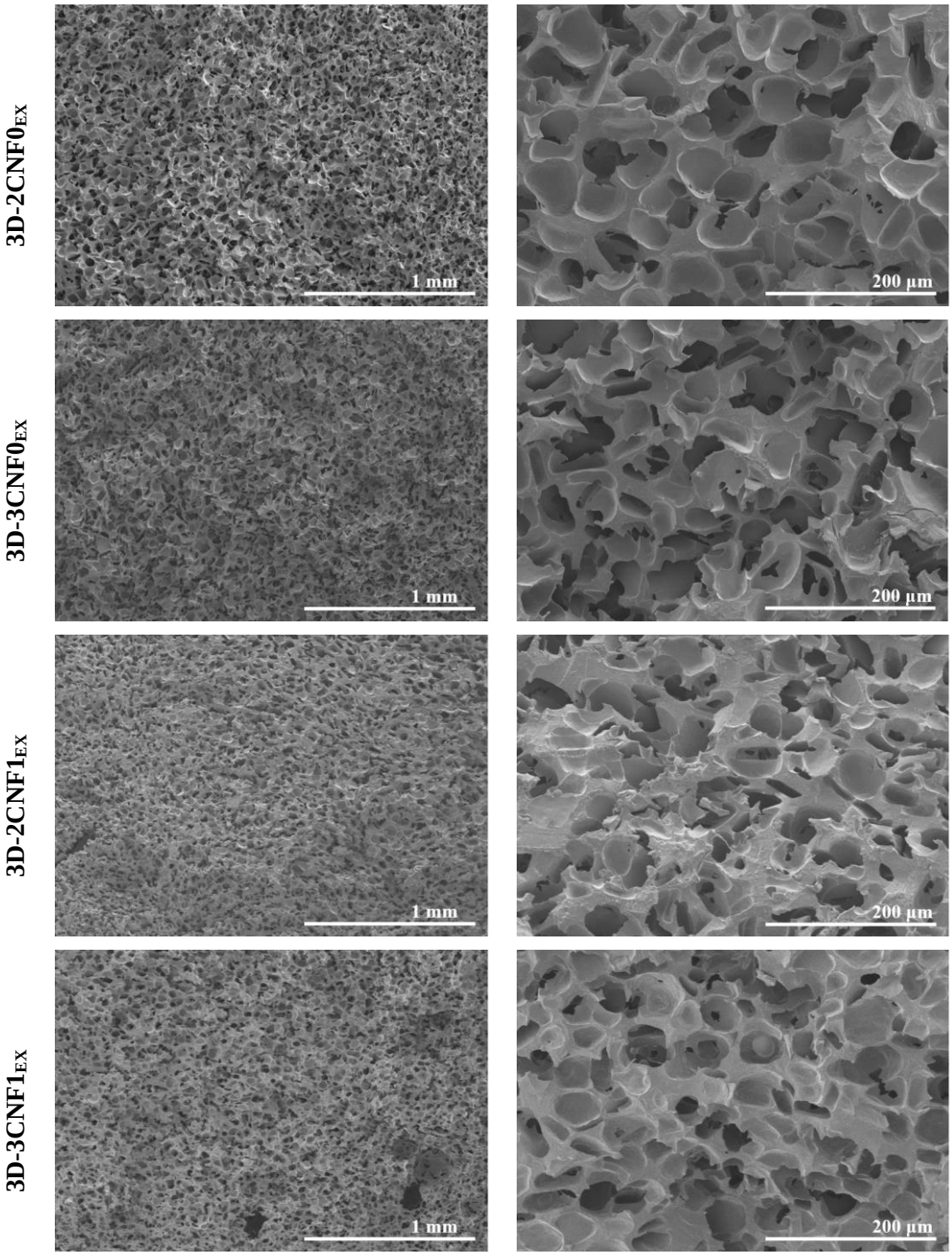

Figure 5.12. SEM images of 3D printed parts from ex-situ prepared CNF containing inks

Moreover, the high homogeneity and spherical pore morphology shown by ex-situ prepared systems was a result of the high viscosity shown by their corresponding inks being able to support the weight of the upper layers [9].

For 3D parts obtained from in-situ prepared inks, however, a very different morphology was observed (Figure 5.13). In these systems, more heterogeneous structures were found. A pore-dominated structure was still present, but these pores no longer showed a spherical shape, instead elongated pores were observed. The lower viscosities shown by in-situ inks were not able to support the weight of the layers on top and collapsed [9,18,22]. As a result, crushed cell walls can be observed when analyzing the morphology (circled in red). This effect was directly related to the viscosity shown by their corresponding inks, with $3CNFr_{IN}$ showing the lower viscosity and 3D-$3CNFr_{IN}$ showing the more collapsed structures.

On the other hand, the higher viscosity shown by $3CNF1_{IN}$ was reflected in a more homogeneous structure and the recovery of spherical pores. 3D-$3CNFr_{IN}$ showed elongated pores with a height of 54.5 ± 15.6 µm and a length of 322.1 ± 38.2 µm. For 3D-$3CNF1_{IN}$ spherical pores with an average diameter of 36.3 ± 11.1 µm were observed.

However, for 3D-$3CNF0_{IN}$ both types of pores can be observed, being the spherical pores (Ø = 46.8 ± 15.0) the predominant shape of the top layers and the elongated pores (h = 43.5 ± 9.9 and l = 247.8 ±52.2) the most present on the bottom layers. Though, $3CNF0_{IN}$ did not present sound enough rheological properties to support upper layers, it also did not flow as easily as $3CNFr_{IN}$. Therefore, for this system, crushed structures were obtained in the bottom zone of the structure, since it was not capable of supporting the weight of the upper layers, but top layer, without that added weight, were able to maintain a steady structure.

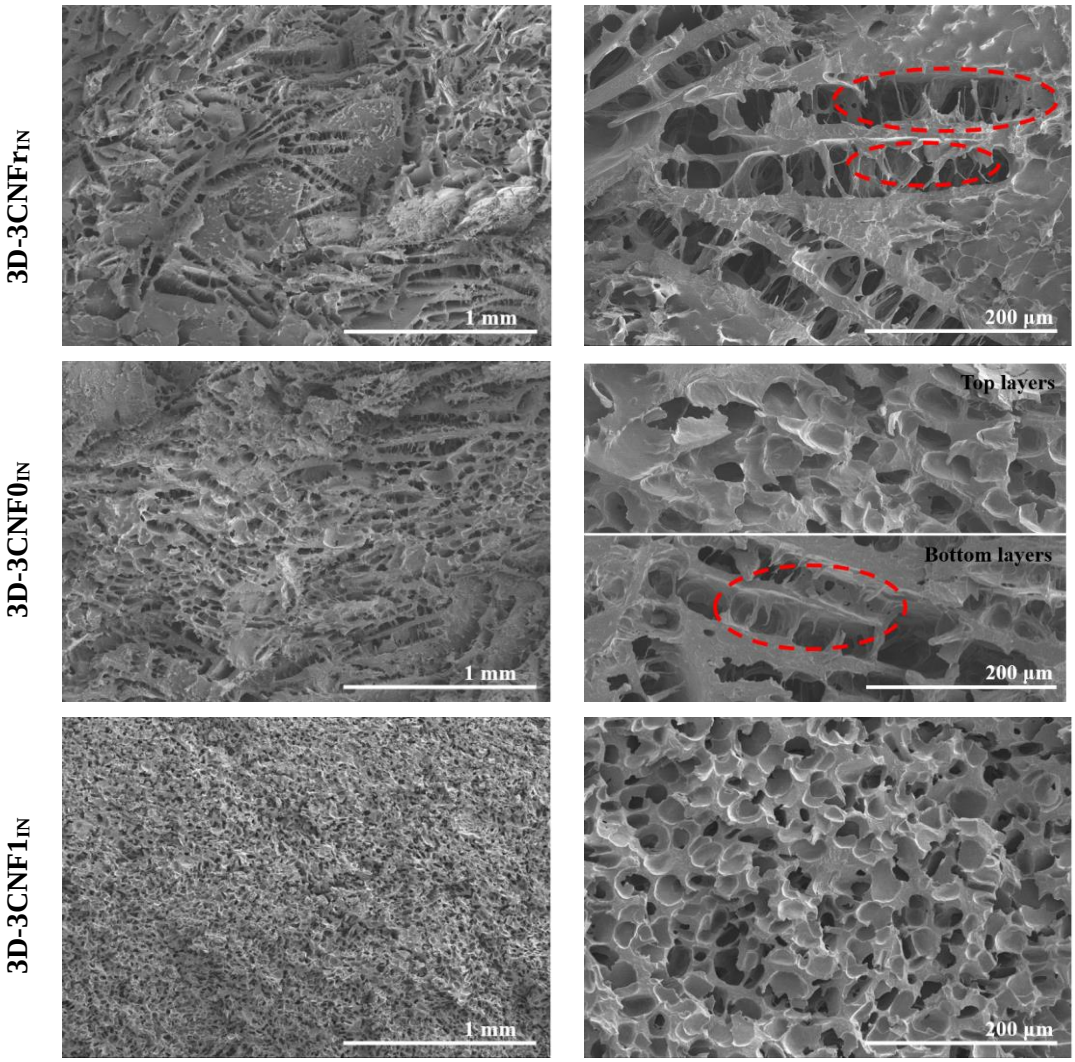

Figure 5.13. SEM images of 3D printed parts from in-situ prepared CNF containing inks

The thermal transitions of the 3D printed parts were studied by DSC. The thermograms for 3D parts obtained from ex-situ and in-situ inks are shown in Figure 5.14 and 5.15, respectively and the measured values are summarized in Table 5.6.

No significant changes can be observed regarding the glass transition temperature of the soft segment, which all systems showing a T_g value around

-50 ºC. However, some changes are observed it the DSC curves when studying the short range ordering transition of the materials. The addition of cellulose to the systems resulted in an increase of the enthalpy of the endothermic peak related to this transition, which is in agreement with the data reported in Chapter 4 for nanocomposite films.

For 3D parts obtained from ex-situ prepared inks, it can be observed that increasing the nanocellulose content and the use of carboxylated nanofibers increased the enthalpy values of the material. This fact suggest, once again, the formation of hydrogen bonding between the PU and the CNF and, therefore, a more difficult breaking process of the short range ordered structures, which is in agreement with other studies based on cellulose-reinforced polyurethanes [23,24].

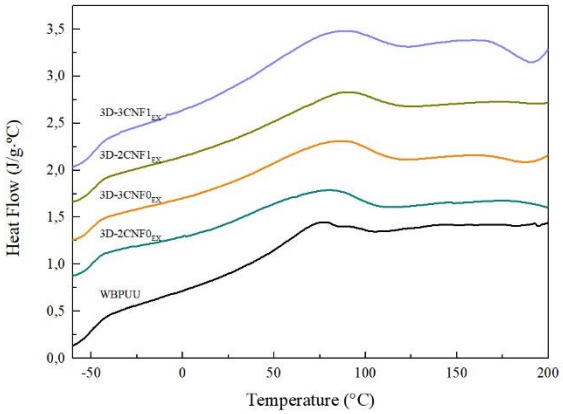

Figure 5.14. DSC scans for 3D parts obtained from ex-situ prepared CNF containing inks

For 3D parts from in-situ preparations, the same behavior is observed regarding enthalpy values. It can be observed that composites reinforced with CNF isolated in the current work, CNF0 and CNF1, showed higher values than those containing the commercial nanocellulose. The carboxylation of CNF1 resulted in a better affinity with the polyurethane and, in consequence, in a higher

amount of fiber/polymer interactions than in systems with commercial nanocellulose.

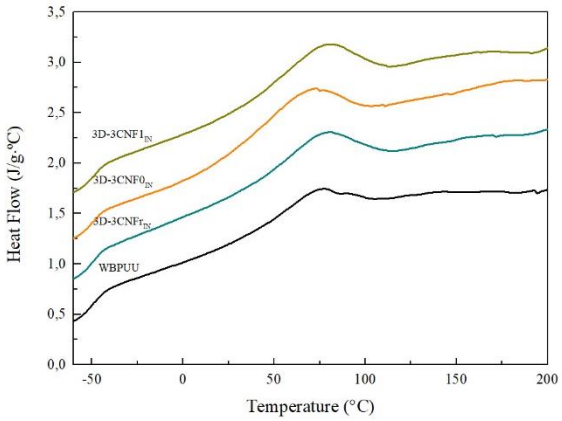

Figure 5.15. DSC scans for 3D parts obtained from ex-situ prepared CNF containing inks

Table 5.6. Thermal properties observed from the DSC curves for 3D printed parts containing CNF

	Sample	T_g (ºC)	T_{HS} (ºC)	ΔH_{HS} (J·g^{-1})
ex-situ	WBPUU	-49.1	74.7	9.0
	3D-2CNF0$_{EX}$	-49.7	78.0	12.4
	3D-3CNF0$_{EX}$	-49.0	82.0	15.5
	3D-2CNF1$_{EX}$	-47.7	86.5	13.9
	3D-3CNF1$_{EX}$	-48.3	81.9	16.0
in-situ	3D-3CNFr$_{IN}$	-50.1	77.7	15.1
	3D-3CNF0$_{IN}$	-50.4	78.7	16.9
	3D-3CNF1$_{IN}$	-48.4	78.0	17.6

The degradation thermograms of the printed parts and their first derivative curves are shown in Figure 5.16 and 5.17 for 3D parts printed from ex-situ and in-situ preparations, respectively.

As happened for composites films, the addition of cellulose resulted in an increase of the thermal stability of the materials. For ex-situ inks based 3D

parts, the onset degradation temperature was delayed, at least, 20 ºC in respect to the neat polyurethane system. The higher stability in nanocomposites was attributed to the stabilization of the urethane and urea groups thanks to the formation of hydrogen bonds with the cellulose [25,26].

As can be observed, this effect is more intense for composites prepared with CNF0, due to the higher stability shown by this type of cellulose nanofibers because of the higher thermal stability of unmodified nanocellulose than carboxylated ones (Chapter 3).

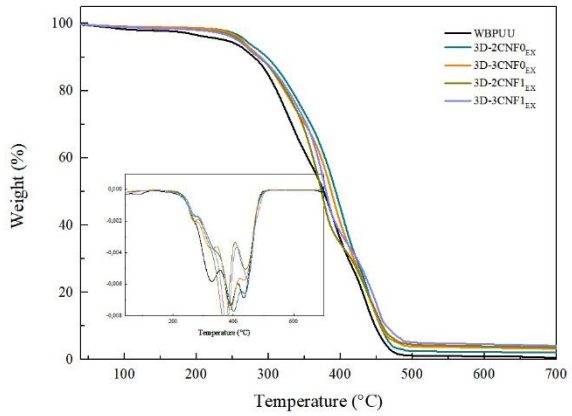

Figure 5.16. TGA and DTG curves for 3D parts obtained from ex-situ prepared CNF containing inks

When studying the stability of the parts printed from in-situ prepared inks, it can be observed that the delay on degradation temperature also took place for these materials. Once again, the effect was more pronounced for unmodified CNF containing composites.

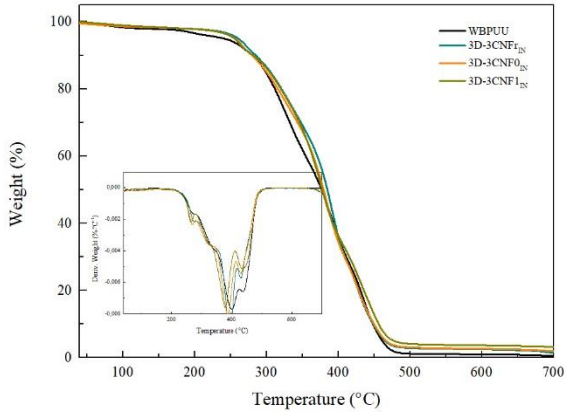

Figure 5.17. TGA and DTG curves for 3D parts obtained from in-situ prepared CNF containing inks

In order to study the mechanical behavior of the printed parts, compression tests were carried out. Obtained results are summarized on Table 5.7, where Young modulus, density, specific Young modulus (determined as explained in Chapter 2), stress and densification strain values are shown. Figure 5.18 shows stress/strain curves of 3D printed parts obtained from ex-situ and in-situ prepared CNF containing inks.

Table 5.7. Young modulus, specific Young modulus, stress at 60% strain and densification strain values for WBPU/CNF 3D printed parts

	Sample	Young modulus (MPa)	Density ($g \cdot cm^{-3}$)	Specific Young modulus ($MPa \cdot cm^3 \cdot g^{-1}$)	Stress at 60% strain (MPa)	Densification strain (MPa)
ex-situ	3D-2CNF0$_{EX}$	12.3 ± 3.8	0.36 ± 0.02	35.0 ± 6.0	2.8 ± 0.8	50.3 ± 0.3
	3D-3CNF0$_{EX}$	11.2 ± 1.4	0.36 ± 0.05	31.3 ± 3.1	2.1 ± 0.1	50.6 ± 0.5
	3D-2CNF1$_{EX}$	13.5 ± 3.5	0.34± 0.03	39.1 ± 8.1	2.5 ± 0.3	51.1 ± 0.5
	3D-3CNF1$_{EX}$	14.3 ± 2.3	0.35 ± 0.04	41.5 ± 4.0	2.5 ± 0.3	51.6 ± 0.6
in-situ	3D-3CNFr$_{IN}$	14.2 ±1.8	0.33 ± 0.02	42.5 ± 1.0	2.4 ± 0.3	51.3 ± 0.9
	3D-3CNF0$_{IN}$	21.0 ± 6.0	0.37 ± 0.02	56.8 ± 11.0	3.4 ±0.5	51.4 ±0.6
	3D-3CNF1$_{IN}$	22.0 ± 5.2	0.35 ± 0.02	59.5 ± 14.9	3.3 ± 0.6	52.0 ± 1.6

As can be observed in Figure 5.18, all printed parts show three different sections in stress vs. strain curves. The first zone is the elastic region, where the walls of the pores begin to bend but are still able to recover when the load is removed; following, at higher loads, a plateau-like step is observed in the plastic zone, where the walls start to buckle and the porous structure starts collapsing; finally, on the last zone, the densification step takes place, where the walls are crushed and the materials behaves like a non-porous material [23,24]. As can be observed in Table 5.7, only specimens reinforced with nanocellulose isolated in the current work and incorporated to the system by the in-situ method showed improvements in the values of modulus and the stress at 60% of strain. For unmodified CNF, it can be observed that after the addition of 3wt.% of nanocellulose by ex-situ method, the values of modulus and the stress at 60% of strain began to decrease. The worse miscibility of unmodified fibers with polyurethane than carboxylated fiber ones may have resulted in the sooner formation of fiber agglomerations [27].

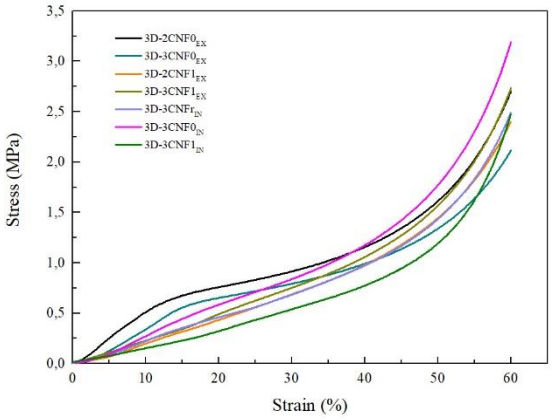

Figure 5.18. Stress/Strain curves from compression tests for WBPU/CNF 3D printed parts

When analyzing parts printed from in-situ prepared inks, reference commercial cellulose (CNFr) containing materials showed lower values than systems reinforced with nanocellulose isolated in the current work. Probably, the poor

reinforcement effect supplied by commercial cellulose could be ascribed to the low amount of fiber/matrix interactions taking place in this material, which resulted in a poor stress transfer from the matrix to the nanoreinforcements.

In-situ method resulted in materials with more enhanced mechanical properties than ex-situ counterparts. The formation of more interactions, both physical and chemical, during the synthesis process resulted in more reinforced materials.

5.4. Conclusions

In this chapters WBPUU/CNF inks were prepared for their use in direct ink writing. In order to modulate the inks rheology, nanocellulose was added to the WBPUU in different contents and by two different incorporation routes, ex-situ and in-situ. Different rheological tests were performed to predict the printability of the inks by DIW 3D printing. By rheological measurements, the capacity of the inks to flow, as well as the capacity to recover material internal structure, was studied. All inks showed shear thinning behavior, necessary for a proper printing process. In-situ prepared inks showed lower viscosity values than their ex-situ counterparts. This fact was attributed to the more direct interactions created between the polymer matrix and the reinforcement and lower nanocellulose/water interactions, compared to ex-situ systems. Spectromechanical tests showed gel-like behavior for most inks, except 2CNFr, with defined yield points, which suggest good printability and shape fidelity. Furthermore, inks exhibited good thixotropic and structural recovery properties.

Inks were used in DIW to produce 3D printed parts, which were later characterized. Ex-situ prepared inks showed better shape fidelity, due to higher viscosity values. SEM images showed a homogeneous porous morphology that showed the ability of the materials to support upper layers. For in-situ preparations, the morphology analyses showed crushed wall due to the weight of the upper layers, except for 3D printed parts obtained from $3CNF1_{IN}$, which

better rheological behavior allow for a successful 3D printing. The formation of interactions between the WBPUU and the CNF was promoted by in-situ incorporation method, seen in DSC and FTIR analyses, which also translates in 3D printed parts with enhanced mechanical properties.

5.5. References

[1] Calafel I, Aguirresarobe RH, Peñas MI, Santamaria A, Tierno M, Conde JI, et al. Searching for rheological conditions for FFF 3D printing with PVC based flexible compounds. Materials 2020;13:178. doi:10.3390/ma13010178.

[2] Li H, Liu S, Li L. Rheological study on 3D printability of alginate hydrogel and effect of graphene oxide. Int J Bioprinting 2016;2:54–66. doi:10.18063/IJB.2016.02.007.

[3] Costakis WJ, Rueschhoff LM, Diaz-Cano AI, Youngblood JP, Trice RW. Additive manufacturing of boron carbide via continuous filament direct ink writing of aqueous ceramic suspensions. J Eur Ceram Soc 2016;36:3249–56. doi:10.1016/j.jeurceramsoc.2016.06.002.

[4] Lewis JA, Smay JE, Stuecker J, Cesarano J. Direct ink writing of three-dimensional ceramic structures. J Am Ceram Soc 2006;89:3599–609. doi:10.1111/j.1551-2916.2006.01382.x.

[5] Jiang J, Oguzlu H, Jiang F. 3D printing of lightweight, super-strong yet flexible all-cellulose structure. Chem Eng J 2021;405:126668. doi:10.1016/j.cej.2020.126668.

[6] Ma T, Lv L, Ouyang C, Hu X, Liao X, Song Y, et al. Rheological behavior and particle alignment of cellulose nanocrystal and its composite hydrogels during 3D printing. Carbohydr Polym 2021;253:117217. doi:10.1016/j.carbpol.2020.117217.

[7] Hoeng F, Denneulin A, Bras J. Use of nanocellulose in printed

electronics: A review. Nanoscale 2016;8:13131–54. doi:10.1039/c6nr03054h.

[8] Rastin H, Ormsby RT, Atkins GJ, Losic D. 3D bioprinting of methylcellulose/gelatin-methacryloyl (MC/GelMA) bioink with high shape integrity. ACS Appl Bio Mater 2020;3:1815–26. doi:10.1021/acsabm.0c00169.

[9] Vadillo J, Larraza I, Calvo-Correas T, Gabilondo N, Derail C, Eceiza A. Role of in situ added cellulose nanocrystals as rheological modulator of novel waterborne polyurethane urea for 3D-printing technology. Cellulose 2021;28:4729–44. doi:10.1007/s10570-021-03826-6.

[10] Sahlin K, Forsgren L, Moberg T, Bernin D, Rigdahl M, Westman G. Surface treatment of cellulose nanocrystals (CNC): effects on dispersion rheology. Cellulose 2018;25:331–45. doi:10.1007/s10570-017-1582-5.

[11] Karppinen A, Vesterinen AH, Saarinen T, Pietikäinen P, Seppälä J. Effect of cationic polymethacrylates on the rheology and flocculation of microfibrillated cellulose. Cellulose 2011;18:1381–90. doi:10.1007/s10570-011-9597-9.

[12] Pääkko M, Ankerfors M, Kosonen H, Nykänen A, Ahola S, Österberg M, et al. Enzymatic hydrolysis combined with mechanical shearing and high-pressure homogenization for nanoscale cellulose fibrils and strong gels. Biomacromolecules 2007;8:1934–41. doi:10.1021/bm061215p.

[13] Moberg T, Sahlin K, Yao K, Geng S, Westman G, Zhou Q, et al. Rheological properties of nanocellulose suspensions: effects of fibril/particle dimensions and surface characteristics. Cellulose 2017;24:2499–510. doi:10.1007/s10570-017-1283-0.

[14] Kayra N, Aytekin AÖ. Synthesis of cellulose-based hydrogels: preparation, formation, mixture, and modification, 2018, p. 1–28. doi:10.1007/978-3-319-76573-0_16-1.

[15] Chen R-D, Huang C-F, Hsu S. Composites of waterborne polyurethane and cellulose nanofibers for 3D printing and bioapplications. Carbohydr Polym 2019;212:75–88. doi:10.1016/j.carbpol.2019.02.025.

[16] Cyriac F, Lugt PM, Bosman R. On a new method to determine the yield stress in lubricating grease. Tribol Trans 2015;58:1021–30. doi:10.1080/10402004.2015.1035414.

[17] Hausmann MK, Siqueira G, Libanori R, Kokkinis D, Neels A, Zimmermann T, et al. Complex-shaped cellulose composites made by wet densification of 3D printed scaffolds. Adv Funct Mater 2020;30:1904127. doi:10.1002/adfm.201904127.

[18] Siqueira G, Kokkinis D, Libanori R, Hausmann MK, Gladman AS, Neels A, et al. Cellulose nanocrystal inks for 3D printing of textured cellular architectures. Adv Funct Mater 2017;27:1604619. doi:10.1002/adfm.201604619.

[19] Vadillo J, Larraza I, Calvo-Correas T, Gabilondo N, Derail C, Eceiza A. Design of a waterborne polyurethane–urea ink for direct ink writing 3D printing. Materials 2021;14:3287. doi:10.3390/ma14123287.

[20] Peak CW, Stein J, Gold KA, Gaharwar AK. Nanoengineered colloidal inks for 3D bioprinting. Langmuir 2018;34:917–25. doi:10.1021/acs.langmuir.7b02540.

[21] Dash R, Foston M, Ragauskas AJ. Improving the mechanical and thermal properties of gelatin hydrogels cross-linked by cellulose nanowhiskers. Carbohydr Polym 2013;91:638–45. doi:10.1016/j.carbpol.2012.08.080.

[22] Lim KS, Schon BS, Mekhileri N V., Brown GCJ, Chia CM, Prabakar S, et al. New visible-light photoinitiating system for improved print fidelity in gelatin-based bioinks. ACS Biomater Sci Eng 2016;2:1752–62. doi:10.1021/acsbiomaterials.6b00149.

[23] Ashby MF. The properties of foams and lattices. Philos Trans R Soc A Math Phys Eng Sci 2006;364:15–30. doi:10.1098/rsta.2005.1678.

[24] Ribeiro Da Silva V, Mosiewicki MA, Yoshida MI, Coelho Da Silva M, Stefani PM, Marcovich NE. Polyurethane foams based on modified tung oil and reinforced with rice husk ash I: Synthesis and physical chemical characterization. Polym Test 2013;32:438–45. doi:10.1016/j.polymertesting.2013.01.002.

[25] Santamaria-Echart A, Ugarte L, Arbelaiz A, Gabilondo N, Corcuera MA, Eceiza A. Two different incorporation routes of cellulose nanocrystals in waterborne polyurethane nanocomposites. Eur Polym J 2016;76:99–109. doi:10.1016/j.eurpolymj.2016.01.035.

[26] Cao X, Habibi Y, Lucia LA. One-pot polymerization, surface grafting, and processing of waterborne polyurethane-cellulose nanocrystal nanocomposites. J Mater Chem 2009;19:7137–45. doi:10.1039/b910517d.

[27] Žepič V, Poljanšek I, Oven P, Čop M. COST-FP1105: Properties of PLA films reinforced with unmodified and acetylated freeze dried nanofibrillated cellulose. Holzforschung 2016;70:1125–34. doi:10.1515/hf-2016-0096.

Chapter 6

WBPUU/CARBONACEOUS NANOSTRUCTURES NANOCOMPOSITE FILMS AND FILAMENTS FOR FDM 3D PRINTING

6. WBPUU/CARBONACEOUS NANOSTRUCTURES NANOCOMPOSITE FILMS AND FILAMENTS FOR FDM 3D PRINTING

6.1. Aim of the chapter

The aim of this chapter is to study the effect of the addition of carbonaceous reinforcements to a waterborne polyurethane matrix. For this study, different types of carbonaceous structures, namely graphene oxide and graphene, were used to prepare nanocomposites containing 1, 3 and 5 wt.% of nanoreinforcement. Nanocomposite films properties were studied regarding their morphology, physico-chemical, thermal and mechanical properties, biocompatibility and electrical conductivity. In order to further enhance electrical conductivity supplied by graphene to composites, the prepared films were coated using G and rGO and the final properties of these new systems were studied, regarding their morphology, electrical conductivity, mechanical and thermal properties and antimicrobial behavior.

Moreover, in order to study the potential of WBPUU nanocomposites reinforced with graphene for fused deposition modeling in 3D printing, filaments were prepared and characterized. For filaments preparation 3 wt.% content was chosen and two different incorporation routes were used, ex-situ and in-situ. Prepared filaments were analyzed by Fourier Transform Infrared spectroscopy, Differential Scanning Calorimetry, Thermogravimetric Analysis, Dynamic Mechanical Analysis and mechanical test. Filaments were later used in FDM and 3D printed parts were obtained. 3D parts were also analyzed and their morphology and thermal and mechanical properties were studied.

6.2. Preparation of WBPUU/G and WBPUU/GO nanocomposite films

WBPUU/graphene and WBPUU/graphene oxide nanocomposite films were prepared by solvent casting. For composite preparation prepared

carbonaceous aqueous dispersions were added to the WBPUU dispersion and were further sonicated 1 hour in an ultrasonic bath. Variating component contents, nanocomposites containing 1, 3 and 5 wt.% of GO or G (graphene dispersed in aqueous media with plant extract, G/E:2/1 (Chapter 3) and denoted from here on as GE) were prepared. Deionized water was added to the mixtures in order to adjust the final volume for all systems. Moreover, for comparison reasons, a WBPUU based film with only *Salvia* extract added was also prepared (WBPUU+E), in order to consider the effect of the addition of *Salvia*. In this case, the highest *Salvia* content used for the G containing films was used (2.5 wt.% of *Salvia*). Table 6.1 shows the amount of each component employed in the preparation on the films, nanocomposites with different compositions were named xGO or xGE, being x the content of reinforcement.

Solvent casting method was used for film preparation. The prepared mixtures were poured on 4x4 cm^2 Teflon molds and left to dry at room temperature for seven days, followed by three days under vacuum (400 mbar) to ensure complete water removal. Films with an approximate thickness of 0.4 mm were prepared.

Table 6.1. WBPUU, GO, G and E contents for composite preparation

Sample	WBPUU dispersion (g) (* solid content 33wt.%)	GO dispersion (g) (* solid content 0.5 wt.%)	G dispersion (g) (* solid content 0.5 wt.%)	*Salvia* Extract (mg)	Deionized water (g)	Total mass (g)
WBPUU	2.43	-	-	-	7.76	10.19
1GO	2.35	1.56	-	-	6.28	10.19
3GO	2.31	4.71	-	-	3.17	10.19
5GO	2.27	7.90	-	-	0.02	10.19
1GE	2.35	-	1.56	3.91	6.28	10.19
3GE	2.31	-	4.71	11.78	3.16	10.19
5GE	2.27	-	7.90	19.74	-	10.19
WBPUU+E	2.32	-	-	19.62	7.85	10.19

Figure 6.1 shows neat WBPUU, WBPUU+E and composite films reinforced with graphene oxide (GO) or with graphene stabilized with plant extracts (GE).

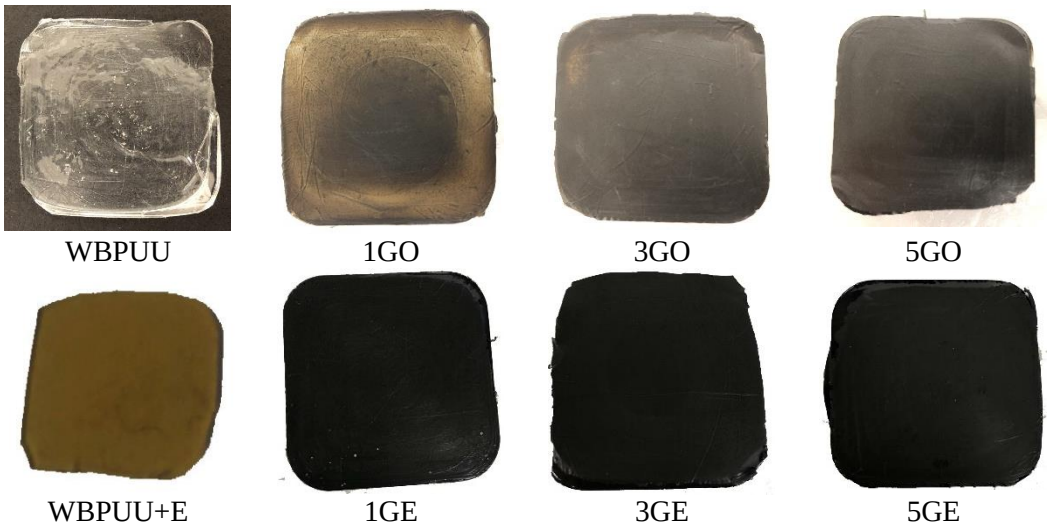

Figure 6.1. Photographs of the prepared neat WBPUU, WBPUU+E and GO and GE reinforced nanocomposites films

The addition of nanoreinforcements resulted in nanocomposites with extremely changed colors. GO containing films had a dark brown tonality, whereas GE containing composites showed a blackish color. The colors shown by the composites were in agreement with the colors of their present nanoreinforcements, being graphene oxide brownish and graphene blackish. In the case of WBPUU+E a green-brown tonality can be seen. Photographs suggest an even and homogeneous distribution of nanoreinforcements in polymer matrix.

6.2.1. Characterization of nanocomposites films

The morphology of cryofractured cross-sections of prepared films were characterized by SEM micrographies. For nanocomposite, films prepared with the highest reinforcement contents (5GO and 5GE) were selected (Figure 6.2).

The high rugosity caused during sample preparation process hindered the morphological study of the systems and difficulted the distinction of reinforcements in the composite. However, no significant reinforcement agglomerations were observed for composites with high GO and GE content.

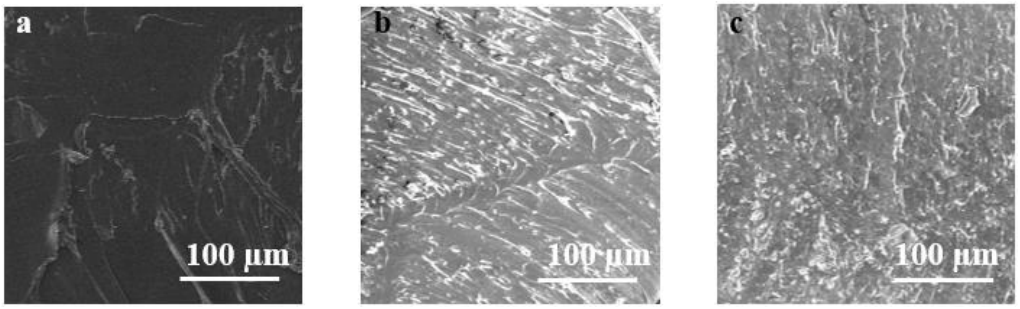

Figure 6.2. SEM images for cryofractured cross-sections of a) neat WBPUU, b) 5GO and c) 5GE

FTIR spectra of the neat WBPUU and the composites are shown in Figure 6.3. All systems showed the characteristic absorption bands of polyurethanes, a band at 3369 cm^{-1}, attributed to hydrogen-bonded N-H groups, a band at 1731 cm^{-1} assigned to the carbonyl vibration of the polyol and urethane groups, a band at 1645 cm^{-1} from the carbonyl group stretching vibration of urea group, a band at 1545 cm^{-1} assigned to the C-N stretching vibration and N-H bending of urethane and urea groups and bands between 1250 and 1000 cm^{-1} attributed to the C-O stretching vibrations [1-3].

After the addition of reinforcements, the most relevant difference was observed in the N-H band. For composites containing GO, this band shifted to lower wavenumbers, suggesting the formation of hydrogen bonds between matrix and GO [4]. For graphene containing nanocomposites, this band shifted also to lower wavenumber, indicating the formation of interactions between the matrix and reinforcement. Considering the lack of O-H or carboxylic groups in graphene, these interactions were likely to be formed

between the WBPUU and the plant extracts, as can be seen in the spectrum of WBPUU+E.

a)

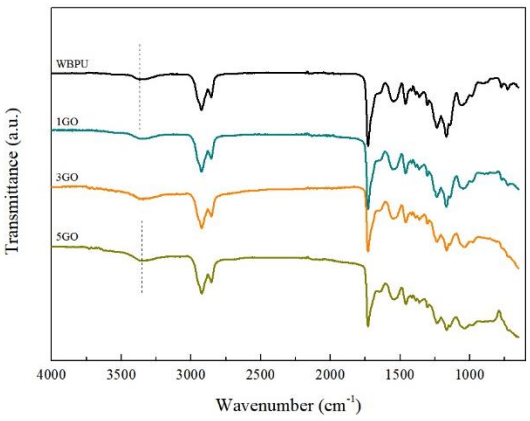

b)

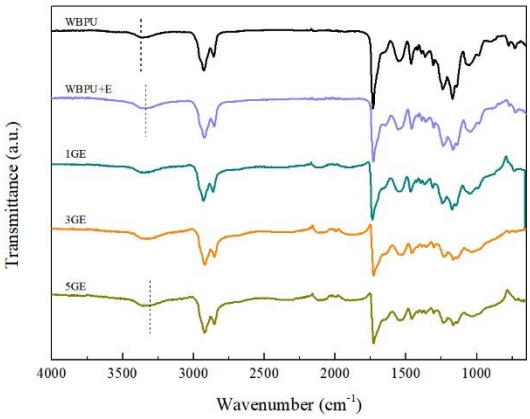

Figure 6.3. FTIR spectra of neat WBPUU and reinforced composites with different contents of a) GO and b) E and G

A schematic representation of the interactions suggested by FTIR analyses for WBPUU/GO and WBPUU/G composites is shown in Figure 6.4. For composites containing graphene oxide, the hydrogen bonds might have taken place between the N-H groups of the polyurethane and the functional groups on the surface of the GO structure. This was not possible for graphene, where there are no functional groups on its structure. The hydrogen bonds suggested

by FTIR are thought to have taken place between the WBPUU and the terpenoids, phenolic acids and diterpenes present on the *Salvia* extract [5].

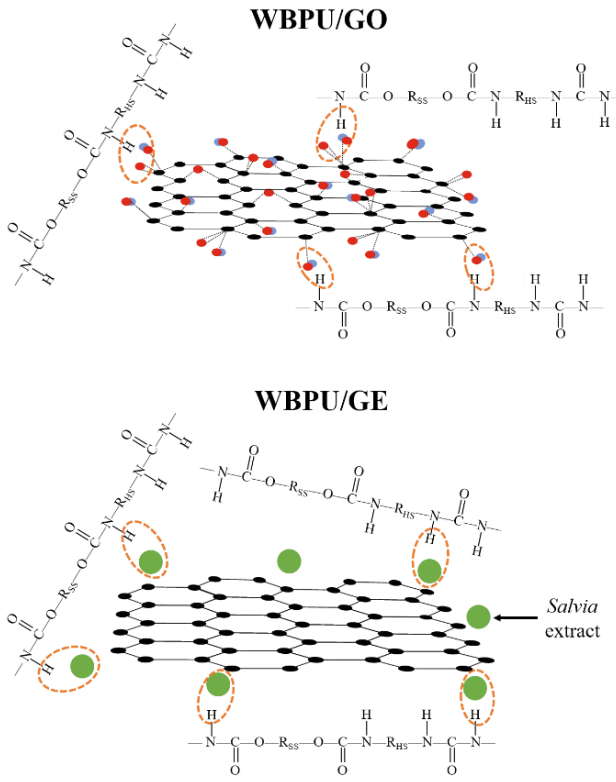

Figure 6.4. Schematic representation of interaction in WBPUU/G and WBPUU/GO composites

To measure transparency and UV absorption capability, films were analyzed and UV-vis, percent transmittance values of pure WBPUU and WBPUU/GO and WBPUU/G nanocomposites are shown in Figure 6.5.

The addition of reinforcement drastically reduced the transmittance. This decrease became more significant for composites containing higher contents of GO, reaching down to almost 0% for 3GO and 5GO. In the case of composites containing graphene in all cases values were proximate to 0%.

These extremely low values of transmittance indicated that the materials had the ability to act as UV light shields and can be used to protect against UV light.

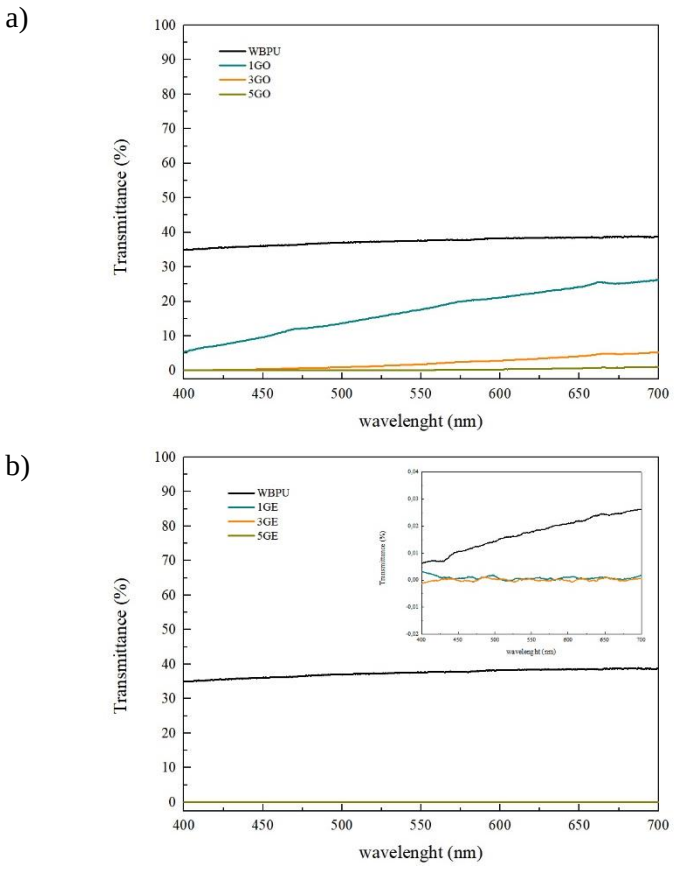

Figure 6.5. UV-vis curves of neat WBPUU and reinforced composites with different contents of a) GO and b) GE

DSC analyses were carried out to study thermal transitions of the composites reinforced with carbonaceous nanostructures (Figure 6.6 and Table 6.2).

GO and GE containing composites showed no significant changes in thermal transitions compared to the neat WBPUU. All systems showed a glass transition (T_g) of the soft segment at around -51 ºC and an endothermal peak related to a breaking of the short range ordered domains at 82 ºC. This peak

attributed to the short range ordered hard domains, formed because of the low crystallinity of the system formed by the non-linear hard segment. It can be observed that the addition of plant extract slightly increases the melting enthalpy and temperature, however, the addition of carbonaceous structures lowers these values. This suggests that the addition of G and GO disrupts the ordering of the hard segment. For composites containing GO, at higher temperatures a big exothermic peak can be seen, which can be related to the beginning of graphene oxide degradation, as seen in the TGA results (Chapter 3).

a)

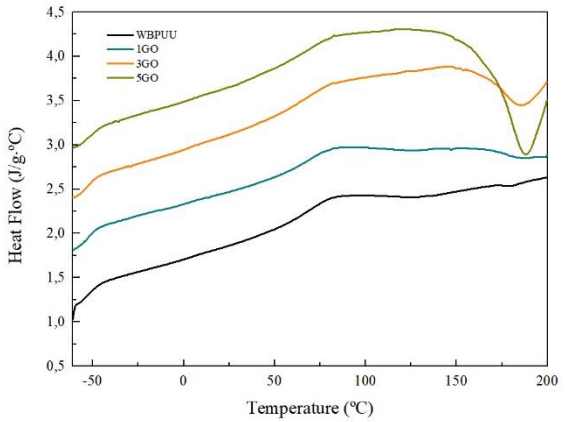

b)

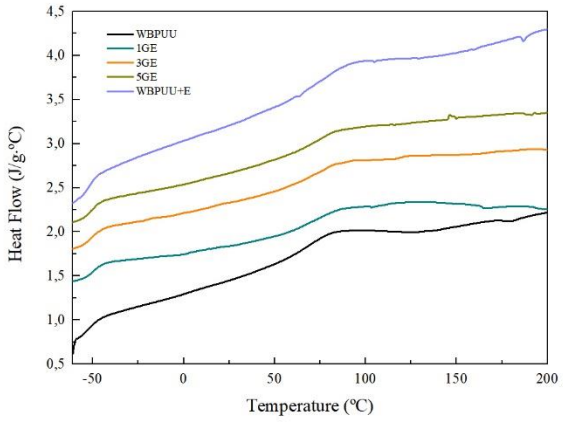

Figure 6.6. Differential Scanning Calorimetry thermograms of neat WBPUU and reinforced composites with different contents of a) GO and b) E and G

Table 6.2. Values of different thermal transitions observed from the DSC curves

Sample	T_g (ºC)	T_{HS} (ºC)	ΔH_{HS} ($J \cdot g^{-1}$)
WBPUU	-52.0	81.4	10.5
WBPUU+E	-51.7	91.3	11.6
1GE	-50.0	86.7	8.4
3GE	-50.4	84.0	7.9
5GE	-49.7	85.0	8.1
1GO	-52.2	82.8	9.2
3GO	-52.7	81.8	9.5
5GO	-50.7	82.8	8.1

In order to study the effect of the addition of the carbonaceous nanoreinforcements on the thermal degradation, Thermogravimetric Analysis were carried out and TGA and DTG curves are shown in Figure 6.7.

It was observed that the addition of GO and GE did not significantly alter the degradation process. All systems followed neat polyurethane degradation trend, showing the two-step degradation process. The first one encompasses the degradation of the HS between 240 and 400 ºC and it is composed by two peaks attributed to the urea and the urethane groups, followed by the degradation of the SS around 450 ºC [6,7]. This relatively unaltered thermal degradation is in agreement with behavior reported in literature [8,9].

For GO containing nanocomposites, a small peak can be seen in DTG curves centered around 190 ºC that agrees with the exothermic peak observed in DSC results. The intensity of this peak increased as GO content increased in the nanocomposites. This peak was related to the degradation of oxygen containing groups of graphene oxide.

For composites containing *Salvia* extract, the degradation temperature related with the degradation of the HS decreased. This temperature reduction was more noticeable for WBPUU+E composite film than for nanocomposites, with the addition of graphene this effect was counteracted with the increased

thermal stability of the system supplied by graphene, as can be observed when comparing WBPUU+E and 5GE degradation curves. Char residue increased with reinforcement content. This was more noticeable in the case of nanocomposites reinforced with graphene, due to both the presence of residue of *Salvia* extract (as seen in Chapter 3) and the higher thermal stability of graphene.

a)

b)

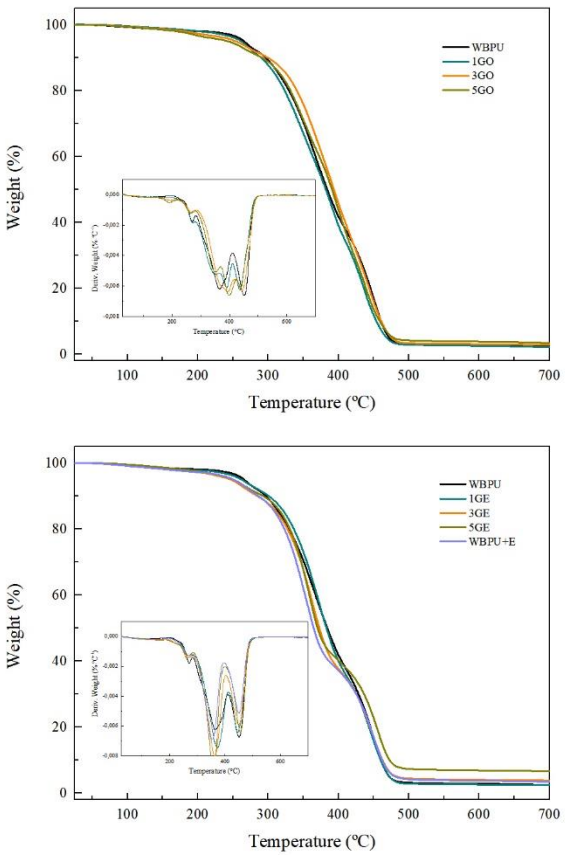

Figure 6.7. Thermogravimetric Analysis curves of neat WBPUU and reinforced composites with different contents of a) GO and b) E and G

Tensile properties of the materials were studied to observe the reinforcement effect supplied by the carbonaceous nanostructures. Results showing Young modulus, stress at yield, stress at break and strain at break values are reported on Table 6.3 and stress vs. strain curves are shown in Figure 6.8.

All composites showed higher Young modulus values than neat WBPUU, the increase in Young modulus was directly realted to the content of reinforcement. This effect was more noticeable for nanocomposites reinforced with graphene oxide. In the case of WBPUU/GO composites, stress at yield values were also improved as well as stress at break values.

Table 6.3. Young modulus, stress at yield, stress at break and strain at break values for neat WBPUU, WBPUU+E and GO or GE reinforced composites

Sample	Young modulus (MPa)	Stress at yield (MPa)	Stress at break (MPa)	Strain at break (%)
WBPUU	37.9 ± 6.2	2.7 ± 0.1	7.2 ± 1.6	739.6 ± 170.2
WBPUU+E	43.9 ± 3.4	2.6 ± 0.2	15.0 ± 4.2	854.0 ± 135.1
1GE	45.6 ± 4.8	2.6 ± 0.2	18.2 ± 3.7	881.2 ± 185.6
3GE	49.3 ± 5.3	2.9 ± 0.1	15.9 ± 5.0	733.5 ± 77.9
5GE	67.0 ± 0.3	3.1 ± 0.2	10.5 ± 0.6	611.8 ± 122.6
1GO	44.4 ± 3.6	2.6 ± 0.1	8.2 ± 2.6	599.1 ± 58.8
3GO	52.4 ± 7.6	4.0 ± 0.3	12.4 ± 2.0	699.8 ± 108.1
5GO	76.9 ± 8.2	5.5 ± 0.3	9.3 ± 0.3	453.4 ± 23.7

When analyzing composites reinforced with G, it can be observed that both Young modulus values and stress at break values increased. WBPUU+E showed also significantly enhanced properties. Therefore, it can be concluded that part of the improvement of the mechanical properties for GE containing composites can be attributed to the presence of *Salvia*.

However, for both composites reinforced with GO and G, it is observed that at high reinforcement contents, tensile strength values started to drop, probably attributed to the formation of reinforcement agglomerations.

Regarding strain at break values, the addition of graphene oxide had a bigger impact in this property. Strain at break values decreased with the addition of GO, as was to be expected for this composites [10]. For WBPUU/G composites, the effect of the *Salvia*, as well as an excellent polymer/graphene interfacial adhesion [11], provided higher stress at break values and impeded a harsh decrease of this property.

a)

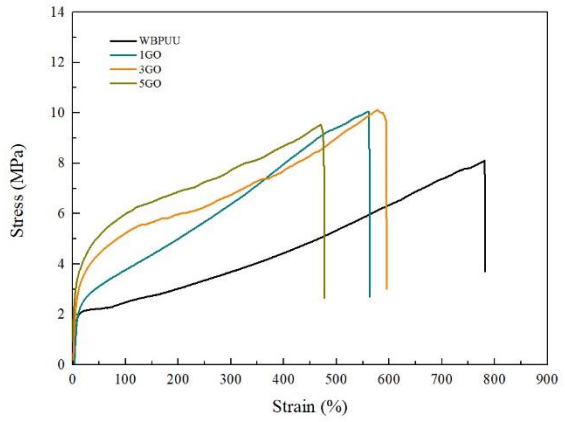

b)

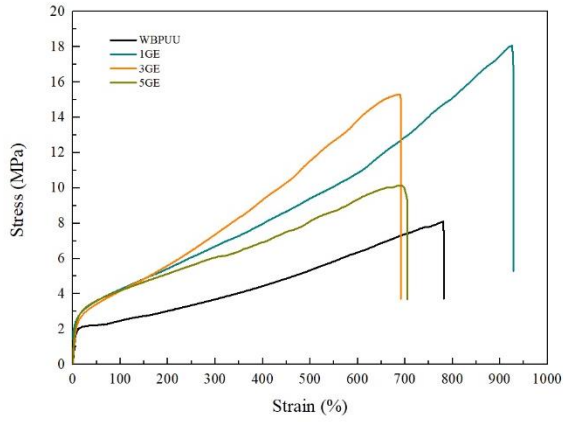

Figure 6.8. Stress/Strain curves for neat WBPUU films and nanocomposites reinforced with a) GO and b) G

The reinforcement effect on the dynamic mechanical behavior of the nanocomposites can be seen in Figure 6.9. All composites showed higher storage modulus values than the neat WBPUU throughout the whole range of temperature. The addition of the nanoreinforcements resulted in the improvement of the thermo-mechanical stability of the materials [61-63].

WBPUU/GO nanocomposites resulted in materials with more enhanced thermo-mechanical properties, which could be due to more favored direct interaction between matrix and reinforcement. Interactions between WBPUU and GO, suggested by FTIR studies, could result in chains with reduced mobility, increased stiffness and, thus, higher storage modulus [64,65]. The

reduction of chain mobility, together with the high modulus and specific surface area of graphene oxide could significantly alter the stiffness of the WBPUU [62]. This higher stiffness is in agreement with results observed from mechanical properties, where both Young modulus and stress values increased with the addition of GO, whereas elongation at break values dropped.

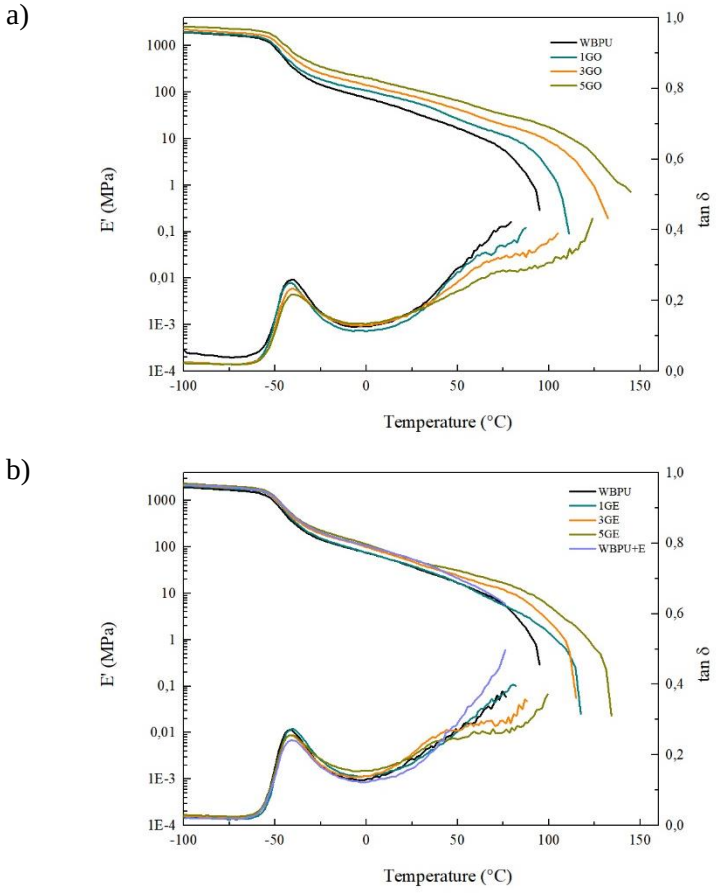

Figure 6.9. Dynamic mechanical curves of neat WBPUU and reinforced composites with different contents of a) GO and b) G

In the case of WBPUU/G nanocomposites higher storage modulus and better thermo-mechanical stability was seen. However, this improvement is less significant than in composites with GO. Probably, in graphene reinforced

composites the presence of *Salvia* could have interfered in the creation of matrix/graphene interactions.

In order to study possible electrical conductivity of the materials supplied by the addition of graphene, electrical properties of GE containing composite films were studied. Neither of the films showed a conductive character. Graphene flakes seemed to have stayed embedded in the polyurethane matrix or the G content was too low and graphene flakes were not able to form a conductive net. Since nanocomposites films did not show electrical conductivity, in the following section a coating of the systems with graphene was studied, with the aim to supply the films with this characteristic.

6.3. Coating of WBPUU/carbonaceous structures composites

For the study of the coated systems the neat polyurethane and the highest content composites, 5GO and 5GE, were chosen. Systems were coated with graphene in order to supply them with conductivity. For this, both the graphene obtained through different methods (Chapter 3), were used, G obtained through exfoliation of graphite and rGO through thermal reduction of graphene oxide.

First G and rGO were dispersed in cyclohexane (10 $mg \cdot mL^{-1}$) in a sonication bath for 45 minutes. Prior to submerging the films in these dispersions, the films were dipped in NMP for just a few seconds, in order to swell them and allow a better penetrability on their surface. The dipped films were later submerged in the G or rGO dispersions in cyclohexane and were sonicated in a sonication bath for 15 minutes. Afterwards, films were extracted and cleaned with water to remove residual cyclohexane and later with a brush to remove not attached G and rGO, and were left to dry at room temperature.

When rGO was used to coat the neat WBPUU and 5GO composite, the coated films were labeled as WBPUU/rGO and 5GO/rGO. When G was used to coat

the neat WBPUU and 5GE films, these coated systems were labeled as WBPUU/G and 5GE/G.

In order to study the changes taken place in film properties after coating process, coated systems were characterized by means of different techniques.

6.3.1. Characterization of coated systems

Electrical properties of the coated systems were analyzed measuring electrical resistance of the material when an electric field was applied, current/voltage curves are shown in Figure 6.10.

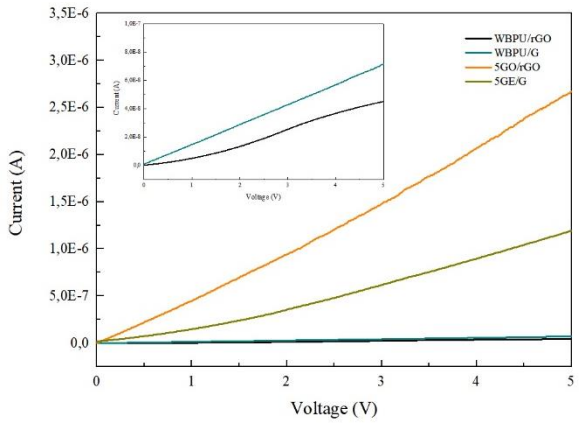

Figure 6.10. Current vs. voltage curves for G and rGO coated films

Results showed that the coating of the materials with carbonaceous structures resulted in systems with an electrical conductive surface. Both coated matrices showed the lowest conductive capacity, being their electrical resistance (155.0 ± 76.0) x10^6 Ω for WBPUU/G and (142.1 ± 20.5) x10^6 Ω for WBPUU/rGO. In the case of coated composites, the resistance values were noticeably lower than coated polyurethane ones. The resistance for 5GE/G composite was (6.6 ± 1.7) x 10^6 Ω, and for GO/rGO was (2.7 ± 1.3) x10^6 Ω.

The higher conductivity shown by nanocomposites was attributed to a better coating process, due to a better affinity between the surface of composite

films and the coating nanoreinforcements. In the case of 5GO coated system, an even better conductivity was achieved. This could be thanks to the remaining oxidized groups in the structure of rGO, which could help improve interactions with films surface, leading to a better coating than for G coated systems.

To further analyze the electrical conductivity of the surface of the systems, EFM analyses were carried out. In EFM analyses, electrostatic forces affect the resonance frequency of the oscillating cantilever, thus this changes are detected and captured in phase images [12]. Phase images will only be obtained for conductive materials. In this case, scans were done at -6, 0, 3, 6 and 12 V, in order to confirm conductivity of the materials and study the effect of the variation of the applied voltage.

As seen by electrical conductivity analyses, all coated systems showed good electrical conductivity, thus for all systems phase images were obtained. As seen in the previous section, coated neat polyurethane films had lower conductive capacity. In this case, that was reflected by images with lower brightness. As can be seen in Figure 6.11, composites showed brighter images due to their better electrical conductivity.

When studying the effect of positively and negatively charged fields, 6 and -6 V were applied and images were obtained. It can be observed that for both positive and negative voltages brighter images were obtained, meaning the presence of repulsive interactions increasing the resonant frequency of the cantilever [13].

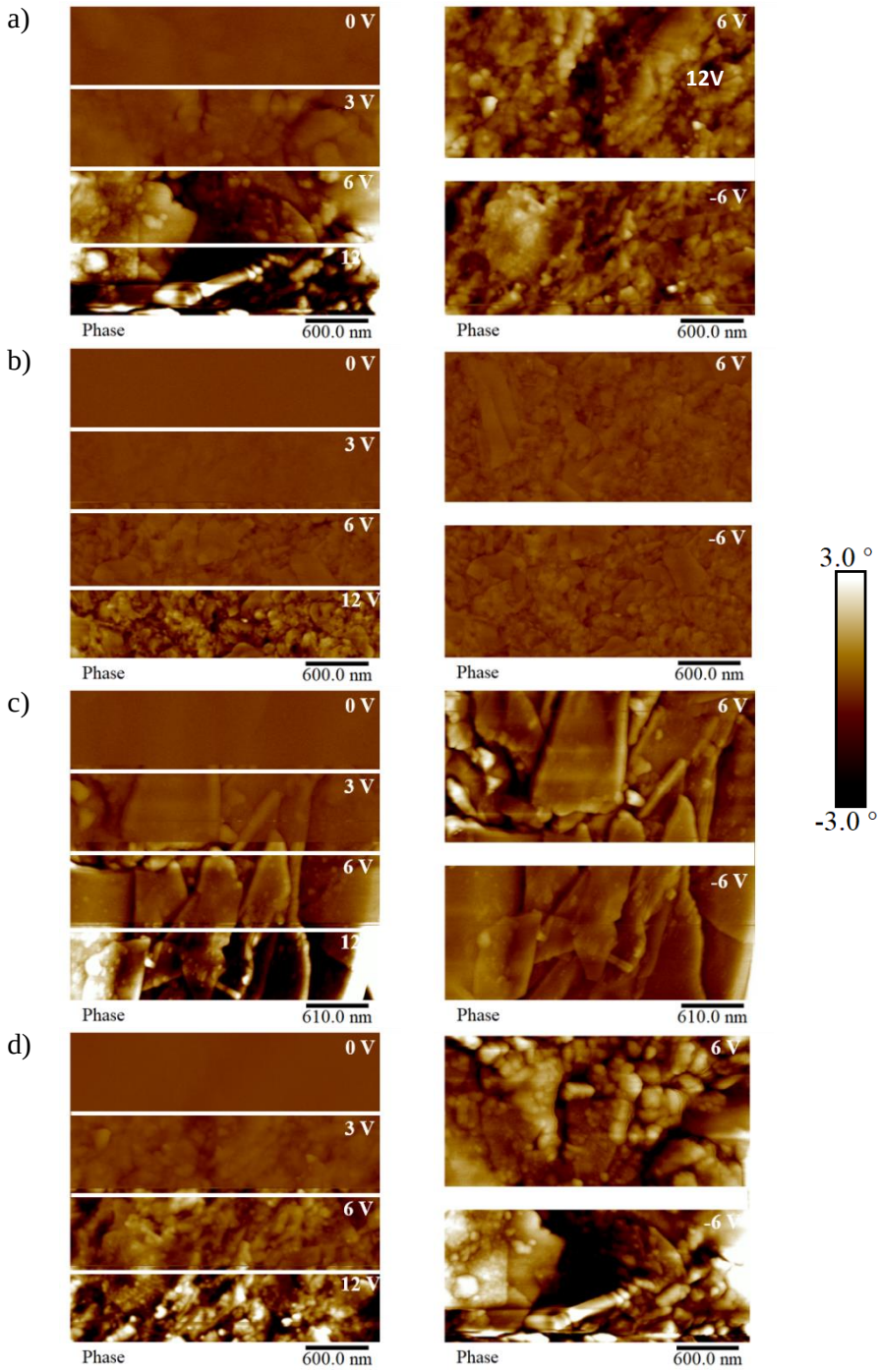

Figure 6.11. EFM phase images at 0, 3, 6 ,12 and -6 V for a) WBPU/G, b) 5GE/G, c) WBPU/rGO and d) 5GO/rGO (Image size: 3x3 µm)

When a range of voltage from 0 to 12 V was applied, it could be seen that higher voltages resulted in brighter images (Figure 6.11). The higher tip voltages resulted in greater phase shifts, due to stronger repulsion forces.

DMA analyses were carried out to evaluate possible damaging of the materials during coating process and to assess thermomechanical behavior of the materials. Figure 6.12 shows storage modulus and tan δ curves for coated systems (WBPUU/rGO, WBPUU/G, 5GO/rGO and 5GE/G). For comparison purposes, in Figure 6.12, the curves of their uncoated homologues (WBPUU, 5GO and 5GE) are included.

After coating process, coated materials showed slightly lower storage modulus values than uncoated counterparts, indicating some damage in the materials. However, a small increase in the thermomechanical stability of the materials was observed, probably due to the formation of a G and rGO shell that protects the internal structure of the material.

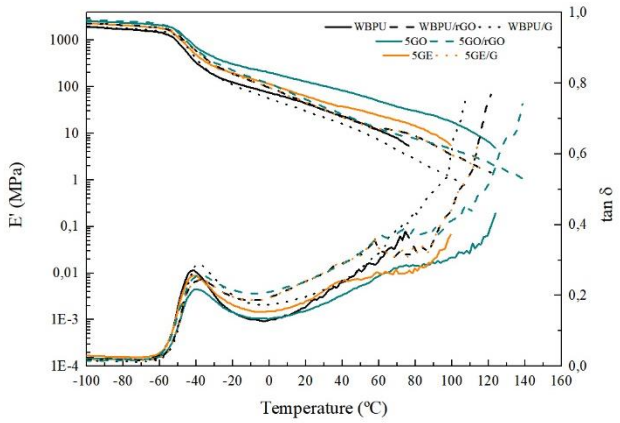

Figure 6.12. Dynamic mechanical curves of coated films and uncoated homologues

The carbonaceous coating of the systems was observed through SEM. A fractured zone, where the coating and the composite film meet, was analyzed. Obtained micrographies are shown in Figure 6.13.

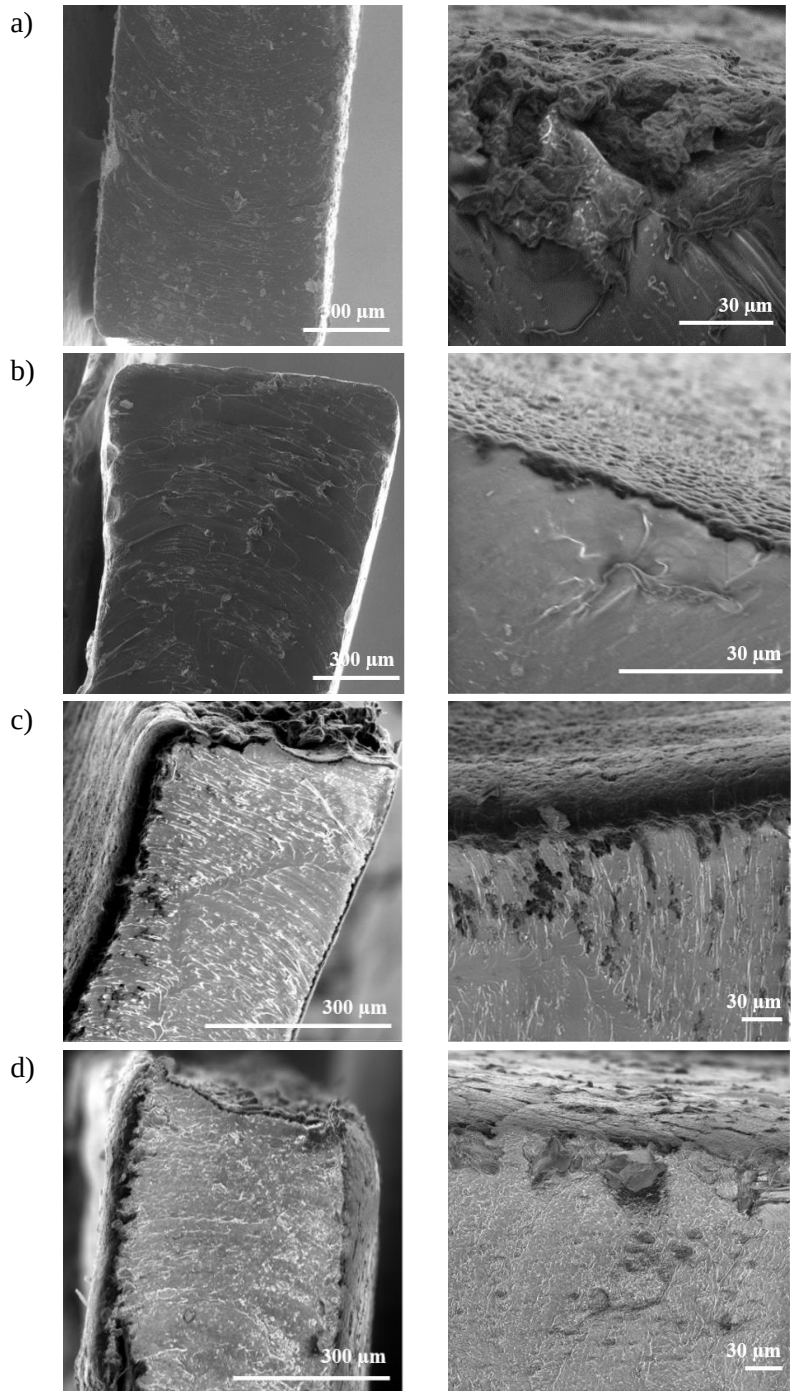

Figure 6.13. SEM images for transversal cuts for a) WBPU/G, b) 5GE/G, c) WBPU/rGO and d) 5GO/rGO

When studying obtained SEM images, for less magnified images, the successful coating of the systems can be clearly seen by a shell surrounding the composites films. For more magnified images, differences in the coating begin to be noticeable. For coated unreinforced polyurethanes, the separation between the coating and the film was sharper. In the case of coated composites, this union was less pronounced, the carbonaceous structures of the coating were able to penetrate the surface a little better, suggesting a better affinity of rGO and G with the composite films than unreinforced films. This improved affinity seems to have helped the adhesion of the graphene and rGO flakes on composite films surface, which resulted in a better conductive capacity for coated composites than for unreinforced films.

Literature reports show that graphene can show antibacterial activity against, both, gram positive and gram negative strains [14,15]. Therefore, in order to study possible antibacterial properties supplied by the coating process, antibacterial analyses were carried out. Moreover, in addition to graphene, *Salvia* extract also shows antimicrobial character [16,17], which could further promote the antimicrobial behavior. In this regard, 5GE/G coated composite was chosen for this analyses.

The testing of the microbicide activity of the film was done using the disk diffusion technique. Two strains were used for testing, one Gram positive, Staphylococcus aureus CECT 239, and one Gram negative, Escherichia Coli CECT 405.

Results for antibacterial test for both bacteria are shown in Figure 6.14. 5GE/G showed antimicrobial activity against both tested trains, as can be seen by the formation of inhibition halos around the samples.

a) b)

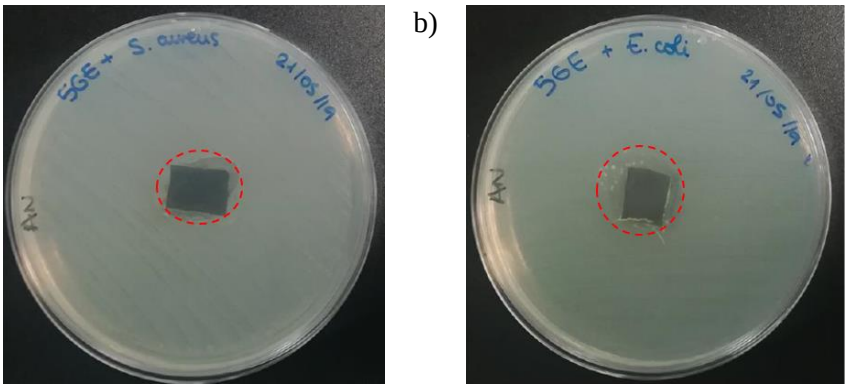

Figure 6.14. Antimicrobial activity shown by 5GE/G against a) S. aureus and b) E. Coli.

6.4. Preparation of WBPUU/rGO filaments

In order to assess the potential use of these composites for FDM 3D printing, filaments were prepared, characterized and tested. For the preparation of filaments, the use of reduced graphene oxide was chosen, in order to have a graphene-like structure but with a faster production process. As done in Chapter 4 for CNF containing composites, two incorporation methods were employed, ex-situ and in-situ, to prepare nanocomposites with 3 wt.% rGO.

For composite preparation prior to filament extrusion, first rGO was dispersed in water. As done with graphene, rGO was dispersed in water using *Salvia* extract as a surfactant, with a rGO:E ratio of 2:1. In the case of the ex-situ composite, it was prepared as explained in the previous section, the sonicated rGO aqueous dispersion was added to the WBPUU dispersion and was further sonicated for an hour in a sonication bath. In the case of in-situ composites the rGO aqueous dispersion was added during the phase inversion step of the synthesis. Both composites were left to dry in Teflon molds for 7 days at room temperature and 3 days at 400 mbar. Ex-situ and in-situ prepared nanocomposites were name $3rGO_{EX}$ and $3rGO_{IN}$, respectively.

For filament preparation, composite pellets of 5x5 mm^2 were prepared and extruded following the procedure explained in Chapter 4. Feeding and extrusion speed were maintained (feeding flow of 0.3 g every 25s at 50 rpm), as well as nozzle size and collection process. However, when optimizing extrusion temperature, it was observed that WBPUU/rGO composites did not need as high temperatures as WBPUU/CNF composites for a good extrusion process. In-situ and ex-situ prepared WBPUU/rGO composites were prepared at 160 ºC and good processability was observed.

Filament of ex-situ and in-situ composites were prepared and named $F3rGO_{EX}$ and $F3rGO_{IN}$.

6.4.1. Characterization of WBPUU/rGO filaments

Neat WBPUU and WBPUU/rGO nanocomposite filaments were characterized regarding their physico-chemical, thermal and mechanical properties.

Figure 6.15 shows pictures of the extruded filaments. As previously seen in Chapter 4, FWBPUU had a transparent aspect, which changed with the addition of the nanoreinforcements. Filaments reinforced with rGO, both $F3rGO_{EX}$ and $F3rGO_{IN}$, were completely black. In this case, the black color of graphene overtook the color of the matrix. In contrast with the extrusion of WBPUU/CNF nanocomposites, rGO based nanocomposites showed a more constant and controllable extrusion and, thus, filaments with a more homogeneous diameter were obtained.

FWBPUU **F3rGO$_{EX}$** **F3rGO$_{IN}$**

Figure 6.15. Photographs of WBPUU and WBPUU/rGO nanocomposites filaments

Fourier Transform Infrared spectroscopy analyses were carried out in order to analyze interaction between the neat WBPUU and the nanoreinforcements. FTIR spectra of WBPUU filament and nanocomposite filaments are shown in Figure 6.16.

FWBPUU, F3rGO$_{EX}$ and F3rGO$_{IN}$ all showed all the previously described characteristic polyurethane peaks. All systems showed the same bands with the only difference residing in the N-H band at 3360 cm^{-1}. For composite filaments this band shifted to higher wavenumber values. This change could be due to an overlapping of the matrix N-H band with the O-H band of the Salvia extract used to dispersed rGO, and some residual oxygenated groups in rGO.

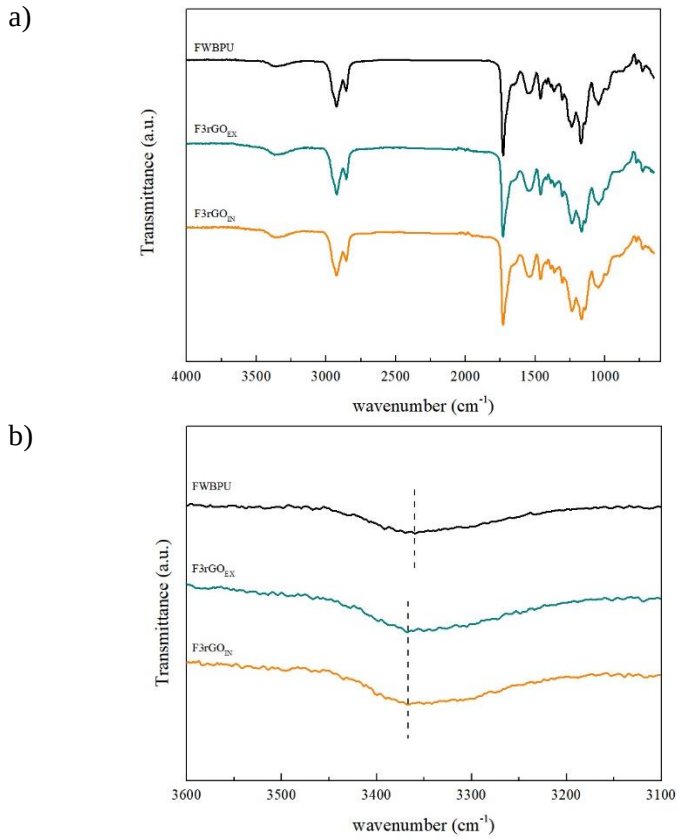

Figure 6.16. FTIR spectra of WBPUU and WBPUU/rGO nanocomposites filaments and b) zoomed FTIR spectra for the 3600-3100 cm^{-1} region.

The thermal stability of the filaments was analyzed by TGA, in order to study changes taken placed in the nanocomposites during the filament preparation process. Obtained TGA and DTG curves are shown in Figure 6.17.

The matrix filament, as previously seen in Chapter 4, showed the two step degradation already described, where the degradation of the hard segment is centered at 340 ºC, followed by the degradation of the soft segment at 420 ºC [6].

For WBPUU/rGO filaments an enhancement on the thermal stability of the materials with the addition of graphene was observed. In the case of filaments containing graphene, both the SS and HS degradation temperatures were

displaced to higher temperatures. For $F3rGO_{EX}$ the HS and SS DTG peaks maximums displaced from 339 ºC of FWBPUU to 394 ºC and from 421 ºC to 439 ºC, whereas for $F3rGO_{IN}$ they displaced to 398 and 440 ºC, respectively. [18,19].

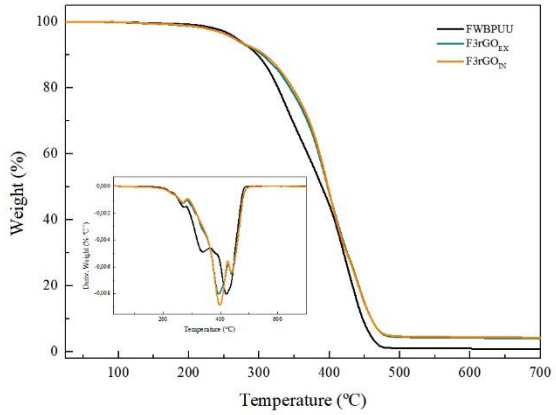

Figure 6.17. TGA and DTG curves for neat WBPUU and WBPUU/rGO nanocomposites filaments

The mechanical properties of the filaments were assessed by tensile tests and changes in mechanical behavior due to the addition of rGO and the filament preparation process were studied. Measured mechanical properties are summarized in Table 6.4 and obtained stress/strain curves are shown in Figure 6.18.

Table 6.4. Young modulus, stress at yield, stress at break and strain at break values for matrix and composites filaments

	Young Modulus (MPa)	Stress at yield (MPa)	Stress at break (MPa)	Strain at break (%)
FWBPUU	6.9 ± 1.3	1.5 ± 0.1	5.4 ± 0.6	821.6 ± 35.4
$F3rGO_{EX}$	32.4 ± 5.6	9.8 ± 0.9	28.2 ± 1.8	914.8 ± 23.8
$F3rGO_{IN}$	36.4 ± 6.3	6.4 ±0.9	25.2 ± 0.9	995.6 ±59.7

A strong reinforcement effect supplied by the addition of rGO can be clearly seen. Both filaments containing rGO showed improved mechanical properties.

Young modulus and stress at break values were significantly enhanced in nanocomposite filaments. This behavior is often seen for polyurethanes reinforced with carbonaceous nanostructures [20,21]. An increase of up to 428% can be seen for Young modulus and up to 422% for stress at break values. Moreover, strain at break values after rGO addition were slightly higher than those shown by the unreinforced filament.

The enhanced mechanical properties shown by F3rGO$_{EX}$ and F3rGO$_{IN}$ could be due to the effect of the addition of rGO, as well as, *Salvia*.

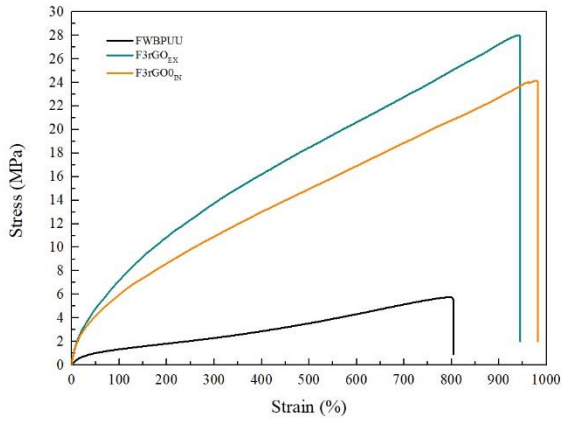

Figure 6.18. Stress/Strain curves for neat WBPUU and rGO reinforced composite filaments

When compared to the previously studied WBPUU/G and WBPUU/GO films, it can be observed that the filament preparation process, in this case, did not damage the mechanical properties of the materials, as opposed to WBPUU/CNF composites. Overall, values of the same order were observed, though higher stress and strain at break values can be seen in filaments compared to films. In this case the presence of remaining oxygenated groups in the surface of rGO, as well as the presence of Salvia, allowed the formation of interaction with the polyurethane-urea matrix, resulting in enhanced mechanical properties. Moreover, the alignment of the reinforcements during

the filament preparation process could further improve the properties of the nanocomposites.

The thermomechanical behavior of the filaments was studied by Dynamic Mechanical Analysis. Storage modulus and tan δ curves are shown in Figure 6.19.

In all temperature range, a strong increase in the modulus values can be seen for composite filaments. This higher storage modulus could be due to high modulus and specific surface area of graphene [22]. Before T_g was reached, the storage modulus was maintained fairly constant for all systems. Moreover, a strong enhancement of the thermomechanical stability of about 50 ºC with the addition of rGO could also be observed. The polymer/reinforcement interactions suggested by previous analyses decreased the mobility of the chains, which together with the reinforcement effect of reduced graphene oxide resulted in stiffer and more stable materials [11].

$F3rGO_{EX}$ and $F3rGO_{IN}$ showed higher modulus values, than those shown by WBPUU/CNF filaments in Chapter 4, and were able to maintain the structural integrity of the material at higher temperatures [11,19].

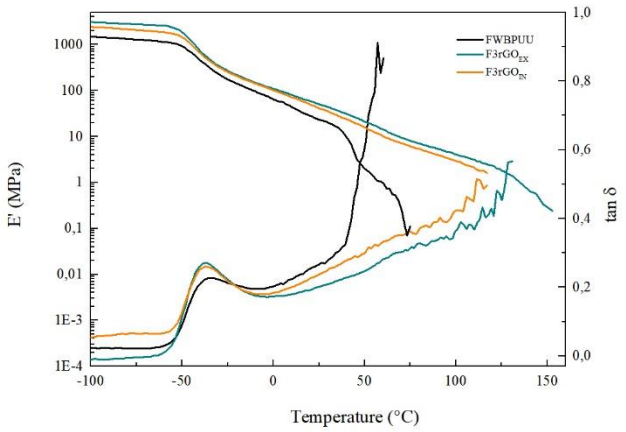

Figure 6.19. Dynamic mechanical curves for WBPUU and WBPUU/rGO nanocomposites filaments

In comparison with filaments prepared from composites reinforced with cellulose nanofibers, WBPUU/rGO filaments presented overall better properties, regarding their thermal, mechanical and thermomechanical behavior. This was attributed to a better extrusion process resulting in less degraded materials, as well as to the strong reinforcement effect and great properties of this carbonaceous nanostructure.

6.5. FDM 3D printing of WBPUU/rGO filament

Prepared filaments were tested for FDM 3D printing. As previously seen in Chapter 4, it was not possible to print FWBPUU due to low rigidity and nozzle obtrusion. The addition of rGO, however, resulted in stiffer materials, as shown by mechanical properties of the filaments. This higher rigidity of these filaments was enough to allow good feeding and extrusion process during FDM printing.

FDM printing of WBPUU/rGO filaments was carried out using a Tumaker Voladora NX printer paired with a Simplify3D software. Printing parameters were optimized for the prepared filaments, varying extruder and bed temperature and printing speed among others. Optimized printing parameters are shown in Table 6.5.

Table 6.5. 3D printing parameters

Parameter	Value
Extruder temperature (ºC)	200
Bed temperature (ºC)	45
Nozzle diameter (mm)	0.6
Printing speed ($mm \cdot s^{-1}$)	10
Layer height (mm)	0.2
Infill Pattern	Rectilinear

Dog-bone specimens were chosen as designed models for 3D printing, to facilitate later testing of the mechanical properties of the printed parts. Dimensions of printed dog-bone specimens are shown in Figure 6.20.

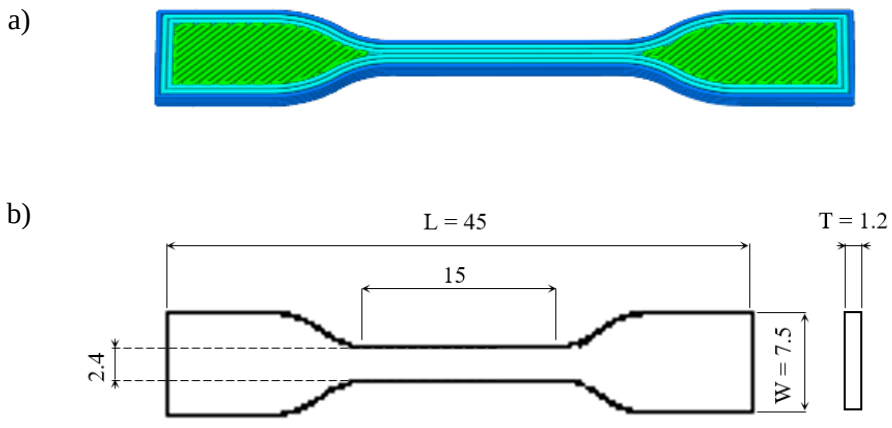

Figure 6.20. a) 3D model of imported dog-bone design and b) dimensions (in mm)

6.5.1. Characterization of 3D printed pieces

3D printed parts from F3rGO$_{EX}$ and F3rGO$_{IN}$ were named 3D-3rGO$_{EX}$ and 3D-3rGO$_{IN}$, respectively. A loyal reproduction of the shape and size of the imported model was obtained, 3D-3rGO$_{EX}$ and 3D-3rGO$_{IN}$ printed parts are shown in Figure 6.21.

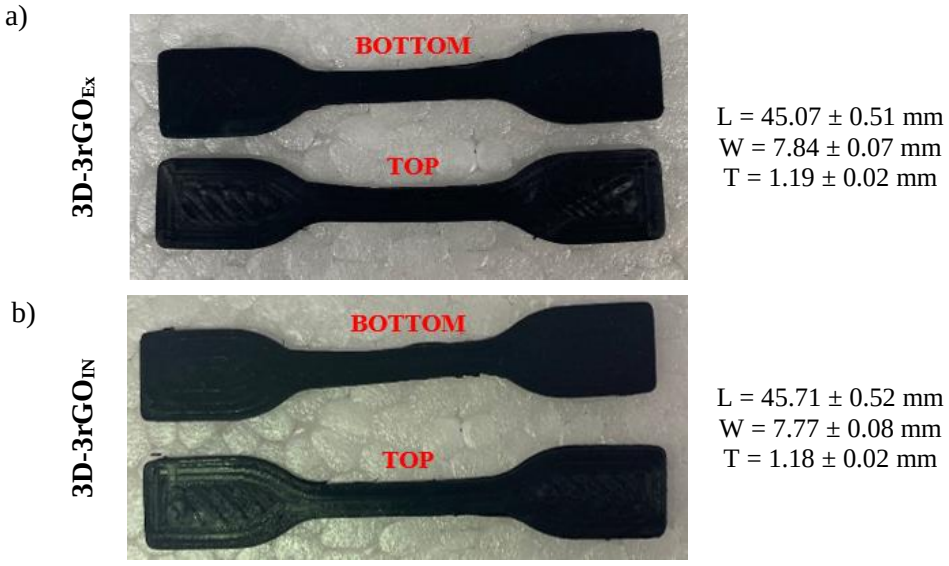

Figure 6.21. Photographs of WBPUU/rGO 3D printed parts by FDM

Printed parts were characterized regarding their morphology and their thermal, mechanical and thermomechanical behavior.

Obtained SEM cryofractured cross-sectional images are shown in Figure 6.22. Both printed systems presented similar morphologies with small differences.

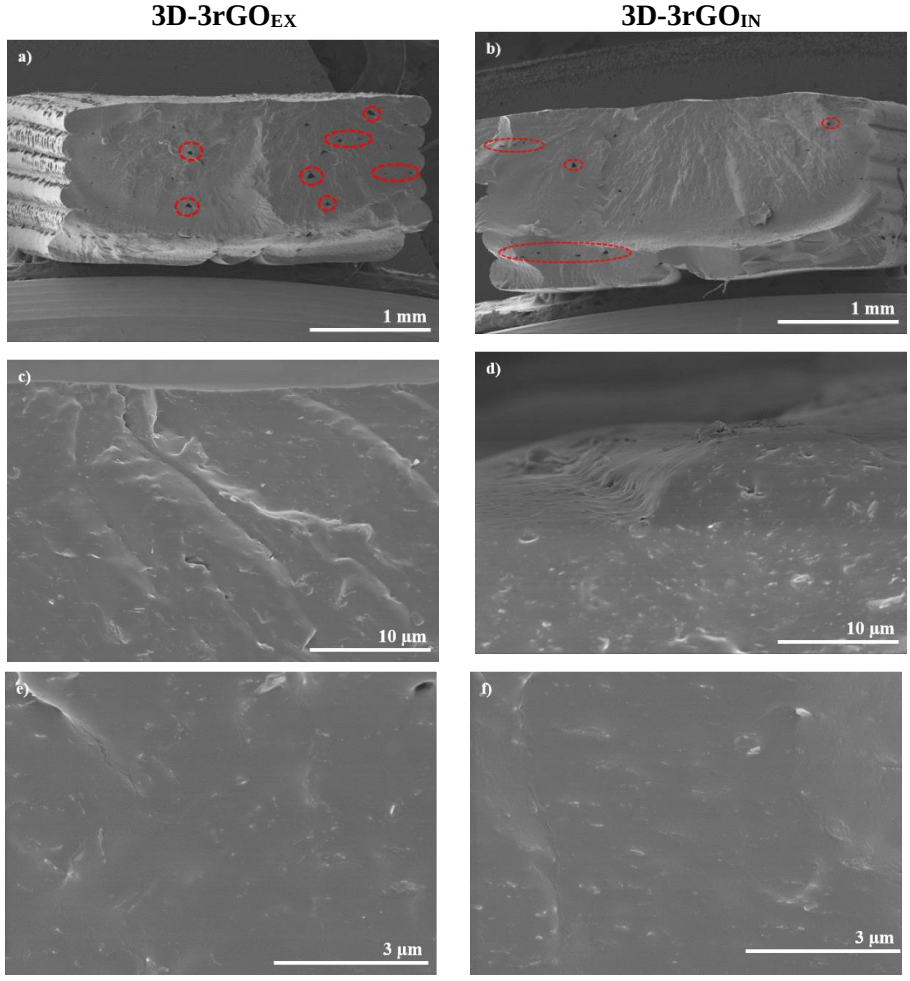

Figure 6.22. SEM images for cryofractured cross-sections of WBPUU/rGO 3D printed parts by FDM

Figures 6.22a and 6.22b show less magnified images of 3D-3rGO$_{EX}$ and 3D-3rGO$_{IN}$ systems, where small imperfections, small holes, formed during the printing process can be observed (circled in red). These imperfections are

more noticeable in the case of 3D-3rGO$_{EX}$, where a higher amount of holes are observed, in contrast to the more compact interior with a very reduced amount of imperfections shown by 3D-3rGO$_{IN}$. Most of these holes seem to align with the junction of the layers, suggesting some adhesion problems between layers.

Figure 6.22c-f show more magnified images of the materials. A good dispersion of the nanoreinforcements can be deduced, since no apparent agglomerations can be observed.

Tensile tests were performed for 3D printed specimens, in order to analyze their mechanical properties. Results summarizing mechanical properties are shown in Table 6.6 and stress/strain curves are shown in Figure 6.23.

Table 6.6. Young modulus, stress at yield, stress at break and strain at break values for WVPU/rGO 3D printed specimens

Sample	Young modulus (MPa)	Stress at yield (MPa)	Stress at break (MPa)	Strain at break (%)
3D3G$_{EX}$	30.7 ± 7.8	3.7 ± 0.2	11.4 ± 0.4	467.5 ± 7.3
3D3G$_{IN}$	46.7 ± 8.2	3.7 ± 0.3	12.4 ± 1.3	451.3 ± 29.2

Changes in mechanical behavior of the material due to printing process can be clearly seen. Some analyzed parameters show deterioration after the printing process. This was not the case for Young modulus values, were good properties are maintained. However, significantly lower stress at yield, stress at break and strain at break values were observed for both printed systems when compared to their corresponding filaments.

This strong deterioration of mechanical behavior shown by printed parts could be attributed to the presence of small imperfection in the structure of the printed parts, as well as the adhesion problems between layers, seen by SEM (Figure 6.22a-d). Another possible reason could be the damage of the material during the printing process. High printing temperatures could have begun

degrading the nanocomposites, resulting in materials with worse mechanical properties.

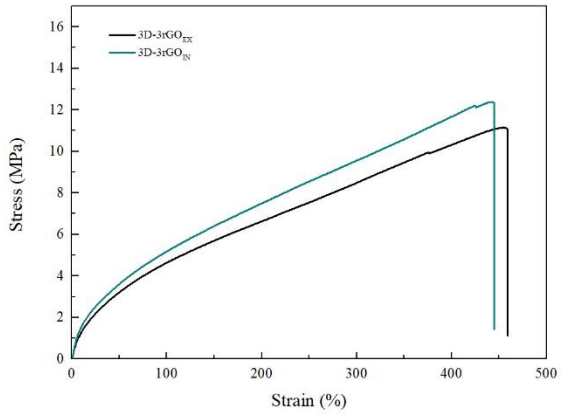

Figure 6.23. Stress/Strain curves for WBPUU/rGO 3D printed specimens

Regarding DMA, it can be observed that both printed systems showed, in general, a good thermomechanical behavior (Figure 6.24). When compared with extruded filaments, a similar behavior was repeated. At low temperatures, printed parts showed similar modulus values to their corresponding filaments, being the value even slightly higher for 3D-3rGO$_{IN}$.

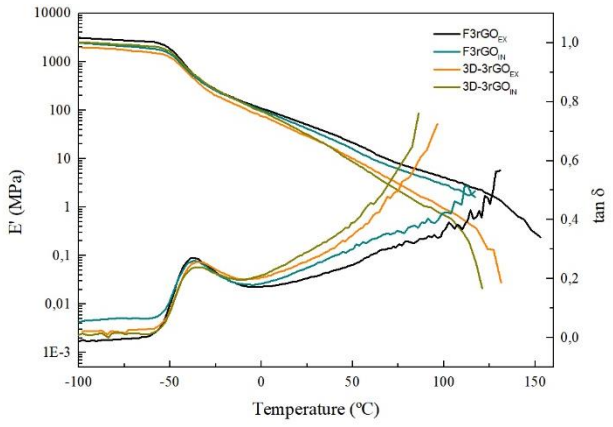

Figure 6.24. Dynamic-mechanical curves of WBPUU/rGO 3D printed parts by FDM

However, a deterioration in stability compared to their filaments counterparts was seen in 3D printed. This lower stability could be due to damage suffered by the materials during the high temperature printing process, as suggested also by mechanical results.

6.6. Conclusions

In this chapter polyurethane-urea films were reinforced with graphene oxide and graphene. Films containing these carbonaceous structures showed opaque brown and black tonalities and showed homogeneuous dispersions of the reinforcement within the matrix. UV light absortion capacity was studied and they showed good shielding behaviors, with extremely low transmitance observed for G containing films and increasing with content of GO. The addition of both GO and G to polyurethane proved great reinforcement capacity since nanocomposites showed strongly enhanced mechancial and thermomechanical behavior. However, neither composite film showed electrical conductive behavior.

In order to supply electrical conductivity to the materials, the coating of the films with graphene and reduced graphene oxide was studied. The coating process resulted in a graphene shell sorrounding the films, which was clearly observed in SEM images. Coated materials showed good electrical conductivity, which was stronger for coated composites rather than coated neat polyurethane-urea. This was attributed to the better affinity of the coating with the nanocomposite films. Materials showed some damage suffered during the coating process and showed some deteriotation on their thermomechanical behavior. Coating showed also good bactericide behavior, thanks to the antibacterial behavior of graphene.

Nanocoposites containing 3 wt.% of reduced graphene oxide were prepared by ex-situ and in-situ methods and they were extruded to obtain WBPU/rGO filaments. The extrusion process of these materials presented lower flux

troubles than in the case of CNF, therefore more homogenoeus and less damaged filaments were obtained. As a result, filaments with great thermal, thermomechanical and mechanical properties were obtained. The higher rigidity shown by these filaments directly translated into better printability.

Filaments were used to produced 3D printed parts by FDM, WBPUU/rGO filaments showed good printability and shape reproducibility. SEM analyses showed good overall layer adhesion with some small imperfections. 3D printed parts showed some deterioration, with some damaging of the mechanical properties, attributed to the imperfections and high printing temperatures, but showed overall good properties.

6.7. References

[1] Ugarte L, Fernández-d'Arlas B, Valea A, González ML, Corcuera MA, Eceiza A. Morphology-properties relationship in high-renewable content polyurethanes. Polym Eng Sci 2014;54:2282–91. doi:10.1002/pen.23777.

[2] Santamaria-Echart A, Fernandes I, Saralegi A, Costa MRPFN, Barreiro F, Corcuera MA, et al. Synthesis of waterborne polyurethane-urea dispersions with chain extension step in homogeneous and heterogeneous media. J Colloid Interface Sci 2016;476:184–92. doi:10.1016/j.jcis.2016.05.016.

[3] Pei A, Malho JM, Ruokolainen J, Zhou Q, Berglund LA. Strong nanocomposite reinforcement effects in polyurethane elastomer with low volume fraction of cellulose nanocrystals. Macromolecules 2011;44:4422–7. doi:10.1021/ma200318k.

[4] Song W, Wang B, Fan L, Ge F, Wang C. Graphene oxide/waterborne polyurethane composites for fine pattern fabrication and ultrastrong ultraviolet protection cotton fabric via screen printing. Appl Surf Sci 2019;463:403–11. doi:10.1016/j.apsusc.2018.08.167.

[5] Santamaria-Echart A, Fernandes I, Barreiro F, Retegi A, Arbelaiz A, Corcuera MA, et al. Development of waterborne polyurethane-ureas added with plant extracts: Study of different incorporation routes and their influence on particle size, thermal, mechanical and antibacterial properties. Prog Org Coatings 2018;117:76–90. doi:10.1016/j.porgcoat.2018.01.006.

[6] Ou CW, Su CH, Jeng US, Hsu SH. Characterization of biodegradable

polyurethane nanoparticles and thermally induced self-assembly in water dispersion. ACS Appl Mater Interfaces 2014;6:5685–94. doi:10.1021/am500213t.

[7] Fuensanta M, Jofre-Reche JA, Rodríguez-Llansola F, Costa V, Iglesias JI, Martín-Martínez JM. Structural characterization of polyurethane ureas and waterborne polyurethane urea dispersions made with mixtures of polyester polyol and polycarbonate diol. Prog Org Coatings 2017;112:141–52. doi:10.1016/j.porgcoat.2017.07.009.

[8] Kumar M, Suk J, Kong B, Jung E, Hyun S. Synthesis of graphene – polyurethane nanocomposite using highly functionalized graphene oxide as pseudo-crosslinker. Mater Lett 2013;106:319–21. doi:10.1016/j.matlet.2013.05.059.

[9] Zhang J, Zhang C, Madbouly SA. In situ polymerization of bio-based thermosetting polyurethane/graphene oxide nanocomposites. J Appl Polym Sci 2015;132:n/a-n/a. doi:10.1002/app.41751.

[10] Bernard C, Goodwin DG, Gu X, Celina M, Nyden M, Jacobs D, et al. Graphene oxide/waterborne polyurethane nanocoatings: effects of graphene oxide content on performance properties. J Coatings Technol Res 2020;17:255–69. doi:10.1007/s11998-019-00267-6.

[11] Pokharel P, Lee DS. Thermal and mechanical properties of reduced graphene oxide/polyurethane nanocomposite. J Nanosci Nanotechnol 2014;14:5718–21. doi:10.1166/jnn.2014.8824.

[12] Bonnell DA. Scanning probe microscopy and spectroscopy: theory, techniques, and applications. 2nd Editio. New York: 2001.

[13] Kim J, Jasper WJ, Hinestroza JP. Charge characterization of an electrically charged fiber via electrostatic force microscopy. J Eng Fiber Fabr 2006;1:155892500600100. doi:10.1177/155892500600100203.

[14] Tu Y, Lv M, Xiu P, Huynh T, Zhang M, Castelli M, et al. Destructive extraction of phospholipids from Escherichia coli membranes by graphene nanosheets. Nat Nanotechnol 2013;8:594–601. doi:10.1038/nnano.2013.125.

[15] Hegab HM, Elmekawy A, Zou L, Mulcahy D, Saint CP, Ginic-Markovic M. The controversial antibacterial activity of graphene-based materials 2016;105:362–76. doi:10.1016/j.carbon.2016.04.046.

[16] Ghorbanpour M, Hatami M, Kariman K, Abbaszadeh Dahaji P. Phytochemical variations and enhanced efficiency of antioxidant and antimicrobial ingredients in Salvia officinalis as inoculated with different rhizobacteria. Chem Biodivers 2016;13:319–30. doi:10.1002/cbdv.201500082.

[17] Santamaria-Echart A, Fernandes I, Barreiro F, Retegi A, Arbelaiz A, Corcuera MA, et al. Development of waterborne polyurethane-ureas added with plant extracts: Study of different incorporation routes and their influence on particle size, thermal, mechanical and antibacterial properties. Prog Org Coatings 2018;117:76–90. doi:10.1016/j.porgcoat.2018.01.006.

[18] Strankowski M. Effect of variation of hard segment content and graphene-based nanofiller concentration on morphological, thermal, and mechanical properties of polyurethane nanocomposites. Int J Polym Sci 2018;2018:1–20. doi:10.1155/2018/1090753.

[19] Nguyen DA, Lee YR, Raghu A V., Jeong HM, Shin CM, Kim BK. Morphological and physical properties of a thermoplastic polyurethane reinforced with functionalized graphene sheet. Polym Int 2009;58:412–7. doi:10.1002/pi.2549.

[20] Pokharel P, Pant B, Pokhrel K, Pant HR, Lim JG, Lee DS, et al. Effects of functional groups on the graphene sheet for improving the thermomechanical properties of polyurethane nanocomposites. Compos Part B Eng 2015;78:192–201. doi:10.1016/j.compositesb.2015.03.089.

[21] Wan T, Chen D. Mechanical enhancement of self-healing waterborne polyurethane by graphene oxide. Prog Org Coatings 2018;121:73–9. doi:10.1016/j.porgcoat.2018.04.016.

[22] Lei L, Xia Z, Zhang L, Zhang Y, Zhong L. Preparation and properties of amino-functional reduced graphene oxide/waterborne polyurethane hybrid emulsions. Prog Org Coatings 2016;97:19–27. doi:10.1016/j.porgcoat.2016.03.011.

Chapter 7

WBPUU/CARBONACEOUS NANOSTRUCTURES INKS FOR DIW 3D PRINTING

7. WBPUU/CARBONACEOUS NANOSTRUCTURES INKS FOR DIW 3D PRINTING

7.1. Aim of the chapter

The aim of this chapter was to develop WBPUU/rGO nanocomposites inks to be used in DIW 3D printing. rGO was added to the WBPUU and to obtain inks with adequate rheological behavior, a high molecular weight polymer, carrageenan (CAR), was included in the formulations.

As previously observed, the amount and type of reinforcements added can strongly affect the rheological behavior of the materials. In this regard, nanocomposite gels with varying contents of reduced graphene oxide and carrageenan were prepared, in order to study their effect on the gel properties. Following previous procedures, rGO and carrageenan were incorporated by two different methods, ex-situ and in-situ. Changes in rheological behaviors of the inks were analyzed by flow tests, dynamic oscillatory tests and structural recovery test.

The addition of rGO and CAR could significantly alter the printing process of the inks, as well as the final properties of the materials. Prepared inks were used in DIW to obtain 3D printed parts. Obtained 3D printed parts were analyzed regarding their morphology, physicochemical, thermal and mechanical properties, and electrical conductivity.

7.2. Preparation and characterization of WBPUU/rGO/CAR nanocomposite inks

The addition of high quantities of graphene is often compromised due to the high hydrophobicity of graphene hindering its dispersion in water. Hence, in order to further regulate the rheology of the systems without excessive increasing rGO content, the addition of another modulating component was necessary. In this case, due to the great properties it offers for this application,

κ-carrageenan was chosen. Carrageenan acts like a gelling agent in aqueous solutions, which in the right concentration will allow for a good 3D printing process.

WBPUU/CAR and WBPUU/rGO/CAR gels were prepared parting from the WBPUU dispersion synthesized in Chapter 3 with a 33 wt.% solid content. For ex-situ nanocomposite gels, vigorous mechanical stirring was used in order to obtain a good dispersion. An ultraturrax homogenizer was employed for this, working at 12000 rpm. First, *Salvia* extract was added to the polyurethane dispersion, acting as a surfactant for improved dispersion of graphene, a ratio of 1:1 for rGO:*Salvia* was used. Afterwards, rGO was added and dispersed with the ultraturrax homogenizer for 20-25 minutes and last carrageenan was added and dispersed for another 10 minutes. Different contents of carrageenan (1 and 2 wt.%) and reduced graphene oxide (0.5 and 1 wt.%) were used to prepare inks (Table 7.1). Nanocomposite inks were named as "xrGOyCAR$_{EX}$", where "x" denotes the content of rGO and "y" the content of carrageenan. For comparative purposes a gel without graphene, just with polyurethane and carrageenan, was prepared (2CAR$_{EX}$), as well as a gel without polyurethane, composed of carrageenan, *Salvia* and graphene dispersed in water (M-0.5rGO2CAR).

Table 7.1. WBPUU, CAR, rGO and Salvia extract contents for ex-situ nanocomposite gels

Sample	WBPUU dispersion (g) (* 33 wt.%)	CAR (g)	rGO (g)	*Salvia* extract (g)	Deionized water (g)	Total weight (g)
2CAR$_{EX}$	19.4	0.4	-	-	0.2	20
0.5rGO1CAR$_{EX}$	19.4	0.2	0.1	0.1	0.2	20
0.5rGO2CAR$_{EX}$	19.4	0.4	0.1	0.1	-	20
1rGO1CAR$_{EX}$	19.4	0.2	0.2	0.2	-	20
M-0.5rGO2CAR	-	0.4	0.1	0.1	19.4	20

For in-situ composite gels, rGO and carrageenan were added dispersed in water during the phase inversion step. *Salvia* extract was first dispersed in

water, followed by rGO, using an ultraturrax homogenizer for 10 minutes, and last carrageenan was added and dispersed, once again using an ultraturrax homogenizer. Quantities used for in-situ prepared nanocomposite gels are shown in Table 7.2.

Table 7.2. WBPUU, CAR, rGO and Salvia extract contents for in-situ nanocomposite gels

Sample	Prepolymer mass (g)	CAR (g)	*Salvia* extract (g)	rGO (g)	Deionized water (g)	Total Weight (g)
$1CAR_{IN}$	30	0.91	-	-	60	90.91
$2CAR_{IN}$	30	1.82	-	-	59.09	90.91
$0.5rGO2CAR_{IN}$	30	1.87	0.47	0.23	58.34	90.91
$1rGO1CAR_{IN}$	30	0.93	0.93	0.47	58.58	90.91

7.2.1. Characterization of WBPUU/rGO/CAR nanocomposite inks

The prepared inks were characterized regarding their rheology, in order to study the behavior that they will show when used in direct ink writing. Following the procedure of Chapter 4 and wanting to consider the effect on both shape fidelity and printability of the materials, three type of test were carried out: flow tests, dynamic oscillatory tests and structural recovery test. For most composite inks, tests were performed using a plate-plate geometry, except for $0.5rGO1CAR_{EX}$, for which the use of concentric cylinders was necessary due to its lower viscosity.

Flow test were performed studying the effect of the shear rate on the viscosity of the inks, viscosity curves are shown in Figure 7.1 and 7.2 for ex-situ and in-situ prepared inks, respectively. Determined viscosity values at different shear rates for the different systems and calculated n values from Power Law (equation 1.1.) are summarized in Table 7.3.

As can be observed, all systems showed shear thinning behavior in the studied shear rate range, necessary for 3D printing [1]. Regarding viscosity values, as

can be seen in viscosity curves and calculated values, both the content of graphene and carrageenan had an effect on the viscosity of the systems, being the inks with higher rGO and CAR contents the ones showing higher viscosities. The content of carrageenan strongly affected the rheological behavior of gels, with mixtures with low concentrations showing lower viscosities [2,3]. This same effect is observed for carbonaceous reinforcement concentration, with viscosity values increasing with reinforcement concentration [4–7].

Table 7.3. Viscosity values measured at different shear rates for ex-situ and in-situ prepared WBPUU, rGO and CAR containing inks

	Sample	η at 0.02 s^{-1} (Pa·s)	η at γ_{nz} (Pa·s)	η at 100 s^{-1} (Pa·s)	n
ex-situ	$2CAR_{EX}$	831.8	68.4	4.1	0.041
	$0.5rGO1CAR_{EX}$	167.6	6.4	0.8	0.186
	$0.5rGO2CAR_{EX}$	1388.0	64.2	4.4	0.137
	$1rGO1CAR_{EX}$	958.0	56.6	4.0	0.139
	M-0.5rGO2CAR	849.3	38.5	2.3	0.082
in-situ	$1CAR_{IN}$	27.5	1.8	0.5	0.374
	$2CAR_{IN}$	271.8	11,8	2.2	0.287
	$0.5rGO2CAR_{IN}$	935.9	26.4	3.2	0.162
	$1rGO1CAR_{IN}$	89.3	6.1	1.3	0.380

For ex-situ prepared inks, $2CAR_{EX}$, $0.5rGO2CAR_{EX}$ and $1rGO1CAR_{EX}$ show similar curves, showing that these compositions resulted in materials with similar viscosities throughout the shear rate scan. $0.5rGO1CAR_{EX}$ ink, however, the low contents of rGO and CAR resulted in lower viscosity values, suggesting an ink with poor shape fidelity. In this case, the low content of carrageenan did not allow for a good gel formation and the low content of rGO was not enough to supply strong flow resistance. When either the content of carrageenan or graphene was increased, $0.5rGO2CAR_{EX}$ and $1rGO1CAR_{EX}$, respectively, inks with significantly higher viscosities were obtained, which will allow for a better printed structures with better shape fidelity [8,9]. It can be observed that the addition of rGO to more concentrated

CAR gels (comparing $2CAR_{EX}$ and $0.5rGO2CAR_{EX}$) showed less influence in the rheological behavior than for less concentrated gels, where this effect was significantly stronger ($0.5rGO1CAR_{EX}$ and $1rGO1CAR_{EX}$), as previously seen in literature reports [10].

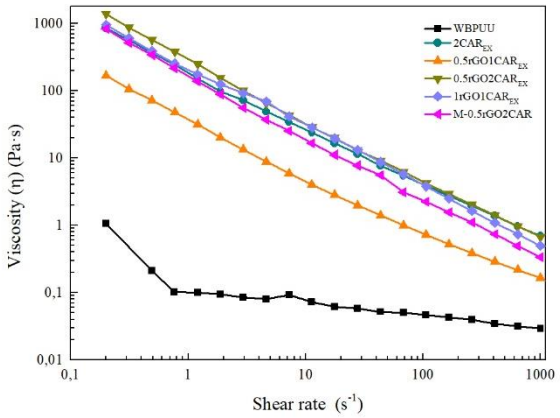

Figure 7.1. Viscosity as a function of shear rate of ex-situ prepared WBPUU, rGO and CAR containing inks

On the other hand, M-0.5rGO2CAR showed similar, though slightly lower, values to $2CAR_{EX}$, $0.5rGO2CAR_{EX}$, and $1rGO1CAR_{EX}$. The moderately lower viscosity shown by M-0.5rGO2CAR shows the effect of WBPUU on the viscosity of the inks. Interactions taking place between the polyurethane-urea and the additive resulted in materials with higher viscosity.

The higher viscosity values shown by 2CAR, $0.5rGO2CAR_{EX}$ and $1rGO1CAR_{EX}$ signal to a better behavior for DIW, due to less flowing after the printing process and, thus, better shape fidelity.

Regarding in-situ prepared inks, a similar behavior was observed (Figure 7.2). Inks with higher carbonaceous reinforcement and carrageenan contents showed higher viscosity values. $0.5rGO2CAR_{IN}$ showed the highest viscosity values, as happened in ex-situ prepared composites, thanks to the high content of carrageenan and it gelling capacity. On the other hands, low content of

carrageenan in $1CAR_{IN,}$ resulted in lower viscosity values, which might result in poor shape fidelity printed parts.

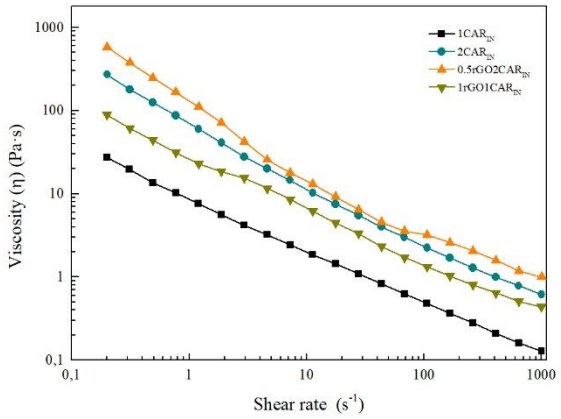

Figure 7.2. Viscosity as a function of shear rate of in-situ prepared WBPUU, rGO and CAR containing inks

Moreover, when comparing in-situ prepared inks with their ex-situ prepared counterparts, in-situ inks showed significantly lower viscosity values. As happened for WBPU/CNF inks, the addition of rGO and CAR during the synthesis process may facilitate the formation of interactions between the polyurethane-urea and the added structures, whereas for ex-situ components, the more difficult formation of these interactions might allow carrageenan to interact with water and form a stronger gel. The lower viscosity of in-situ inks at printing shear rate will allow a better flow and will facilitate the extrusion process. However, the higher viscosity values, at a rest-like state, shown by ex-situ prepared inks, will enhance the shape fidelity of the printed structures.

In order to determine the yield and flow points of the inks, spectromechanical analyses were performed with increasing shear stress. Storage and loss moduli vs. shear stress curves are shown in Figure 7.3 and 7.4. Yield point and flow point values were calculated as the point where the storage modulus begins to deviate from linearity [11] and the crossover point, respectively, and obtained values are shown in Table 7.4.

Regarding ex-situ preparations, it can be observed that 0.5rGO1CAR$_{EX}$ showed low yield point and flow point, beginning to flow and behaving like a liquid at very low shear stress values. The low contents of graphene and carrageenan, as seen for viscosity test, were not enough to form a strong gel.

Carrageenan content strongly influenced the strength of the gels, with systems with higher CAR contents showing higher yield and flow points [12,13]. The more stable gel structure was observed for the ink prepared without polyurethane, indicating that the presence of polyurethane weakens the gel structure and allows for an easier flow. Among polyurethane-urea containing inks, 2CAR$_{EX}$ showed the highest yield and flow points. In this case, because of the lack of graphene and *Salvia* hampering direct water/carrageenan and polyurethane-urea/carrageenan interactions, a better gel structure could be formed [14].

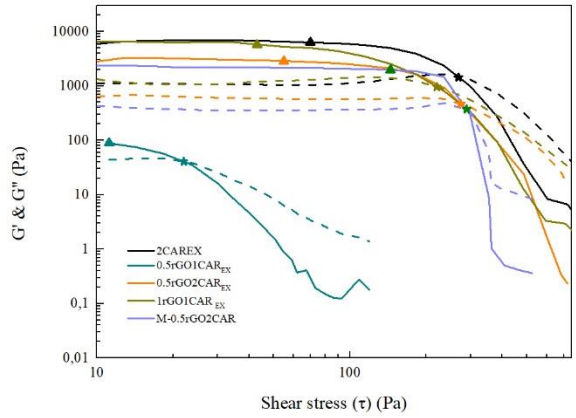

Figure 7.3. Storage (solid line) and loss (dotted line) moduli as a function of shear stress and yield (◢) and flow (★) points of ex-situ prepared WBPUU, rGO and CAR containing inks

For in-situ prepared inks, once again it can be observed that 2CAR$_{IN}$ showed the highest yield and flow points, followed by 0.5rGO2CAR$_{IN}$. 1rGO1CAR$_{IN}$ showed significantly lower values, due to insufficient carrageenan content for a strong gel formation by this method. 1CAR$_{IN}$ composition was also

analyzed and it was observed that it did not present a gel like behavior, due to its low carrageenan content, showing throughout the entire shear stress scan G”>G’.

Regarding the effect of the addition method, in the case of in-situ prepared inks, as happened in viscosity test, lower values than those of ex-situ inks were obtained. $2CAR_{IN}$, $0.5rGO2CAR_{IN}$ and $1rGO1CAR_{IN}$ showed lower yield and flow points than their ex-situ counterparts, attributed to the previously suggested disruption of carrageenan/water gel structure.

The lower values shown by in-situ preparations, may allow for a better extrusion process, due to easy flow at low applied shear. The defined yield point for all inks (except $1CAR_{IN}$) indicates shape fidelity capacity to certain degree [8,15]. The higher storage modulus shown by ex-situ prepared inks may result in 3D printed parts with better shape fidelity.

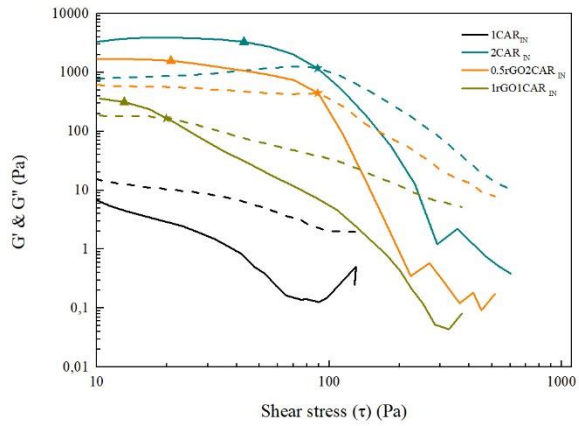

Figure 7.4. Storage (solid line) and loss (dotted line) moduli as a function of shear stress and yield (◢) and flow (★) points of in-situ prepared WBPUU, rGO and CAR containing inks

Table 7.4. Yield and Flow point values for ex-situ and in-situ prepared WBPUU, rGO and CAR containing inks

	Sample	Yield point (Pa)	Flow point (Pa)
ex-situ	$2CAR_{EX}$	98.8	241.8
	$0.5rGO1CAR_{EX}$	11.29	22.1
	$0.5rGO2CAR_{EX}$	69.8	242.1
	$1rGO1CAR_{EX}$	39.8	188.1
	M-0.5rGO2CAR	160.7	291.4
in-situ	$1CAR_{IN}$	-	-
	$2CAR_{IN}$	43.0	89.1
	$0.5rGO2CAR_{IN}$	18.5	65.1
	$1rGO1CAR_{IN}$	12.3	20.3

The structural integrity, thixotropic behavior and potential shape fidelity of the inks were studied by recovery tests, in which the capacity of a material to recover its initial viscosity after a high shear rate state was analyzed. A quick and good viscosity recovery is important to obtain 3D printed parts with good shape fidelity [4]. Figure 7.5 and 7.6 shows the viscosity values of the different inks when different shear rate values are applied. The recovery capacity of each system was calculated using equation 2.1, considering their viscosity after 80 seconds of the low shear rate, simulating a state of rest. Calculated recovery values for inks prepared ex-situ and in-situ are shown in Table 7.5.

As can be observed in Figures 7.5 and 7.6, when a shear rate of 100 s^{-1} was applied, the viscosity of all inks drastically dropped to low values, which would allow for a good flow during printing process. Moreover, it can be seen that when this shear force was removed, the viscosity of the systems immediately went back to higher values.

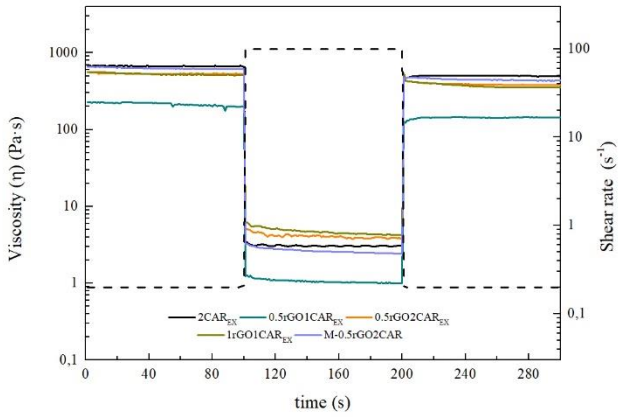

Figure 7.5. Structure recovery tests of ex-situ prepared WBPUU, rGO and CAR

Regarding the effect of the incorporation method, similar average values were obtained regardless this parameter. However, it is worth mentioning that ex-situ preparation systems showed high deviation values, signaling to more heterogeneous systems.

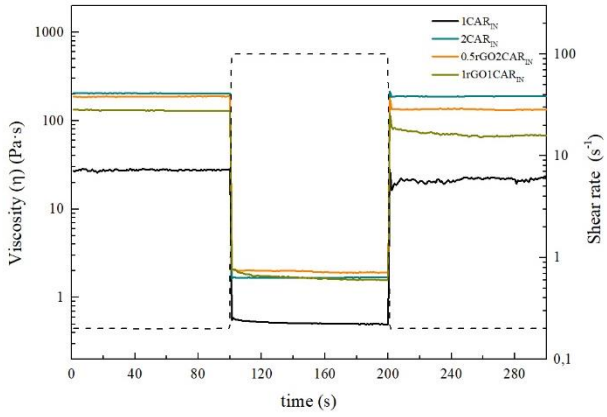

Figure 7.6. Structure recovery tests of in-situ prepared WBPUU, rGO and CAR containing inks

Table 7.5. Structure recovery capacity of ex-situ and in-situ prepared WBPUU, rGO and CAR containing inks

	Sample	Structural recovery (%)
ex-situ	$2CAR_{EX}$	84 ± 8
	$0.5rGO1CAR_{EX}$	53 ± 26
	$0.5rGO2CAR_{EX}$	63 ± 9
	$1rGO1CAR_{EX}$	59 ± 11
	M-0.5rGOCAR	59 ± 15
in-situ	$1CAR_{IN}$	74 ± 13
	$2CAR_{IN}$	91 ± 3
	$0.5rGO2CAR_{IN}$	64 ± 5
	$1rGO1CAR_{IN}$	54 ± 3

7.3. DIW 3D printing of WBPUU/rGO/CAR inks

The prepared inks were used in DIW to obtain 3D printed parts. DIW printing of the inks was carried out using an adapted Tumaker Volaradora printer. As for CNF containing inks in Chapter 5, 3D printed parts were printed at room temperature at 6 $mm \cdot s^{-1}$ using a nozzle with a diameter of 0.8 mm. As design, a cylinder was chosen, with a diameter of 10 mm and a height of 5 mm (Figure 5.7 in Chapter 5). When the printing process finalized, obtained parts were freeze-dried. 3D printed parts were named "3D-X", where "X" is the name of their corresponding inks.

Obtained parts are shown in Figure 7.7. Materials printability and shape fidelity was conditioned by the rheology of the inks.

In agreement with the rheological results, $0.5rGO1CAR_{EX}$ did not show good characteristics for a correct DIW printing process. Though it was able to easily flow and be printed, its low viscosity and low storage modulus resulted in a poor capacity to maintain shape and, thus, in materials with extremely poor shape fidelity, as can be seen in Figure 7.7. Both 3D-$0.5rGO1CAR_{EX}$ and 3D-M-0.5rGO2CAR were not able to fully retain the given shape, due to their poor structural recovery capacity and, thus, low viscosities after printing

process, making them lose height and gain in width due to material flowing. 3D-0.5rGO1CAR$_{EX}$ parts were discarded, due to the poor printing process exhibited and, thus, low precision 3D printed parts.

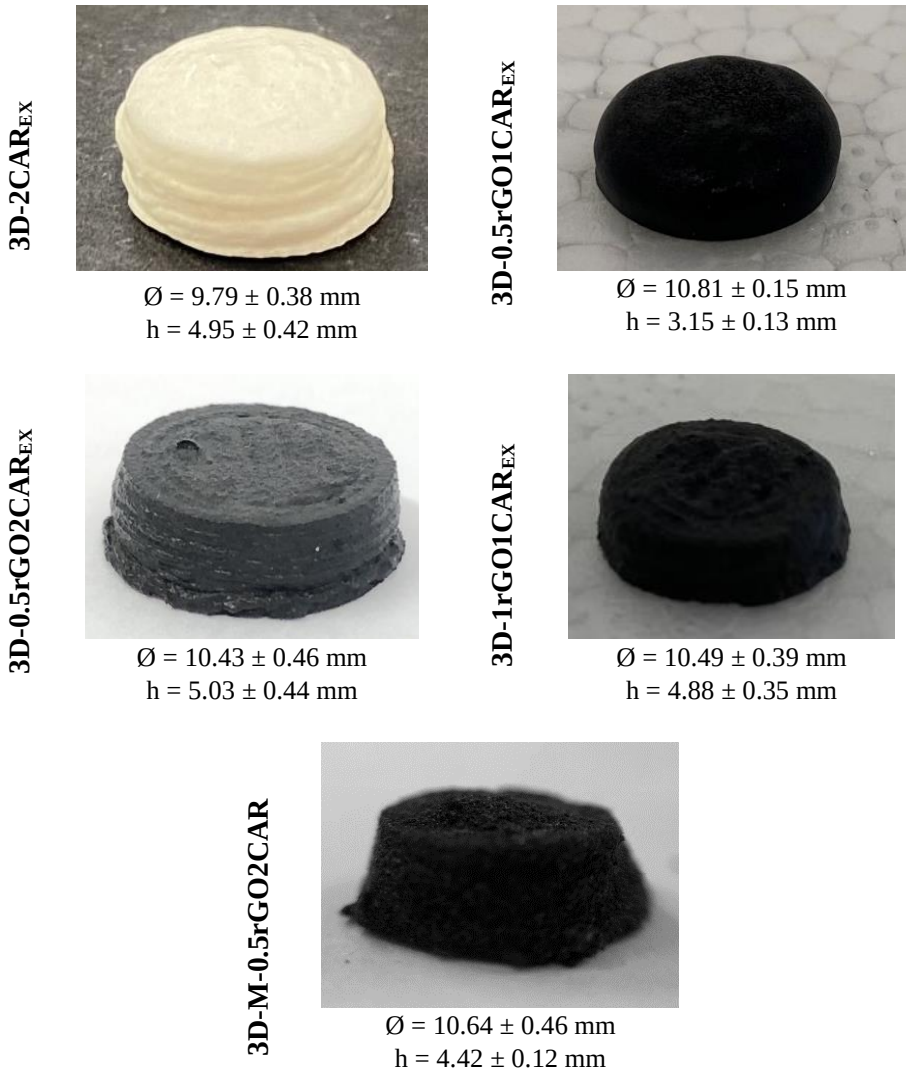

Figure 7.7. Photographs of 3D printed cylinders from ex-situ prepared inks

On the other hand, 2CAR$_{EX}$ and 0.5rGO2CAR$_{EX}$ inks resulted in 3D printed parts with good shape fidelity and with gel layers able to support the structure on top prior to freeze-drying. 3D-1rGO1CAR$_{EX}$ show poorer shape fidelity

than parts produced from inks with 2 wt.% of carrageenan, due to less homogeneous flow caused by nozzle obstructions.

3D printed parts obtained from in-situ prepared inks are shown in Figure 7.8. As suggested by rheological results, best shape fidelity was obtained in parts printed from $2CAR_{IN}$ and $0.5GO2CAR_{IN}$. The low viscosity and liquid-like behavior of $1CAR_{IN}$ did not allow for a good printing process and it was not possible to obtain 3D printed parts from this ink. For 3D-$1rGO1CAR_{IN}$ a good extrusion process was carried out thanks to its low viscosity under high shear rates and low yield and flow points, but it was unable to fully retain shape and 3D parts with low shape fidelity were obtained.

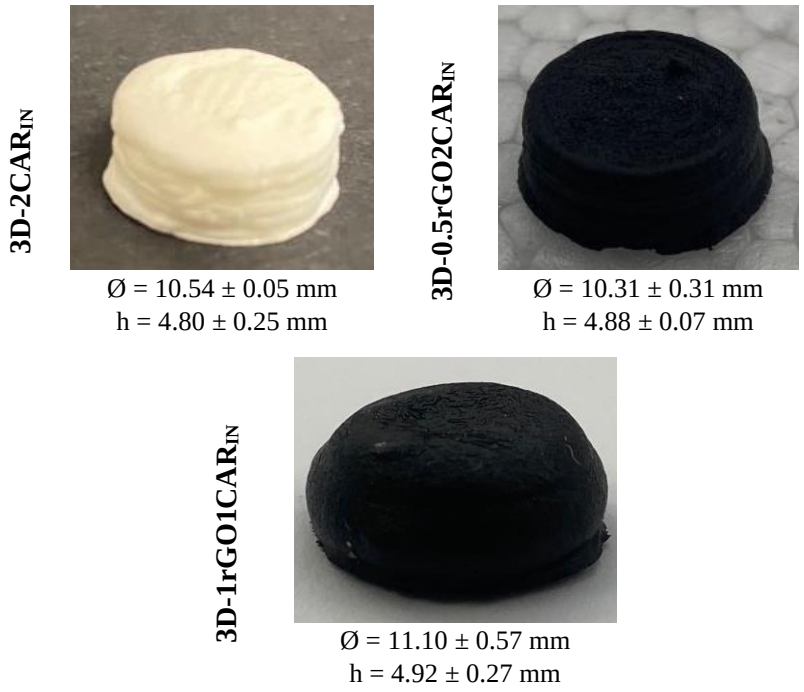

Figure 7.8. Photographs of 3D printed cylinders from in-situ prepared inks

Regardless the preparation method, it is worth noting that systems containing 2 wt.% of carrageenan show the best shape fidelity.

It is also worth noting that, as happened in Chapter 5, ex-situ prepared gels show some trouble during printing process, due to the presence of agglomerations obstructing the nozzle. This fact suggested a poorer dispersion of reinforcements than in their in-situ counterparts. However, these obstructions only happened few and far between and did not impede the correct obtaining of 3D printed parts.

7.3.1. Characterization of 3D printed parts

3D printed parts were analyzed by FTIR spectroscopy, in order to observe possible interaction between the different components of inks.

The spectra of the printed parts obtained from ex-situ and in-situ prepared inks are shown in Figure 7.9 and 7.10, respectively. All spectra showed the characteristic polyurethane bands related to N-H, CH_2, CH_3, C=O, C-N and C-O-C, except 3D-M-0.5rGO2CAR. 3D-M-0.5rGO2CAR is prepared without polyurethane and it shows bands corresponding to carrageenan spectrum; bands at 3277, 2918, 1378, 1227, 1124, 1032, 1000, 920 and 843 cm^{-1} can be seen, corresponding to O-H stretching, CH stretching, sulphates, O=S=O asymmetric stretching, asymmetric stretching of glycosidic bonds, C-OH +S=O, glycosidic bonds, C-O-C and C4-O-S stretching, respectively [16].

For 3D parts containing polyurethane-urea no major differences are observed in the spectra. The main difference lays on the N-H band, located around the 3300 cm^{-1} region (Figure 7.9 inset). An increase of the intensity of this band can be observed with the addition of carrageenan and graphene, being 3D-0.5rGO2CAR$_{EX}$ the one showing the most intense band. The presence of carrageenan and *Salvia* extract altered this band, which could be attributed to the overlapping of the bands of each component [17,18].

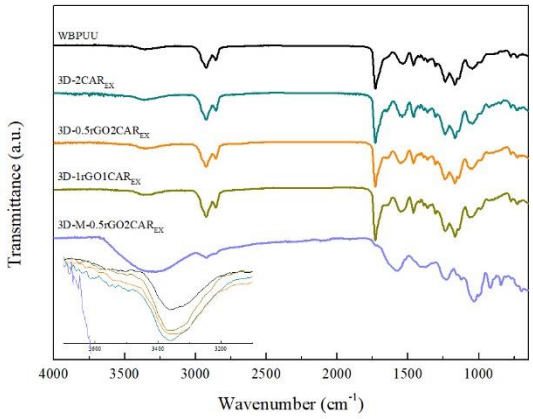

Figure 7.9. FTIR spectra of 3D printed parts from ex-situ prepared CAR and rGO containing inks

FTIR spectra of 3D printed parts from in-situ prepared inks are shown in Figure 7.10. The same behavior than for parts printed from ex-situ prepared inks was observed, with an increase of the intensity of the N-H band for systems containing higher amounts of carrageenan and graphene (Figure 7.10 inset).

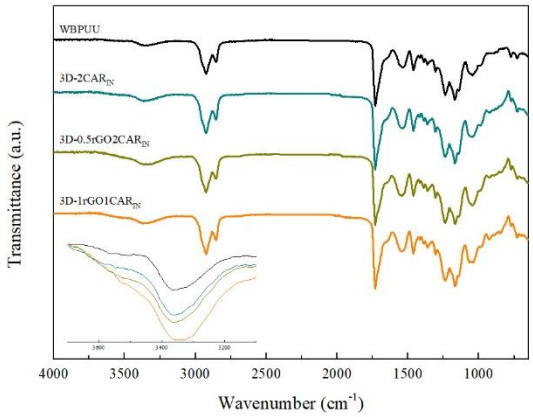

Figure 7.10. FTIR spectra of 3D printed parts from in-situ prepared CAR and rGO containing inks

The morphology of the printed parts was studied by SEM. Figure 7.11 shows SEM images of the different 3D printed parts at different magnifications. It

can be observed that the morphology of the 3D printed parts was strongly influenced by the presence and amount of carrageenan, graphene and *Salvia*, as well as by the ink preparation method.

For 3D printed parts obtained from ex-situ prepared inks, it can be observed that 3D-2CAR$_{EX}$ showed the most homogeneous morphology, presenting spheric pores with an average diameter of 45.4 ± 9.1 µm. However when rGO and *Salvia* are added, changes on the morphology can be obseved. The addition of carbonaceous nanostructures to a carrageenan-based hydrogel can result in bigger pores [19]. For 3D-0.5rGO2CAR$_{EX}$ bigger and slightly more elongated pores can be observed, with an average length of 142.8 ± 30.6 µm and with of 44.2 ± 3.8 µm, as well as some spherical pores with an average diameter of 67.0 ± 13.2 µm. For 3D-1rGO1CAR$_{EX}$ spherical-like pores are observed again (Ø = 55.4 ± 7.4 µm), however, in this case the pores are less defined and showing a more open structure.

Two types of water can be found in hydrogels, free and bonded water, which will have an impact in the porosity of the systems. For 3D-2CAR$_{EX}$, due to the higher amount of interactions between the carrageenan and the water, the amount of free water was lower. However, these interactions can be altered by the addition of rGO and *Salvia*. New interactions formed between the carrageenan and the new components will result in more free water. The liberation method of each type of water will strongly alter the pores sizes and shape in each system, resulting in materials with overall bigger pores [20].

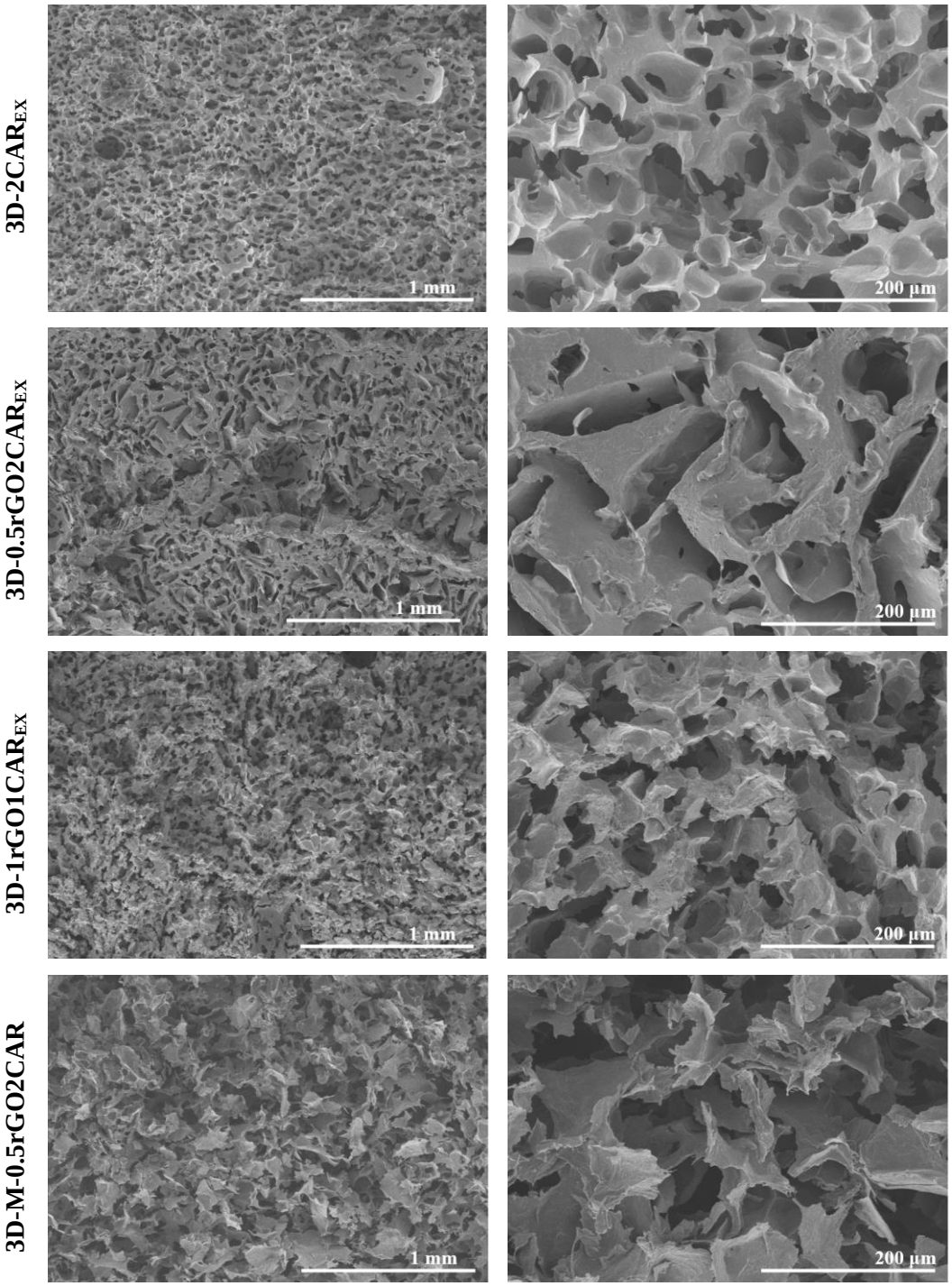

Figure 7.11. SEM images of 3D printed parts from ex-situ prepared inks

It can be observed that without the presence of polyurethane, for 3D-M-0.5rGOCAR, a more open cell structure is seen, governed by the presence of pores. It is also worth noting, that without WBPUU the total solid content was significantly lower, being the content of water to be removed significantly higher and the density of the 3D printed part much lower.

For 3D printed parts obtained from in-situ preparations, a very different morphology is observed (Figure 7.12). As previously suggested in rheological studies, in-situ preparations promoted interaction between polyurethane-urea, carrageenan, *Salvia* extract and remaining oxidized groups in rGO, instead of with water. As a result, there was a larger amount of free water present on the hydrogels. The resulting morphology is attributed to the removal of this free water by freeze-drying.

3D printed parts obtained from in-situ ink showed elongated pores. 3D-2CAR$_{IN}$ exhibits pores with a length of 303.0 ± 37.8 μm and a width of 72.7 ± 13.9 μm, for 3D-0.5rGO2CAR$_{IN}$ the pore size increased to 433.9 ± 60.2 and 78.4 ± 7.5 μm, and lastly for 3D-1rGO1CAR$_{IN}$ pores of 417.8 ± 62.9 x 65.9 ±8.9 μm were observed. As can be seen circled in red, for 3D-1rGO1CAR$_{IN}$, the crushing of the cell walls began to take place.

Though in-situ prepared inks presented lower viscosity values, it can be observed that high storage modulus and strong reinforcement supplied by the addition of rGO did not allow for the structures to be crushed and no broken cell walls were observed, as happened in Chapter 5.

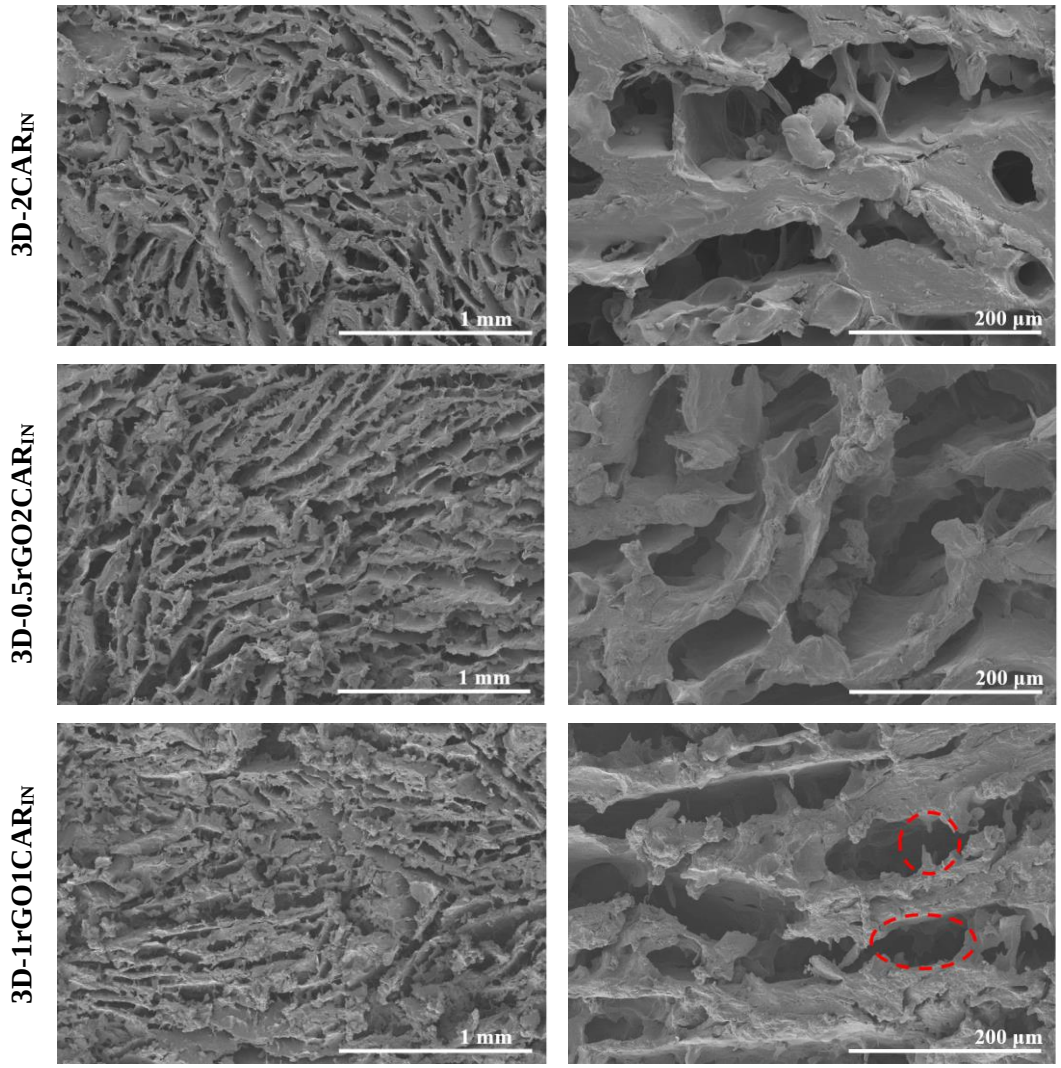

Figure 7.12. SEM images of 3D printed parts from in-situ prepared inks

DSC test were carried out to study the thermal transitions of the printed materials. Obtained thermograms are shown in Figure 7.13 and 7.14 for parts printed from ex-situ and in-situ prepared inks, respectively, and T_{gSS}, T_{HS} and ΔH_{HS} values are summarized in Table 7.6.

It is worth noting that the addition of neither carrageenan, nor graphene, nor *Salvia* had an important effect on the glass transition related soft segment of the polyurethane.

For printed parts from ex-situ prepared inks, an intense increase of the enthalpy related to the short ordering of the hard segment can be seen. The interactions that have formed between the matrix and the *Salvia* and/or the carrageenan increased the ordering in the structures, which hindered the melting process of the materials [18,21]. As a result, higher transition temperatures are also observed for composites containing graphene, *Salvia* and carrageenan. The highest values are observed for 3D-1rGO1CAR$_{EX}$, are attributed to the higher amount of *Salvia* resulting in more interaction and the higher amount of graphene interfering in the melting process.

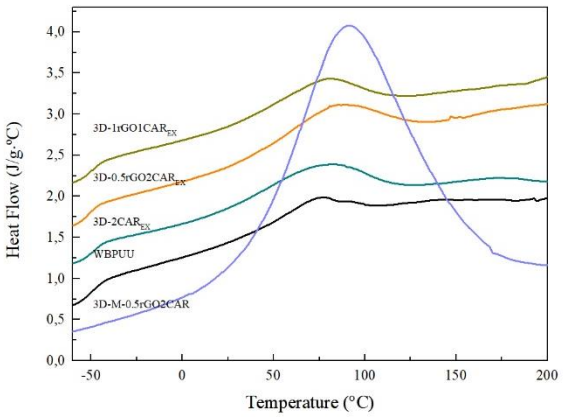

Figure 7.13. DSC scans for 3D parts obtained from ex-situ prepared CAR and rGO containing inks

For in-situ inks based composites, an even higher increase of both the T_{HS} and the ΔH_{HS} is observed. This suggests that the addition of the components during the synthesis process of the polyurethane favored the interactions and helped form more stable materials, needing more energy for the breaking of the interaction on their structures.

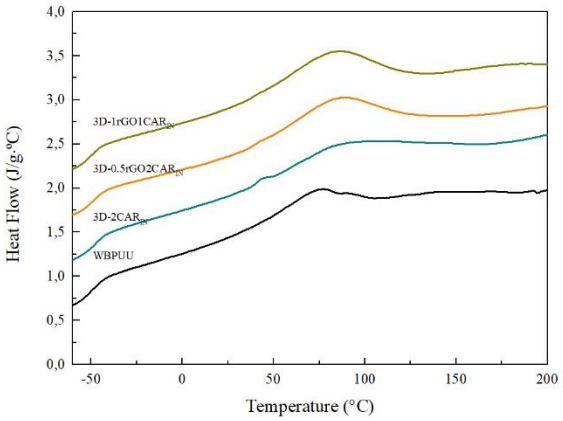

Figure 7.14. DSC scans for 3D parts obtained from in-situ prepared CAR and rGO containing inks

Table 7.6. Thermal transitions' values observed from the DSC curves for 3D printed parts containing CAR and rGO

	Sample	T_g (ºC)	T_{HS} (ºC)	ΔH_{HS} (J·g^{-1})
ex-situ	WBPUU	-49.1	74.7	9.0
	3D-2CAR	-48.7	78.3	17.5
	3D-0.5rGO2CAR$_{EX}$	-49.0	78.7	17.6
	3D-1rGO1CAR$_{EX}$	-51.1	80.7	21.0
	3D-M-0.5rGOCAR	-	-	-
in-situ	3D-2CAR$_{IN}$	-47.7	89.0	19.0
	3D-0.5rGO2CAR$_{IN}$	-48.4	86.0	19.8
	3D-1rGO1CAR$_{IN}$	-49.7	83.0	21.2

Thermogravimetric analysis were performed in order to study the thermal stability of the printed parts. TGA and DTG curves are shown in Figure 7.15 and 7.16 for 3D printed parts prepared from ex-situ or in-situ preparations, respectively.

Different composition resulted in material with different thermal behavior. 3D-M-0.5rGOCAR, due to its lack of polyurethane followed a different trend than other systems, similar to that of pure κ-carrageenan [22,23]. It showed an

initial weight loss at low temperatures, attributed to water evaporation. The degradation of this system began at lower temperatures than for WBPUU containing composites, however due to high graphene content on the systems, at 700°C a high amount of residue remained.

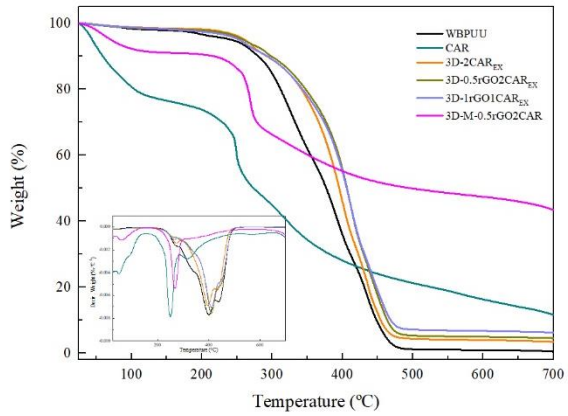

Figure 7.15. TGA and DTG curves for 3D parts obtained from ex-situ prepared CAR and rGO containing inks

Regarding ex-situ inks based 3D printed parts, it can be observed that all three systems containing polyurethane-urea show a similar curve. 3D-2CAR$_{EX}$ showed the three degradation peaks of urea groups, urethane groups and soft segment typical of polyurethane-ureas. However, it can be observed that an improvement of the thermal degradation took place with the addition of carrageenan, attributed to the formation of interactions stabilizing the urethane-urea groups [24]. For graphene containing parts, the curves are slightly different. Systems containing graphene showed higher thermal stability than 3D-2CAR$_{EX}$. As seen in previous chapters, graphene has extremely high thermal stability and its use as nanoreinforcement can enhance stability of systems [17,25], as happened for composite films and filaments (Chapter 4). In 3D-0.5rGO2CAR$_{EX}$ and 3D-1rGO1CAR$_{EX}$ DTG curves, the last peak is only appreciated as a shoulder. The protection supplied by reduced graphene oxide delayed the degradation process of the polyurethane and peaks overlap. Moreover, the shoulder attributed to urea groups is more

pronouncedly seen in curves containing carrageenan, due to degradation of CAR coinciding with degradation temperature of urea groups, as seen in carrageenan degradation curve [22].

For 3D printed parts obtained from in-situ preparations, the same behavior was observed. The addition of CAR resulted in an improvement of the thermal stability of the materials, which was further enhanced with the addition of reduced graphene oxide. Regarding the effect of the incorporation method, it can be observed that in-situ preparation based composites showed slightly higher stability, attributed to the higher amount of interactions present.

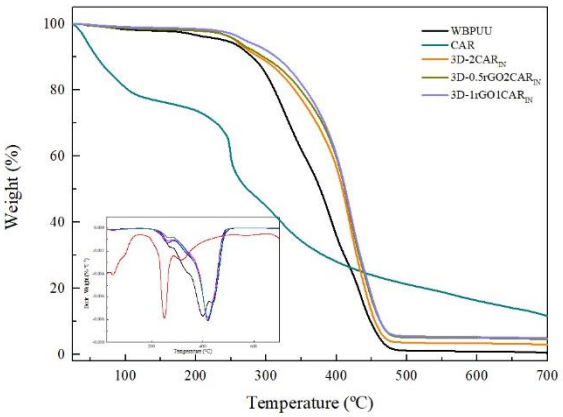

Figure 7.16. TGA and DTG curves for 3D parts obtained from in-situ prepared CAR and rGO containing inks

The mechanical properties of the printed parts were analyzed by compressions tests. Young modulus, density, specific Young modulus, stress at 60% strain and densification strain values are shown on Table 7.7. Moreover, Figure 7.17 shows stress vs strain curves for parts prepared from ex-situ and in-situ prepared inks, respectively.

Table 7.7. Young modulus, specific Young modulus, stress at 60% strain and densification strain values for WBPU/rGO/CAR 3D printed parts

	Sample	Young modulus (MPa)	Density ($g \cdot cm^{-3}$)	Specific Young modulus ($MPa \cdot cm^3 \cdot g^{-1}$)	Stress at 60% strain (MPa)	Densification Strain (%)
ex-situ	3D-2CAR	23.1 ± 3.7	0.39 ± 0.05	60.6 ± 12.7	3.1 ± 0.2	48.9 ± 1.3
	3D-0.5rGO2CAR$_{EX}$	7.6 ± 1.6	0.38 ± 0.03	20.4 ± 5.4	1.4 ± 0.2	50.3 ± 0.5
	3D-1rGO1CAR$_{EX}$	12.4 ± 3.6	0.40 ± 0.01	30.9 ± 8.9	1.9 ± 0.1	51.8 ± 0.8
	3D-M-0.5rGO2CAR	0.4 ± 0.1	0.04 ± 0.01	9.4 ± 2.3	0.1 ± 0.0	48.9 ± 1.4
in-situ	3D-2CAR$_{IN}$	24.6 ± 2.0	0.39 ± 0.01	62.6 ±5.3	2.6 ± 0.2	49.6 ± 0.3
	3D-0.5rGO2CAR$_{IN}$	24.7 ± 3.5	0.38 ± 0,01	64.3 ±9.3	2.1 ± 0.3	49.8 ± 1.0
	3D-1rGO1CAR$_{IN}$	38.0 ± 3.6	0.41 ± 0.02	92.8 ± 9.3	3.0 ± 0.3	50.7 ±0.6

As happened in Chapter 5, stress/strain curves show the typical three step compression behavior, divided in the elastic, the plastic and the densification zones.

When analyzing the results shown by parts obtained from ex-situ prepared inks, the great influence of polyurethane on the behavior of the material can be observed. 3D-M-0.5rGOCAR showed very different properties to those containing WBPUU, showing significantly lower values of Young modulus and stress, due to the more brittle behavior of its governing carrageenan [26]. When comparing other systems, it can be seen that 3D-2CAR system showed higher modulus and stress values than systems containing graphene. The poor reinforcements effect supplied by graphene could be attributed to two factor. On the first place, the addition of graphene could have interfered in the formation of the gel structure, as seen previously on rheological analyses, and, thus, result in poorly structured materials. On the other hand, the harder homogenation process for these materials, and, in consequence, the longer

high shear agitation process might have damaged graphene flakes, resulting in smaller flakes and, therefore, in worse reinforcement effect [27,28].

In the case of printed parts obtained from in-situ prepared inks, a different trend is observed with the addition of graphene. Materials with higher Young modulus and stress values were obtained when graphene and carrageenan were added by this method. Despite the phase inversion and chain extension steps of the synthesis being carried out at low temperatures in order to favor NCO and NH2 reaction, it is possible that some OH groups of carrageenan and rGO may have reacted with NCO, and formed chemical bonds.

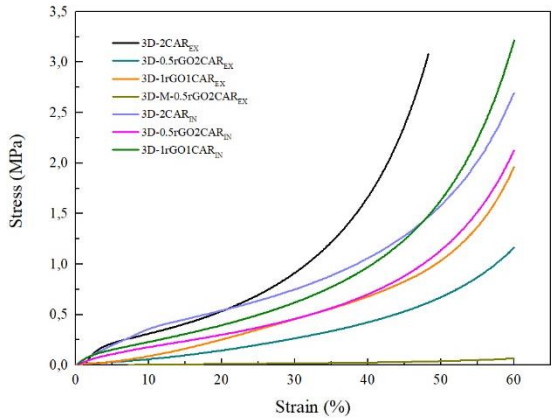

Figure 7.17. Stress/Strain curves from compression tests for WBPU/rGO/CAR 3D printed parts

When a small amount of graphene was added but the carrageenan content was maintained, the addition of graphene showed no significant effects. However, for higher amounts of graphene, the reinforcement effect can be clearly seen, with 3D-1rGO1CAR$_{IN}$ showing enhanced mechanical properties, with higher Young modulus, specific modulus and stress values, proving the characteristic reinforcement capacity of graphene [17,25,29], as well as reinforcement supplied by *Salvia*, as seen in Chapter 4.

7.4. Coating of printed pieces

In order to supply electrical conductive capacity to the 3D printed parts, a graphene coating was applied, as done for nanocomposite films in Chapter 6. 3D-2CAR$_{IN}$ and 3D-0.5rGO2CAR$_{IN}$ were selected based on their good shape fidelity and shown properties. 3D printed parts were submerged for a few seconds in NMP to allow a better penetration of the coating, and were then sonicated in a sonication bath for 15 minutes in a rGO dispersion in cyclohexane (10 mg·mL^{-1}). Coated materials were then cleaned with distilled water and left to dry at room temperature.

3D-2CAR$_{IN}$ and 3D-0.5rGO2CAR$_{IN}$ were named 3D-2CAR$_{IN}$/rGO and 3D-0.5rGO2CAR$_{IN}$/rGO, respectively, after coating process.

The electrical conductivity of the coated 3D printed parts was analyzed measuring conductive capacity when voltage was applied.

Tests showed both coated systems showed electrical conductive behavior, however, strong differences were observed between the coated parts. 3D-0.5rGO2CAR$_{IN}$/rGO showed better conductivity than 3D-2CAR$_{IN}$/rGO, with resistance values of (7.4 ± 11.5) x 10^6 Ω and (373.0 ± 44.2) x 10^6 Ω, respectively.

The higher conductivity shown by the coated composite is in agreement with results observed in Chapter 6, once again suggesting that the better affinity between the composite surface and the coating rGO result in a better coating process.

Morphology of the coated materials was analyzed by Scanning Electron Microscopy, where both the internal morphology of the systems (Figure 7.18a-f) and the coating layer (Figure 7.18c-f) were observed.

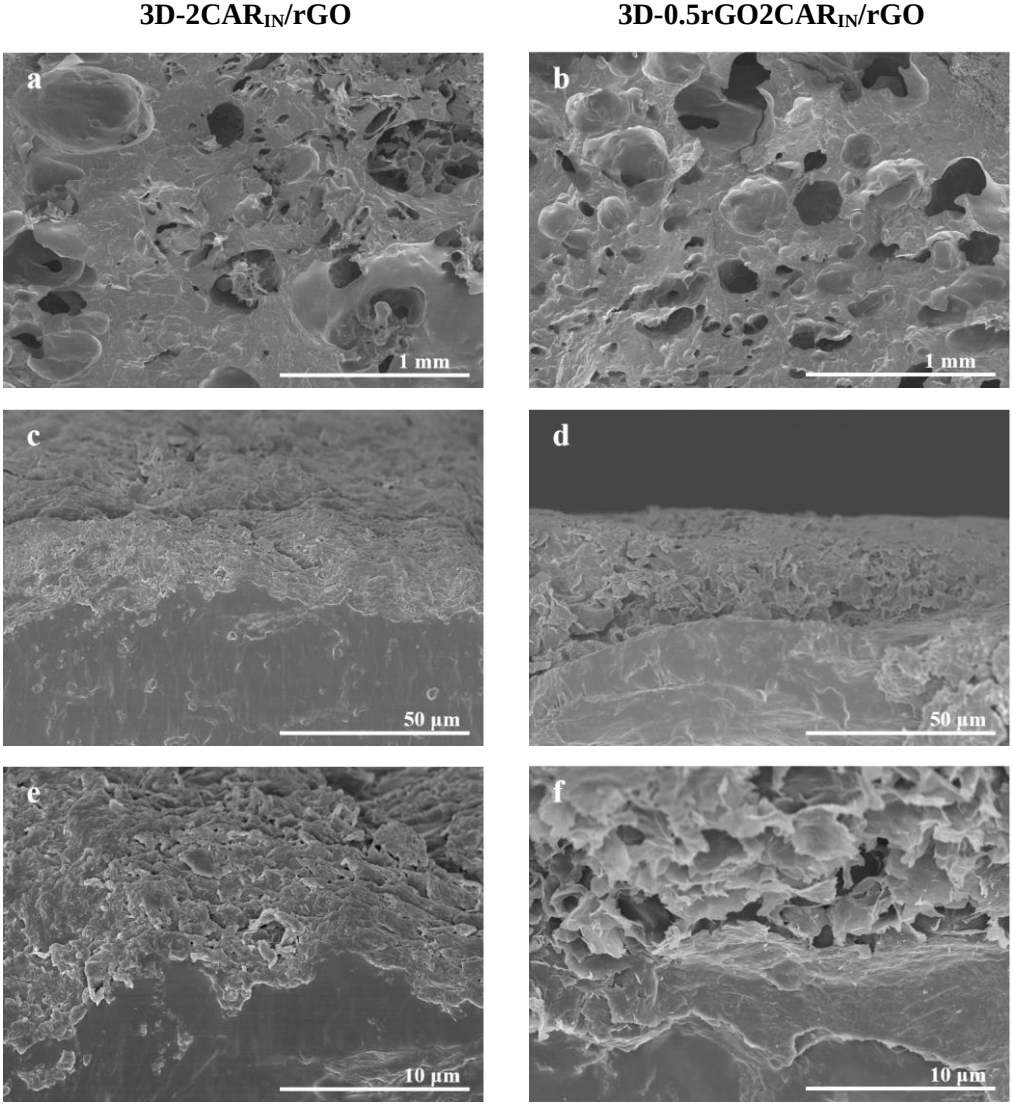

Figure 7.18. SEM images of rGO-coated 3D printed parts

Figures 7.18a and 7.18b show damage taken place in the structure of the materials during the coating process. It can be observed that after coating process both materials lost the initial porous structure shown by their uncoated homologues. Though materials still presented a somewhat porous structure, the elongated porous shape previously observed was no longer

present. 3D-0.5rGO2CAR$_{IN}$/rGO showed a slightly less damaged structure, with a more homogeneous structure, formed by relatively similarly shaped and homogenously dispersed porous. The graphene present in the structure might have helped protect the material and impede further damaging.

When studying the formed coat (Figure 7.18c-f), a successful coating process can be assumed, a rGO shell surrounding the sample can be seen. As happened in Chapter 4, a thicker coat was obtained in the case of the coated composite, suggesting that the better affinity between the composite and the coating material resulted in a better adhesion, which in turns results in a better electrical conductivity.

In order to assess the effect that the coating process might have had in the structure and mechanical behavior of the printed parts, dynamic mechanical analyses were performed for coated parts and their uncoated counterparts. Obtained curves are shown in Figure 7.19.

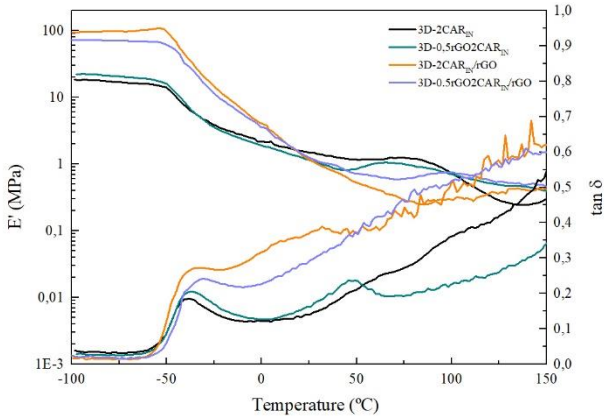

Figure 7.19. Dynamic-mechanical curves of coated 3D printed parts and uncoated homologues

As can be observed, coated parts show higher storage modulus values than uncoated counterparts at low temperatures, that could be attributed to the

formation of the graphene shell surrounding the material, observed by SEM. However, as temperature rises the lower thermomechanical stability of coated parts is clearly seen. The resulting damaged structures, after the coating process, showed poorer thermomechanical behavior of the systems than their uncoated counterparts, resulting in materials with lower stiffness throughout the temperature scan.

7.5. Conclusions

In this chapter, WBPUU based inks containing rGO were prepared, in which carrageenan was used to modulate the rheology of the inks. All inks exhibited shear thinning behavior, with defined yield points and good structural recovery capacity, in general. However, it could be observed that the addition of graphene and *Salvia* to the inks disrupted the gel structure formed by carrageenan, lowering viscosity, yield and flow point and recovery capacity. In-situ prepared inks showed, once again, lower rheological values, attributed to the formation of direct interactions between the matrix and the reinforcement.

Inks were used in DIW to prepare 3D printed parts. Inks with higher contents of carrageenan showed better shape fidelity, whereas inks containing low CAR and rGO contents showed no capacity to maintain the printed shape. 3D printed parts showed very different morphologies, depending on the method the inks were prepared, with in-situ inks producing larger and more elongated pores. Morphology changes were attributed to the effect of the viscosity of the inks and the state of the water present on them. Composition and preparation method of the inks affected the content of free or bonded water of the samples, and the liberation of each type of water resulted in different pore structures. When analyzing mechanical properties, a very different behavior was observed depending on the incorporation method of the reinforcements. In-situ prepared inks resulted in 3D printed parts with enhanced mechanical behavior, due to the great reinforcement effect of graphene and *Salvia*, as well

as due to the possible formation of chemical bonds by this preparation method. On the other hand, 3D printed parts prepared from ex-situ preparations did not exhibit this behavior, due to the longer high shear agitation times needed that could have destroyed the graphene flakes. After coating process, 3D printed parts exhibited electrical conductivity, however during coating process their structures were slightly damaged.

7.6. References

[1] Lewis JA, Smay JE, Stuecker J, Cesarano J. Direct ink writing of three-dimensional ceramic structures. J Am Ceram Soc 2006;89:3599–609. doi:10.1111/j.1551-2916.2006.01382.x.

[2] Liu S, Chan WL, Li L. Rheological properties and scaling laws of κ-carrageenan in aqueous solution. Macromolecules 2015;48:7649–57. doi:10.1021/acs.macromol.5b01922.

[3] Bui TNTV. Structure, rheological properties and connectivity of gels formed by carrageenan extracted from different red algae species. Le Mas Université, 2019.

[4] Li H, Liu S, Li L. Rheological study on 3D printability of alginate hydrogel and effect of graphene oxide. Int J Bioprinting 2016;2:54–66. doi:10.18063/IJB.2016.02.007.

[5] Pinargote NWS, Smirnov A, Peretyagin N, Seleznev A, Peretyagin P. Direct ink writing technology (3d printing) of graphene-based ceramic nanocomposites: A review. Nanomaterials 2020;10:1–48. doi:10.3390/nano10071300.

[6] Loh HA, Graves AR, Stinespring CD, Sierros KA. Direct ink writing of graphene-based solutions for gas sensing. ACS Appl Nano Mater 2019;2:4104–12. doi:10.1021/acsanm.9b00572.

[7] Manapat JZ, Mangadlao JD, Tiu BDB, Tritchler GC, Advincula RC.

High-strength stereolithographic 3D printed nanocomposites: graphene oxide metastability. ACS Appl Mater Interfaces 2017;9:10085–93. doi:10.1021/acsami.6b16174.

[8] Vadillo J, Larraza I, Calvo-Correas T, Gabilondo N, Derail C, Eceiza A. Role of in situ added cellulose nanocrystals as rheological modulator of novel waterborne polyurethane urea for 3D-printing technology. Cellulose 2021;28:4729–44. doi:10.1007/s10570-021-03826-6.

[9] Schwab A, Levato R, D'Este M, Piluso S, Eglin D, Malda J. Printability and shape fidelity of bioinks in 3D bioprinting. Chem Rev 2020;120:11028–55. doi:10.1021/acs.chemrev.0c00084.

[10] Autio K, Vesterinen E, Stolt M. Rheological properties of mixed starch-κ-carrageenan gels in relation to enzymatic digestibility. Food Hydrocoll 2002;16:169–74. doi:10.1016/S0268-005X(01)00074-1.

[11] Cyriac F, Lugt PM, Bosman R. On a new method to determine the yield stress in lubricating grease. Tribol Trans 2015;58:1021–30. doi:10.1080/10402004.2015.1035414.

[12] Chen Y, Liao M-L, Dunstan DE. The rheology of K+-κ-carrageenan as a weak gel. Carbohydr Polym 2002;50:109–16. doi:10.1016/S0144-8617(02)00009-7.

[13] Derkach SR, Ilyin SO, Maklakova AA, Kulichikhin VG, Malkin AY. The rheology of gelatin hydrogels modified by κ-carrageenan. LWT - Food Sci Technol 2015;63:612–9. doi:10.1016/j.lwt.2015.03.024.

[14] Liu S, Bao H, Li L. Thermoreversible gelation and scaling laws for graphene oxide-filled κ-carrageenan hydrogels. Eur Polym J 2016;79:150–62. doi:10.1016/j.eurpolymj.2016.04.027.

[15] Zhang X, Huo W, Liu J, Zhang Y, Zhang S, Yang J. 3D printing

boehmite gel foams into lightweight porous ceramics with hierarchical pore structure. J Eur Ceram Soc 2020;40:930–4. doi:10.1016/j.jeurceramsoc.2019.10.032.

[16] Prado-Fernández J, Rodríguez-Vázquez JA, Tojo E, Andrade JM. Quantitation of κ-, ι- and λ-carrageenans by mid-infrared spectroscopy and PLS regression. Anal Chim Acta 2003;480:23–37. doi:10.1016/S0003-2670(02)01592-1.

[17] Lee JH, Kim SH. Fabrication of silane-grafted graphene oxide and its effect on the structural, thermal, mechanical, and hysteretic behavior of polyurethane. Sci Rep 2020;10:1–13. doi:10.1038/s41598-020-76153-8.

[18] Santamaria-Echart A, Fernandes I, Ugarte L, Barreiro F, Corcuera MA, Eceiza A. Green nanocomposites from Salvia-based waterborne polyurethane-urea dispersions reinforced with nanocellulose. Prog Org Coatings 2021;150:105989. doi:10.1016/j.porgcoat.2020.105989.

[19] Mokhtari H, Kharaziha M, Karimzadeh F, Tavakoli S. An injectable mechanically robust hydrogel of Kappa-carrageenan-dopamine functionalized graphene oxide for promoting cell growth. Carbohydr Polym 2019;214:234–49. doi:10.1016/j.carbpol.2019.03.030.

[20] Tarashi S, Nazockdast H, Sodeifian G. Reinforcing effect of graphene oxide on mechanical properties, self-healing performance and recoverability of double network hydrogel based on κ-carrageenan and polyacrylamide. Polymer 2019;183:121837. doi:10.1016/j.polymer.2019.121837.

[21] Nguyen DA, Lee YR, Raghu A V, Jeong HM, Shin CM, Kim BK. Morphological and physical properties of a thermoplastic polyurethane reinforced with functionalized graphene sheet. Polym Int 2009;58:412–7. doi:10.1002/pi.2549.

[22] Mahmood WAK, Khan MMR, Yee TC. Effects of reaction temperature on the synthesis and thermal properties of carrageenan ester. J Phys Sci 2014;25:123–38.

[23] Mahdavinia GR, Massoudi A, Baghban A, Shokri E. Study of adsorption of cationic dye on magnetic kappa-carrageenan/PVA nanocomposite hydrogels. J Environ Chem Eng 2014;2:1578–87. doi:10.1016/j.jece.2014.05.020.

[24] Cao X, Habibi Y, Lucia LA. One-pot polymerization, surface grafting, and processing of waterborne polyurethane-cellulose nanocrystal nanocomposites. J Mater Chem 2009;19:7137–45. doi:10.1039/b910517d.

[25] Król P, Król B, Pielichowska K, Špírková M. Composites prepared from the waterborne polyurethane cationomers—modified graphene. Part I. Synthesis, structure, and physicochemical properties. Colloid Polym Sci 2015;293:421–31. doi:10.1007/s00396-014-3417-3.

[26] Nussinovitch A, Corradini MG, Normand MD, Peleg M. Effect of sucrose on the mechanical and acoustic properties of freeze-dried agar, κ-carrageenan and gellan gels. J Texture Stud 2000;31:205–23. doi:10.1111/j.1745-4603.2000.tb01417.x.

[27] Nawaz K, Ayub M, Ul-Haq N, Khan MB, Niazi MBK, Hussain A. Effects of selected size of graphene nanosheets on the mechanical properties of polyacrylonitrile polymer. Fibers Polym 2014;15:2040–4. doi:10.1007/s12221-014-2040-8.

[28] Gao W, Zhao N, Yao W, Xu Z, Bai H, Gao C. Effect of flake size on the mechanical properties of graphene aerogels prepared by freeze casting. RSC Adv 2017;7:33600–5. doi:10.1039/c7ra05557a.

[29] Pokharel P, Pant B, Pokhrel K, Pant HR, Lim JG, Lee DS, et al. Effects of functional groups on the graphene sheet for improving the

thermomechanical properties of polyurethane nanocomposites. Compos Part B Eng 2015;78:192–201. doi:10.1016/j.compositesb.2015.03.089.

Chapter 8

INCORPORATION OF BIOACTIVE PLANT EXTRACTS TO WBPUU INKS FOR 3D PRINTING

8. INCORPORATION OF BIOACTIVE PLANT EXTRACTS TO WBPUU INKS FOR 3D PRINTING

8.1. Aim of the chapter

In this chapter the possibility to add natural extract in order to supply the inks with new functionalities, such as antimicrobial behavior, was analyzed. In this regard, three types of natural extracts were selected, *Haematoxylon campechianum L.* (Logwood (LW)), *Castanea sativa L.* (Chestnut (CN)) and *Rhamnus frangula L.* (Alder Buckthorn (AB)). Natural extracts often show good antimicrobial behavior, which could be of interest for 3D printable inks in order to further propel their potential.

For gels preparations, high solid contents waterborne polyurethane-urea dispersions were prepared. Natural extracts were added by two different methods, ex-situ and in-situ, and in different contents to analyze the effect of the addition method and their amount on the inks, as well as the type of extract used.

The rheological behavior of each ink was analyzed in order to predict their potential for DIW 3D printing. Moreover, the physicochemical properties and the antimicrobial behavior of the neat plant extracts and the dried composites were analyzed. Afterwards, the more suitable inks were chosen and used to obtain 3D printed parts, which were later characterized regarding their morphology and mechanical properties.

8.2. The use of natural extracts

The wide and natural abundance of plant extracts, together with their reported extend beneficial effects, makes natural extracts a very interesting additive option [1–5]. Many plant extracts such as *Haematoxylum campechianum L.*, *Castanea sativa L.* and *Rhamnus frangula L*, also known as logwood, chestnut and alder buckthorn, have long been used as natural dyes [6–9], due to their

characteristic pigmentation (Figure 8.1). The mentioned extracts are obtained from plants original to Europe and Central America and they are used in traditional medicine, thanks to their shown antioxidant, antimicrobial, antiviral, antifungal, antitumor and anticancer behavior among others [6,10–13]. Therefore, by the incorporation of these extract to WBPUU inks, materials with interesting characteristics for biomedical applications could be obtained.

Figure 8.1. Picture of a) logwood, b) chestnut and c) alder buckthorn extracts

Plant extracts are composed by a wide variety of components, mainly polyphenols. Among the many components of logwood extract, hematoxylol A, epihematoxylol B and, mainly, hematoxylin (Figure 8.2a) are found as the most bioactive compounds [14,15]. For chestnut extracts, a great variety of components are found, being tannins and some other phenolic compounds the principal components, vescalin, castalin, gallic acid, vescalagin, castalagin, kurigalin, acutissimin A and ellagic acid (Figure 8.2b) [7,10]. In alder buckthorn extract structures such as anthraquinones, among them chrysophanol, physcione and emodine [12,16], and some other important constituents such as frangulin A and B and glucofrangulin A and B (Figure 8.2c) are found [17].

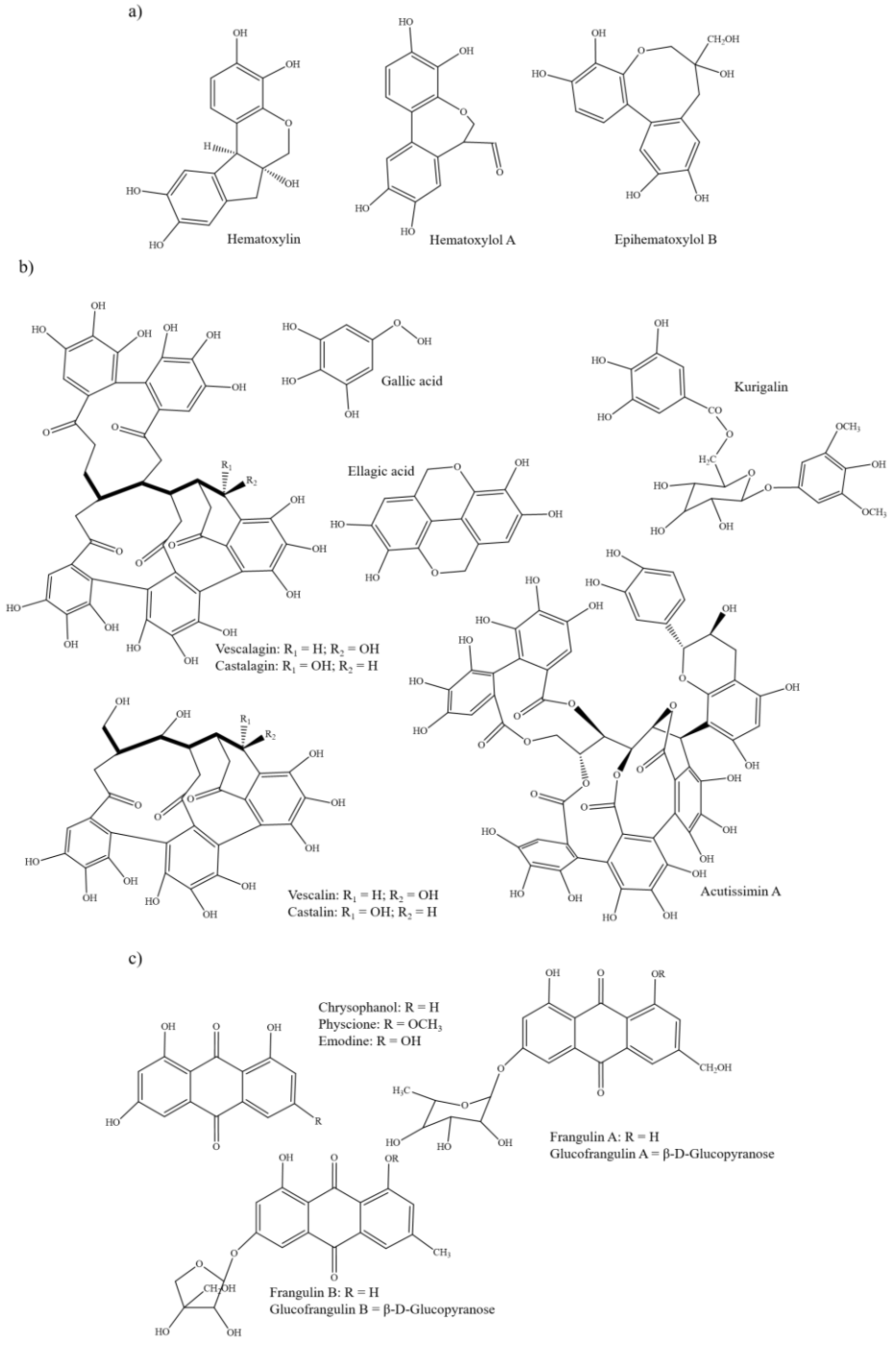

Figure 8.2. Structures of some on the components found in a) logwood, b) chestnut and c) alder buckthorn extracts

The wide range of components and different structures found on these natural extracts could influence the printability of the inks and final composite properties.

8.3. Preparation of WBPUU/natural extracts inks

For inks preparation, viscosity of the systems was modulated by increasing the solid content of the WBPUU dispersions and adjusting it for a proper gel-like structure.

For ex-situ preparations, a WBPUU dispersion with 50 wt.% solid content was prepared ($WBPUU_{50}$) and later used for composite preparation. Extracts were added in 1, 3 and 5 wt.% by mechanical agitation, until homogeneous dispersions were obtained. Ex-situ prepared inks were named "xLW_{EX}", "xCN_{EX}" and "xAB_{EX}" for composite inks containing logwood, chestnut or alder buckthorn extract, respectively, and where the "x" refers to the content of extract on the ink regarding the weight of the dried content, as specified on Table 8.1.

Table 8.1. WBPU and natural extract contents for ex-situ inks preparation

Sample	WBPUU dispersion (g) (50.4 wt.%)	WBPUU (g)	Logwood extract (g)	Chestnut extract (g)	Alder Buckthorn extract (g)
$WBPUU_{50}$	20.0	10.08	-	-	-
$1LW_{EX}$	20.0	10.08	0.10	-	-
$3LW_{EX}$	20.0	10.08	0.31	-	-
$5LW_{EX}$	20.0	10.08	0.53	-	-
$1CN_{EX}$	20.0	10.08	-	0.10	-
$3CN_{EX}$	20.0	10.08	-	0.31	-
$5CN_{EX}$	20.0	10.08	-	0.53	-
$1AB_{EX}$	20.0	10.08	-	-	0.10
$3AB_{EX}$	20.0	10.08	-	-	0.31
$5AB_{EX}$	20.0	10.08	-	-	0.53

For in-situ preparations, the natural extracts were first dispersed in water and were added during the phase inversion step of the synthesis. Since the addition

of the natural extract during the synthesis process had a strong effect on the dispersion homogeneity and viscosity, the total solid content needed to be adjusted in some systems.

For logwood and alder buckthorn extracts, the addition of high contents destabilized the correct gel formation at 50 wt.% WBPUU, resulting in too viscous mixtures for a correct agitation and, thus, dispersions with poor homogeneity were obtained. Hence, in order to add a 5 wt.% of extract during the synthesis process, it was necessary to slightly decrease the polyurethane-urea solid content to lower values. After optimization process, this content was set to 47.5 wt.%. The composition of the in-situ prepared inks are shown on Table 8.2.

Moreover, in order to further modulate the rheology of the inks and improve their behavior for DIW 3D printing, cellulose nanofibers were added to the inks containing the lowest solid contents. For this, 2% of the commercial nanocellulose (CNFr) was added to the inks and was mixed with vigorous mechanical stirring, at 12000 rpm for 10 minutes. The effect of the addition of cellulose on the inks properties, as well as on the final material, was studied.

It is worth noting that the addition of chestnut extract during the synthesis process strongly destabilized the formation of a homogeneous dispersion, resulting in extremely high viscosity phase separated dispersions. The preparation of in-situ added 3 and 5 wt.% of chestnut extract containing inks was discarded, due to the poor dispersion capacity observed for these systems. Complex polyphenolic molecules of chestnut extract, mainly tannins with a very high amount of hydroxyl groups, were likely to quickly form physical interactions or covalent bonds with isocyante groups when added by this method, which destabilized the proper dispersion formation and thus a homogeneous phase inversion was unable to be achieved.

Table 8.2. WBPU and natural extract contents for in-situ inks preparation

Sample	WBPUU content (wt.%)	Logwood content (wt.%)	Alder Buckthorn content (wt.%)	Prepolymer mass (g)	Logwood extract (g)	Alder Buckthorn extract (g)
$3LW_{IN}$	50.0	3	-	30	0.93	-
$5LW_{IN}$	47.5	5	-	30	1.58	-
$3AB_{IN}$	50.0	-	3	30		0.93
$5AB_{IN}$	47.5	-	5	30		1.58

8.3.1. Characterization of WBPUU/natural extracts inks

The increase of the solid content resulted in a clear increase of the viscosity of the materials. However, this high solid content could have an impact on the stability of the systems [18,19]. In order to analyze this effect, the particle size and zeta potential of the prepared 50 wt.% WBPUU and in-situ prepared inks were analyzed. Obtained values are shown in Table 8.3.

Table 8.3. Particle size and Z-potential values for high solid content WBPUU dispersions

Sample	Particle size (nm)	Z-potential (mV)
$WBPUU_{50}$	130.1 ± 4.4	-51.0
$3LW_{IN}$	118.5 ± 6.5	-51.9
$5LW_{IN}$	126.7 ± 4.0	-53.0
$3AB_{IN}$	140.2 ± 9.7	-47.9
$5AB_{IN}$	133.1 ± 5.7	-49.0

All systems showed a similar particle size around 130 nm. These values are similar to those reported on literature [20–22]. The high solid content and addition of natural extract did not significantly affect this property on the WBPUU dispersions.

When analyzing the effect of the solid content and extract incorporation on the stability of the systems, it can be observed that all systems still present a good

stability, with zeta potential values far for the required limits for stable dispersions, above +30 mV or below -30 mV [23].

Results proved that neither the high solid contents nor the addition of natural extract resulted in unstable materials. Systems showed small enough particle which were able to remain suspended, and showed, also, stable zeta potential values.

In order to study the potential of the prepared inks for their use on DIW 3D printing, rheological characterization was carried out, where the printability and shape fidelity of the inks was predicted. For rheological tests, $5LW_{IN}$ ink measurements were carried out with concentric cylinders geometry, other inks were studied using plate-plate geometry.

Viscosity vs. shear rate curves are shown in Figure 8.3 and 8.4 for ex-situ and in-situ prepared inks, respectively. Moreover, Table 8.4 summarizes the viscosity values of the inks at different shear rates and the n value calculated from Power Law (equation 2.2).

All systems showed shear-thinning behavior, necessary for DIW 3D printing. However, the type and content of natural extract added, as well as the incorporation route, significantly affected the viscosity values of the inks.

Logwood containing systems presented lower viscosity values than those exhibited by chestnut or alder buckthorn containing inks. Probably, the smaller molecular size and the lack of carboxylic groups of logwood extract components are beneficial for an easier flow. Regarding the content of extract incorporated, in general, in all inks with extracts, it was observed that the higher is the extract content on the ink, the lower is the viscosity. It must be highlighted that except inks with 1% content of either chestnut and alder buckthorn extracts, other systems show lower viscosity values than the ink without extract.

For ex-situ prepared inks, the change of the viscosity could be due to the natural extract surfactant effect [5,24,25]. The interaction of surfactant molecules with the polymer macromolecules can increase or decrease the solution's viscosity due to extension, shrinking, and bridging of polymer macromolecules. Several factors affect the surfactant and polymer interactions, being the structure of surfactant one of them. However, the complex behavior of mixed additives in solutions is far from being well understood [26].

The decrease of viscosity was more prominent when increasing the content of extracts in inks, as well as when the size of extract's molecules was small and without carboxylic groups, as in logwood extract. However, when the size of extract's molecular compounds was big, as in chestnut and alder buckthorn extracts, a different effect was observed. At low extract content, 1 wt.%, the incorporated extract amount is not enough to reduce the viscosity of the WBPUU ink, on the contrary, the viscosity slightly increased. Observed viscosity changes indicate the formation interactions of the natural extracts with polyurethane molecules. The high concentration of functional groups present on the components of the natural extracts are likely to interact with urethane-urea groups. This interaction could translate in viscosity changes of inks.

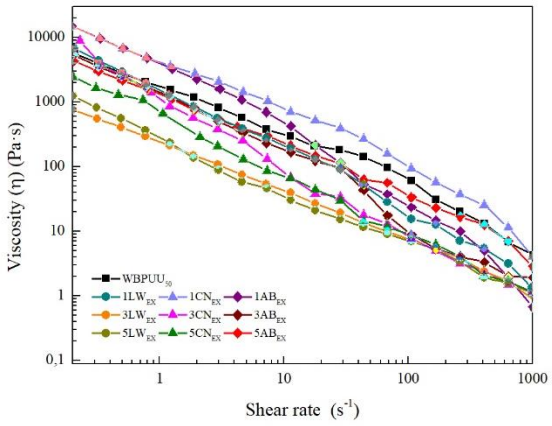

Figure 8.3. Viscosity as a function of shear rate of ex-situ prepared WBPUU and natural extracts containing inks

As for in-situ prepared inks, it can be observed that the addition of natural extracts resulted in inks with lower viscosities. The many hydrophilic groups present in the phenolic compounds of the extracts facilitated the dispersion formation during the synthesis process, and thus dispersions with lower viscosity were obtained [5].

As in the case of ex-situ prepared inks, inks with alder buckthorn extract resulted in materials with higher viscosities than the addition of logwood extract, due to the presence of bigger and more complex molecules.

$5LW_{IN}$ and $5AB_{IN}$, due to their lower solid content, showed significantly lower viscosities, which increased with the addition of CNF. Cellulose, as seen in Chapter 5, can be used to modulate inks' viscosities and, thus, improve 3D printing process [27,28].

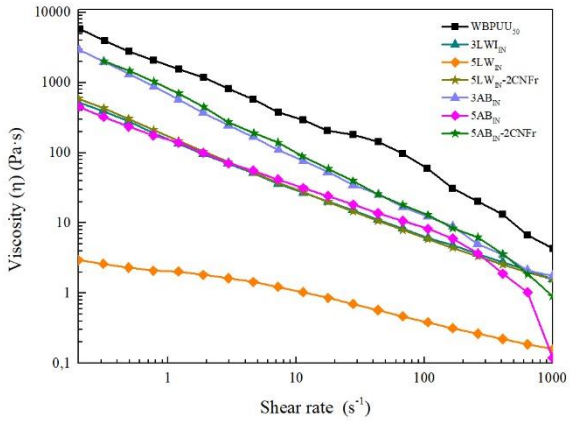

Figure 8.4. Viscosity as a function of shear rate of in-situ prepared WBPUU and natural extracts containing inks

The high viscosity exhibited by some of the inks may difficult the extrusion process of 3D printed parts.

Observed results agree with behavior seen in previous chapters, where in-situ preparation promoted interactions between the WBPUU and the additives,

whereas for ex-situ preparation interactions with the water present in the systems were more likely and thus higher systems with higher viscosities are obtained.

Table 8.3. Viscosity values measured at different shear rates for ex-situ and in-situ prepared WBPUU and natural extracts containing inks

	Sample	η at 0.02 s^{-1} (Pa·s)	η at γ_{nz} (Pa·s)	η at 100 s^{-1} (Pa·s)	n
ex-situ	$WBPUU_{50}$	7598.1	481.1	56.0	0.189
	$1LW_{EX}$	6578.5	1753.9	16.6	0.056
	$3LW_{EX}$	1094.3	57.9	7.6	0.166
	$5LW_{EX}$	1021.4	48.2	7.1	0.168
	$1CN_{EX}$	14984.8	1647.3	100.8	0.197
	$3CN_{EX}$	5577.3	219.2	8.3	0.068
	$5CN_{EX}$	2454.9	220	9	0.08
	$1AB_{EX}$	14524.1	1394.7	24.8	0.066
	$3AB_{EX}$	5704.2	533.9	9.6	0.053
	$5AB_{EX}$	4867.3	996.2	36.1	0.228
in-situ	$3LW_{IN}$	536.8	29.9	5.4	0.289
	$5LW_{IN}$	2.3	0.6	0.4	0.658
	$5LW_{IN}$-2CNFr	1061.9	17.9	3.3	0.308
	$3AB_{IN}$	2814.1	145.7	12.3	0.123
	$5AB_{IN}$	626.9	50	8.5	0.22
	$5AB_{IN}$-2CNFr	2891	183	14.2	0.132

Spectromechanical analysis were performed in order to analyze the gel behavior of each ink under applied stress. Figure 8.5 and 8.6 show storage and loss moduli vs. shear stress curves for ex-situ and in-situ prepared inks, respectively. Moreover, following the procedure explained in previous chapters, yield and flow points were measured and are summarized on Table 8.4.

As can be observed for ex-situ preparations, the addition of natural extracts resulted in an overall decrease of the yield and flow point, as well as in a decrease of the storage and loss modulus values in the linear zone. Natural extracts reduced the gel-like strenght of the systems and were only able to maintain this behavior at low shear stress values. Following results observed by

flow tests, logwood containing inks showed lower gel-like behavior, being these inks the more willing to flow.

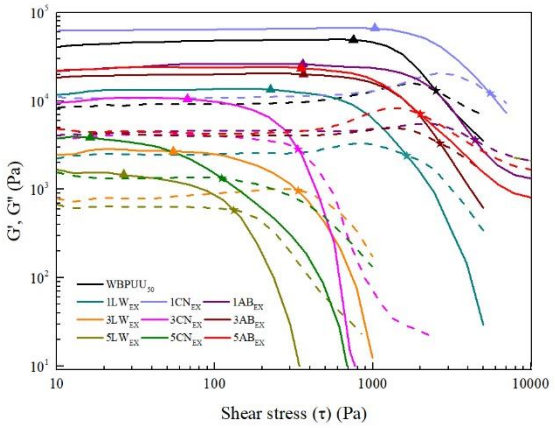

Figure 8.5. Storage (solid line) and loss (dotted line) moduli as a function of shear stress and yield (◢) and flow (★) points of ex-situ prepared natural extracts containing inks

Table 8.4. Yield and flow point values for ex-situ and in-situ prepared WBPUU and natural extracts containing inks

	Sample	Yield point (Pa)	Flow point (Pa)
ex-situ	$WBPUU_{50}$	609.0	2567.6
	$1LW_{EX}$	253.4	1663.3
	$3LW_{EX}$	40.7	254.6
	$5LW_{EX}$	23.4	120.7
	$1CN_{EX}$	985.6	5524.2
	$3CN_{EX}$	97.0	892.0
	$5CN_{EX}$	16.3	111.8
	$1AB_{EX}$	476.9	3988.3
	$3AB_{EX}$	373.8	2310.9
	$5AB_{EX}$	188.9	1986
in-situ	$3LW_{IN}$	89.8	283.4
	$5LW_{IN}$	-	-
	$5LW_{IN}$-2CNFr	38.6	109.5
	$3AB_{IN}$	266.6	837.5
	$5AB_{IN}$	61.0	220.1
	$5AB_{IN}$-2CNFr	88.9	641.4

As for in-situ prepared inks, significantly lower yield and flow points were measured. The strong surfactant effect supplied by natural extracts by this method and the promotion of dispersion formation resulted in systems with lower gel-like behavior. As can be observed, $5LW_{IN}$ did not show a gel-like structure. However, the addition of cellulose changed this, and effectively increased the yield and flow points of the inks, as well as their G' and G" values [28,29].

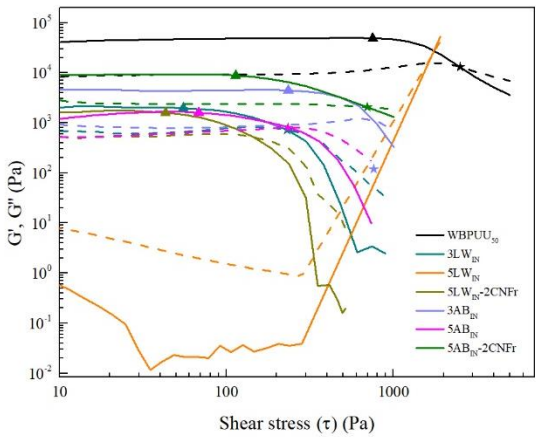

Figure 8.6. Storage (solid line) and loss (dotted line) moduli as a function of shear stress and yield (◢) and flow (★) points of in-situ prepared natural extracts containing inks

The defined yield points and high G' values observed for all systems, except $5LW_{IN}$, suggests a good shape fidelity when used in DIW 3D printing [30]. However, the high yield points shown by some systems, especially in the case of ex-situ prepared inks, might difficult the printability of the inks during the extrusion process. In this regard, lower yield points of in-situ preparations may allow for a better printability of the inks.

Structural recovery tests were also carried out for these inks, in order to predict the shape fidelity that they will show when used in DIW 3D printing. However, it is worth noting that some troubles were found when performing these tests. It was observed that during the high shear rate section of the tests, inks tent to

slip through the geometry, as a result a gap between the material and the geometry was formed. This gap hindered the correct measurement and, therefore, mistrustful results were obtained. High solid content materials show a tendency to slip through the geometries rather than deformed, causing artifacts in the rheological measurements [31].

8.4. Characterization of WBPUU/natural extracts composites

In order to further characterize the prepared materials, WBPUU/natural extracts composites were prepared. For this, inks were poured on Teflon molds and were later freeze-dried. Obtained dried composites were named as their corresponding inks.

For dried composite characterization, first FTIR spectroscopy analyses were performed, in order to analyze possible interactions taking place between the waterborne polyurethane-urea and the added natural extracts. The obtained spectra for the neat polyurethane-urea, composites obtained from ex-situ preparations and their corresponding natural extracts are shown in Figure 8.7a, 8.7b and 8.7c, for logwood, chestnut and alder buckthorn extracts, respectively.

$WBPUU_{50}$ shows all the characteristic peaks of polyurethane-ureas seen in previous chapters, being the more representative regions the bands related to N-H and C=O of urethane and urea groups, located in the 3500-3100 cm^{-1} and 1800-1600 cm^{-1} ranges, respectively [32,33]. In the case of the natural extracts, spectra of logwood, chestnut and alder buckthorn extracts show a very wide band between 3700 and 3000 cm^{-1}, which is related to the O-H groups of the many phenolic groups present on their structure [34]. A band around 1600 cm^{-1} is present in the spectra of the three natural extract, attributed to the C=C of the aromatic rings [35,36]. Moreover, for chestnut and alder buckthorn extracts a band related to the carbonyl groups of their phenolic compounds can also be seen at around 1720 cm^{-1}.

a)

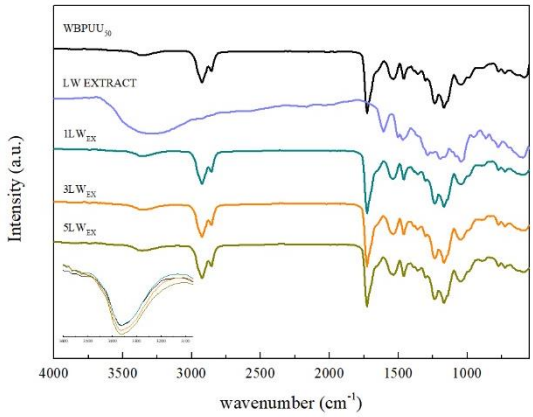

b)

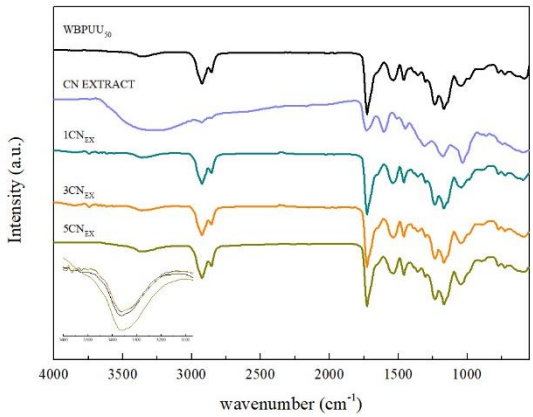

c)

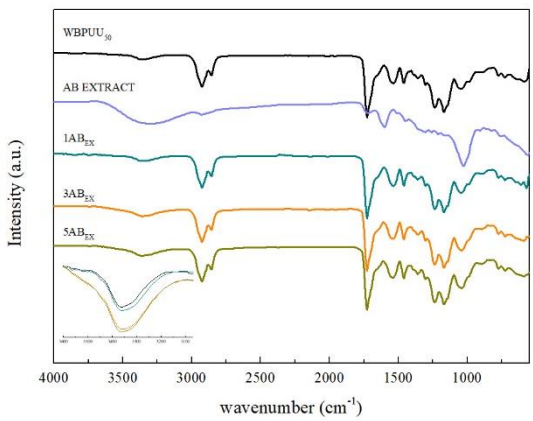

Figure 8.7. FTIR spectra of neat WBPUU, natural extracts and ex-situ prepared composites with different contents of a) logwood extract, b) chestnut extract and c) alder buckthorn extract

When analyzing the spectra of the composites, it can be observed that the addition of the natural extracts did not cause any major change regarding shifts of wavenumbers. However, an increase in the intensity of the N-H band can be observed with the addition and content of extracts (Figure 8.7a-c inset), which is attributed to the overlapping of bands.

FTIR spectra for composites obtained from in-situ prepared inks, as well as for their corresponding natural extracts and for neat polyurethane-urea, are shown in Figure 8.8a and 8.8b for logwood and alder buckthorn extracts containing systems, respectively.

a)

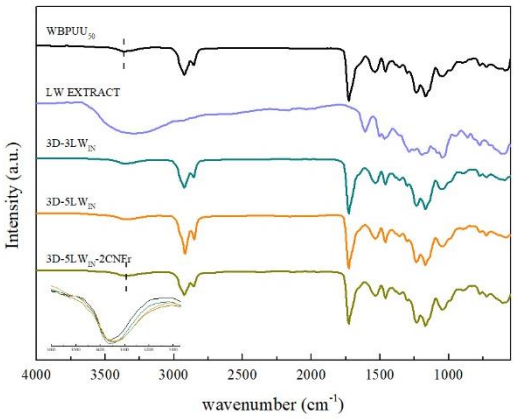

b)

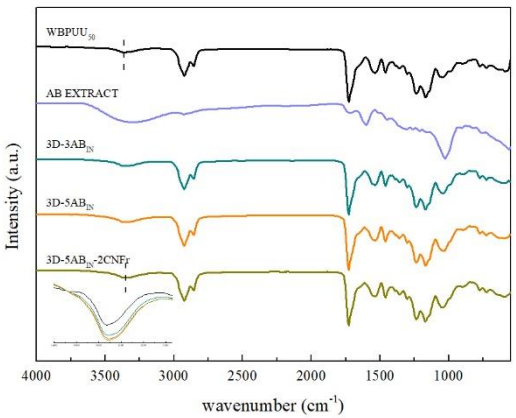

Figure 8.8. FTIR spectra of neat WBPUU, natural extracts and in-situ prepared composites with different contents of a) logwood extract, b) chestnut extract and c) alder buckthorn extract

As can be observed, the addition of natural extracts by this incorporation route further altered the N-H band. For in-situ prepared composites, besides the increase of intensity of this band, a shift towards lower wavenumbers also took place, which was more intense for higher contents of extracts and the addition of CNF. This band, centered at 3362 cm^{-1} in $WBPUU_{50}$ spectra, went down up to 3346 and 3350 cm^{-1}, for $5LW_{IN}$-2CNFr and $5AB_{IN}$-2CNr, respectively. This shift to lower wavenumbers suggests the formation of interactions between the polyurethane-urea matrix and the natural extracts, as well as with the cellulose [37].

In order to analyze antibacterial behavior supplied by the added natural extracts, antimicrobial tests were performed using the disk diffusion technique. For this test, two strains were used, a gram positive one (Staphylococcus aureus ATCC 19213) and a gram negative one (Escherichia coli ATCC 10536).

The antimicrobial behaviors of the extracts by themselves were also analyzed, in order to assess the effect of their concentration. Aqueous solutions of each extract were prepared at different concentration and were named “xLW”, “xCN” and “xAB” for logwood, chestnut and alder buckthorn extract, respectively, and where “x” refers to the content of extract present on their ink counterparts.

After 1 day of incubation (Figure 8.9 and 8.10), pure extracts showed good bactericide behavior against both strains, agreeing with their good reported antibacterial behavior [38–44]. Inhibition zones shown by the extracts were dependent on the type and content of extract. Logwood extract showed the stronger antimicrobial behavior, with inhibition zones of 25 mm in diameter against *S. aureus*, even larger than those shown by the antibiotic, and 10 mm against E. coli.

$WBPUU_{50}$ showed bacteriostatic behavior against both strains after 1 day of incubation. Tough no inhibition zone can be observed, no bacteria growing over

the material was observed either. Regarding ex-situ prepared composites in S. aureus tests, $1LW_{EX}$, $1CN_{EX}$ and all systems containing alder buckthorn extract presented bacteriostatic behavior. Moreover, composites containing higher contents of logwood and chestnut extract also exhibited an inhibition zone, which was proportional to the content of the extracts. For in-situ prepared composites, lower inhibition areas were measured, however, the addition of CNF further enhanced the bactericide behavior [45]. Tests against E. coli strain showed lower antimicrobial activity. All systems exhibited bacteriostatic behavior, with no bacterial growing over the tested samples. Moreover, some in-situ preparations, $3LW_{IN}$, $5LW_{IN}$-2CNFr, $3AB_{IN}$ and $5AB_{IN}$-2CNFr, did show an inhibition area, proving bactericide behavior.

The capacity to maintain the antimicrobial behavior over longer periods of time was analyzed, Figure 8.11 and 8.12 show disks after 4 days of incubation. As can be observed, all the systems showed similar behavior, proving antibacterial behavior of the material over time.

The good antibacterial behaviour exhibited by WBPUU/natural extracts composites makes them a potential great material for many applications, namely in the biomedical and pharmaceutical fields. Moreover, the processing of these materials by 3D printing in order to obtain customizable parts could be of great interest.

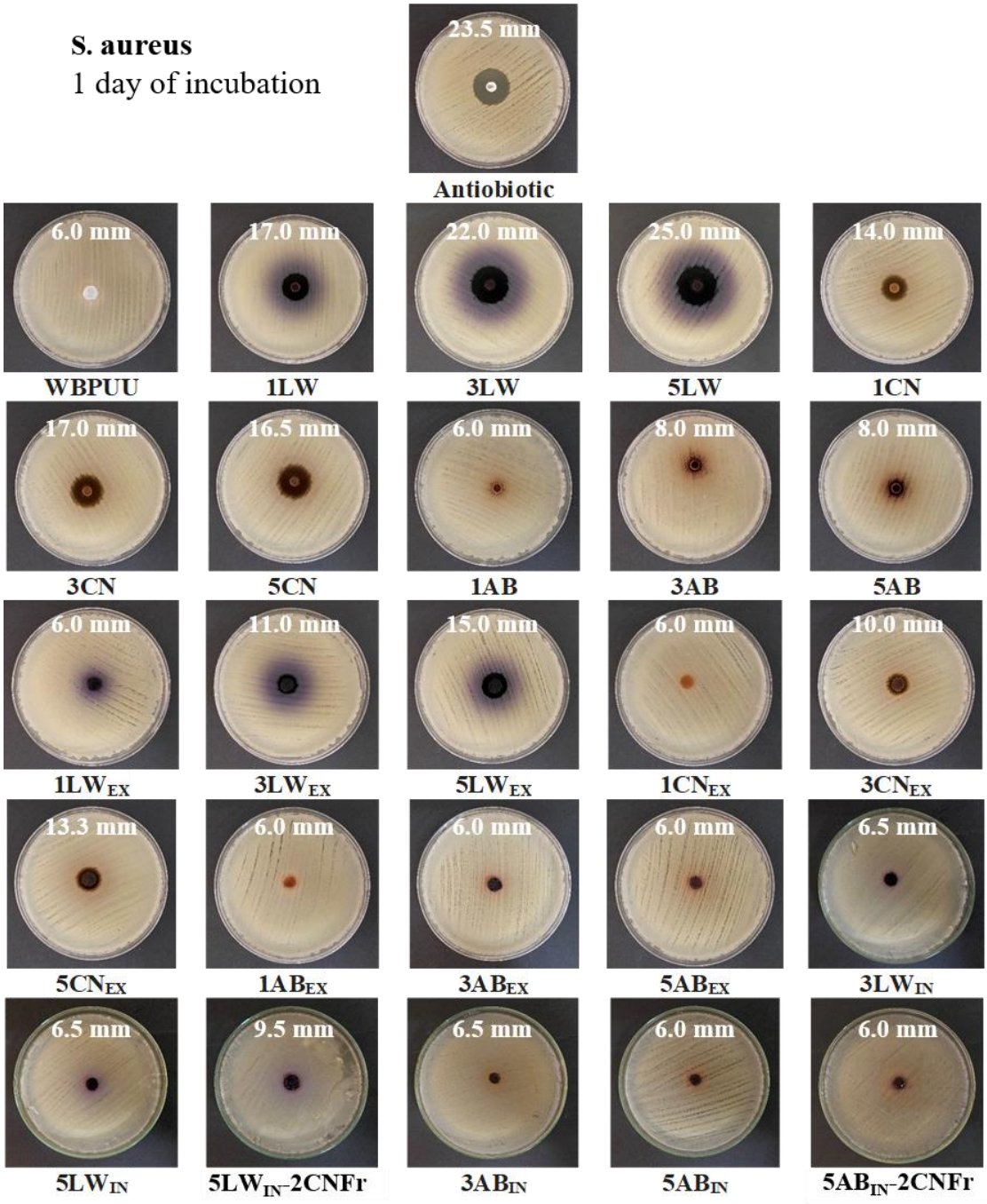

Figure 8.9. Antibacterial tests for neat WBPUU, natural extracts and WBPUU/natural extract composites against S. aureus after 1 day of incubation at 37 °C

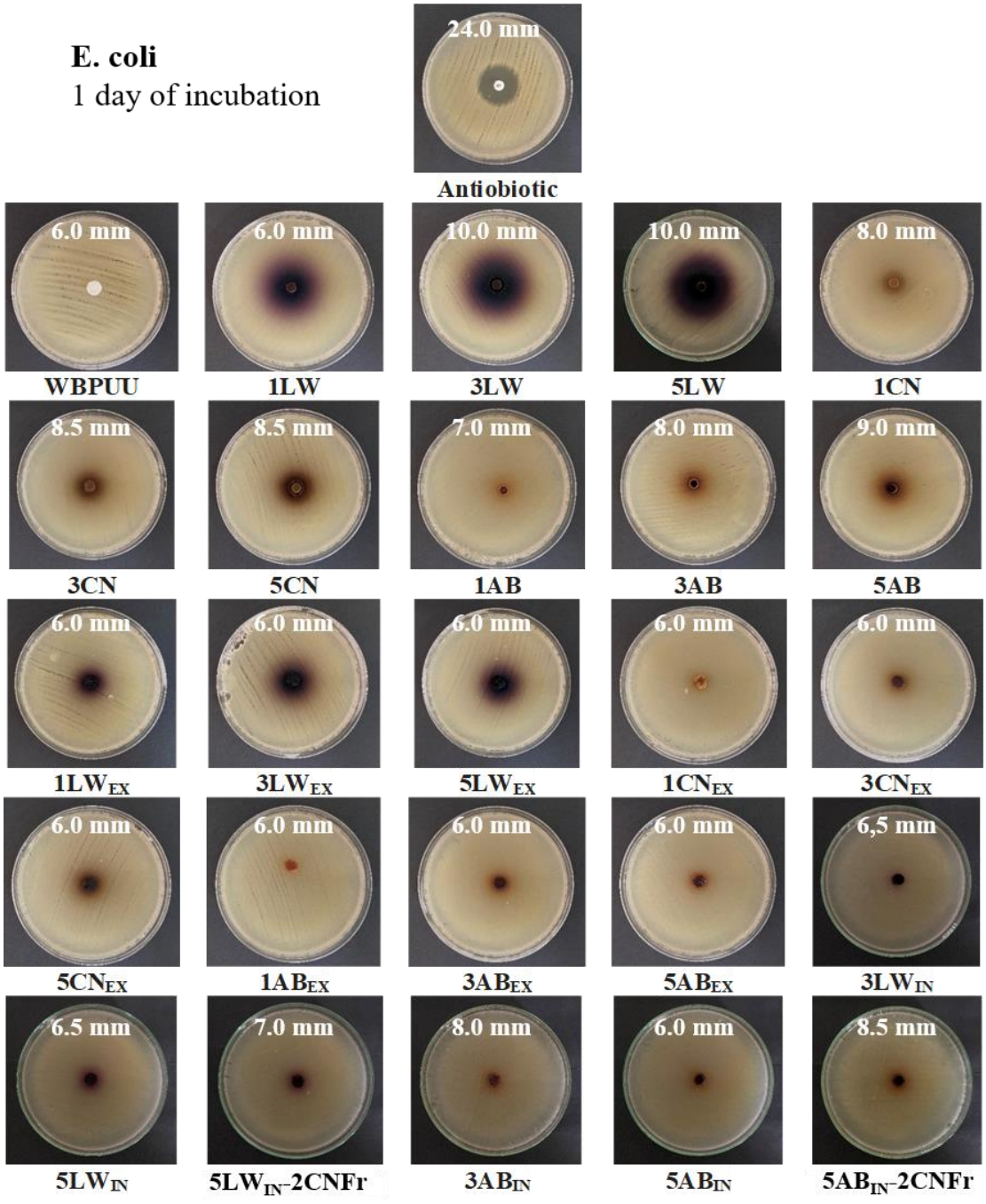

Figure 8.10. Antibacterial tests for neat WBPUU, natural extracts and WBPUU/natural extract composites against E. coli after 1 day of incubation at 37 °C

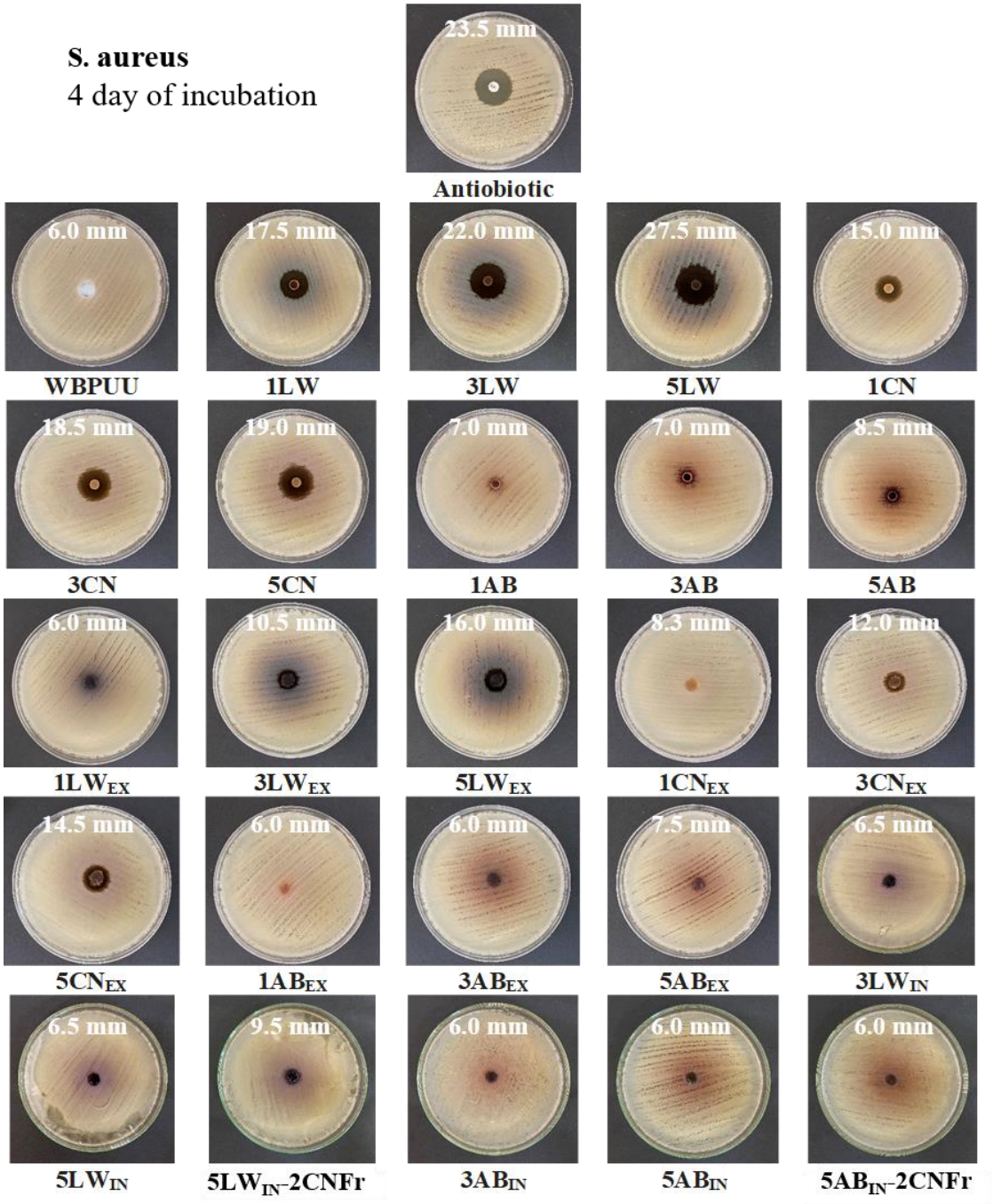

Figure 8.11. Antibacterial tests for neat WBPUU, natural extracts and WBPUU/natural extract composites against S. aureus after 4 days of incubation at 37 °C

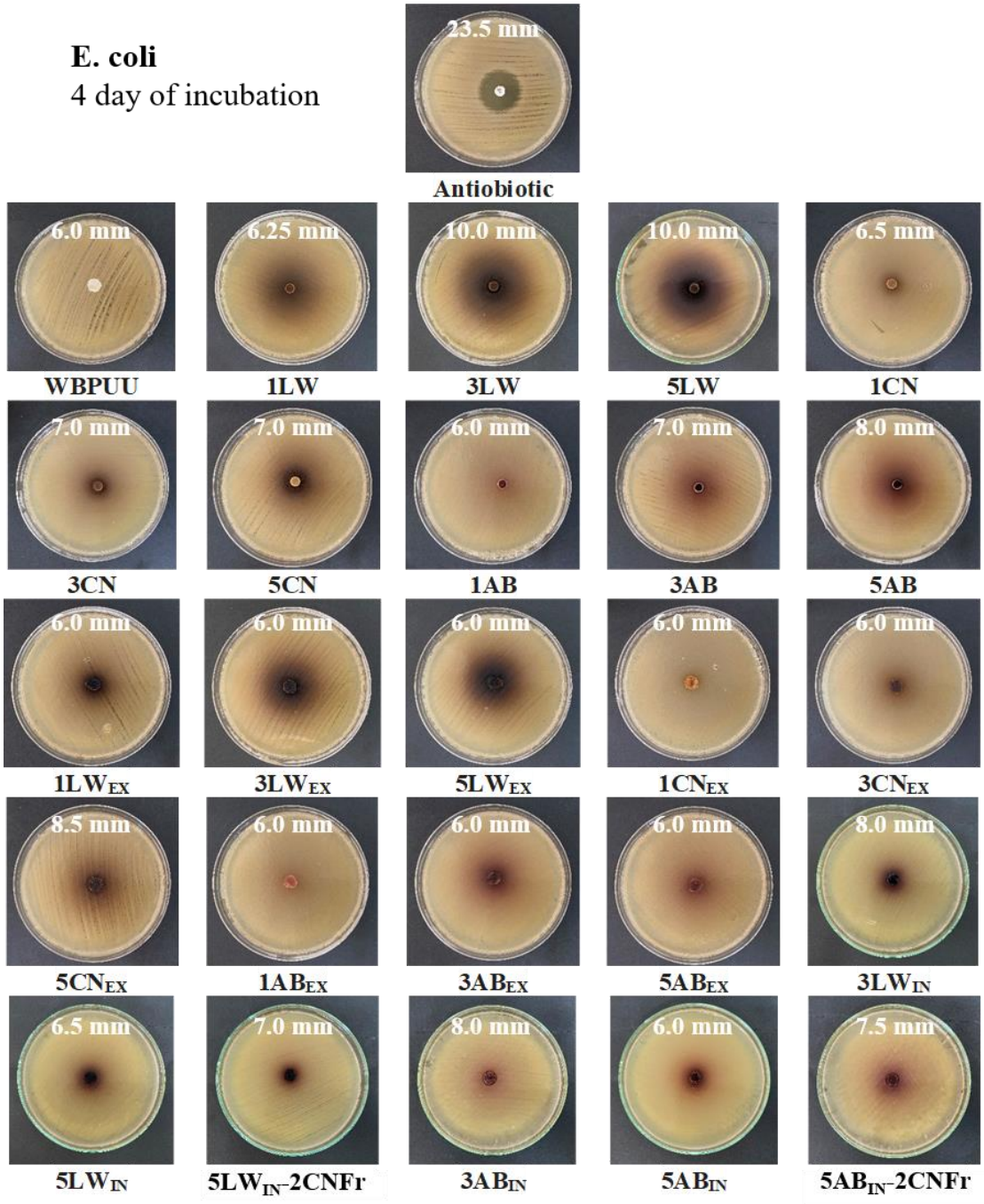

Figure 8.12. Antibacterial tests for neat WBPUU, natural extracts and WBPUU/natural extract composites against E. coli after 4 days of incubation at 37 °C

8.5. DIW 3D printing of WBPUU/natural extracts inks

Natural extracts containing inks were used to obtain 3D printed parts by DIW. The different rheological behavior shown by different inks strongly affected the 3D printing process.

Regarding ex-situ prepared inks, systems containing 1 wt.% of natural extracts, due to their extremely high viscosities, even at high shear, and their high yield points, showed trouble when printing. During extrusion process a discontinuous flow was observed, therefore, it was not possible to successfully obtain 3D printed parts. For higher contents of natural extracts, the inks showed better printability. However, for 5 wt.% natural extracts containing inks, some obstruction problems were occasionally encountered. The high amount of natural extracts may have resulted in poorer dispersability, and, thus, in some agglomerations obstructing the nozzle.

Overall, inks containing 3 wt.% of natural extracts showed the best printability. Their lower viscosities under shear allowed for a better printing process than inks with lower extracts content, whereas their high viscosities at rest and defined yield point resulted in better shape fidelity.

$WBPUU_{50}$, showed significantly better printability than that of 1 wt.% natural extracts containing inks. The lower viscosity measured under printing shear rate seems to have allowed for a more homogeneous printing process.

Considering the printability shown by the inks, 3D printed parts were produced with $3LW_{EX}$, $3CN_{EX}$ and $3AB_{EX}$ in order to observe the effect of the type of extract used. Moreover, 3D printed parts from $5AB_{EX}$ were also obtained, to study the effect of content of natural extracts. Obtained 3D printed parts are shown in Figure 8.13. In general, the shape fidelity was not very accurate for the studied systems.

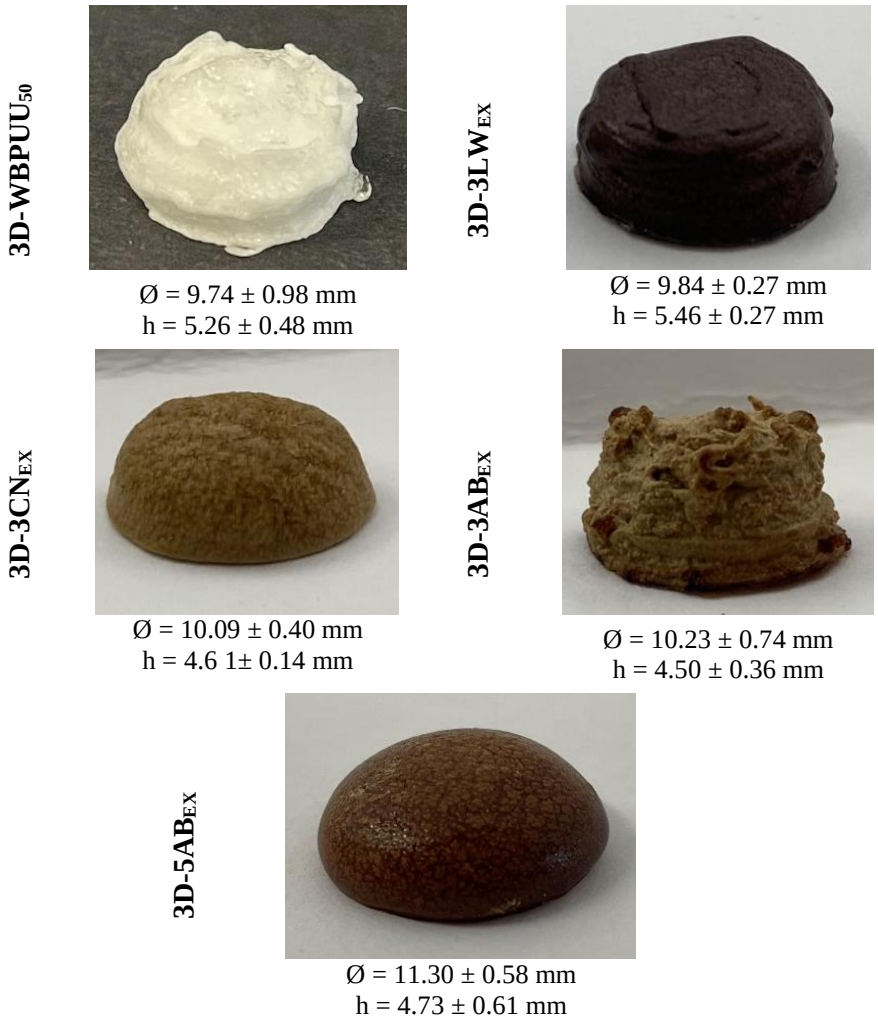

Figure 8.13. Photographs of 3D printed cylinders from ex-situ prepared inks

For in-situ preparations, inks showed better printability, as well as shape fidelity. The better dispersion achieved by this incorporation route impeded the formation of agglomerations, and as consequence no nozzle obstruction problems were observed. The addition of cellulose greatly and positively influenced the printing process. From nanocellulose containing inks, 3D printed parts with better shape fidelity were obtained, as seen in Figure 8.14.

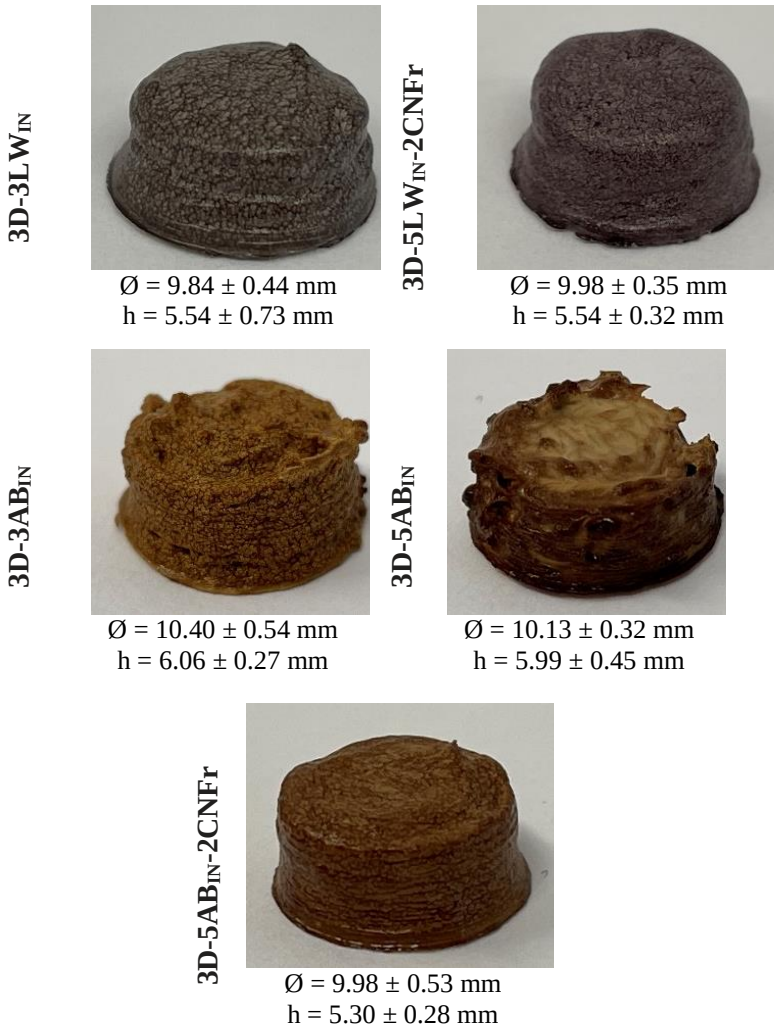

Figure 8.14. Photographs of 3D printed cylinders from in-situ prepared inks

High solid content dispersions showed a more sticky-like behavior than inks obtained in previous chapters. This stickiness resulted in less precise 3D printed parts, since the ink tended to stick to the nozzle and create sharp points, as can be seen in some of the printed parts in Figure 8.14. The addition of CNFr solved this problem and smoother parts were produced.

8.5.1. Characterization of 3D printed parts

The morphology of the printed parts was studied by SEM and obtained micrographies are shown in Figure 8.15 and 8.16 for 3D parts obtained from ex-situ and in-situ prepared inks, respectively. As can be observed the addition of natural extracts, as well as their type, content and method of incorporation strongly affected the morphology of the materials.

3D-$WBPUU_{50}$ shows a quite homogeneous porous structure, formed by spherical pores with an average diameter of 60.2 ±12.9 µm. When natural extracts were added, by the ex-situ method, this morphology was severely altered. 3D-$3LW_{EX}$ shows a similar morphology to that of the neat polymer, formed by spherical pores with an average diameter of 24.5 ± 3.5 µm. However, composites containing chestnut and alder buckthorn extracts presented very different morphologies. For 3D-$3CN_{EX}$ a more open wall structure is seen, with pores completely connected between themselves and not a continuous solid structure. On the other hand, 3D-AB_{EX} shows porous similar to those observed for 3D-$WBPUU_{50}$ and 3D-$3LW_{EX}$ when examined up close. However, at lower magnifications, the presence of holes in the system can be clearly observed, as a result of the non-continuous printing process due to poor flow and the constant obstruction taking place in the nozzle.

3D parts obtained from in-situ prepared inks showed a morphology similar to 3D-WBPUU50, with some difference due to the addition on the natural extracts. As can be observed the addition of extracts resulted in the reduction of pore size, with 3D-$3LW_{IN}$ showing pores with a diameter of 15.3 ± 2.8 µm and 3D-$3AB_{IN}$ showing pores with a diameter of 34.4 ± 6.5 µm. Both systems showed homogeneous structures with spherical pores, proving the good rheological behavior shown by the inks being able to support the printed structure.

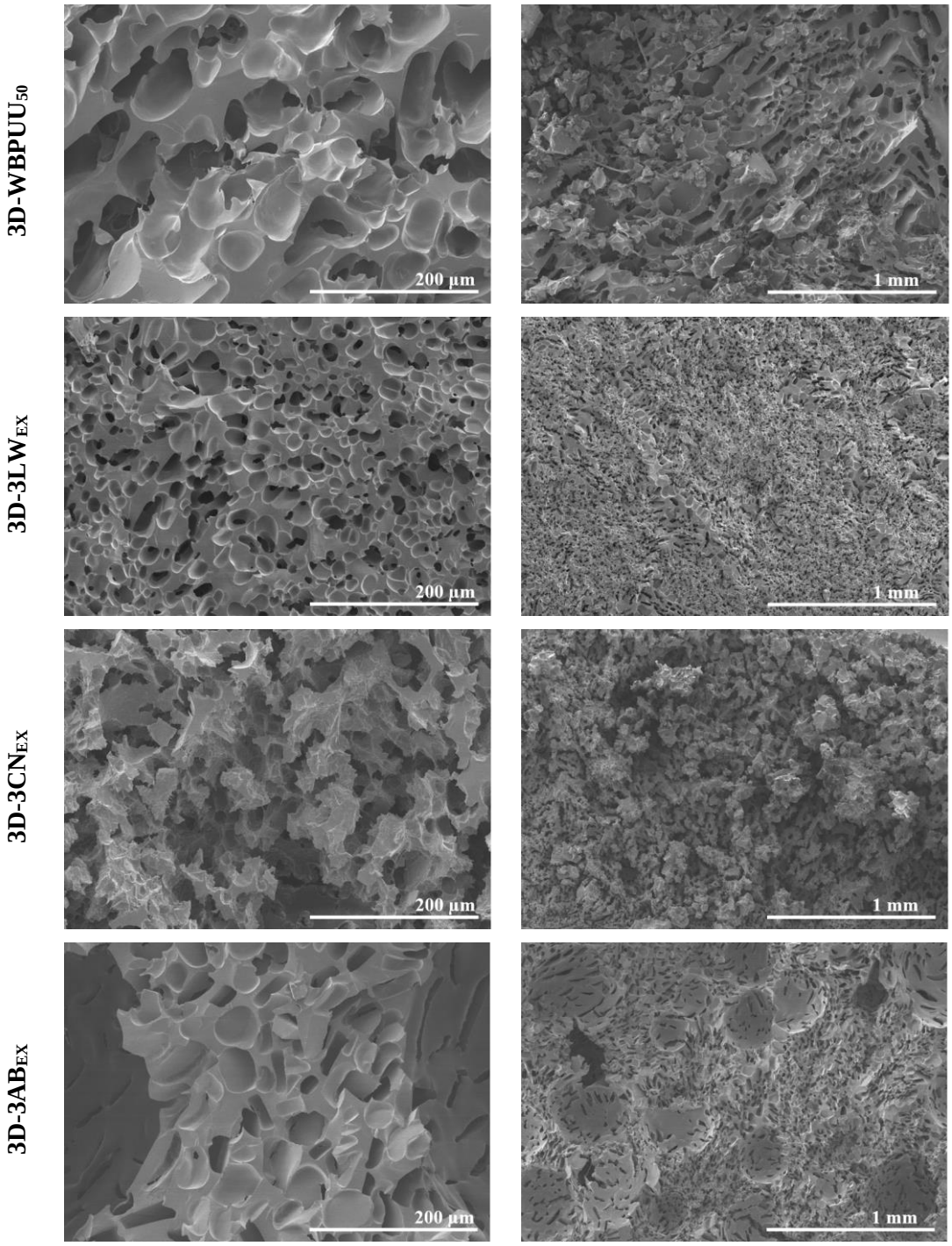

Figure 8.15. SEM images of 3D printed parts from ex-situ prepared inks

For 3D-5AB$_{IN}$, however, a different behavior was observed. In the case of this system a more heterogeneous morphology was seen, with bottom layer showing more elongated pores (244.2 ± 30.3 x 53.0 ± 6.0 µm) and upper layers showing once again a spherical porous structures (Ø = 16.9 ± 3.9 µm). The lower viscosity shown by this system, due to its lower solid content, was not enough to support the weight of the layers on top and, therefore, the structure collapsed when other layers were deposited. The addition of CNF easily solved this problem, for 3D-5AB$_{IN}$-2CNFr the recovery of a homogeneous spherical porous morphology can be observed, with pores showing a diameter of 33.6 ± 4.6 µm. 3D-5LW$_{IN}$-2CNFr shows a similar morphology with 38.5 ± 7.9 µm diameter pores.

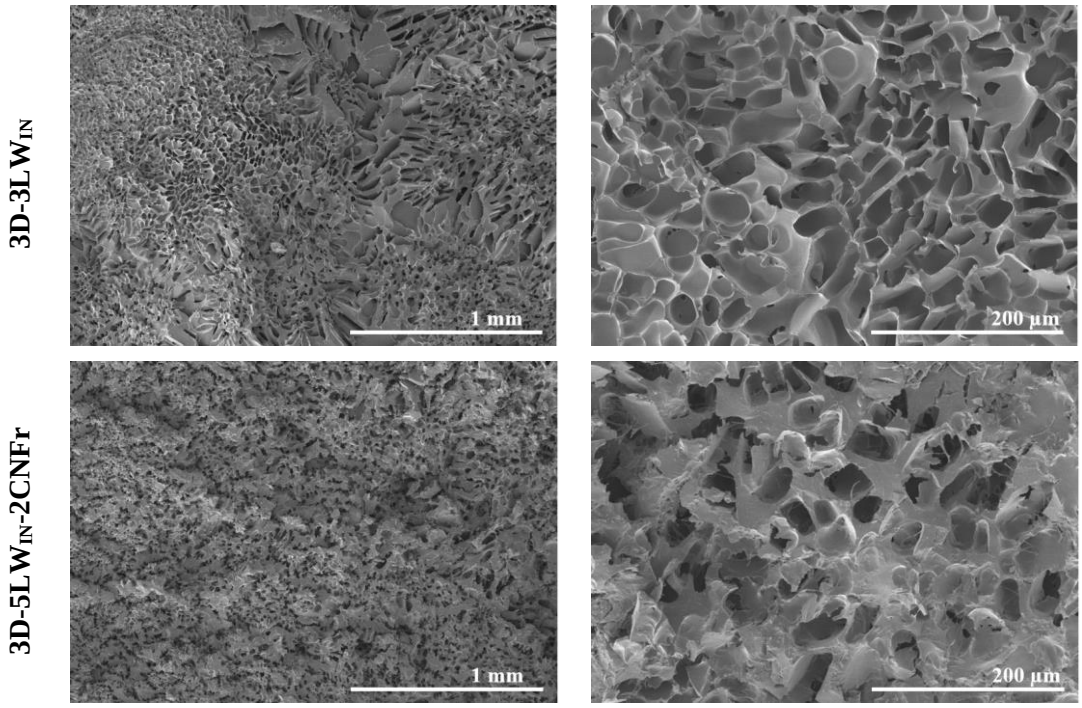

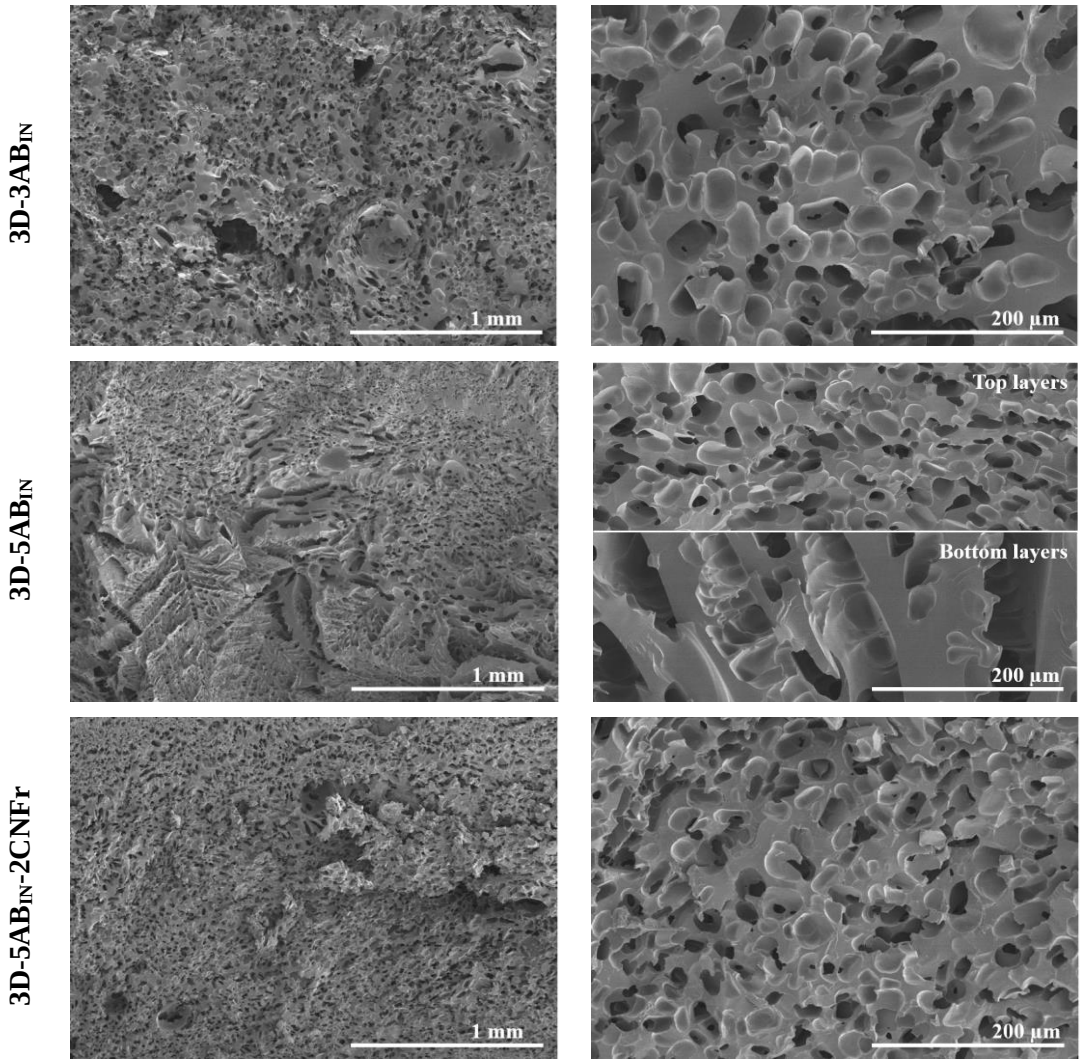

Figure 8.16. SEM images of 3D printed parts from ex-situ prepared inks

The mechanical properties of the 3D printed parts obtained from WBPUU and natural extracts containing inks were analyzed by compressions tests. Young modulus, density, specific Young modulus, stress at 60% strain and densification strain values are summarized on Table 8.5. Stress/strain curves are shown in Figure 8.17.

Table 8.5. Young modulus, specific Young modulus, stress at 60% strain and densification strain values for WBPU and natural extracts containing 3D printed parts

	Sample	Young modulus (MPa)	Density ($g \cdot cm^{-3}$)	Specific Young modulus ($MPa \cdot cm^3 \cdot g^{-1}$)	Stress at 60% strain (MPa)	Densification strain (%)
ex-situ	3D-$WBPUU_{50}$	4.3 ± 0.8	0.35 ± 0.04	12.2 ± 1.8	1.2 ± 0.2	49.3 ± 1.4
	3D-$3LW_{EX}$	29.9 ± 3.3	0.44 ± 0.04	66.6 ± 8.8	5.1 ± 0.4	51.1 ± 0.1
	3D-$3CN_{EX}$	13.5 ± 2.2	0.33 ± 0.01	41.1 ± 6.2	2.4 ± 0.5	49.4 ± 0.9
	3D-$3AB_{EX}$	7.1 ± 3.1	0.31 ± 0.03	23.0 ± 8.5	1.4 ± 0.3	49.5 ± 1.2
	3D-$5AB_{EX}$	10.2 ± 2.6	0.37 ± 0.05	27.5 ± 6.0	1.9 ± 0.5	51.4 ± 0.3
in-situ	3D-$3LW_{IN}$	36.9 ± 4.0	0.49 ± 0.03	75.3 ± 5.6	6.3 ± 0.1	49.7 ± 1.2
	3D-$5LW_{IN}$-2CNFr	64.6 ± 4.7	0.53 ± 0.04	122.0 ± 8.0	9.3 ± 1.0	50.6 ± 0.7
	3D-$3AB_{IN}$	11.6 ± 2.3	0.44 ± 0.05	26.9 ± 8.1	2.6 ± 0.3	50.7 ± 0.8
	3D-$5AB_{IN}$	29.6 ±4.2	0.46 ± 0.02	65.1 ± 8.9	5.1 ± 0.6	51.9 ± 0.6
	3D-$5AB_{IN}$-2CNFr	46.8 ± 9.0	0.50 ± 0.03	93.4 ± 12.6	6.8 ± 1.1	51.8 ±1.3

The addition of natural extracts strongly affected the mechanical behavior of the polyurethane-urea, increasing their Young modulus, specific Young modulus and stress at 60% strain. This data agrees with the reinforcement effect supplied by plant extract (*Salvia*) in Chapter 6. Results showed that the type, content and incorporation method influenced the mechanical behavior of the material. Regarding the effect of the type of the natural extract used, it can be observed that logwood extract supplied the stronger reinforcement effect, with composites containing this extract presenting the highest values of Young modulus and specific Young modulus. Chestnut and alder buckthorn extracts also added rigidity and strength to the systems, but the effect was less pronounced for systems containing these extracts.

Analyzing the effect of the incorporation route, it can be observed that the in-situ addition resulted in higher Young modulus, specific Young modulus and stress values. The higher amount of physical or chemical interactions formed by this method, as suggested by FTIR analyses, and the good dispersion

achieved by this method may be responsible for this higher reinforcement effect. Materials with higher rigidity and better transference of stress were obtained. On the other hand, the addition of cellulose further reinforces the material, more pronouncedly seen in Young modulus and specific Young modulus values [29].

Regarding the densification strain, no significant differences were observed in this property for composites.

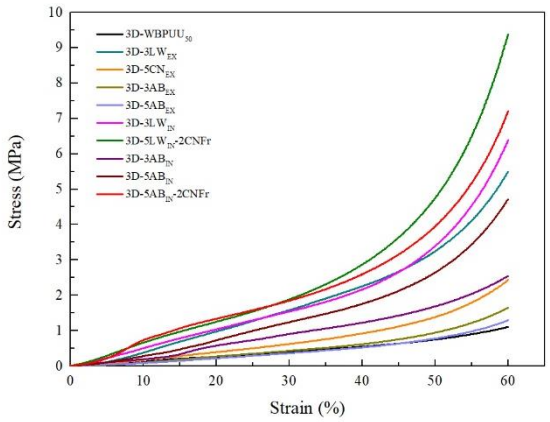

Figure 8.17. Strain/Stress curves for 3D printed parts obtained from WBPUU$_{50}$ and natural extracts containing inks

It is worth noting the big differences measured in density for parts printed from different systems. This is related to the poor printability of the materials, which did not allow for a good printing process and thus not completely filled materials were obtained, as was also observed in SEM studies.

8.6. Conclusions

Willing to benefit from the bioactive behavior of natural extracts, in this chapter WBPUU inks were prepared using three types of plant extracts, namely logwood, chestnut and alder buckthorn extracts. In order to modulate the rheological behavior, in this chapter a WBPUU dispersion with high solid

content was prepared. High solid content dispersion showed good gel-like behavior, suggesting good behavior for DIW 3D printing. Inks were prepared by ex-situ and in-situ addition of natural extracts. The in-situ addition of extracts had an intense effect on the dispersion process, and for chestnut extract it did not allow for a good dispersion formation. CNF was used to further modulate rheological behavior the dispersions with lower solid contents.

Rheological tests proved shear-thinning behavior of inks with very high viscosity values for high solid content dispersions, even at high shear rate. Though the addition of extract had a surfactant effect and reduced viscosity, high viscosity values remained. Moreover, inks showed also high yield and flow points. For in-situ preparation significantly reduced values were observed, which may result in better printability when used in DIW

The antibacterial behavior of the extracts and the composites was analyzed against a gram positive and a gram negative strain. Extract showed bactericide behavior against both strains. Regarding composites, it was observed that all systems showed, at least, bacteriostatic behavior, which was improved with the addition of the extracts, especially for logwood containing system.

The inks' behavior in DIW was studied and it was observed that in-situ prepared inks showed better printability, due to higher homogeneity and easier flow. For ex-situ prepared inks, more troubles were encountered. 1 wt.% natural extracts containing inks showed extremely poor flow and were not able to continuously print, whereas 5 wt.% natural extracts containing inks showed some nozzle obstruction, caused by poor homogeneity. CNF containing inks showed better flow and shape fidelity.

It was observed that the addition of natural extract resulted in a reinforcement effect in the mechanical properties of the material, significantly higher Young modulus and stress were observed. The addition of cellulose not only improved

printability and shape fidelity, but also strongly reinforced mechanical behavior.

8.7. References

[1] Ong G, Kasi R, Subramaniam R. A review on plant extracts as natural additives in coating applications. Prog Org Coatings 2021;151:106091. doi:10.1016/j.porgcoat.2020.106091.

[2] Wali AF, Alchamat HAA, Hariri HK, Hariri BK, Menezes GA, Zehra U, et al. Antioxidant, antimicrobial, antidiabetic and cytotoxic activity of crocus sativus L. petals. Appl Sci 2020;10:1519. doi:10.3390/app10041519.

[3] Lin Y-S, Lin W-S, Tung J-W, Cheng Y-C, Chang M-Y, Chen C, et al. Antioxidant capacities of jujube fruit seeds and peel pulp. Appl Sci 2020;10:6007. doi:10.3390/app10176007.

[4] Ahmed S, Ahmad M, Swami BL, Ikram S. A review on plants extract mediated synthesis of silver nanoparticles for antimicrobial applications: A green expertise. J Adv Res 2016;7:17–28. doi:10.1016/j.jare.2015.02.007.

[5] Santamaria-Echart A, Fernandes I, Barreiro F, Retegi A, Arbelaiz A, Corcuera MA, et al. Development of waterborne polyurethane-ureas added with plant extracts: Study of different incorporation routes and their influence on particle size, thermal, mechanical and antibacterial properties. Prog Org Coatings 2018;117:76–90. doi:10.1016/j.porgcoat.2018.01.006.

[6] Escobar-Ramos A, Lobato-García CE, Zamilpa A, Gómez-Rivera A, Tortoriello J, González-Cortazar M. Homoisoflavonoids and chalcones isolated from haematoxylum campechianum L., with spasmolytic activity. Molecules 2017;22:1–10. doi:10.3390/molecules22091405.

[7] Lampire O, Milla I, Raminosoa M, Michon V, Du Penhoat CH, Faucheur N, et al. Polyphenols isolated from the bark of castanea. Phytochemistry 1998;49:623–31.

[8] Petroviciu I, Vanden Berghe I, Cretu I, Albu F, Medvedovici A. Identification of natural dyes in historical textiles from Romanian collections by LC-DAD and LC-MS (single stage and tandem MS). J Cult Herit 2012;13:89–97. doi:10.1016/j.culher.2011.05.004.

[9] Puntener AG, Schlesinger U. Natural Dyes. In: Freeman HS, Peters AT, editors. Color. Non-Textile Appl. 1st ed., Elsevier; 2000, p. 382–455.

[10] Chiarini A, Micucci M, Malaguti M, Budriesi R, Ioan P, Lenzi M, et al. Sweet chestnut (Castanea sativa Mill.) bark extract: Cardiovascular activity and myocyte protection against oxidative damage. Oxid Med Cell Longev 2013;2013. doi:10.1155/2013/471790.

[11] Vekiari SA, Gordon MH, García-Macías P, Labrinea H. Extraction and determination of ellagic acid contentin chestnut bark and fruit. Food Chem 2008;110:1007–11. doi:10.1016/j.foodchem.2008.02.005.

[12] Kremer D, Kosalec I, Locatelli M, Epifano F, Genovese S, Carlucci G, et al. Anthraquinone profiles, antioxidant and antimicrobial properties of Frangula rupestris (Scop.) Schur and Frangula alnus Mill. bark. Food Chem 2012;131:1174–80. doi:10.1016/j.foodchem.2011.09.094.

[13] Ortiz-Hidalgo C, Pina-Oviedo S. Hematoxylin: Mesoamerica's gift to histopathology. Palo de Campeche (Logwood tree), pirates' most desired treasure, and irreplaceable tissue stain. Int J Surg Pathol 2019;27:4–14. doi:10.1177/1066896918787652.

[14] Lin LG, Liu QY, Ye Y. Naturally occurring homoisoflavonoids and their pharmacological activities. Planta Med 2014;80:1053–66. doi:10.1055/s-0034-1383026.

[15] Escobar-Ramos A, Lobato-García CE, Zamilpa A, Gómez-Rivera A, Tortoriello J, González-Cortazar M. Homoisoflavonoids and chalcones isolated from haematoxylum campechianum L., with spasmolytic activity. Molecules 2017;22:2–11. doi:10.3390/molecules22091405.

[16] Gonçalves RS, Silva EL, Hioka N, Nakamura CV, Bruschi ML, Caetano W. An optimized protocol for anthraquinones isolation from Rhamnus frangula L. Nat Prod Res 2018;32:366–9. doi:10.1080/14786419.2017.1356836.

[17] Kar A. Frangula-Buckthorn bark; Alder buckthorn; Black dogwood; Berry alder; Arrow wood; Persian berries 2012. http://www.epharmacognosy.com/2012/03/frangula-buckthorn-bark-alder-buckthorn.html (accessed June 22, 2021).

[18] Hou J, Ma Y, Zhang Z, Yang X, Huang M, Chai C. The relationship between solid content and particle size ratio of waterborne polyurethane. Coatings 2019;9:1–9. doi:10.3390/COATINGS9060401.

[19] Bao L, Fan H, Chen Y, Yan J, Zhang J, Guo Y. Synthesis of 1,4-butanediol di(3-diethylamino-2-hydroxylpropyl alcohol) ether and cationic waterborne polyurethane with high solids content. Adv Polym Technol 2018;37:906–12. doi:10.1002/adv.21736.

[20] Wang C, Zhang J, Huang J, Wang H, He M, Ding L. Flame retardant modified bio-based waterborne polyurethane dispersions derived from castor oil and soy polyol. Eur J Lipid Sci Technol 2021;123:1–7. doi:10.1002/ejlt.202000248.

[21] Peng SJ, Jin Y, Cheng XF, Sun TB, Qi R, Fan BZ. A new method to synthesize high solid content waterborne polyurethanes by strict control of bimodal particle size distribution. Prog Org Coatings 2015;86:1–10. doi:10.1016/j.porgcoat.2015.03.013.

[22] Díez-García I, Santamaría-Echart A, Eceiza A, Tercjak A. Synthesis and

characterization of environmentally-friendly waterborne poly(urethane-urea)s. Eur Polym J 2018;99:240–9. doi:10.1016/j.eurpolymj.2017.12.026.

[23] Lee J, Kim M, Hong CK, Shim SE. Measurement of the dispersion stability of pristine and surface-modified multiwalled carbon nanotubes in various nonpolar and polar solvents. Meas Sci Technol 2007;18:3707–12. doi:10.1088/0957-0233/18/12/005.

[24] González K, García-Astrain C, Santamaria-Echart A, Ugarte L, Avérous L, Eceiza A, et al. Starch/graphene hydrogels via click chemistry with relevant electrical and antibacterial properties. Carbohydr Polym 2018;202:372–81. doi:10.1016/j.carbpol.2018.09.007.

[25] Sharma T, Suresh Kumar G, Chon BH, Sangwai JS. Viscosity of the oil-in-water Pickering emulsion stabilized by surfactant-polymer and nanoparticle-surfactant-polymer system. Korea Aust Rheol J 2014;26:377–87. doi:10.1007/s13367-014-0043-z.

[26] Yang J, Pal R. Investigation of surfactant-polymer interactions using rheology and surface tension measurements. Polymers 2020;12:1–20. doi:10.3390/polym12102302.

[27] Jiang J, Oguzlu H, Jiang F. 3D printing of lightweight, super-strong yet flexible all-cellulose structure. Chem Eng J 2021;405:126668. doi:10.1016/j.cej.2020.126668.

[28] Ma T, Lv L, Ouyang C, Hu X, Liao X, Song Y, et al. Rheological behavior and particle alignment of cellulose nanocrystal and its composite hydrogels during 3D printing. Carbohydr Polym 2021;253:117217. doi:10.1016/j.carbpol.2020.117217.

[29] Vadillo J, Larraza I, Calvo-Correas T, Gabilondo N, Derail C, Eceiza A. Role of in situ added cellulose nanocrystals as rheological modulator of novel waterborne polyurethane urea for 3D-printing technology.

Cellulose 2021;28:4729–44. doi:10.1007/s10570-021-03826-6.

[30] Liu S, Bao H, Li L. Thermoreversible gelation and scaling laws for graphene oxide-filled κ-carrageenan hydrogels. Eur Polym J 2016;79:150–62. doi:10.1016/j.eurpolymj.2016.04.027.

[31] Cloitre M, Bonnecaze RT. A review on wall slip in high solid dispersions. Rheol Acta 2017;56:283–305. doi:10.1007/s00397-017-1002-7.

[32] Mishra AK, Chattopadhyay DK, Sreedhar B, Raju KVSN. FT-IR and XPS studies of polyurethane-urea-imide coatings. Prog Org Coatings 2006;55:231–43. doi:10.1016/j.porgcoat.2005.11.007.

[33] Santamaria-Echart A, Fernandes I, Saralegi A, Costa MRPFN, Barreiro F, Corcuera MA, et al. Synthesis of waterborne polyurethane-urea dispersions with chain extension step in homogeneous and heterogeneous media. J Colloid Interface Sci 2016;476:184–92. doi:10.1016/j.jcis.2016.05.016.

[34] Nasrollahzadeh M, Issaabadi Z, Sajadi SM. Green synthesis of a Cu/MgO nanocomposite by: Cassytha filiformis L. extract and investigation of its catalytic activity in the reduction of methylene blue, congo red and nitro compounds in aqueous media. RSC Adv 2018;8:3723–35. doi:10.1039/c7ra13491f.

[35] Rafiee Z, Barzegar M, Sahari MA, Maherani B. Nanoliposomal carriers for improvement the bioavailability of high – valued phenolic compounds of pistachio green hull extract. Food Chem 2017;220:115–22. doi:10.1016/j.foodchem.2016.09.207.

[36] Shabbir M, Islam SU, Bukhari MN, Rather LJ, Khan MA, Mohammad F. Application of Terminalia chebula natural dye on wool fiber—evaluation of color and fastness properties. Text Cloth Sustain 2017;2. doi:10.1186/s40689-016-0011-8.

[37] Santamaria-Echart A, Fernandes I, Ugarte L, Barreiro F, Corcuera MA, Eceiza A. Green nanocomposites from Salvia-based waterborne polyurethane-urea dispersions reinforced with nanocellulose. Prog Org Coatings 2021;150:105989. doi:10.1016/j.porgcoat.2020.105989.

[38] Pershin GN, Malovanova SN, Kakeeva OO. Antimicrobial activity of vinyloxyphenylazomethines. Russ Pharmacol Toxicol 1978;41:175.

[39] Živković J, Zeković Z, Mujić I, Vidovic S, Cvetkovič D, Lepojević Ž, et al. Scavenging capacity of superoxide radical and screening of antimicrobial activity of Castanea sativa mill. extracts. Czech J Food Sci 2010;28:61–8. doi:10.17221/155/2009-cjfs.

[40] Bacha A Ben, Jemel I, Moubayed NMS, Abdelmalek I Ben. Purification and characterization of a newly serine protease inhibitor from Rhamnus frangula with potential for use as therapeutic drug. Biotech 2017;7:1–13. doi:10.1007/s13205-017-0764-z.

[41] Yasunaka K, Abe F, Nagayama A, Okabe H, Lozada-Pérez L, López-Villafranco E, et al. Antibacterial activity of crude extracts from Mexican medicinal plants and purified coumarins and xanthones. J Ethnopharmacol 2005;97:293–9. doi:10.1016/j.jep.2004.11.014.

[42] Sadowska B, Paszkiewicz M, Podsędek A, Redzynia M, Rózalska B. Vaccinium myrtillus leaves and Frangula alnus bark derived extracts as potential antistaphylococcal agents. Acta Biochim Pol 2014;61:163–9. doi:10.18388/abp.2014_1939.

[43] Nejabatdoust A, Daemi HB, Salehzadeh A, Azimi SC. Comparing of effects of hydro-alcoholic , ethanolic , and methanolic extracts of the frangula alnus : Chemical composition , antimicrobial , and synergism 2020;6:20–33. doi:10.22080/jgr.2020.2538.

[44] Đukanović S, Cvetković S, Lončarević B, Lješević M, Nikolić B, Simin N, et al. Antistaphylococcal and biofilm inhibitory activities of Frangula

alnus bark ethyl-acetate extract. Ind Crops Prod 2020;158. doi:10.1016/j.indcrop.2020.113013.

[45] Zarayneh S, Sepahi AA, Jonoobi M, Rasouli H. Comparative antibacterial effects of cellulose nanofiber, chitosan nanofiber, chitosan/cellulose combination and chitosan alone against bacterial contamination of Iranian banknotes. Int J Biol Macromol 2018;118:1045–54. doi:10.1016/j.ijbiomac.2018.06.160.

Chapter 9

GENERAL CONCLUSIONS, FUTURE WORKS AND PUBLICATIONS

9. GENERAL CONCLUSIONS, FUTURE WORKS AND PUBLICATIONS

9.1. General Conclusions

The aim of this work was to study the possibility to use a waterborne polyurethane-urea for different 3D-printing techniques, by modulating its behavior by the addition of nanoreinforcements. In order to do so, different types of nanoreinforcements were prepared, and the effect of their type, content and incorporation method was analyzed.

After the synthesis process of a stable, biocompatible and high molecular weight WBPUU, Nanoreinforcements were prepared parting from cellulose and graphite, from which cellulose nanofibers, graphene and graphene oxide were obtained. Willing to improve matrix/reinforcement miscibility, carboxylation of the cellulose was carried out and cellulose nanofibers with different carboxylation degrees were obtained. The carboxylation of the CNF had an effect on the properties of the materials, showing modified fibers lower degradation temperatures, as well as lower crystallinity degree. In the case of the carbonaceous structures, after optimization process graphene, graphene oxide and reduced graphene oxide were successfully produced, however materials show defects being formed on their structure during the production process. All systems still showed great thermal stability proper of carbonaceous materials and, furthermore, G and rGO show electrical conductive capacity.

In order to first confirm a proper reinforcement effect supplied by the nanostructures, nanocomposite films were prepared. For WBPUU/CNF nanocomposite films, materials with enhanced properties were obtained. Moreover, the better compatibility of the matrix and the reinforcements show the promotion of interactions and furtherly enhanced mechanical and thermomechanical properties. For WBPUU/G and WBPU/GO nanocomposites, once again materials with improved properties were obtained,

showing UV-light shielding properties and good mechanical and thermomechanical behavior. The addition of graphene however, did not supply electrical conductivity to the nanocomposites, in order to do so a graphene or reduced graphene oxide coating was applied to the films, which proved good electrical conductivity.

Considering the good properties shown by the prepared nanocomposites, their use for filament production to be used in FDM 3D-printing was analyzed. Neat WBPUU showed extremely high flexibility, which in turns resulted in poor printability, due to problems in the feeding and extruding processes. The stronger materials produced by nanoreinforcements addition show promising capacity to show this problem. CNF reinforced materials, however, show poor flow during the extruding process and needed higher processing temperatures. As a result, slightly deteriorated filaments were obtained, which did not show sound enough properties for a good 3D-printing process. On the other hands, WBPUU/rGO composites showed a more constant extrusion process, which resulted in more homogeneous and less damaged structures. These filaments show more rigid behavior, which allow for a good printing process. The high temperatures during the 3D-printing process did, however, slightly affect the mechanical properties of the final parts. WBPUU/rGO filaments, either by ex-situ or in-situ preparation, showed potential to be used in the FDM, thanks to their good shown printability and shape fidelity.

WBPUU could also be a great candidate to be used in DIW 3D-printing, however, in order to do so, its rheology must be modulated. The rheological behavior was altered by the addition of CNF or rGO and carrageenan. Additives were incorporated via ex-situ and in-situ, and the effect of the incorporation method was analyzed. In both cases, inks prepared in-situ showed lower viscosities. This was explained by direct matrix/reinforcement interactions formed in in-situ preparations, whereas interactions in ex-situ preparation also included water, which allow for a more gel-like behavior. The overall more gel-

like behavior shown by rGO and carrageenan containing inks over CNF containing inks, resulted in 3D-printed parts with better shape fidelity. Materials with too low viscosity, often caused by low contents of reinforcements, showed poor printability, with lower layers being crushed It was also observed, that the more direct interactions formed in in-situ preparations improved the mechanical behavior of the final 3D-printed parts.

Willing to further benefit from the use of WBPUU in DIW and as another way of rheological modulation, high solid content dispersions were prepared. In order to further potentiate the WBPUU properties for the biomedical field, natural extracts were added to supply it with bioactive behavior. Extracts obtained from three different plants were employed, namely logwood, chestnut and alder buckthorn. The high solid content of polyurethane resulted in extremely high viscosities, which were somewhat reduced by the addition of the extracts. The incorporation method also had a big impact in the rheological behavior of the inks. Inks presented very altered rheologies, depending on the amount type and incorporation method of the extracts. The different rheologies translated into different degrees of success in the printing process. Overall, inks with lower contents of extract did not allowed for a good printing process, due to poor flow, and higher contents sometimes show dispersability problems. In-situ prepared inks show better printability, which was further enhanced by the addition of CNF. 3D-printed parts show significantly enhanced mechanical properties with the addition of inks, more pronounce for logwood extract. Moreover, all systems show good bacteriostatic behavior, and for higher extract content bactericide behavior was also seen.

9.2. Future works

Based on results obtained in this work and with the aim of continuing with the research in this field, different proposals are displayed, which can complete this work more thoroughly as well as can lead to suitable new outlines for other woks related with this field:

- The further optimization process of WBPUU/CNF filaments printing by FDM, by using a different feeding method and the obtaining of less damaged filaments.
- The further study of the biocompatibility of the materials, in order to continue analyzing the use of these materials for the biomedical field. In this regards, biocompatibility test for printed material should be carried out.
- The preparation of graphene/CNF hybrid inks and the study of their used in DIW 3D-printing, to study the synergic effect of both reinforcements in both the rheological behavior of the materials, as well as the properties of the final 3D-printed parts.
- The preparation of inks containing plant extracts with lower solid contents, and modulating rheology with addition of CNF. In order to produced materials with higher inhibition capacity and better shape fidelity.

9.3. List of publications and communications

9.3.1. List of publications

Authors:	Izaskun Larraza, Julen Vadillo, Tamara Calvo-Correas, Álvaro Tejado, Sheyla Olza, Cristina Peña-Rodríguez, Aitor Arbelaiz, Arantxa Eceiza
Title:	Cellulose and Graphene Based Polyurethane Nanocomposites for FDM 3D Printing: Filament Properties and Printability
Journal:	Polymers
Year:	2021
Impact factor:	4.329 (JCR 2020)
Rank:	POLYMER SCINCE 18/88 (JCR 2020)

Authors:	Izaskun Larraza, Borja Alonso-Lerma, Kizkitza Gonzalez, Nagore Gabilondo, Raúl Perez-Jimenez, María Angeles Corcuera, Aitor Arbelaiz, Arantxa Eceiza
Title:	Waterborne polyurethane and graphene/graphene oxide based nanocomposites: Reinforcement and electrical conductivity

Journal:	eXPRESS Polymer Letters
Year:	2020
Impact factor:	4.161 (JCR 2020)
Rank:	POLYMER SCIENCE 20/88 (JCR 2020)

Authors:	Izaskun Larraza , Lorena Ugarte, Aintzane Fayanas, Nagore Gabilondo , Aitor Arbelaiz, María Angeles Corcuera, Arantxa Eceiza
Title:	Influence of Process Parameters in Graphene Oxide Obtention on the Properties of Mechanically Strong Alginate Nanocomposites
Journal:	Materials
Year:	2020
Impact factor:	3.623 (JCR 2020)
Rank:	PHYSICS, CONDENSED MATTER 27/69 (JCR 2020) METALLURGY & METALLURGICAL ENGINEERING 17/80 (JCR 2020) CHEMISTRY, PHYSICAL 79/162 (JCR 2020) PHYSICS, APPLIED 51/160 (JCR 2020) MATERIALS SCIENCE, MULTIDISCIPLINARY 152/333 (JCR 2020)

Authors:	Izaskun Larraza, Julen Vadillo, Arantzazu Santamaria-Echart, Álvaro Tejado, Maider Azpeitia , Eneritz Vesga, Ander Orue, Ainara Saralegi, Aitor Arbelaiz, Arantxa Eceiza
Title:	The Effect Of The Carboxylation Degree On Cellulose Nanofibers And Waterborne Polyurethane/Cellulose Nanofiber Nanocomposites Properties
Journal:	Polymer Degradation and Stability
Year:	2020
Impact factor:	5.030 (JCR 2020)
Rank:	POLYMER SCIENCE 12/88 (JCR 2020)

Collaborations

Authors:	Julen Vadillo, Izaskun Larraza, Tamara Calvo-Correas, Nagore Gabilondo, Maud Save, Christophe Derail, Arantxa Eceiza
Title:	Design of a Waterborne Polyurethane–Urea Ink for Direct Ink Writing 3D Printing
Journal:	Materials
Year:	2021
Impact factor:	3.623 (JCR 2020)
Rank:	PHYSICS, CONDENSED MATTER 27/69 (JCR 2020) CHEMISTRY, PHYSICAL 79/162 (JCR 2020) MATERIALS SCIENCE, MULTIDISCIPLINARY 152/333 (JCR 2020)

Authors:	Tamara Calvo-Correas, Lorena Ugarte, Izaskun Larraza, Cristina Peña-Rodríguez, María Angeles Corcuera, Arantxa Eceiza
Title:	Residues from rigid foams and graphene for the synthesis of hybrid polyurethane flexible foams composites
Journal:	Journal of Materials Research and Technology
Year:	2021
Impact factor:	5.039 (JCR 2020)
Rank:	MATERIALS SCIENCE, MULTIDISCIPLINARY 104/333 (JCR 2020) METALLURGY & METALLURGICAL ENGINEERING 9/80 (JCR 2020)

Authors:	Julen Vadillo, Izaskun Larraza, Tamara Calvo-Correas, Nagore Gabilondo, Maud Save, Christophe Derail, Arantxa Eceiza
Title:	Role of in situ added cellulose nanocrystals as rheological modulator of novel waterborne polyurethane urea for 3Dprinting technology
Journal:	Cellulose

Year:	2021
Impact factor:	5.044 (JCR 2020)
Rank:	MATERIALS SCIENCE, PAPER & WOOD 1/22 (JCR 2020) MATERIALS SCIENCE, TEXTILES 2/25 (JCR 2020) POLYMER SCIENCE 1/88 (JCR 2020)
Authors:	Borja Alonso-Lerma, Izaskun Larraza, Leire Barandiaran, Lorena Ugarte, Ainara Saralegi, María Angeles Corcuera, Raúl Perez-Jimenez, Arantxa Eceiza
Title:	Enzymatically produced cellulose nanocrystals as reinforcement for waterborne polyurethane and its applications
Journal:	Carbohydrate Polymers
Year:	2021
Impact factor:	9.381 (JCR 2020)
Rank:	POLYMER SCIENCE 3/88 (JCR 2020) CHEMISTRY, ORGANIC 3/57 (JCR 2020) CHEMISTRY, APPLIED 4/74 (JCR 2020)
Authors:	Borja Alonso-Lerma, Leire Barandiaran, Lorena Ugarte, Izaskun Larraza, Antonio Reifs, Raquel Olmos-Juste, Nerea Barruetabeña, Iban Amenabar, Rainer Hillenbrand, Arantxa Eceiza, Raul Perez-Jimenez
Title:	High performance crystalline nanocellulose using an ancestral endoglucanase
Journal:	Communication Materials
Year:	2020
Impact factor:	N/A
Rank:	N/A
Authors:	Julen Vadillo, Izaskun Larraza, Aitor Arbelaiz, María Angeles Corcuera, Maud Save, Christophe Derail, Arantxa Eceiza

Title:	Influence of the addition of PEG into PCL-based waterborne polyurethane-urea dispersions and films properties
Journal:	Journal of Applied Polymer Science
Year:	2019
Impact factor:	3.125 (JCR 2020)
Rank:	POLYMER SCIENCE 35/88 (JCR 2020)

9.3.2. Conferences

Authors:	Izaskun Larraza, Julen Vadillo, Kizkitza Gonzalez, Álvaro Tejado, Ainara Saralegi, María Angeles Corcuera, Aitor Arbelaiz, Arantxa Eceiza
Title:	Green Waterborne Polyurethane Nanocomposites Reinforced with Cellulose and Graphene: Synthesis and Characterization
Conference:	7th International COnference on BIOdegradable and BIObased POLymers
Contribution:	Poster Communication
Year:	2019
Place:	Stockholm (Sweden)

Authors:	Izaskun Larraza, Kizkitza Gonzalez, Tamara Calvo-Correas, María Angeles Corcuera, Aitor Arbelaiz, Arantxa Eceiza
Title:	Efecto de la Incorporación de Grafeno y Oxido de Grafeno en las Propiedades de Poliuretanos en Base Agua
Conference:	X Congreso de Jóvenes Investigadores en Polímeros
Contribution:	Oral Communication
Year:	2019
Place:	Burgos (España)

Authors:	Izaskun Larraza, Julen Vadillo, Oihane Echeverria, Álvaro Tejado, Maider Azpeitia, Eneritz Vesga, Ander Orue, Aitor Arbelaiz, Arantxa Eceiza
Title:	Synthesis and characterization of a waterborne polyurethane reinforced with chemically modified cellulose nanofibers

Conference:	10th ECNP International Conference of Nanostructured Polymers and Nanocomposites
Contribution:	Poster Communication
Year:	2018
Place:	Donostia (Spain)

Authors:	Izaskun Larraza, Julen Vadillo, Oihane Echeverria, Alvaro Tejado, Maider Azpeitia, Eneritz Vesga, Ander Orue, Aitor Arbelaiz, Arantxa Eceiza
Title:	Synthesis and characterization of a waterborne polyurethane reinforced with chemically modified cellulose nanofibers
Conference:	6th Young Polymer Scientist Conference
Contribution:	Oral Communication
Year:	2018
Place:	Donostia (Spain)

Authors:	Izaskun Larraza, Julen Vadillo, Oihane Echeverria, Alvaro Tejado, Maider Azpeitia, Eneritz Vesga, Ander Orue, Aitor Arbelaiz, Arantxa Eceiza
Title:	Reinforcement of a waterborne polyurethane matrix with carboxylated nanofibers and the effect of the carboxylation degree
Conference:	International Conference on Materials & Energy – Icome
Contribution:	Poster Communication
Year:	2018
Place:	Donostia (Spain)

Collaborations

Authors:	Julen Vadillo, Izaskun Larraza, Aitor Arbelaiz, María Angeles Corcuera, Maud Save, Christophe Derail, Arantxa Eceiza
Title:	Effect Of PCL/PEG Ratio On The Properties Of Waterbore Polyurethane-Urea Dispersions
Conference:	9th Conference Green Chemistry and Nanotechnologies in Polymeric Materials

Contribution:	Poster Communication
Year:	2018
Place:	Krakow (Poland)

Authors:	Gabriel Arner, Izaskun Larraza, Olatz Guaresti, Leire Urbina, Aloña Retegi, Arantxa Eceiza, Nagore Gabilondo
Title:	Bacterial Cellulose Nanofibrils Embedded In In-Situ Formed Chitosan/Alginate Particles
Conference:	10th ECNP International Conference of Nanostructured Polymers and Nanocomposites
Contribution:	Poster Communication
Year:	2018
Place:	Donostia (Spain)

Authors:	Aitor Arbelaiz, Gurutz Mondragon, Izaskun Larraza, Cristina Peña-Rodríguez, Arantxa Eceiza
Title:	Characterization of cellulosic samples obtained from sisal fibers
Conference:	XII Congreso Nacional de Materiales Compuestos – MATCOMP
Contribution:	Oral Communication
Year:	2017
Place:	Donostia (Spain)

ANNEXES

LIST OF TABLES

Chapter 3. WBPUU synthesis and nanoentities preparation

Chapter 4. WBPUU/CNF nanocomposite films and filaments for FDM 3D printing

Chapter 5. WBPUU/CNF nanocomposite inks for direct inks writing 3D printing

Chapter 6. WBPUU/carbonaceous nanostructures nanocomposite films and filaments for FDM 3D printing

Chapter 7. WBPUU/carbonaceous nanostructures inks for direct inks writing 3D printing

Chapter 8. Incorporation of bioactive plant extracts to WBPUU inks for 3D printing

LIST OF FIGURES

Chapter 1. Introduction

Chapter 2. Materials and methods

Chapter 3. WBPUU synthesis and nanoentities preparation

Chapter 5. WBPUU/CNF nanocomposite inks for direct inks writing 3D printing

Chapter 6. WBPUU/carbonaceous nanostructures nanocomposite films and filaments for FDM 3D printing

Chapter 7. WBPUU/carbonaceous nanostructures inks for direct inks writing 3D printing

Chapter 8. Incorporation of bioactive plant extracts to WBPUU inks for 3D printing

LIST OF ABBREVIATIONS

3D Printing	Three-dimensional printing
AB	Alder buckthorn
AFM	Atomic force microscopy
AM	Additive manufacturing
ANOVA	Two-way analysis of variance
bHKP	Bleached hardwood kraft pulp
CAD	Computer-aided design
CAR	Carrageenan
CI	Crystallinity index
CN	Chestnut
CNC	Cellulose nanocrystals
CNF	Cellulose nanofibers
DABCO	1,4-diazabicyclo octane
DBTDL	Dibutyltin dilaurate
DIW	Direct ink writing
DMA	Dynamic mechanical analysis
DMPA	2,2-bis(hydroxymethyl) propionic acid
DMSO	Dimethyl sulfoxide
DSC	Differential scanning calorimetry
E. Coli	Escherichia coli
EA	Elemental analysis
EDA	Ethylendiamine

EFM	Electrostatic force microscopy
FDM	Fused deposition modeling
FTIR	Fourier transform infrared spectroscopy
G	Graphene
GO	Graphene oxide
GPC	Gel permeation chromatography
Gr	Graphite
HRTEM	High resolution transmission electron microscopy
HS	Hard segment
IPDI	Isophorone diisocyante
LW	Logwood
MDI	4,4'-diphenylmethane diisocyanate
NMP	n-methyl pyrrolidone
PI	Polydispersity index
PU	Polyurethanes
PUU	Polyurethane-urea
rGO	Reduced graphene oxide
S. Aureus	Staphylococcus aureus
SEM	Scanning electron microscopy
SnOc	Stannous octoate
SS	Soft segment
TDI	Toluene diisocyanate
TEA	Tryethylamine

TEM	Transmission electron microscopy
TGA	Thermogravimetric analysis
UV-Vis	Ultraviolet-visible spectrophotometry
VOC	Volatile organic compounds
WBPU	Waterborne polyurethanes
WBPUU	Waterborne polyurethane-ureas
XRD	X-ray diffraction

LIST OF SYMBOLS

η	Viscosity
$\dot{\gamma}$	Shear rate
$\dot{\gamma}_n$	Shear rate on the nozzle
γ_{nz}	Shear rate on the wall of the nozzle
τ	Shear Stress
K	Consistency index
n	Flow index
λ	Incident radiation wavelength
d	Distance between two successive planes the crystal
θ	Angle of incidence of the primary rays.
T_{gSS}	Glass transition temperature of the soft segment
T_{HS}	Melting temperature of the hard segment
ΔH_{HS}	Melting enthalpy of the hard segment
T_0	Onset degradation temperature
T_d	Maximum degradation temperature
E	Young modulus
σ_y	Stress at yield
σ_b	Stress at break
ε_b	Elongation at break
Ø	Diameter
A	Area
L	Length

h	Height
R	Electrical resistance
ρ	Resistivity
σy	Conductivity
I_D/I_G	Intensity ratio of D and G bands
L_a	Size of the sp^2 domain crystals
G'	Storage modulus
G''	Loss modulus
tan δ	Tangent of phase angle
E'	Storage modulus
E''	Loss modulus
M_W	Molecular weight

Polyurethane-ureas are very versatile polymers that can be process in many ways and used in an extremely wide field of applications. At the same time, 3D printing offers the opportunity to make one on one personalized designs, a quality remarkably beneficial for the biomedical field. In this work, the use of a waterborne polyurethane-urea synthesized for its used in 3D printing is studied.

The addition of different nanoentities is analyzed, such as cellulose nanofibers, carboxylated nanofibers, graphene oxide, graphene and natural extracts and their effect on the printability and properties of the materials is assessed. The potential of these nanocomposites for two 3D printing methods is analyzed, namely fused deposition modeling and direct ink writing.

eman ta zabal zazu

Universidad del País Vasco

Euskal Herriko Unibertsitatea